



**HAL**  
open science

# Irradiation effect in triple junction solar cells for spatial applications

Seonyong Park

► **To cite this version:**

Seonyong Park. Irradiation effect in triple junction solar cells for spatial applications. Atomic Physics [physics.atom-ph]. Université Paris Saclay (COMUE), 2018. English. NNT : 2018SACLX039 . tel-02024207

**HAL Id: tel-02024207**

**<https://pastel.hal.science/tel-02024207>**

Submitted on 19 Feb 2019

**HAL** is a multi-disciplinary open access archive for the deposit and dissemination of scientific research documents, whether they are published or not. The documents may come from teaching and research institutions in France or abroad, or from public or private research centers.

L'archive ouverte pluridisciplinaire **HAL**, est destinée au dépôt et à la diffusion de documents scientifiques de niveau recherche, publiés ou non, émanant des établissements d'enseignement et de recherche français ou étrangers, des laboratoires publics ou privés.

# Influence de l'irradiation dans les cellules solaires triple jonctions pour des applications spatiales

Thèse de doctorat de l'Université Paris-Saclay  
préparée à École Polytechnique

École doctorale n°573 Interfaces : approches interdisciplinaires,  
fondements, applications et innovations (Interfaces)  
Spécialité de doctorat : Physique

Thèse présentée et soutenue à Palaiseau, le 10 juillet 2018, par

**M. Seonyong Park**

Composition du Jury :

M. Yvan Bonnassieux Professeur, LPICM, École Polytechnique	Président
Mme. Marie France Barthe Directrice de recherche, CEMHTI, CNRS	Rapporteur
M. Stefan Janz Chef du département, Fraunhofer ISE	Rapporteur
M. Claus Zimmermann Expert senior, Airbus DS GmbH	Examineur
M. Carsten Baur Ingénieur, ESA ESTEC	Examineur
M. Erik Johnson Chargé de recherche, LPICM, École Polytechnique	Examineur
M. Bruno Boizot Responsable accélérateur, LSI, École Polytechnique	Directeur de thèse
M. Victor Khorenko Chef de projet R&D, AZUR Space Solar Power GmbH	Invité





THESE DE DOCTORAT  
DE L'UNIVERSITE PARIS-SACLAY

Préparée à

L'ECOLE POLYTECHNIQUE

ECOLE DOCTORALE N°573  
Interfaces (EDI)

Spécialité de doctorat : Physique

par

Seonyong Park

Influence de l'irradiation dans les cellules solaires  
triple junctions pour les applications spatiales

Cette thèse a été soutenue le 10 juillet 2018 à 14h00  
Amphithéâtre Becquerel – Ecole Polytechnique

Composition du jury :

Marie France Barthe	(CNRS CEMHTI Orléans)	Rapporteur
Stefan Janz	(Fraunhofer ISE)	Rapporteur
Yvan Bonnassieux	(Ecole Polytechnique)	Président du jury
Erik Johnson	(Ecole Polytechnique)	Examineur
Claus Zimmermann	(Airbus Defence and Space)	Examineur
Carsten Baur	(ESA ESTEC)	Examineur
Victor Khorenko	(Azurspace Solar Power)	Invité
Bruno Boizot	(Ecole Polytechnique)	Directeur de thèse



# *Acknowledgements*

I firstly want to thank Dr. Stefan Janz and Dr. Marie France Barthe, who accepted to review this thesis manuscript, as well as Pr. Yvan Bonnassieux, Dr. Erik Johnson, Dr. Claus Zimmermann, Dr. Carsten Baur for accepting to be part of jury and Dr. Victor Khorenko for accepting the invitation.

I am most grateful to my supervisor, Dr. Bruno Boizot, for his excellent guiding throughout these three years and half. You were always so patient even when I was little bit lost and you led me to the good direction. I would also express my greatest gratitude for that you gave me a lot of opportunities such as to participate in several European projects, to attend to big international conferences and so many big and small things. I want to thank Dr. Jacques C. Bourgoin for his insightful guidance on tricky questions related to radiation induced defects in LILT condition. A great part of my thesis could be succeeded thanks to his effort.

I am indebted to Olivier Cavani who is the true master of electron accelerator. Without his work, it was impossible to obtain such nice experimental results. Whenever I had a trouble or difficulty with my equipment, you always brought me generous solutions! Your problem-solving thinking has inspired me tremendously.

I dearly thank Prof. Kyu Chang Park who taught me during the first year of master degree. You permitted for me to freely explorer the experimental physics and again I thank Dr. Erik Johnson for accepting me as an internship student in your team. It was a great chance for me to start the solar cell physics. In addition, I want to thank all professors at Kyung-Hee University and at Ecole Polytechnique who taught me invaluable courses. Your classes contributed a lot to make me a professional person to physics, material science and electrical engineering from my undergraduate to master period.

I am sincerely thankful to all my French speaking colleagues! You trained me a lot (even if you weren't aware of it). C'est devenu mon grand atout et ma capacité importante.

Throughout my studying in France, I was never lonely because I had many priceless best friends Jinwoo Choi, Heechul Woo, Heejae Lee, Heeryung Lee and all from EP-KHU program. Especially, I can't imagine how it would be different if Thomas Sanghyuk Yoo was not here. Thank you all for spending your precious time with me. I will never regret spending a huge part of my '**jeunesse**' at LSI, Ecole Polytechnique Campus and in France. I also thank my friends in Korea, in France and in all of the world, and my parents and sister who have always believed me and cheered me up. Your support has become a great energy for me.

Et fin vraiment, merci beaucoup Virginie, j'exprime ma chaleureuse reconnaissance à toi pour ton soutien et support avec une grande patience et ton grand amour. Si je n'étais pas avec toi, comment pourrais-je supporter ses longues années de doctorat ? Je ne peux même pas l'imaginer. Également, je saurais gré à ta famille qui m'a inconditionnellement encouragé.

# Content

<b>Acknowledgements</b> .....	<b>5</b>
<b>General introduction</b> .....	<b>9</b>
<b>1 Fundamentals of solar cells for space applications</b> .....	<b>13</b>
1.1 Basics of Photovoltaics .....	14
1.1.1 Basic solar cell equations .....	14
1.1.2 Diffusion current .....	18
1.1.3 Generation-recombination current.....	20
1.1.4 Temperature dependence of solar cells.....	22
1.1.5 Spectral response of PN solar cells.....	24
1.2 Theoretical aspect of radiation damage .....	27
1.2.1 Displacement damage and atomic displacement .....	28
1.2.2 Primary and secondary displacements.....	30
1.2.3 Ionization.....	33
1.3 Nature of irradiation-induced defects in solar cell materials .....	34
1.3.1 Production of defects in n- and p-doped Gallium-Arsenide (GaAs) .....	35
1.3.2 Production of defects in n- and p-doped Gallium-Indium-Phosphide (GaInP) .....	40
1.3.3 Production of defects in n- and p-doped Germanium (Ge) .....	45
1.4 Mechanism of the degradation induced by the defects .....	49
1.4.1 Effects in carrier lifetime and diffusion length.....	49
1.4.2 Effects in properties of solar cells .....	50
1.5 Simulation of radiation effects in solar cells.....	51
1.5.1 The concept of equivalent damage (JPL method) .....	51
1.5.2 The concept of displacement damage dose (NRL method).....	51
Conclusion of the chapter 1 .....	52
Reference.....	54
<b>2 Experimental details and Materials</b> .....	<b>58</b>
2.1 Low Intensity Low Temperature (LILT) measurement system setup .....	59
2.1.1 Irradiation Facilities.....	60
2.1.2 Solar Simulator.....	64
2.1.3 Cryostat Chamber and measurement units .....	67

2.2	Structure of lattice matched GaInP/GaAs/Ge triple junction solar cell .....	69
2.3	Photon recycling effect in a component cell.....	71
2.4	In-situ characterization of TJ cells and its component cells .....	75
2.4.1	Indirect temperature measurement .....	75
2.4.2	Beginning Of Life performance of the cells .....	79
2.4.3	Electron and proton irradiation campaigns.....	83
	References .....	89
<b>3</b>	<b>Proton irradiation .....</b>	<b>90</b>
3.1	Proton irradiation of TJ cells in LILT conditions .....	92
3.1.1	Analysis of I-V characteristics before and after 1 MeV proton irradiations .....	93
3.1.2	Degradation of key parameters in TJ cells .....	94
3.2	Approach to the component cells.....	95
3.2.1	Degradation of $I_{SC}$ and $V_{OC}$ at different temperatures .....	95
3.2.2	Electric field dependence of I-V characteristics .....	100
3.2.3	Orientation dependence of proton irradiation.....	102
3.2.4	Isochronal annealing in component cells.....	108
3.3	Discussion of the chapter 3 .....	110
3.3.1	Temperature and fluence dependences of the degradation.....	110
3.3.2	Recovery of proton irradiation-induced defects .....	113
3.3.3	Recombination of photo generated current by irradiation-induced defects.....	114
	Conclusion of the chapter 3.....	116
	Reference.....	117
<b>4</b>	<b>Electron irradiation.....</b>	<b>119</b>
4.1	Irradiation of TJ cells in LILT conditions.....	120
4.1.1	Analysis of I-V characteristics before and after 1 MeV electron irradiations .....	121
4.1.2	Degradation of key parameters in TJ cells .....	125
4.2	Approach to the component cells.....	126
4.2.1	Degradation of $I_{SC}$ and $V_{OC}$ at different temperatures .....	126
4.2.2	The excess leakage current in dark I-V characteristics.....	128
4.3	Annealing effect of electron irradiated cells .....	133
4.4	Discussion of the chapter 4 .....	134
4.4.1	Uncertainty of the TJ cell degradation induced by electron irradiations .....	134
4.4.2	Origin of the excess current.....	135
	Conclusion of the chapter 4.....	136

Reference.....	138
<b>5 General discussion.....</b>	<b>140</b>
5.1 Comparison of electron and proton irradiation in LILT conditions.....	141
5.2 Distribution of BOL and EOL data set: Case of electron and proton irradiated TJ cells	149
5.3 Correlation of radiation induced defects with electrical property of the solar cell	151
Conclusion of the chapter 5.....	153
Reference.....	154
<b>General Conclusions .....</b>	<b>155</b>
<b>Annexe – Résumé de thèse en français.....</b>	<b>157</b>
<b>List of Publications.....</b>	<b>162</b>
<b>List of Figures .....</b>	<b>163</b>
<b>List of Tables.....</b>	<b>167</b>

# *General introduction*

The history of solar cell has begun since 1839 by a great discovery of a French physicist Edmond Becquerel about the production of an electrical charge in solution by the light source. Then, during the late 19<sup>th</sup> century, there were some scientific researches related to the photovoltaic (PV) effect. For example, a discovery of PV effect in solids at 1870 and a discovery of a Selenium PV with ~1 % efficiency at 1880. However, these scientific works did not gain a big interest from the energy industry. At 1905, Albert Einstein published an article about the photoelectric effect based on the quantum bias. Much later, at 1950, there was a great improvement on single crystal solar cell using a crystallization technique called as Czochralski (CZ) Method developed by a Polish chemist Jan Czochralski. Since then, the solar cell technology has been highlighted as a new source to generate electricity. The photo conversion efficiency was hugely increased up to more than 10 % thanks to the CZ crystallization method. Few years later, the first practical solar cell based on a single crystal silicon was invented by Bell Labs at 1950s. This solar cell was designed to be equipped to a satellite, having an average efficiency of 10 %.



Figure 0-1. the first solar powered satellite Vanguard 1<sup>1</sup>.

The satellite named Vanguard 1 was the first solar cell powered satellite (and 4<sup>th</sup> artificial Earth satellite). The Vanguard 1 was launched at 1958 and is still orbiting the Earth! This event is generally considered as a birth of commercial space application of PV. After few decades, at 1970s, the energy crisis occurred and this triggered the research on PV. As shown in Figure 0-2, since late 1970s, many researchers have been dedicated to the development of PV technologies. Today, in many different ways (based on silicon, germanium, III-V compounds such as GaAs, CIGS, CdTe, dye sensitized cells, perovskite cells, ...), researches are ongoing to extend the knowledge on PV and to apply it as a renewable energy source.

---

<sup>1</sup> <https://nssdc.gsfc.nasa.gov/nmc/spacecraftDisplay.do?id=1958-002B>

Early age of space industry, on the most of solar powered satellites, single crystalline silicon based solar panels were equipped. However, the silicon based solar cell inherently exhibited worse characteristics under the low temperature, the weak light intensity and radiation exposure condition than gallium arsenide (GaAs) based solar cells. One of main reasons of not using the GaAs crystal is because of the expensive cost for the fabrication such as MBE and MOCVD processes.

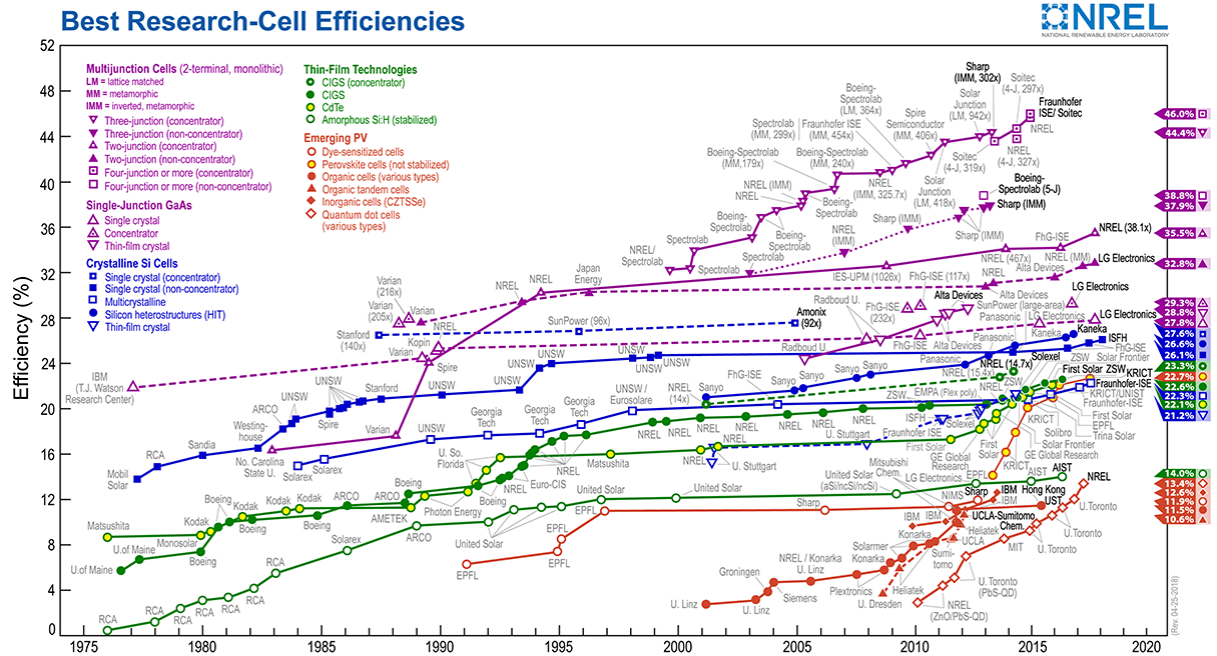


Figure 0-2. Chart of best research-cell efficiencies updated by NREL at 25/04/2018<sup>2</sup>.

Once these technologies become matured, the GaAs based solar cells have been used widely for solar powered satellites (SPS) and concentrated photovoltaics (CPVs). For both SPS and CPVs, the highest achievable efficiency was the main interest. Consequently, multijunction cells were developed at the beginning of 2000s, and today, the state of the art multijunction cell is so called triple junction solar cells based on gallium-arsenide (GaAs), gallium-indium-phosphor (GaInP) and germanium (Ge). More recently, NASA launched a space probe named Juno at 2011 for the explorer mission of the Jupiter.

<sup>2</sup> <https://www.nrel.gov/pv/>



Figure 0-3. Juno mission to Jupiter (2010 Artist's concept)<sup>3</sup>.

The GaInP/GaAs/Ge based triple junction solar cell was first used for the deep space explorer mission. In succession to Juno, ESA will launch their spacecraft at 2022. The mission named JUICE<sup>4</sup> is the first large class mission in ESA's cosmic vision 2015-2025 program to explore the gigantic gaseous planet Jupiter and its moons, Ganymede, Callisto and Europa. The Jupiter's environment which is called as Jovian system is surrounded by a huge magnetic field of the Jupiter. Particles such as electrons and protons which are come out from the Sun are captured by the magnetic field, and then get accelerated by Lorentz force. Up to here, the situation sounds similar to the orbit of the earth. However, it must be also considered that Jupiter is very far from the Sun and that the intensity of the solar spectrum is going down to only 3.7 % of AM0. Furthermore, the absolute temperature in average is about 120 K near Jupiter, while the average temperature near the Earth is supposed to be 300 K. In order to successfully perform the ESA missions, evaluating an accurate end of life performance of the solar cell which will be equipped to the spacecraft is one of the prime importance. In this frame, LSI has participated to the JUICE annealing verification study, performing the electron irradiation with their SIRIUS electron accelerator and the proton irradiation at CSNSM in University of Paris-Sud in Orsay.

---

<sup>3</sup> <https://www.jpl.nasa.gov/news/news.php?feature=4818>

<sup>4</sup> Jupiter Icy Moon Explorer



Figure 0-4. Artist's impression of JUICE mission<sup>5</sup>.

Performing the irradiation test on the state of the art GaInP/GaAs/Ge triple junction (TJ) solar cell for JUICE mission, scientific questions concerning their behavior in deep space condition like near Jupiter have arisen. Thus, through this thesis work, we will try to find answers to some questions like defects generation in complex TJ solar cells as a function irradiation temperature, fluences and the nature of the particle and the influence of these defects on the TJ cells electrical properties. For that purpose, the **Chapter 1** will present some fundamental knowledge to understand the physics of solar cell, theory of radiation damage, nature of radiation induced defects in semiconductors, and the simulation of solar cell degradation by radiation exposure in space. In **chapter 2**, we will be introducing irradiation facilities and experimental instruments for measurements. Then, non-irradiated samples will be described. Lastly, the irradiation steps and data treatment will be discussed. Subsequently, we will be separately focusing on the aspect of electron and proton irradiations of TJ solar cells in Low Intensity Low Temperature (LILT) conditions in **chapter 3** and **chapter 4**, respectively. In **chapter 5**, we will generally discuss the effect of electron and proton irradiations, correlating the degradation with nature of radiation induced defects. At the end of this book, we will briefly conclude our research and let some perspectives to be continued in near future.

---

<sup>5</sup> <http://sci.esa.int/juice/59935-juice-ground-control-gets-green-light-to-start-development-of-jupiter-operations/>

# *1 Fundamentals of solar cells for space applications*

1.1	Basics of Photovoltaics .....	14
1.1.1	Basic solar cell equations .....	14
1.1.2	Diffusion current .....	18
1.1.3	Generation-recombination current.....	20
1.1.4	Temperature dependence of solar cells.....	22
1.1.5	Spectral response of PN solar cells.....	24
1.2	Theoretical aspect of radiation damage .....	27
1.2.1	Displacement damage and atomic displacement .....	28
1.2.2	Primary and secondary displacements.....	30
1.2.3	Ionization.....	33
1.3	Nature of irradiation-induced defects in solar cell materials .....	34
1.3.1	Production of defects in n- and p-doped Gallium-Arsenide(GaAs) .....	35
1.3.2	Production of defects in n- and p-doped Gallium-Indium-Phosphide(GaInP) .....	40
1.3.3	Production of defects in n- and p-doped Germanium (Ge) .....	45
1.4	Mechanism of the degradation induced by the defects .....	49
1.4.1	Effects in carrier lifetime and diffusion length.....	49
1.4.2	Effects in properties of solar cells .....	50
1.5	Simulation of radiation effects in solar cells.....	51
1.5.1	The concept of equivalent damage (JPL method) .....	51
1.5.2	The concept of displacement damage dose (NRL method).....	51
	Conclusion of the chapter 1 .....	52
	Reference.....	54

The aim of this chapter is to understand the working principle of solar cell and impact of defects induced by radiation on its physical and electrical properties. Therefore, in the physics of photovoltaics, we will first discuss the electrical description of photovoltaic device using the knowledge in semiconductors, then the physics of radiation damage in semiconductor and defect creation in some key solar cell materials will be described. Finally, combining all these aspects, we will describe simulation techniques which are currently well adapted to the space solar cell research and industry.

## 1.1 Basics of Photovoltaics

Photovoltaics means by the definition that the conversion of light energy into the electricity occurring in semiconducting materials. It is also referred as photovoltaic effects, and when this type of semiconducting materials is used for the purpose of harvesting light energy, it is called solar cell (or solar panel for large area with interconnection). These days, photovoltaic effects are being studied in several domains not only in physics, but also photochemistry and electrochemistry. In addition, there exists numerous different solar cells architecture from inorganic solar cells based on Silicon (Si) or III-V compounds to recently highlighted Perovskite solar cells [1]. Inorganic solar cells are now well commercialized while other solar cell technologies are still in development by a lot of researchers in the world. In principle, solar panels are installed where sustainable energy production is required. For terrestrial use, a solar settlement system on roofs can be considered for examples for cities and solar farms (also known as a photovoltaics power station) in case of large scale areas such as deserts and agricultural areas. For spatial use, solar panels are equipped to the body of satellites and spacecrafts or installed as wings which can be rotated to maximize the absorption of solar spectrum in any conditions. Since the space solar cells are exposed in very extreme conditions (huge variation of temperature, radiation and intensity of solar spectrum), solar cell engineers have developed space relevant experiment systems in laboratories to simulate solar cells in space conditions and simulation techniques to predict their performances in different space conditions. This will be discussed at the end of this chapter. In this sub-chapter, we will first discuss the physical understanding of solar cell operation.

### 1.1.1 Basic solar cell equations

Figure 1-1 shows an equivalent circuit diagram of an illuminated solar cell. It describes a combination of current generation by light absorption in semiconducting materials and loss mechanism due to several causes. The light absorption is represented by the light generator symbol. As shown in this diagram, there are two diodes in parallel together with the light generator. The first diode ( $D_1$ ) illustrates a bias-dependent dark current ( $I_1$ ), which is considered to originate from the diffusion of minority carriers into its neighboring n- or p- type layer. The second diode ( $D_2$ ) indicates a current flow by the carrier generation and recombination via defects which are located in depletion region ( $I_2$ ). Finally, the third loss mechanism in parallel with the light generator is a shunt current ( $I_{sh}$ ) due to a shunt resistance ( $R_{sh}$ ).

Thus, these three currents flow to reverse direction from the direction of the light generation current ( $I_{ph}$ ).

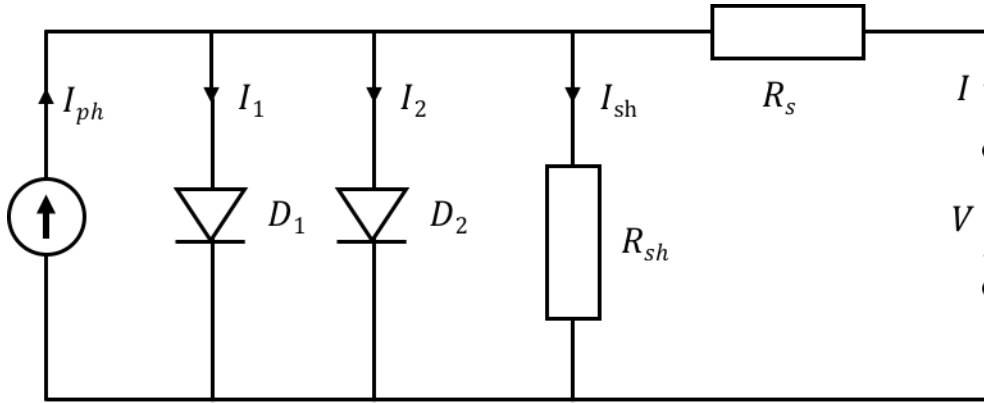


Figure 1-1. Equivalent circuit diagram of an illuminated solar cell based on two diodes model.

Eq. (1-1) represents the diode equation of a solar cell, under illumination, that has two diodes by the reason explained above. The current which arrives to an external circuit is the result of subtraction of  $I_1$ ,  $I_2$  and  $I_{sh}$  from  $I_{ph}$ . Each term of  $I_1$  and  $I_2$  is described with Shockley diode equation and saturation current ( $I_{01}$  and  $I_{02}$ ) typically defined by the material's semiconducting property and temperature.

$$I = I_{ph} - I_{01} \left[ \exp \left( \frac{q(V + IR_s)}{kT} \right) - 1 \right] - I_{02} \left[ \exp \left( \frac{q(V + IR_s)}{2kT} \right) - 1 \right] - \frac{V + IR_s}{R_{sh}} \quad (1-1)$$

In the diode equation,  $q$  is a charge of electron,  $k$  is Boltzmann constant,  $R_s$  is series resistance, and  $T$  is kelvin temperature (K). It can be also written as Eq. (1-2) to simplify the equation.

$$I = I_{ph} - I_1 - I_2 - I_{sh} \quad (1-2)$$

In order to simplify the diode equation of a solar cell, two diodes terms in the equation can be replaced by one diode term which have an ideality factor  $n$ . the ideality factor ranges between 1 and 2 depending on whether the diffusion current or the generation-recombination current is dominant and it can be varied along with operating voltage. Furthermore, saturation currents by diffusion and recombination-generation are unified into one parameter  $I_0$ .

$$I = I_{ph} - I_0 \left[ \exp \left( \frac{q(V + IR_s)}{nkT} \right) - 1 \right] - \frac{V + IR_s}{R_{sh}} \quad (1-3)$$

In most solar cells, the series resistance is small ( $R_s < 0.1$  ohms) and the shunt resistance is large ( $R_{sh} > 1 \times 10^4$  ohms). Terms involving  $R_s$  and/or  $R_{sh}$  in Eq. (1-3) is relatively too small to affect to I-V characteristics compared to other terms. Thus, neglecting these small terms, the equation is again simplified as below:

$$I = I_{ph} - I_0 \left[ \exp\left(\frac{qV}{nkT}\right) - 1 \right] \quad (1-4)$$

This basic solar cell equation is mostly used in practice. For a single junction solar cell, assuming that minority carrier lifetime of two charge neutral regions is sufficiently long, when the cell is illuminated, its current-voltage curve is shifted to -y axis by the amount of photo generated current ( $I_{ph}$ ). When the voltage is zero biased, the current that the solar cell exhibits is called as short circuit current ( $I_{SC}$ ). The point of voltage where no current flows in the circuit is called open circuit voltage ( $V_{OC}$ ). The power consumption of the diode under illumination at fourth quadrant is negative, that is, the cell is delivering power to load. We can also find a maximum power point ( $P_{MAX}$ ) from the I-V curve. The current and the voltage where the power is maximum is called  $I_{MPP}$  and  $V_{MPP}$ , respectively. A representative diagram is described in Figure 1-2.

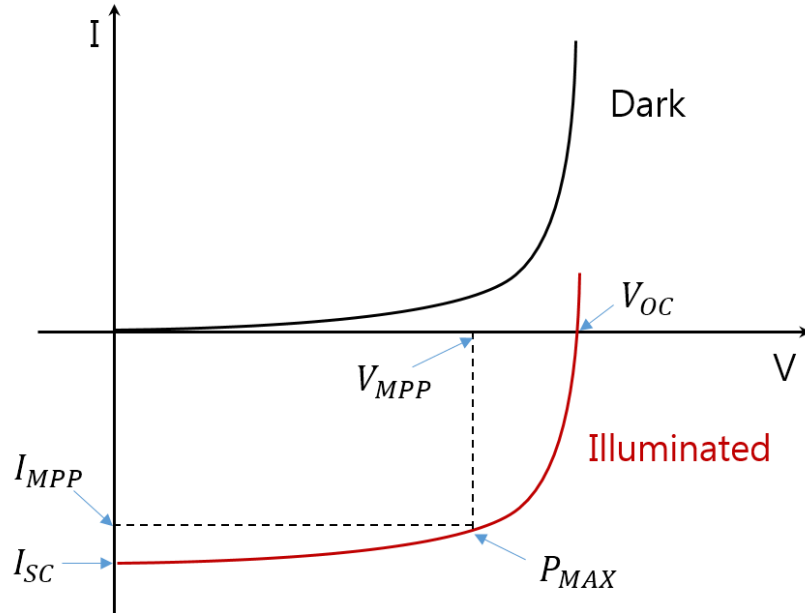


Figure 1-2. Current-Voltage (I-V) curve of a solar cell in dark and under illumination.

In fact, from Eq. (1-4), if we know all parameters such as ideality factor  $n$ , photo-generated current  $I_{ph}$ , saturation current  $I_0$ ,  $V_{OC}$  can be solved (where the current equals to zero):

$$V_{OC} = \frac{nkT}{q} \ln\left(\frac{I_{ph}}{I_0} + 1\right) \cong \frac{nkT}{q} \ln\left(\frac{I_{ph}}{I_0}\right) \quad (1-5)$$

Theoretical approach to these parameters will be also discussed in this sub-chapter. To evaluate I-V curve of an illuminated solar cell, we also use a parameter called fill factor (FF) which describes a ratio of  $P_{MAX}$  versus product  $I_{SC}$  and  $V_{OC}$  as shown in Eq. (1-6). Through this parameter, one can easily guess whether the cell is close to the ideal solar cell or it contains anomalies due to series and shunt resistances or other effects related to recombination or tunneling of carriers.

$$FF = \frac{P_{MAX}}{I_{SC} \times V_{OC}} = \frac{I_{MPP} \times V_{MPP}}{I_{SC} \times V_{OC}} \quad (1-6)$$

If a solar cell behaves like an ideal diode, its FF becomes close to 1 ( $I_{SC} \approx I_{MPP}$ ,  $V_{OC} \approx V_{MPP}$ ). However, in reality, this is not possible since the solar cell must have a contact to extract currents from itself ( $R_s$  arises) and the semiconducting material can never be 100 % pure without any defect, especially when doped. This is one of the causes of  $R_{sh}$ . As a consequence, the I-V curve of an illuminated solar cell behaves like the red curve of Figure 1-3. Conventionally, the I-V curve of illuminated solar cells is inverted as presented below to describe its parameters in positive sign. The effect of shunt resistance is reflected to the slope of linear region close to  $I_{SC}$ . As the  $R_{sh}$  becomes smaller from infinity, the flatness of diode near  $I_{SC}$  before its turn-on point decreases (in other word, one can say the slope near  $I_{SC}$  increase in negative direction). On the other hand, when the  $R_s$  is larger, the steepness of the slope near  $V_{OC}$  decreases.

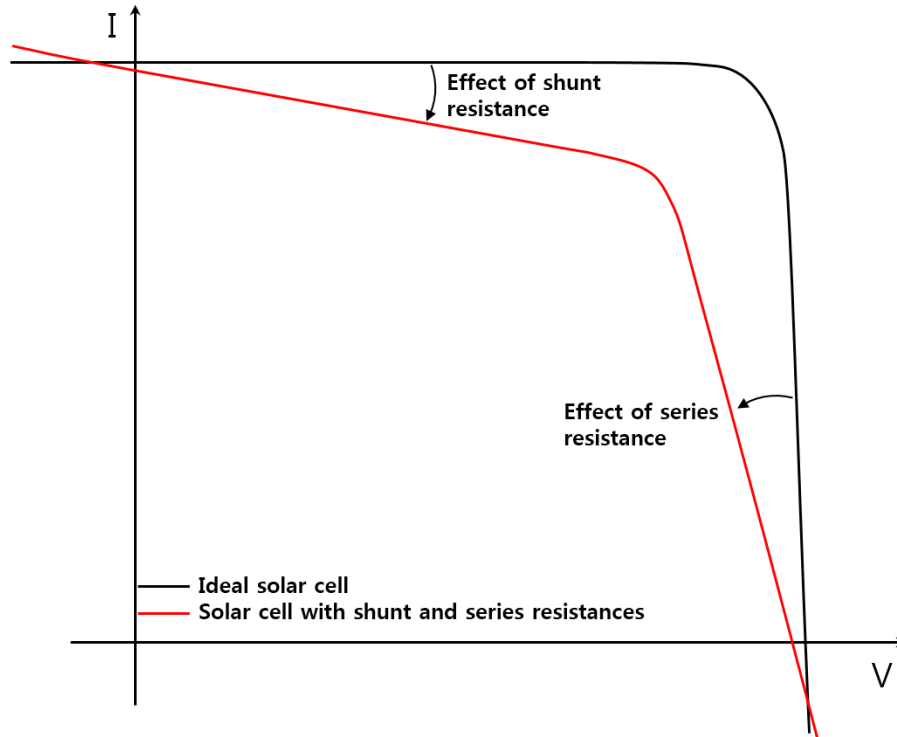


Figure 1-3. Conventional I-V curve of an illuminated solar cell (effect of series and shunt resistances on electrical characteristics).

One of the most important parameter in solar cell is photo conversion efficiency ( $\eta$ ) which is obtained by dividing the output power ( $P_{OUT}$ ) into the input power ( $P_{IN}$ ). In general, the maximum efficiency ( $\eta_{MAX}$ ) of the cell is referred as the efficiency of the cell, and for  $\eta_{MAX}$ ,  $P_{MAX}$  value is taken.

$$\eta = \frac{P_{OUT}}{P_{IN}} \quad \text{and} \quad \eta_{MAX} = \frac{P_{MAX}}{P_{IN}} \quad (1-7)$$

For a solar cell which is based on the single pn junction structure, there is a theoretical limit on its photo conversion efficiency, i.e. Shockley-Queisser limit [2]. To calculate this theoretical limit, Shockley and Queisser have defined the following assumptions:

- One photon creates only one electron-hole pair.
- Cell is illuminated with unconcentrated light.
- Thermal relaxation of the electron-hole pair occurs only in excess of the bandgap.

Under these assumptions, the limit of conversion from photo energy to electricity is induced by several physical phenomena such as: blackbody radiation which exists in any material above 0 Kelvin, recombination of electron-hole pairs, spectrum losses (higher energy of photons than the bandgap of material). With a single pn junction solar cell, their calculations predicted the maximum efficiency of around 33.7 % when the cell has a bandgap of 1.4 eV under AM1.5 solar spectrum (1000 W/m<sup>2</sup>). By minimizing the losses listed above, developing optimal structure, and purifying materials, some improvement has been made. With single crystalline silicon cells, the efficiency of 26.7 ± 0.5 % has been experimentally realized and with single GaAs junction cells, 28.8 ± 0.9 % has been achieved under the global AM1.5 spectrum (1000 W/m<sup>2</sup>) at 25 °C [1].

On the other hand, there exists many of other researches trying to exceed the limit with different approaches. The most widely taken method to achieve higher efficiency is to fabricate multi junction solar cells (also called as tandem solar cells).

### 1.1.2 Diffusion current

The diffusion current is composed of majority carrier electrons in n-type material surmounting the electric potential barrier to diffuse to p-type material side and majority carrier holes in p-type material diffusing to n-type side so that they become minority carriers in neighboring p- and n-type side. The hole diffusion current density at any point  $x_n$  in n-type material can be calculated following the equation below:

$$J_p(x_n) = -qD_p \frac{d\delta p(x_n)}{dx_n} = q \frac{D_p}{L_p} \Delta p_n e^{-x_n/L_p} = q \frac{D_p}{L_p} \delta p(x_n) \quad (1-8)$$

where  $D_p$  and  $L_p$  are the diffusion coefficient and the diffusion length of hole, respectively. Then, the total hole current density near at  $x_{n0}$  is simply obtained by evaluating Eq. (1-8) at  $x_n = 0$ :

$$J_p(x_{n0}) = \frac{qD_p}{L_p} \Delta p_n = \frac{qD_p}{L_p} p_n \left[ \exp\left(\frac{qV}{kT}\right) - 1 \right] \quad (1-9)$$

Similar approach can be applied to the minority carrier electrons in p-type material, then, total current density by diffusion of electrons and holes can be described as:

$$J_1 = \left( \frac{qD_p p_{n0}}{L_p} + \frac{qD_n n_{p0}}{L_n} \right) \left[ \exp\left(\frac{qV}{kT}\right) - 1 \right] = J_{01} \left[ \exp\left(\frac{qV}{kT}\right) - 1 \right] \quad (1-10)$$

Eq. (1-10) is the diode equation which we have already seen in Eq. (1-1) for the second term. However, in this case, resistances are not considered. By using a relationship  $L_p = \sqrt{D_p \tau_p}$  and  $L_n = \sqrt{D_n \tau_n}$ , where  $\tau_p$  and  $\tau_n$  are the minority carrier lifetime of holes and electrons, and according to the mass action law,  $np = n_i^2$ ,  $n_{p0} = n_i^2/p_{n0} \approx n_i^2/N_A$  most authors are assuming that the concentration of holes in p-type material is approximately the same as the concentration of acceptors,  $N_A$ . Similarly, if we consider n-type material,  $p_{n0} = n_i^2/n_{n0} \approx n_i^2/N_D$  where  $N_D$  is the concentration of donor.  $n_i$  is intrinsic carrier concentration in semiconductor. Then, Eq. (1-10) may be rewritten as given:

$$J_{01} = qn_i^2 \left[ \frac{1}{N_D} \left( \frac{D_p}{\tau_p} \right)^{\frac{1}{2}} + \frac{1}{N_A} \left( \frac{D_n}{\tau_n} \right)^{\frac{1}{2}} \right] \quad (1-11)$$

In fact, for most pn junction solar cells, the doping concentration of n-type and p-type materials is not equivalent. Generally, where  $p_{n0}$  is much larger than  $n_{p0}$  (abrupt  $p^+n$  junction), the second term of Eq. (1-11) is much smaller than the first term. In other word, the diffusion current in n-type region can be neglected as seen in below:

$$J_{01} = qD_p \frac{p_{n0}}{L_p} = \sqrt{\frac{D_p}{\tau_p}} \frac{n_i^2}{N_D} \quad (1-12)$$

Eq. (1-12) indicates that we can calculate the reverse-saturation current density by diffusion  $J_{01}$  once the doping concentration, diffusion coefficient, and carrier lifetime are known.

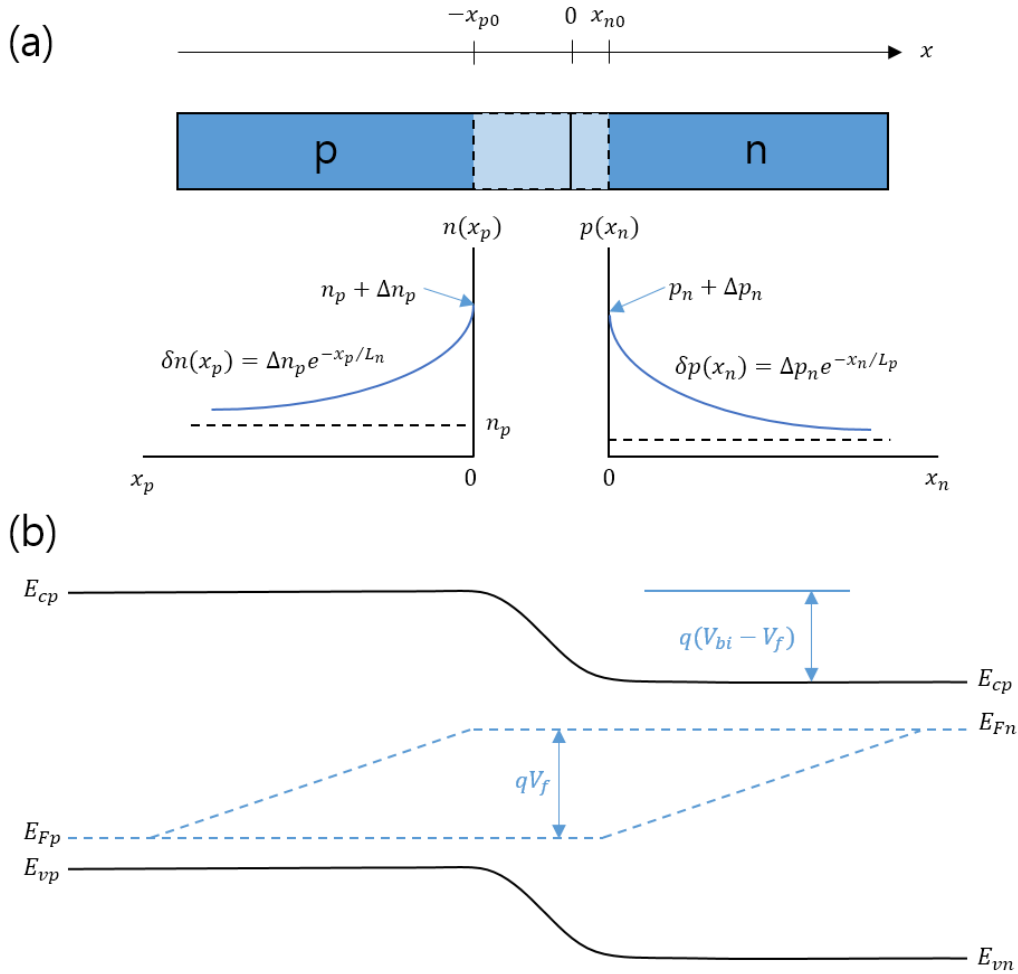


Figure 1-4. A pn junction in forward bias: (a) minority carrier distribution in two side of depletion region with a graphical instruction of distance  $x_n$  and  $x_p$  from the interface of depletion and charge neutral regions; (b) band banding diagram with variation of quasi-Fermi level with position[3].

### 1.1.3 Generation-recombination current

The term  $I_2$  described in Eq. (1-2) is a current flow by the generation-recombination of carriers in the depletion region. When the thermal equilibrium of a physical system in the junction is broken due to an external cause such as applying voltage, the system tends to turn back to its initial equilibrium state and this phenomenon occurs as generation-recombination current which leads the process. A theory describing this recombination-generation current was first developed by Sah, Noyce, and Shockley in 1957 [4]. To establish their theory, they have made simplified assumptions that lifetimes, mobilities, and doping concentrations on both n- and p-type materials were equals, and that the recombination of carriers were caused only due to a single recombination center in a forbidden level at  $E_i$ , near intrinsic Fermi level. Following these assumptions, the generation-recombination rate,  $U$  can be described as:

$$U = \frac{pn - n_i^2}{(n + n_1)\tau_{p0} + (p + p_1)\tau_{n0}} \quad (1-13)$$

where  $\tau_{p0}$  and  $\tau_{n0}$  are the hole and electron lifetimes in heavily doped n- and p-type materials and  $n_1$  and  $p_1$  are the free-carrier densities when the Fermi level is coincided with the trap level:

$$\begin{aligned} n_1 &= N_C \exp\left(\frac{E_t - E_C}{kT}\right) \\ p_1 &= N_V \exp\left(\frac{E_V - E_t}{kT}\right) \end{aligned} \quad (1-14)$$

The recombination current density in the depletion region can be obtained by integrating the generation-recombination rate  $U$  over the depletion width  $x$ :

$$J_{rg} = q \int_{x_1}^{x_2} U dx \quad (1-15)$$

In forward bias condition, majority carrier electrons in n-type material are injected to the depletion region due to the diffusion process, similar to the holes in p-type materials, and they recombine if significant number of carriers exists in the center of depletion region. Recombination current is dominant in forward bias, and the generation current in depletion region is negligible. The recombination current density is maximum at the center of the depletion width and can be described as:

$$\text{Ideal Case:} \quad J_r = \frac{qn_i W}{\tau_0} \cdot \frac{\exp\left(\frac{V}{2kT}\right)}{\frac{(V_{bi} - V)}{kT}} \cdot \frac{\pi}{2} \quad (1-16)$$

where  $\tau_0$  is the lifetime of electron and hole in the depletion region (assumed that the electron and hole have same lifetime in this calculation).

Under reverse bias, the injection of carriers from charge neutral region to the depletion region abruptly decreases, and the generation current density becomes dominant:

$$\text{Ideal Case:} \quad J_g = \frac{qn_i W}{2\tau_0} \quad (1-17)$$

In the more general case of the Sah-Noyce-Shockley (S-N-S) theory, the lifetime of electron and hole carriers are not the same in the depletion region. Thus, Hovel has extended the S-N-S theory [5] and concluded for forward bias,

$$\text{Recombination Current (S-N-S): } J_r = \frac{qn_i W}{\sqrt{\tau_{p0}\tau_{n0}}} \cdot \frac{2 \sinh\left(\frac{V}{2kT}\right)}{\frac{(V_{bi} - V)}{kT}} \cdot \frac{\pi}{2} \quad (1-18)$$

when the applied voltage is higher than  $4 kT$ , but does not exceed  $V_{bi} - 10 kT$ , and the average lifetime of carriers are computed from lifetimes of electrons and holes at each type of materials. As to the reverse bias condition, the current is dominated by generation,

$$\text{Generation Current (S-N-S): } J_g = \frac{qn_i W}{2\sqrt{\tau_{p0}\tau_{n0}}} \left[ \cosh\left(\frac{E_t - E_i}{kT} + \frac{1}{2} \ln \frac{\tau_{p0}}{\tau_{n0}}\right) \right]^{-1} \quad (1-19)$$

An extended study has been done with different doping concentrations of each side by Choo [6]. The works of Hovel and Choo has provided more realistic generation - recombination current equation to be applied for a practical diode equation since this extended equation is sufficiently accurate within the limitations of the theory. Note also that, depending on the bias (either forward or reverse), one must use Eq. (1-18) or (1-19) to describe  $I_2$  in Eq. (1-1).

As a matter of historical interest, the generation-recombination current density  $J_{rg}$  is often denoted by  $J_{02}$ , and can be described as:

$$J_{rg} = J_{02} = \frac{qW}{2} \sigma v_{th} N_t n_i \quad (1-20)$$

Assuming that there exists a single trap in the middle of the bandgap with a density  $N_t$ . The lifetime of carriers in the depletion region,  $\tau$ , is related to the trap density through:

$$\tau_p = \frac{1}{\sigma_p v_{th} N_t} \quad \text{and} \quad \tau_n = \frac{1}{\sigma_n v_{th} N_t} \quad (1-21)$$

where  $\sigma_n$  and  $\sigma_p$  are the electron and hole capture cross sections,  $W$  is the width of the depletion region, and  $v_{th}$  is the thermal carrier velocity. Through this equation, we can find that the generation-recombination current has a linear dependence on the trap density  $N_t$ . Note that, depending on the bias (forward or reverse), As we will discuss later, we would expect to see the increase of  $I_2$  when the solar cell is exposed to an irradiation.

#### 1.1.4 Temperature dependence of solar cells

Either for terrestrial or for spatial purposes, solar cells are exposed to different temperatures. In semiconducting materials, temperature can affect to the mobility and density of carriers and even the bandgap of the material. Therefore, understanding the effects of changing temperature on the solar cell

properties is important. By carefully looking at the diode equation of a solar cell under illumination, we can suspect whether each of component can be affected by the change of temperature. First, the reverse saturation current by diffusion which has been derived in Eq. (1-12) can be rewritten as:

$$J_{01} = \left[ T^3 \exp\left(\frac{-E_g}{kT}\right) \right] T^{\frac{\gamma}{2}} = T^{(3+\frac{\gamma}{2})} \exp\left(\frac{-E_g}{kT}\right) \quad (1-22)$$

following the assumption that has been made by Sze [7] ( $D_p/\tau_p$  is proportional to  $T^\gamma$  where  $\gamma$  is a constant). This equation indicates that the terms including temperatures are both proportional to the temperature, therefore, at higher temperature,  $J_{01}$  becomes larger than at lower temperature. Furthermore, at room temperature, intrinsic carrier concentration for GaAs is about  $2 \times 10^6 \text{ cm}^{-3}$  in comparison to the value for Si of around  $1.5 \times 10^{10} \text{ cm}^{-3}$ . This difference results primarily from the difference in bandgap energies. The bandgap energy itself is a function of temperature and is described by Thurmond [8]:

$$E_g(T) = E_g(0) - \frac{\alpha T^2}{T + \beta} \quad (1-23)$$

The values of  $E_g(0)$ ,  $\alpha$ , and  $\beta$  are given for each material depending on its crystallinity. The crystallinity indicates how perfectly the semiconductor material has a periodic lattice structure. For example in the single crystalline GaAs structure, intrinsic GaAs has  $E_g$  of 1.42 eV at 300 K. But, in high doping condition, its bandgap is narrowed by  $\Delta E_g \approx 2 \cdot 10^{-11} \cdot N_a^{-1/2}$  (eV) where  $N_a$  is the concentration of dopant in  $\text{cm}^{-3}$  since dopants play as impurities which break the periodicity of GaAs structure. Therefore, the intrinsic carrier concentration of material can also affect  $J_{01}$  and it is also temperature dependent. In summary,  $J_{01}$  is obviously temperature dependent, and since this parameter is directly used for calculation of  $V_{OC}$  (Eq. (1-5)), it is considered to be a factor which decrease  $V_{OC}$  when temperature increases.

Concerning the generation-recombination current  $I_2$ , whether it is forward or reverse biased, it is proportional to  $n_i$ , whereas the diffusion current  $I_1$  is proportional to  $n_i^2$ . As a result, the temperature dependence of  $I_2$  is weaker in exponential term  $\exp(-E_g/2kT)$ , than  $I_1$  in  $\exp(-E_g/kT)$ .

The short circuit current ( $I_{SC}$ ) under illumination corresponds to the collected electron hole pairs from photo excitation at zero bias condition. Thus, generation rate over the depth of material, and lifetimes of electron and hole at each side including the depletion region is involved to calculate  $I_{SC}$ . It is quite complex but actual measurement gives a small variation of  $I_{SC}$  as a function of temperature. When the diffusion length of carriers is sufficiently long,  $I_{SC}$  can be approximated given by [9]:

$$I_{SC} \approx qg_0(L_p + L_n) \quad (1-24)$$

Where  $g_0$  is generation rate of electron-hole pairs per volume unit. Using the relation of diffusion length, coefficient and lifetime ( $L = \sqrt{D\tau}$ ) and Einstein relation ( $D/\mu = kT/q$ ), it is possible to find a temperature dependence of diffusion length. Shockley, Read, and Hall [10], [11] have found that the temperature dependence of minority carrier lifetime of electron in p-side and hole in n-side.

$$\begin{aligned}\tau_p &= \tau_{p0} \left[ 1 + \exp\left(\frac{E_T - E_F}{kT}\right) \right] \\ \tau_n &= \tau_{n0} + \tau_{p0} \exp\left(\frac{E_T + E_F - 2E_i}{kT}\right)\end{aligned}\tag{1-25}$$

Where  $\tau_{p0}$  is the lifetime of hole in n-type material in which all traps are filled,  $E_T$  is energy level of the trap, and  $E_F$  is the Fermi energy level. Similarly, electron lifetime  $\tau_{n0}$  can be calculated, where  $E_i$  is intrinsic energy level. Even though Eq. (1-25) contains a temperature term in equation, since the Fermi level is also moved close to the intrinsic energy level, the exponential term remains to be very small. Thus, in both type of materials, lifetime of minority carriers is expected to be a relatively constant in temperature ranges for practical applications. In addition, the diffusion length  $L$  is primarily determined by the temperature dependence of the carrier mobility.

In practice, the dependence of  $I_{SC}$  on temperature mostly comes from the change of the bandgap. When temperature increases, the bandgap becomes smaller. Then, more photons with lower energy can have opportunity to excite electrons from the valence to the conduction band creating electron-hole pairs, harvesting more solar energy spectrum, it can eventually cause an increase of  $I_{SC}$ .

### 1.1.5 Spectral response of PN solar cells

The absorption of solar energy is a fundamental of the solar cell operation. It can be also described as the absorption of electromagnetic radiation (or the optical injection of carriers). When incident photons are penetrating a material at a depth  $x$ , the photons can be absorbed with a specific optical absorption rate  $\alpha(\lambda)$  depending on its wavelength and the remaining of unabsorbed photons in depth  $x$  follows the Beer - Lambert law:

$$F = F_0 \exp[-\alpha(\lambda)x]\tag{1-26}$$

where  $F_0$  is the total number of incident photons per  $\text{cm}^2$  per second per unit wavelength. Assuming that all absorbed photons are generating one carrier of each, the generation rate at certain wavelength  $G(\lambda)$  at depth  $x$  can be determined as:

$$G(\lambda) = \alpha(\lambda)F_0[1 - R(\lambda)]\exp[-\alpha(\lambda)x]\tag{1-27}$$

where  $R(\lambda)$  is a loss rate due to the front surface reflection.

Prior to get into a detail of calculation of photo-generated current, the spectral response of a pn junction solar cell can be simply summarized as:

$$SR(\lambda) = \frac{\sum J}{qF_0(\lambda)} (A/W) \quad (1-28)$$

i.e. total excess current density divided into intensity of total number of incident photons per unit wavelength. Ideally, SR can be 1 if all incident photons produce one excess carrier in a pn junction.

In most of cases, the solar cell is operating in low injection condition (concentration of photo generated excess carriers  $n_p \ll n_{p0}$  in p-type material). When excess electron carriers are generated in p-side, a diffusion current occurs aside from the diffusion current in dark under forward bias. Similar to the diffusion current density of diode in dark given by Eq. (1-8), the equation of diffusion hole current density  $J_n$  due to the excess current can be also described by the same mechanism and assuming that there is no electric field in the charge neutral region,  $J_n$  is given by:

$$J_n = qD_n \frac{d(n_p - n_{p0})}{dx} \quad \text{in } p - \text{type cells} \quad (1-29)$$

And similarly, for holes:

$$J_p = -qD_p \frac{d(p_n - p_{n0})}{dx} \quad \text{in } n - \text{type cells} \quad (1-30)$$

Each of diffusion current density of electrons or holes by the excess carrier density is directly related to a result of differentiation of the excess carrier density over the depth  $x$ . To get a final current density value, it is necessary to find the excess carrier density with respect to  $x$ . In order to do that, we need to first take into account the fact that the generation rate must be equal to the sum of recombination rate and particle loss due to the diffusion, then, we can write the generation rate as below:

$$G(\lambda) = \frac{n_p - n_{p0}}{\tau_n} - \frac{1}{q} \frac{dJ_n}{dx} \quad (1-31)$$

And for holes in n-type materials:

$$G(\lambda) = \frac{p_n - p_{n0}}{\tau_p} + \frac{1}{q} \frac{dJ_p}{dx} \quad (1-32)$$

Subsequently, by combining Eqs. (1-27), (1-30), and (1-31), and integrating it over  $x$ , the general solution of the excess hole carrier density ( $p_n - p_{n0}$ ) is obtained as follow:

$$p_n - p_{n0} = A \cosh \frac{x}{L_p} + B \sinh \frac{x}{L_p} - \frac{\alpha F_0 (1 - R) \tau_p}{\alpha^2 L_p^2 - 1} \exp(-\alpha x) \quad (1-33)$$

by putting the boundary conditions at the front surface,  $D_p d(p_n - p_{n0})/dx = S_p(p_n - p_{n0})$  at  $x = 0$ , and at the interface between the charge neutral region and the depletion region,  $p_n - p_{n0} = 0$  at  $x = x_j$ , where  $x_j$  is the width of n-type layer in this example, the unknown parameters A and B can be found. Once we solve Eq. (1-30) using the excess carrier density equation of (1-33), the hole diffusion current density  $J_p$  by the excess carrier in n-type material can be computed. In the same manner, the electron diffusion density  $J_n$  by the excess carrier in p-type material can be obtained. Complete equations of  $J_p$  and  $J_n$  can be found in Annex A.

Aside from the current generation from n- and p-type regions, some photo-generated current can occur in the depletion region. In a typical abrupt pn junction structure, it is expected that all excess carriers generated in the depletion region can easily collected due to the high internal electric field without any recombination loss.

$$J_{dr} = qF_0(1 - R)\exp(-\alpha x_j)[1 - \exp(-\alpha W)] \quad (1-34)$$

Therefore, the total excess current density in the pn junction will be:

$$J_{tot} = J_p + J_n + J_{dr} \quad (1-35)$$

With this total excess current density, we can calculate the internal spectral response (*ISR*) not taking into account the effect of front window layer and the reflection loss:

$$ISR(\lambda) = \frac{J_p + J_n + J_{dr}}{qF_0(\lambda)[1 - R(\lambda)]} \quad (A/W) \quad (1-36)$$

However, in practice the incident photons are also absorbed by the window layer. In this case, the calculation becomes more complex. In this discussion, we will not enter into a detail of mathematical calculation of all components of current densities occurring in each layer (for more discussion, see ref [12]). Figure 1-5 shows the current densities generated by absorption of light (generation of excess carriers) in layer components in an actual single junction solar cell. The current density in window layer noted as  $J_D$  is not contributing a total current generation in the cell since this part is not collected. Thus,  $J_D$  must be eliminated from the calculation of total current density to find a spectral response of a solar cell.

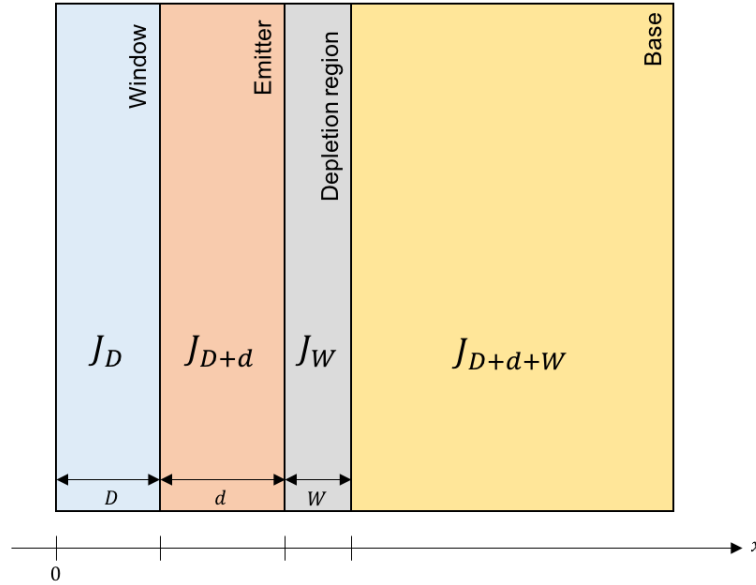


Figure 1-5. Illustration of a structure of solar cell with a window layer on the top of junction. Current densities in window, emitter, depletion region, and base due to excess carriers are noted as  $J_D$ ,  $J_{D+d}$ ,  $J_W$ , and  $J_{D+d+W}$ , respectively.

As a consequence, the external spectral response which will be the practical spectral response of a completely structured solar cell can be given as:

$$ESR(\lambda) = \frac{J_{(D+d)}(\lambda) + J_{(D+d+W)}(\lambda) + J_W(\lambda)}{qF_0(\lambda)} \quad (1-37)$$

## 1.2 Theoretical aspect of radiation damage

Irradiation damage to the solar cells is mostly caused by atomic displacements which break periodic lattice structure of the semiconducting materials and they interfere the movement of minority carriers resulting in decrease of carrier lifetime. These irradiation atomic displacements can also affect properties of other electrical devices such as battery, detectors and communication instruments which are equipped for a space mission. For this reason, the radiation effect has gained a lot of interests in the study of degradation of this kind of materials and devices including solar cells. In space, the origin of irradiation is mostly due to energetic particles like electrons and protons. When these particles hit the surface of materials and enter into, they interact in several ways with these materials since they have mass, energy and some particles are charged. Once a charged particle penetrates a material, it slows down by consuming or transferring its energy with electrons and nuclei in the material. In this process, several types of interactions can occur and these interactions can also vary with the speed and the energy of an incident particle [13].

Basically, two types of interactions exist between charged particles and matter; elastic collisions and inelastic collisions. First, the inelastic collisions occur between the projectile and the cloud of electrons of target. By doing interactions with electrons, the incident particles lose its energy and slow down its velocity of moving. Independent on target materials, once the velocity of moving ion is two times slower

than that of electrons at the top of the Fermi level, electrons cannot be excited. This threshold energy can be determined for each material, in keV. Thus, below this incident energy, the collision between the projectile and the target is mainly elastic. By the elastic collision, the projectile directly transfers the energy to the target atom, not losing the energy by ionization of the target. As a consequence, the energy transfer of projectile-target is almost conserved. This process is a main cause of displacement damage and responsible for the degradation of solar cell.

### 1.2.1 Displacement damage and atomic displacement

Considering only the elastic collision process of radiation of heavy charged particles, we will see how the particle is transferring its energy to the target atom and the equation describing irradiations with electrons, comparing the relativistic velocities. In practice, depending on the energy of incident particle, elastic collisions are distinguished. If the particles have higher energies so that the projectile can penetrate the cloud of electrons surrounding the target atom and transfer the energy directly to the atom, it is called Rutherford collisions. Meanwhile, when the particles have lower energies, they cannot penetrate the electron cloud. As a result, the collisions occur between the projectile and the cloud electrons, known as hard sphere collisions.

The displacements induced by the interaction between the incident-charged particle and the target atom are considered as primary displacements. Depending on the initial energy of incident particle, the primary atomic displacement can be either due to Rutherford collisions or hard sphere collisions. When the atoms are detached from his lattice site by collisions with the projectile, these species are called primary knock-ons (PKA) atom and they have enough kinetic energy to produce other displacements known as secondary displacements. In elastic collisions the interaction of two atoms can be described with a screened Coulomb potential energy given in the form of:

$$V(r) = \frac{(Z_1 Z_2 q^2)}{r} \exp\left(-\frac{r}{a}\right) \quad (1-38)$$

where  $r$  is the distance between the two atoms,  $Z_1$  and  $Z_2$  are the atomic numbers of the moving and target particles, respectively, and  $a$  is the screening radius given by the approximate relation:

$$a = \frac{a_0}{\sqrt{(Z_1^{2/3} + Z_2^{2/3})}} \quad (1-39)$$

where  $a_0$  is the Bohr radius of hydrogen. If the energy of incident particle is high enough, the particle can come closer to the target atom so that  $r$  is small for Eq. (1-38) to be a classical Coulomb's potential equation. In this case, the collision will be the Rutherford collision. However, if the energy is small

enough, the hard sphere collision will occur between the projectile and the target. There is a critical energy  $E_A$  which separates these two collisions. Assuming that there is no screening effect (when the particle has a high enough energy), the closest distance between the incident particle and the target atom (called the collision diameter) is classically described as below:

$$b = \frac{2Z_1Z_2q^2}{\mu v^2} \quad (1-40)$$

where  $\mu$  is the reduced mass of two atoms  $= M_1M_2/(M_1 + M_2)$ , and  $v$  is velocity of the incident particle. So, when the energy of incident particle is higher than  $E_A$ , the Rutherford collision occurs since  $b \ll a$ , and when energy is smaller than  $E_A$ , collisions will be the hard sphere collisions ( $b \gg a$ ). The critical energy can be calculated from Eqs. (1-39) and (1-40) as follow [14]:

$$E_A = 2E_R \frac{(M_1 + M_2)}{M_2} Z_1 Z_1 \sqrt{(Z_1^{2/3} + Z_2^{2/3})} \quad (1-41)$$

where  $E_R$ , the Rydberg energy  $= q^2/(2a_0)$ , and  $M_1$  and  $M_2$  are the masses of the incident and target atoms, respectively. For the calculation of damage induced by irradiation, the energy transfer from the incident particle to the target atom is one of the most importance. When the collision between two atoms occur in elastic condition, the energy and the momentum of particles are conserved. Then, the maximum energy transfer  $T_m$  can be derived as follow in the nonrelativistic case:

$$T_m = \frac{4M_1M_2}{(M_1 + M_2)^2} E \quad (1-42)$$

where  $E$  is the energy of incoming particle to a target atom and  $M_1$  and  $M_2$  are the masses of incoming and target atoms, respectively. In the case of radiation with electrons, compared to the case of protons, because of their small mass, much high velocity is required to have a sufficient energy to detach lattice atoms. For electrons, Eq. (1-42) should be modified following the relativistic version:

$$T_m = \frac{2mE}{M_2} \left( \frac{E}{mc^2} + 2 \right) \cos^2 \theta \quad (1-43)$$

where  $m$  is the mass of electron and  $\theta$  is the scattering angle of the displaced atom with respect to the incident direction of electrons. Under electron radiation condition, the maximum transfer energy can be achieved when  $\theta = 0$ .

As discussed above in this section, both inelastic and elastic collisions happen in radiation environments. Indeed, most of energies from the incident charged particles (electrons or protons) are absorbed by the cloud of electrons surrounding target atoms. Furthermore, this energy transfer from the incident particles to the cloud determines the penetration depth in target materials. Nevertheless, the incoming particle can still come closer to the nuclei and transfer enough energy to the target atom so that the atom is dislodged from the lattice and go far from its original site. Subsequently, the displaced atom and its associated vacancy can form defects in lattice structure. These defects often react between them or dopant atoms resulting in more complex defects structures. The defect formation can finally affect the performance of solar cell operation. This aspect will be discussed in the sub chapter 1.4. Back to the point of this section, when the proton is incoming to an atom in the lattice, the target atom is dislodged if it receives the energy higher than the displacement energy  $E_d$  from the proton. For this atomic displacement, the proton must have an energy higher than the threshold energy  $E_t$ . The relation of these two energies can be obtained using the Eq. (1-42) in the same manner as:

$$E_d = \frac{4M_p M_2}{(M_p + M_2)^2} E_t \quad (1-44)$$

where  $M_p$  is the mass of the proton.

Similarly, under the radiation with electrons, it is necessary to use the relativistic mass and energy and Eq. (1-43), then the displacement energy is given by:

$$E_d = \frac{2mE_t}{M_2} \left( \frac{E_t}{mc^2} + 2 \right) \cos^2 \theta \quad (1-45)$$

For example, in a III-V compound material Gallium/Arsenide (GaAs) which is very widely used for semiconductor devices, average displacement energy is about 10 eV [15]. When calculating this displacement energy with the proton irradiation, according to Eq. (1-44), the threshold energy of the proton is around 180 eV, which is a tow low energy for proton accelerators. On the other hand, the same calculation with the electron irradiation gives few hundreds of keV of the threshold energy, which is possible to achieve using electron accelerators. Therefore, the electron irradiation is usually used to experimentally determine the atomic displacement energy of materials and to compare it with theoretical calculations.

### 1.2.2 Primary and secondary displacements

In the case of Rutherford collisions (incident particle energy is higher than  $E_A$ ), collisions have chance to probably produce small energy transfers. To establish a quantification model of radiation to the material, it is necessary to solve the cross section for kinetic energy transfer from incoming particle to

the target atom. For this, we first need to approach to the differential cross section from  $T$  to  $T + dT$  is given by:

$$d\sigma = \frac{\pi b^2}{4} T_m \frac{dT}{T^2} = \left( 4\pi a_0^2 \frac{M_1}{M_2} Z_1^2 Z_2^2 \frac{E_R^2}{E} \right) \frac{dT}{T^2} \quad (1-46)$$

where  $E$  is the energy of the incident particle and  $T$  is a transferring energy. This equation is valid for collisions which result in the maximum energy transfer,  $T_m$ , down to some small but finite lower limit, where electronic screening cannot be neglected. Then it is assumed that the target atom is always displaced when it receives an energy greater than  $E_d$ , while it is never dislodged if the energy is smaller than  $E_d$ . Under these conditions, the cross section for the energy transfer can be described as:

$$\begin{aligned} \sigma_d &= \int_{T=E_d}^{T=T_m} d\sigma = 16\pi a_0^2 Z_1^2 Z_2^2 \frac{M_1^2}{(M_1 + M_2)^2} \frac{E_R^2}{T_m^2} \left( \frac{T_m}{E_d} - 1 \right) \\ \text{or} \quad \sigma_d &= 4\pi a_0^2 \frac{M_1}{M_2} \frac{Z_1^2 Z_2^2 E_R^2}{E E_d} \end{aligned} \quad (1-47)$$

As previously discussed, hard-sphere collisions occur in the energy region where the incident particle has energy lower than  $E_A$ . In this case, all energy transfers from 0 to  $T_m$  are equally probable, and the differential cross section for kinetic energy transfer from  $T$  to  $T + dT$  [13] is given by:

$$d\sigma = \pi a_1^2 \frac{dT}{T_m} \quad (1-48)$$

where  $a_1$  is the diameter of the hard sphere, taken to be approximately the screening radius. Like the case of Rutherford collision, primary atomic displacement can only take place when the received energy is higher than the displacement energy. Thus, the interval of integration to calculate the cross section should be started from  $E_d$  to  $T_m$ . Then the total cross section for production of primary displacements in the hard sphere region becomes:

$$\sigma_d = \frac{\pi a_1^2}{T_m} \int_{T=E_d}^{T=T_m} dT = \pi a_1^2 \frac{T_m - E_d}{T_m} \quad (1-49)$$

In case of the radiation with electrons, when incident electrons are scattered in the target material, they induce displacements primarily by the Coulomb interaction between the incident electrons and the target nucleus. Incident electrons which produce displacements typically have much higher velocity of movement than the case of protons. Thus, they can easily penetrate the cloud of electrons surrounding the target atom and directly interact with the target nucleus. Therefore, the collisions always occur in

Rutherford region. However, it is also necessary to modify the scattering cross section concerning the relativistic velocity of the electrons. The problem has been initiated by Mott [16], [17] and McKinley and Feshbach [18] has simplified the Mott's equation. Today, McKinley - Feshbach scattering cross section equation is widely accepted to treat the problem with electrons [19]:

$$\sigma_d = \frac{\pi b'^2}{4} \left[ \left( \frac{T_m}{E_d} - 1 \right) - \beta^2 \ln \frac{T_m}{E_d} + \pi \alpha \beta \left( 2 \left[ \left( \frac{T_m}{E_d} \right)^{\frac{1}{2}} - 1 \right] - \ln \frac{T_m}{E_d} \right) \right] \quad (1-50)$$

where  $\alpha = Z_2/137$ ,  $b'^2 = b/\gamma$ ,  $\beta$  is the ratio of the electron velocity to the speed of light.

When an atom is detached from its lattice site, it could have considerable kinetic energy and travel through the lattice. This kind of atoms which are knocked out of the lattice are also called as knock-on atoms (or PKAs) and capable of producing secondary displacements. However, such a secondary displacement is produced by a hard sphere collision since the energy of PKAs is always lower than  $E_A$ . Kinchin and Pease have proposed a model [20] which describes the production of secondary displacements depending on the energy of PKAs, and today, this model is being widely accepted. A full Kinchin-Pease (K-P) result is presented as follow:

$$\begin{aligned} \rho(T) &= 0 & T < E_d \\ \rho(T) &= 1 & E_d \leq T < 2E_d \\ \rho(T) &= \frac{T}{2E_d} & 2E_d \leq T < E_c \\ \rho(T) &= \frac{E_c}{2E_d} & E_c \leq T \end{aligned} \quad (1-51)$$

where  $E_c$  is the cut-off energy. It is assumed that the energy loss by electron stopping is given by this cut-off energy. If the PKA energy is greater than  $E_c$ , there is no more increase of generation rate of secondary displacements. The full curve describing K-P model is presented in Figure 1-6.

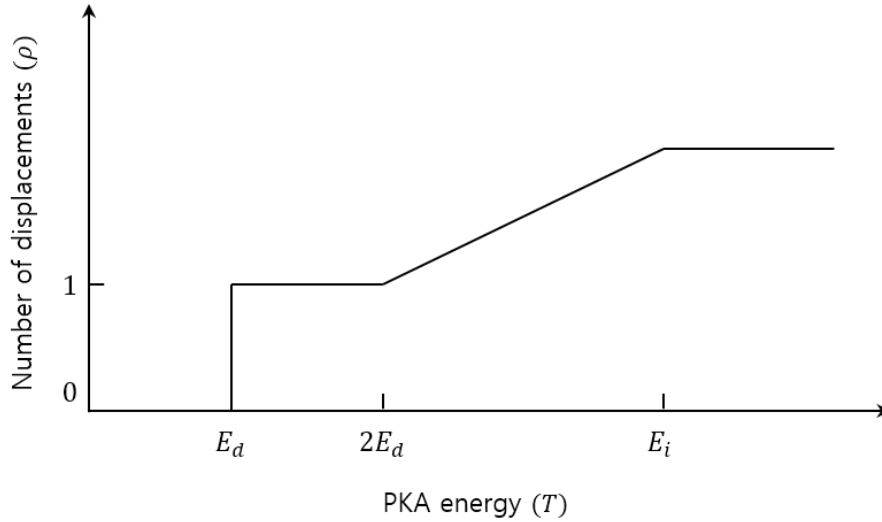


Figure 1-6. The number of displacement by the cascade as a function of PKA energy (from K-P model).

The average number of displacement,  $\bar{\rho}$ , is obtained by taking an average of  $\rho$  over the energy spectrum of the PKAs. In a form calculated by reference [13],  $\bar{\rho}$  is:

$$\bar{\rho} = \frac{1}{2} \left( \frac{T_m}{T_m - E_d} \right) \left( 1 + \ln \frac{T_m}{2E_d} \right) \quad (1-52)$$

For particles that have energy greater than the threshold energy, the total number of an atomic displacement,  $N_d$ , can be described in terms of a displacement cross section,  $\sigma_d$ , along with an average number of secondary displacements,  $\bar{\rho}$ , induced by the primary displacement and the irradiation fluence,  $\Phi$  as given in the relationship:

$$N_d = n_a \sigma_d \bar{\rho} \Phi \quad (1-53)$$

where  $n_a$  is the number of atoms per unit volume of a target absorber. By combining Eqs. (1-49) or (1-50) with Eqs. (1-52) and (1-53), it is possible to estimate the total number of displacement for an incident particle of energy  $E$ .

### 1.2.3 Ionization

When a target material receives an energy from incident particle, the energy received can remove electrons on the orbital from target atoms. This process is called as ionization. The Ionization process is the main cause of energy loss of charged particle travelling a target material. The absorbed radiation dose of incident particles is measured in Gy (J/kg, preferred SI unit). The calculation of absorbed dose units is started by considering a radiation through a slice of material which has a thickness of  $dx$ . Then, the energy deposition at each slice of material ( $dE/dx$ ) is tabulated with respect to the kinetic energy

of incident particle. It is also called as stopping power. By multiplying radiation fluence, the formula for electrons and protons is obtained as below:

$$Dose (Gy) = 1.6 \times 10^{-6} \frac{dE}{dx} \left( \frac{MeV \cdot cm^2}{g} \right) \Phi (cm^{-2}) \quad (1-54)$$

Note that the stopping power is a unique value for each material for each type of particle radiation. Thus, one must take into account to choose a proper value of stopping power. One of advantages of calculating the absorbed dose in Gy is that the conversion of absorbed dose between different particles (for example, between electron and proton).

The calculation programs of stopping power that has been developed by Berger et al [21] are available for most of solar cell materials. A program for electron computation is called as ESTAR, and for protons called as PSTAR, respectively.

### 1.3 Nature of irradiation-induced defects in solar cell materials

The study of defect is one of the most important problem in semiconductor physics. In crystalline or amorphous structure, the existence of defects can affect its electrical or optical properties in complex ways. Today, it is possible to theoretically predict a qualitative energy levels associated with some ideal simple intrinsic defects [22]. However, it is still not yet possible to qualitatively identify defects for the lattice distortion, and relaxation. To verify the theoretical prediction of defects, the experiments must be carried out to produce simple defects because tracking its mechanism after the production is already very complicated. The primarily created intrinsic defects, i.e. vacancies and interstitials are presumably moved out very fast and interact with other defects or impurities. Therefore, to irradiate with electrons is a proper choice to properly identify defects in a material. Then, once the defects are sufficiently identified, the comparison with proton irradiation result can be fulfilled. In this section, we collected and summarized some identified defects and their characteristics from the literature. We will discuss the production of defects and their behaviors in different kind of solar cell materials (GaAs, GaInP, and Ge) depending on the type of irradiation and temperatures. However, we have to keep in mind that the identified defects are limited as single defects, that is, complex of defects like cluster and their outcome property might not be measurable with modern measurement techniques. Furthermore, as we will mainly discuss below, most of defects that we are interested in for our study have been analyzed through either magnetic or electric way. So, we should be aware of that there could be still more veiled or non-identified defects by our irradiation conditions.

### 1.3.1 Production of defects in n- and p-doped Gallium-Arsenide (GaAs)

Study of irradiation induced-defects in Gallium-Arsenide (GaAs) compound has been continued since 1970s. There are several review articles which contain a considerable amount of works [23], [24]. For these studies, electron irradiation has been mainly used since it is an easy way to produce vacancies and interstitials in both Ga and As sublattices, and to follow the transformation of these primary defects when they become mobile and interact with each other or with various impurities in the material. Ions have been also used for irradiation. However, the complications have arisen due to the heavy mass of incident particle, when the ions penetrate into the material, it displaces a large number of atoms from the lattice creating a displacement cascade, i.e. to induce clusters of defects along the heavy ions path. As a consequence, it became one of difficulties to identify defects induced by ions, such as protons. In this reason, proton induced defects have not yet been extensively studied for GaAs. There are not so many data in literature. In fact, in spite of a large amount of work for electron irradiated GaAs, the identification of defects in n- and p-type GaAs is still not fully understood because of the nature of III-V compound material. The direct identification of defects can be provided by electron paramagnetic resonance (EPR) which is difficult to apply to this type of material due to its large magnitude of hyperfine and superhyperfine interactions of the paramagnetic defects with the nuclear spin of the different Gallium isotopes [22] compared to other materials such as II-VI and silicon. Fortunately, by using a combination with more sensitive technique called deep-level transient spectroscopy (DLTS), optical detection of magnetic resonance or of electron-nuclear double resonance, some defects in GaAs could be identified. Following to the section, some identified irradiation induced-defects in n-type and p-type GaAs will be presented.

#### 1.3.1.1 *Electron irradiation-induced defects in GaAs*

The first observation of defects and their identification of electron irradiated n-type GaAs have been done by Lang and Kimerling using DLTS [25]. The individual electron trap is determined by individual Arrhenius plot versus reciprocal temperature, i.e.  $\log[e_n(T)/T^2]$  vs  $1/T$ , where  $e_n(T)$  is the electron emission rate per trap. The associated trap energy level is determined by apparent capture cross section at  $T = \infty$ ,

$$\sigma = \sigma_{\infty} \frac{g_0}{g_1} e^{\Delta S/k} \quad (1-55)$$

And the energy level,

$$E_e = \Delta H + E_{\sigma} \quad (1-56)$$

Here we generally assume a thermally activated cross section for carrier capture,

$$\sigma_n(T) = \sigma_{\infty} e^{-E_{\sigma}/kT} \quad (1-57)$$

Following the electron irradiation, they found eight electron traps, labeled E1-E5, E7-E9, and three hole traps H1-H3. In their findings, the peak E6 was also presented but they concluded that this peak was due to the gold barrier layer interacting with the irradiated Schottky diode [26]. All the traps labeled above could be easily measured by DLTS technique when the special care is taken into account to prevent an enhancement of emission rate of electron traps which can be caused by the change of electric field. However, this information still remains indirectly, which gives only electrical and thermal properties of traps. So, in order to identify traps through this technique, it is often necessary to combine it with other information such as radiation fluence, doping concentrations, growth techniques and/or with other measurement techniques: electron paramagnetic resonance (EPR), IR absorption, CL...

Table 1-1. Identification of electron irradiated induced defects in n-type GaAs: Peak temperature  $T_0$  (for an emission rate of  $70 \text{ s}^{-1}$ ), introduction rate  $\tau$  for 1 MeV electron irradiation, energy level  $E_e$  (from the conduction band), capture cross-section  $\sigma$ , annealing temperature  $T_a$ , activation energy associated with the annealing  $E_a$ , pre-exponential factor of the annealing rate  $\nu$  [25], [26].

Trap	$T_0$ (K)	$\tau$ ( $\text{cm}^{-1}$ )	$E_e$ (eV)	$\sigma$ ( $\text{cm}^{-2}$ )	$T_a$ (K)	$E_a$ (eV)	$\nu$ ( $\text{s}^{-1}$ )
E1	20	1.5	0.045	$2.2 \times 10^{-15}$	500	1.55 – 16	$10^{13.5} - 10^{12.5}$
E2	50	1.5	0.14	$1.2 \times 10^{-13}$	500	1.55 – 16	$10^{13.5} - 10^{12.5}$
E3	160	0.4	0.30	$6.2 \times 10^{-15}$	500	1.55	$10^{13.5}$
E4	310	0.08	0.76	$3.1 \times 10^{-14}$	500	1.5	$10^{13}$
E5	360	0.1	0.96	$1.9 \times 10^{-12}$	500	1.55	$10^{13.5}$
E7	40	$\sim 5 \times 10^{-4}$	-	-	250	0.7	$10^{12}$
E8	80	$\sim 5 \times 10^{-4}$	-	-	-	-	-
E9	110	$\sim 2 \times 10^{-3}$	-	-	250	0.7	$10^{12}$
P1	200	$10^{-2}$	0.36	$6.9 \times 10^{-15}$	-	-	-
P2	280	$10^{-2}$	0.50	$1.4 \times 10^{-15}$	650<	-	-
P3	350	$10^{-2}$	0.72	$1.4 \times 10^{-13}$	650	1.5	$10^9$

In the electron irradiated n-type GaAs, the traps observed do not depend on the quality of material, rather than that, it was only influenced by the irradiation condition. This strongly indicates that the nature of the traps observed by DLTS corresponds to intrinsic defects like primary vacancies and interstitials. The three electron traps, so called E1, E2 and E3, are directly produced by 4 K irradiation. In addition, through the anisotropy of defect creation [15], it was possible to conclude that these defects are primary defects in the As sublattice: As vacancies ( $V_{As}$ ) and As interstitials ( $-As_i$ ). By contrary, no stable defect is analyzed in the Ga sublattice. In principle, the E1, E2, and E3 traps are detected at 20, 50, and 160 K, respectively. However, these defects can also be observed at 4 K under the phonon-assisted tunneling condition which enhances the emission rate of these traps. The anisotropy of the E4 and E5 traps is also consistent with an As displacement. Later, the systematic study of annealing revealed that the traps E3,

E4 and E5 were certainly associated with vacancy-interstitial pairs [27]. The E7 and E9 traps are founded only after low-temperature irradiation ( $T < 200$  K) and they correspond to double displacements. Therefore, they do not exhibit any anisotropy. The identified traps by DLTS and their properties are listed in Table 1-1.

The electron traps are always produced with same introduction rate in n-type materials, whatever the concentration and nature of the impurities [28] and of the native defects it contains. This is a strong evidence that the traps are the result of stable intrinsic defects because they do not interact with the various impurities contained in the material.

On the other hand, in p-type GaAs, the situation seems to be more complicated than in n-type material. Loualiche et al [29] have already reported that the defects created by the irradiation exhibit different hole traps in liquid-phase epitaxy (LPE) and vapor-phase epitaxy (VPE) grown GaAs, indicating that some intrinsic defects interact with impurities, and they are mobile at the temperature where the material is irradiated. H1 to H3 traps were also detected in p-type material by Lang and Kimerling [30] and Loualiche et al [29]. An additional trap, labeled H0, has been discovered by Pons [31]. The last hole trap, H0, is actually the most important hole trap since it is not observed in n-type material, but can potentially exist, undetected because it is probably masked by one of electron traps. The introduction rates of the H0 and H1 traps were measured during 4 K irradiation [31]. These traps exhibit practically same introduction rates both at 4 K and at room temperature, indicating that they are related to primary defects (like E1 to E3). The H2 and H3 traps seem to be related to the impurities contained in the materials. They can be understood in the way as the formation of the  $As_{Ga}$  antisite of the complexes Boron(B) -  $As_i$  and Carbon(C) -  $As_i$ : namely, through the mobility of  $As_i$  induced by electron-hole pair injection. The  $As_{Ga}$  antisite defect is also called as EL2 defect. Since EL2 can exist in stable form as isolated  $As_{Ga}$  and in unstable state by forming a complex with impurities (such as Boron and Carbon), this defect has metastable characteristics.

Table 1-2. Identification of electron irradiation induced defects in p-type GaAs: Peak temperature  $T_0$  (for an emission rate of  $70 \text{ s}^{-1}$ ), introduction rate  $\tau$  for 1 MeV electron irradiation, energy level  $E_e$  (from the valence band), capture cross-section  $\sigma$ , annealing temperature  $T_a$  [29], [31].

Trap	$T_0$ (K)	$\tau$ ( $\text{cm}^{-1}$ )	$E_e$ (eV)	$\sigma$ ( $\text{cm}^{-2}$ )	$T_a$ (K)
H0	50	0.8	0.06	$1.6 \times 10^{-16}$	-
H1	150	0.1 – 0.7	0.29	$5 \times 10^{-15}$	500
H2	190	-	0.41	$2 \times 10^{-16}$	-
H3 (B)	340	~0.2	0.71	$1.2 \times 10^{-14}$	-

Due to the metastability, it has gained a lot of interests at a technological point in defect research. The  $As_{Ga}$  antisite has been analyzed using EPR technique, together with DLTS by several researchers [32],

[33]. They have proposed several models to explain the behavior of EL2 defect. The identified hole traps in electron irradiated n- and p-type GaAs and their information are summarized in Table 1-2. The defects produced by electron irradiation in n-type GaAs are annealed in three stages: stage I at ~ 230 K, stage II around 280 K and stage III around 500 K. Annealing experiments using the DLTS technique show that traps E<sub>7</sub> and E<sub>9</sub> must be ascribed to stage I while all other electron traps (E1 to E5) are annealed out in stage III [23], [26]. No trap having a thermal behavior corresponding to stage II has been found. After the annealing stage III, other traps appear, labeled P<sub>1</sub>, P<sub>2</sub> and P<sub>3</sub> [26]. The concentration of P<sub>1</sub> increases with the annealing temperature, around 500 K. Clearly, the appearance of the trap P<sub>1</sub> is correlated with the annealing of the primary defects. This is not so for P<sub>2</sub> and P<sub>3</sub>. These traps are probably directly created by the irradiation, i.e. before any annealing has occurred. P<sub>3</sub> is annealed around 650 K and P<sub>2</sub> at a slightly higher temperature [26].

### 1.3.1.2 Proton irradiation-induced defects in GaAs

Even though the amount of work is relatively few, proton irradiation results on the n-type GaAs also exist in the literature. As it was already observed from the electron irradiation on the GaAs, proton irradiation produces nearly same kind of defects in the material. Brunkov et al [34] have found E<sub>3</sub>, E<sub>4</sub>, E<sub>5</sub> and EL2 defects from proton irradiated n-type GaAs (6.7 MeV proton, irradiation at 300 K). They varied the proton irradiation fluence from  $1 \times 10^{10}$  to  $1 \times 10^{12}$  cm<sup>-2</sup>. At low irradiation fluence ( $1 \times 10^{10}$  cm<sup>-2</sup>), only two deep level E<sub>3</sub> (E<sub>C</sub> - 0.33 eV) and EL2 (E<sub>C</sub> - 0.76 eV) were detected from DLTS measurement. At  $1 \times 10^{11}$  cm<sup>-2</sup>, the DLTS spectrum showed E<sub>4</sub> (E<sub>C</sub> - 0.61 eV) defect together with E<sub>3</sub> and EL2. Then the irradiation with a fluence of  $1 \times 10^{12}$  cm<sup>-2</sup> resulted in an increase of defect concentration of E<sub>3</sub>, E<sub>4</sub> and EL2, forming another defect E<sub>5</sub> (E<sub>C</sub> - 0.82 eV). This behavior seems to be related to the fluence dependence of defect formations i.e. at lower dose, isolated defects are formed, and then at higher dose, the defect concentration increases and then their interactions are intensified resulting in the new type of trap level like E<sub>5</sub>. Furthermore, the behavior of defect concentration of EL2 is related to the interaction between E<sub>2</sub> and E<sub>3</sub>. Due to this reaction, increase of EL2 concentration at high dose was relatively remained as constant while the E<sub>4</sub> and E<sub>5</sub> defects are greatly generated. Besides, EL2 defect exhibits the persistent photoquenching (PPQ) effect and is identified as the isolated antisite defect As<sub>Ga</sub> like already discussed in the electron irradiation case.

In the meantime, Guillot et al [35] have similarly performed an analysis on n-type GaAs with relatively low proton energy (100 keV, irradiation at 77 K and 300 K) using DLTS technique, together with deep level optical spectroscopy (DLOS). They identified the electron traps E<sub>2</sub>, E<sub>3</sub>, E<sub>4</sub> and E<sub>5</sub> including I and D1 traps. In their research, E<sub>2</sub> and E<sub>3</sub> have been found to be related to the primary defect, having a thermal activation energy of E<sub>C</sub> - 0.16 and E<sub>C</sub> - 0.35 eV, respectively.

Table 1-3. Identification of 6.7 MeV proton irradiation induced defects in n-type GaAs: energy level  $E_e$  (from the conduction band), capture cross-section  $\sigma$  [34].

Trap	$E_e$ (eV)	$\sigma$ ( $\text{cm}^{-2}$ )
E3	0.33	$2 \times 10^{-15}$
E4	0.61	$1.6 \times 10^{-14}$
E5	0.82	$1.6 \times 10^{-12}$
EL2	0.76	$1.2 \times 10^{-14}$

In addition, after irradiation at 77K, they found a new trap, labeled as I in their study, which has an energy level of  $E_C - 0.26$  eV between E2 and E3. Concerning the trap levels E4 and E5 in comparison with the trap E3, they compared these traps for electron irradiated and proton irradiated samples. It seems that the formation mechanism of E4 and E5 during proton irradiation is more complex than the case of E3 because the proton irradiated sample showed much higher introduction rates of these traps (factor of 5 compared to the electron irradiated sample). The defect D1 has not been detected in electron irradiated GaAs grown by both LPE and VPE methods, but this defect is found in the case of proton irradiation with the average irradiation fluence, indicating that it is related to the proton implantation in GaAs since the heavy particles such as proton and neutron can produce more complex defects than electrons. The energy level of D1 is below 0.3 eV from the conduction band.

Table 1-4. Identification of 100 keV proton irradiation induced defects in n-type GaAs: energy level  $E_e$  (from the conduction band), capture cross-section  $\sigma$  [35].

Trap	$E_e$ (eV)	$\sigma$ ( $\text{cm}^{-2}$ )
E2	0.16	$7 \times 10^{-12}$
D1	0.3	$3 \times 10^{-14}$
E3	0.33	$3 \times 10^{-15}$
E4	0.65	$6.8 \times 10^{-14}$
E5	0.85	$8 \times 10^{-12}$

### 1.3.1.3 Summary of defects in GaAs

The picture of the defects produced by electron irradiation in GaAs is the following: they are in principle primary defects in the As sublattice, i.e. made up of  $V_{As}$  and  $As_i$  which are distributed in pairs. All the E traps are associated with these pairs. This should also be the case for the H traps although certain information is still missing so we cannot draw a clear picture for H traps. Only the  $E_7$  and  $E_9$  traps are associated with a more complicated defect resulting from two adjacent displacements (probably the

association of  $V_{As}$  with a  $Ga_{As}$  antisite). No defects are observed in the Ga sublattice because the  $V_{Ga} - Ga_i$  pairs recombine immediately after their creation, even at the lowest temperature, presumably because of Coulomb attraction. Other defects can be created following irradiation at room temperature if special conditions are satisfied, i.e. when  $As_i$  can be migrated by hole injection. Then the migrating  $As_i$  can form complexes with impurities such as B and C. Furthermore, in some cases, they exchange their interstitial sites for the substitutional sites of impurities on Ga sites, resulting in the formation of  $As_{Ga}$  antisites (EL2 defects). Similarly, the proton irradiation of n-GaAs produced traps related to the primary defects in the As sublattice. Trap levels have been correlated to the case of electron ones. But, when the proton energy is low enough, the proton irradiation creates a new trap level which is probably related to the complex defect formation due to the proton implantation.

In summary, to contain all information in one picture, we have categorized all the traps according to their energy levels and the type of defects within the bandgap of GaAs as shown in Figure 1-7.

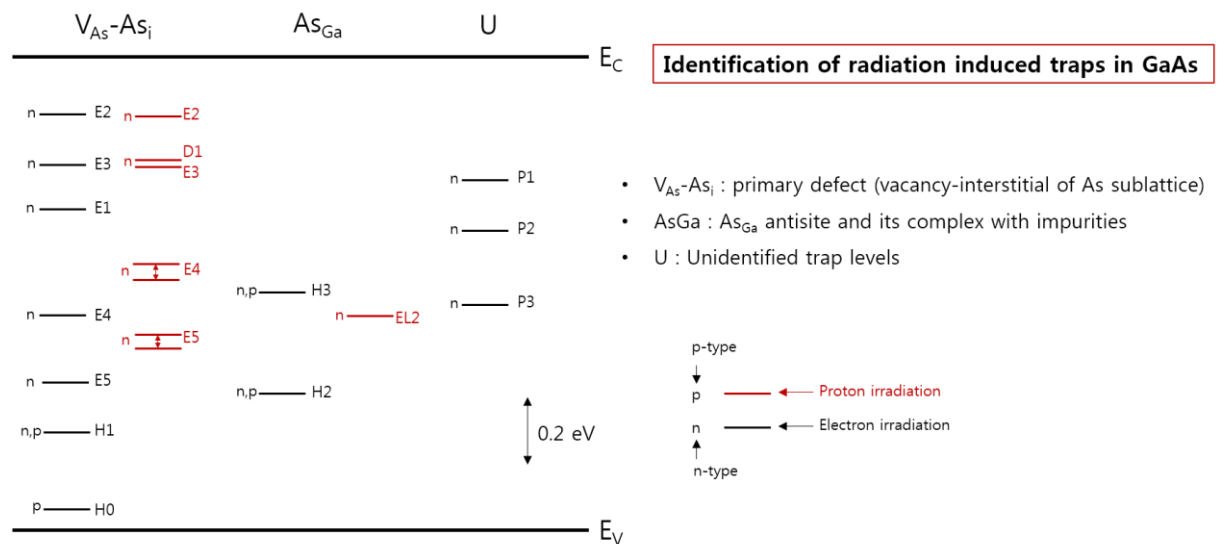


Figure 1-7. Tentative representation of identification of radiation induced traps in GaAs.

### 1.3.2 Production of defects in n- and p-doped Gallium-Indium-Phosphide (GaInP)

After the knowledge of the GaAs material became mature, GaInP compound has gained an interest since 1990s. The research on GaInP has been accelerated in demand to apply this material to the multijunction solar cell technology based on GaAs. Then, naturally, it was required to study the nature of defects in this material. Before the rising on demand of knowledge of defect nature of GaInP, study of defects introduced by high energy electron irradiation has been already done for InP [36]-[39] and GaP [40]-[42], but not for GaInP yet. Thus, the identification of defects in GaInP induced by irradiation was based on the information which already exists in InP and GaP. Unfortunately, only Ga vacancy related defects has been identified by EPR [40]. Except the traps related to the Ga vacancy, others were indirectly identified from capacitance transient spectroscopy, annealing rates, introduction rates, variation of

growth techniques, etc. In fact, defects introduced by electron irradiation in InP exhibited annealing stages below 300 K indicating that there can exist a formation of more complex defects between primary defects and impurities. Therefore, it was obliged to do a low temperature irradiation to properly identify defects and their trap levels. As to the GaP compound, a limited characterization of defects has been made using the capacitance transient spectroscopy [42].

### 1.3.2.1 Electron irradiation-induced defects in GaInP

Under this situation, Zaidi et al [43], as the first attempt, have performed electron irradiation to n-type GaInP at room temperature with 1 MeV of electron energy. From this study, they found four electron traps, labeled IE1 - IE4, emitting DLTS signals at around 80, 220, 320, and 365 K, respectively, while no hole traps have been detected. Then, their associated energy levels were found through the Arrhenius plot of electron emission rates versus temperature. Energy levels of traps IE1 and IE2 were placed shallow under the conduction band;  $E_C-0.13$  and  $E_C-0.347$  eV, respectively. But, IE3 and IE4 were detected in deeper levels;  $E_C-0.66$  and  $E_C-0.83$  eV, respectively. Interesting observation is that the introduction rates of all these traps were very low as compared to the theoretical ones (see Table 1-5). Indeed, if we consider similar displacement energy for GaInP and InP (in the range of 7 – 10 eV for a P displacement and 3 – 5 eV for In displacement) [37], the introduction rate  $\tau$  of traps, expected if the defects originates from primary displacements, i.e. defects are isolated vacancies and interstitials, then  $\tau$  should be of the order of  $1 - 10 \text{ cm}^{-1}$  at 1 MeV electron irradiation conditions. This indirectly indicates that the defects induced by electron irradiation in n-type GaInP at room temperature are not primary defects, rather, they are results of secondary reaction of these ones; they could be already recombined or interact with other primary defects to form secondary defects or with impurities, resulting in complex defects.

Table 1-5. Identification of 1 MeV electron irradiated induced defects in n-type ( $1.2 \times 10^{19} \text{ cm}^{-3}$ ) GaInP: Peak temperature  $T_0$ , introduction rate  $\tau$ , thermal activation energy level  $E_e$  (from  $E_C$  for electron traps, from  $E_V$  for hole traps), capture cross-section  $\sigma$ , annealing temperature  $T_a$  [43].

Trap	$T_0$ (K)	$\tau$ ( $\text{cm}^{-1}$ )	$E_e$ (eV)	$\sigma$ ( $\text{cm}^{-2}$ )	$T_a$ (K)
IE1	80	$4 \times 10^{-3}$	0.13	$4.2 \times 10^{-14}$	-
IE2	220	0.1	0.347	$1.9 \times 10^{-15}$	-
IE3	320	0.13	0.66	$2.7 \times 10^{-13}$	-
IE4	364	0.41	0.83	$2.5 \times 10^{-12}$	-

In addition, the trap levels IE3 and IE4 exhibit large barrier for electron capture (this is why the capture cross section of the two traps are especially smaller than the other two traps). In a classical III-V compound, this is apparently not a common behavior. A similar behavior has been observed in GaAlAs

alloys. This finding suggests that the variation of barrier level for capture of minority carrier can be dependent on the conduction band structure, which can be modulated by adjusting the compound ratio (for example, varying  $x$  of  $\text{Ga}_x\text{In}_{1-x}\text{P}$ ).

Concerning the 1 MeV electron irradiation on the p-type GaInP, Khan et al [44] have detected three hole traps, labeled H1 ( $E_V + 0.20$  eV), H2 ( $E_V + 0.50 - 0.55$  eV), and H3 ( $E_V + 0.76$  eV), through majority carrier trap spectra and three electron traps, labeled E1 ( $E_C - 0.20 - 0.29$  eV), E2 ( $E_C - 0.36$  eV), and E3 ( $E_C - 0.72$  eV), from minority carrier trap spectra of DLTS technique. They first, observed the change of amplitude of H2 peak during a room temperature (RT) storage. For H1 trap, the change of amplitude of H1 peak differed from sample to sample. Therefore, it was not possible to make any conclusions for H1 trap. As to H3, since its peak lies at about 375 K, room temperature annealing study could not solve the annealing property of this trap. Came back to the trap H2, after 40 days of RT annealing, the concentration of H2 trap has been decreased about 25 %. Similar to the case of InP [45], [46], any other evolution induced by annealing was not observed. Then, they combined their defect analysis with the I-V characteristics of a studied  $n^+p$  GaInP solar cell. The RT annealing of H2 traps result in a recovery of  $I_{SC}$  of the cell, which probably indicates the recovery of minority carrier diffusion length in the base region of the solar cell, i.e. p-type GaInP. However, the extent of recovered  $I_{SC}$  is relatively small, while the concentration of H2 is decreased by 25 %. It is because the carrier removal effects in p-layer is not recovered during the RT annealing. In addition, the result suggests that other traps are also involved to the degradation of electrical performance of the solar cell. The systematic analysis using annealing study has been conducted for all detected traps as shown in Table 1-6. Through the injection and thermal annealing behavior of H2 level, they tentatively concluded that the H2 trap is related to the phosphorous Frenkel pairs ( $V_P - P_i$ ), similar to the H4 trap level in InP [36], [45].

Table 1-6. Identification of 1 MeV electron irradiated induced defects in  $n^+p$  GaInP solar cell: Peak temperature  $T_0$ , introduction rate  $\tau$ , thermal activation energy level  $E_e$  (from  $E_C$  for electron traps, from  $E_V$  for hole traps), capture cross-section  $\sigma$ , annealing temperature  $T_a$  [44].

Trap	$T_0$ (K)	$\tau$ ( $\text{cm}^{-1}$ )	$E_e$ (eV)	$\sigma$ ( $\text{cm}^{-2}$ )	$T_a$ (K)
E1	180	0.05	0.2 – 0.29	$9.9 \times 10^{-16}$	673
E2	290	0.14	0.36	$3.3 \times 10^{-17}$	673
E3	350	0.2	0.72	$2.5 \times 10^{-17}$	648
H1	90	0.02	0.2	$3.7 \times 10^{-17}$	473
H2	220	0.05	0.5 – 0.55	$4.2 \times 10^{-16}$	573
H3	360	0.04	0.76	$5.2 \times 10^{-16}$	573

Meanwhile, the electron traps E1 and E2 existed before irradiation, then E<sub>1</sub> has been suppressed when the sample has been irradiated. The trap E1 has a DLTS peak near 150 K, which is also labeled DX in other studied of n-type GaInP [47]-[49], indicating that the E1 is native defect in n<sup>+</sup> layer of the n<sup>+</sup>p GaInP solar cell. On the other hand, the other native defect which lies at E<sub>C</sub>-0.39 eV, also labeled E2, is significantly enhanced by electron irradiation. The behavior of E2 can be explained in the following ways:

- (i) Electrically inactive defects are activated by irradiation, e.g., by transformation from the interstitial to the substitutional site as a result of vacancy generation, implying that E2 is a complex involving a substitutional atom (In, Ga, or P).
- (ii) Or, the concentration of E2 defect, which is already composed of complex with a substitutional atom, is enhanced by irradiation.

By the way, the existence of electron traps E1, E2, and E3 is not crucial importance for the n<sup>+</sup>p junction solar cell since the performance of this type of solar cell is mainly determined of minority carrier lifetime of p-type layer.

### 1.3.2.2 Proton irradiation-induced defects in GaInP

Similarly, Dharmarasu et al have conducted the irradiation to n<sup>+</sup>p GaInP solar cells with 3 MeV proton [50]. As detected from electron irradiation study by Khan et al [44], a few kinds of traps were found at the same level; E1 (E<sub>C</sub> - 0.20 eV), E2 (E<sub>C</sub> - 0.38 eV), and H2 (E<sub>V</sub> + 0.55 eV). E1 and E2 traps are related to the native defect of GaInP, and H2 trap is from the phosphorous Frenkel pair as discussed in the electron irradiation case.

Table 1-7. Identification of 3 MeV proton irradiated induced defects in n<sup>+</sup>p GaInP solar cell: thermal activation energy level E<sub>e</sub> (from E<sub>C</sub> for electron traps, from E<sub>V</sub> for hole traps), density of traps N<sub>T</sub> [50].

Trap	E <sub>e</sub> (eV)	N <sub>T</sub> (cm <sup>-3</sup> )
E1	-0.20	2.3x10 <sup>15</sup>
E2	-0.38 +/- 0.02	5.0x10 <sup>14</sup>
H2	+0.55	5.4x10 <sup>14</sup>
EP1	-0.54	8.1x10 <sup>14</sup>
EP2	-0.79 +/- 0.02	9.0x10 <sup>14</sup>
HP1	+0.90 +/- 0.05	1.1x10 <sup>15</sup>
HP2	+0.73 +/- 0.05	1.8x10 <sup>15</sup>

On the other hand, there are new 4 traps which have been detected from this proton irradiation, labeled EP1, EP2, HP1, and HP2. The HP1 and HP2, together with H2, act as recombination centers and play an important role in determining the minority carrier lifetime. It is found that the H2 trap anneals out on

minority carrier injection due to nonradiative electron-hole recombination enhanced annealing. However, it is not the case for HP1, HP2, and EP1. In the meantime, HP2 trap is annihilated at 573 K (673 K for HP1). The high temperature annealing of HP1 trap maybe indicate that this defect is from the  $V_P$  related complexes and/or transformed defects from  $V_P$  such as  $Ga_P$  or  $In_P$  antisites. Interestingly, it seems that EP1 is transformed to EP2 when it undergoes the annealing at 573 K. Similar defect transformations have been already detected in InP [36]. In the meantime, Dekker et al [51], [52] was also working on the proton irradiation to identify defects in n- and p-type GaInP. The irradiation was always performed at room temperature. As a measurement method, they have introduced positron annihilation spectroscopy (PAS), together with DLTS technique. They have also found three hole traps, labeled P1, P2, and P3. These hole traps lie at the same energy level of hole traps H1, H2, and H3 detected from electron irradiation.

### 1.3.2.3 Summary of defects in GaInP

The amount of information of identified defects in GaInP was relatively few compared to that of GaAs. However, by comparing properties of defects in GaInP with that of InP, GaP, it was possible to build a preliminarily representative defect identification in GaInP as shown in Figure 1-8. Indeed, in GaInP, there also exist several kinds of defects, which eventually again diversify the localized trap levels. One of the most interesting point is that when we compare the electron and proton radiation induced traps, we could find the same level of trap from a defect related to the Phosphorous Frenkel pair and defects derived from the native defects. On the other hand, when the traps are related to the complex with impurities or secondary defects, the trap levels of electron induced defects and proton induced defects appeared totally differently.

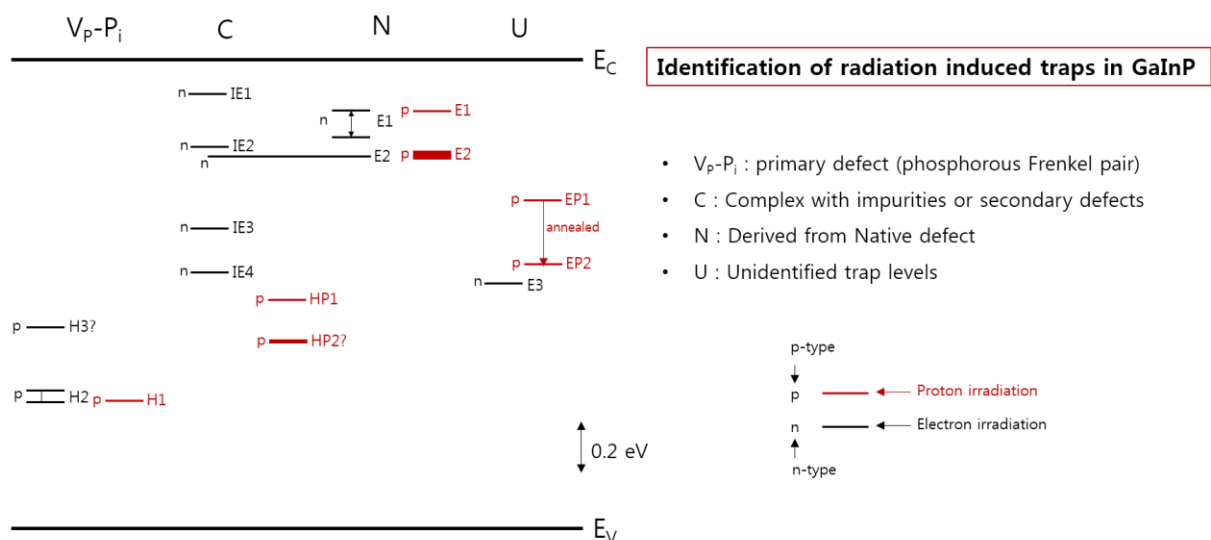


Figure 1-8. Tentative representation of identification of radiation induced traps in GaInP.

### 1.3.3 Production of defects in n- and p-doped Germanium (Ge)

When it comes to the germanium, we often compare its property with the one of silicon. However, our knowledge of point defect of germanium is still far behind that of defects in silicon. The reason is that spectroscopic techniques which have been applied very well to the silicon in identifying most of the simple defects in silicon, which are not so good to detect defects in germanium. It is in principle due to the fact that EPR signal is too weak in germanium (related to the short spin orbit relaxation time) and germanium exhibits practically no hyperfine interaction [53], [54]. Furthermore, IR absorption bands are difficult to observe due to the lack of vibrational mode associated with oxygen related defects [55]-[57]. As a consequence, most of all information on defects in germanium has been obtained from electrical measurements, i.e. counting the total number of electrically active defects, mobility and lifetime of free carriers, and etc.

#### 1.3.3.1 *Electron irradiation-induced defects in Ge*

Bourgoin et al have summarized extensive amount of previously performed studies of electron irradiation in germanium [58]. In lightly n-doped ( $1 \times 10^{13} \text{ cm}^{-3}$ ) germanium, when it is irradiated with electrons (energy: 2 MeV maximum) at room temperature, four majority (electron) carrier traps, labeled E1, E2, E4, and E5, and minority (hole) carrier traps, labeled H1, H2, H3, and H4. The concentration of traps varies with the energy of irradiation [59], [60] in such a way for traps E1, E2, H2, H3, and H4 the variation of their creation rate follows a theoretical curve corresponding to  $T_d = 20 - 30 \text{ eV}$  while for traps H1, E4, and E5 it corresponds to  $T_d = 40 - 50 \text{ eV}$ . This observation indicates that the traps E1, E2, H2, H3, and H4 are related to vacancy or interstitial complexes. Concerning the other three traps, i.e. H1, E4, and E5, because the  $T_d$  is approximately 2 times greater than the theoretical value of displacement energy, it must be associated with the displacement of two neighboring atoms, that is, they must be related to divacancy.

Another very interesting point is that the defect introduction rate in germanium seems to vary a lot depending on the type of dopant and doping concentration. Experimentally, 1 MeV electron irradiation at 4 – 10 K gives  $\tau_{ex} \cong 1 \text{ cm}^{-1}$  in n-doped ( $\sim 10^{14} \text{ cm}^{-3}$  and  $\sim 10^{18} \text{ cm}^{-3}$ ) germanium [61], [62]. But in lightly doped ( $10^{13} \text{ cm}^{-3}$ ) n-type germanium,  $\tau_{ex}$  was about  $10^{-2} \text{ cm}^{-1}$  and it becomes negligibly small in p-type material [63].

However, Different from the early authors, Lindberg et al have succeeded to fabricate a good quality n<sup>+</sup>p mesa Ge diode[64]. With this structure, a significant fraction of antimony (Sb) atoms from n<sup>+</sup> doped side diffuse over the junction where they can be used as an efficient marker for mobile vacancies. The recent research work by Mesli et al [65] has identified two defect levels in p-doped ( $\sim 10^{15} \text{ cm}^{-3}$ ) germanium (2 MeV electron irradiation with a fluence of  $2 \times 10^{14} \text{ cm}^{-2}$  at 22 K). One is tentatively assigned to the vacancy where  $E_v + 0.14 \text{ eV}$  and the other is made on the hole midgap trap ( $E_v + 0.33 \text{ eV}$ ), which may stem from the Ga interstitial. These two defects disappear once the sample reaches to

the room temperature without converting to any other defect such as divacancy (V – V) or  $Ga_i - V$ . Concerning to the Frenkel pair (FP), it is still much less stable in p-type Ge than it is in n-type, although the FP defect remains very unstable in n-type Ge as well.

From the annealing study, it has been found that up to 95 % of defects disappears at 65 K [61]. Furthermore, the defects which annihilate are not close pairs, rather long-distance pairs [66]. Thus, it is possible to conclude that the recombination of V-I pairs is due to the mobility of one element of the pair. Indeed, at 65 K, the interstitial is mobile, then the vacancy becomes mobile at 100 K [55].

The mobility of interstitial can be changed by illuminating the bandgap light into the germanium. When Ge sample is illuminated, the annealing stage at 65 K is shifted to 27 K [62], [66]. It is also valid to shift the annealing stage through the radiation down to 4.2 K [67], [68]. Let's assume that there is a localized energy level  $E_T$ , which corresponds to the defect related to the interstitial, labeled I1. The trap I1 is now assumed to be a charge state of the interstitial when the Fermi level  $E_F$  is above  $E_T$ , and  $I2 = I1 - e^-$  is its second charge state when  $E_F$  is below  $E_T$ . Therefore, by absorbing the minority (hole) carrier, it can change its charge state and vice versa. It is a consequence of the fact that the interstitials alternatively trap electrons and holes and therefore pass back and forth between the I1 and the I2 states.

In other way, the interstitials interact with the impurity in germanium. In this case, the annealing stage is found at 35 K [62]. The “35 K” stage is due to the thermally induced mobility of the interstitial impurity which annihilates with a vacancy.

Table 1-8. Identification of 1 MeV electron irradiated induced defects in n-type Ge: Thermal activation energy level  $E_e$  (from  $E_c$  for electron traps, from  $E_v$  for hole traps), capture cross-section  $\sigma$  [58].

Trap	$E_e$ (eV)	$\sigma$ (cm <sup>-2</sup> )	Trap	$E_e$ (eV)	$\sigma$ (cm <sup>-2</sup> )
E1	0.26	$9.9 \times 10^{-16}$	H1	0.16	-
E2	0.41	$3.3 \times 10^{-17}$	H2	0.30	-
E4	0.38	$2.5 \times 10^{-17}$	H3	0.37	-
E5	0.37	$3.7 \times 10^{-17}$	H4	0.52	-
M2	0.05	-	M5	0.26	-
M3	0.12	-	M7	0.1 to 0.2	-

Mooney et al carried out DLTS measurement of  $10^{13}$  and  $10^{15}$  cm<sup>-3</sup> n-type doped germanium, irradiated in the range 4 – 10 K with 1 MeV electron with a fluence of  $10^{15}$  cm<sup>-2</sup>, and they detected other new electron traps (labeled M1 to M7) at lower temperature (50 – 240 K). Trap M1 is already present before irradiation, and trap M4 ( $E_c - 0.12$  eV) is found only after a second irradiation stage following a RT annealing after a first irradiation. Signal of trap M6 ( $E_c - 0.36$  eV) is too small to be correctly studied. Trap M7 ( $E_c - 0.1$  to  $0.2$  eV) is difficult to study since it anneals at the temperature it is observed, for the lowest emission rate possible ( $\sim 5$  s<sup>-1</sup>). This defect could be on configuration of A-center (vacancy-

oxygen complex), its growth being due to the vacancy mobility at 100 K. Traps M2 ( $E_C - 0.05$  eV) and M3 ( $E_C - 0.13$  eV), being in equal concentration and annealing at the same temperature, are probably ascribed to the same defect. Since they exist at temperatures lower than the temperature at which the vacancy becomes mobile, they are probably associated with an interstitial related defect. This conclusion has been supported by IR absorption measurement [55], which gave rise at  $630\text{ cm}^{-1}$ , showing a partial recovery of a configuration of A-center at around 200 K, the temperature at which this interstitial related defect anneals. As to the trap M5 ( $E_C - 0.26$  eV), its annealing behavior and energy level are correlated to the  $2.4\text{ }\mu\text{m}$  IR absorption band which has been observed by Stein [57]. Including the information of energy levels of M traps, all detected traps are listed in Table 1-8. All of E and H traps are evidently associated with secondary defects since they are only detected after irradiation at room temperature. The only way to identify these defects is to correlate annealing stages, energy levels and their variations with the nature and the concentration of the impurities contained in the material. Their detailed annealing behavior is described in the Figure 6 of the reference [58].

- Traps E4, E5, and H1 anneal at the same temperature (423 K). This confirms that their identification is same as divacancy.
- The trap E1 is associated with the E-center (vacancy-doping impurity complex).
- The H2 traps is ascribed to the defect containing oxygen.
- The E3 trap anneals in the range of 530 – 600 K, similar to the  $620\text{ cm}^{-1}$  IR band attributed to A-center.
- The H3, H4, and E2 traps have same annealing behavior which can be correlated to the IR band of  $715 - 808\text{ cm}^{-1}$  due to oxygen complexes [55] and as the EPR spectrum associated with an oxygen defect [53].

### 1.3.3.2 Proton irradiation-induced defects in Ge

Fage-Pedersen et al have performed a great work on proton irradiation induced defects in n-type germanium, in comparison with the results obtained from the electron irradiation [69]. In addition, they tried to collect all possible data from the literature. They varied samples depending on the type of dopant (Sb or Ox) and the doping concentration and fixed the irradiation energy as 2 MeV for electron and proton.

The irradiation has been conducted at room temperature. After the proton irradiation on Sb-doped ( $1.4 \times 10^{15}\text{ cm}^{-3}$ ) Ge (Sb2), following an annealing at 380 K, they have detected 4 electron traps, labeled  $E_{0.21}$ ,  $E_{0.23}$ ,  $E_{0.29}$ , and  $E_{0.37}$ , and one hole trap  $H_{0.30}$  before annealing. In their case, label number means energy level from the conduction or the valence bands. For the same type of sample, irradiated with 2 MeV electrons, they have found three electron traps  $E_{0.21}$ ,  $E_{0.23}$ , and  $E_{0.37}$ . As to another Sb-doped ( $3.5 \times 10^{14}\text{ cm}^{-3}$ ) Ge sample (Sb1), they have only performed electron irradiations and found very different kinds of traps:  $E_{0.13}$ ,  $E_{0.19}$ ,  $E_{0.23}$ ,  $E_{0.27}$  and  $E_{0.37}$ . An Ox-doped, proton irradiated Ge exhibited again different traps, labeled  $E_{0.14}$ ,  $E'_{0.19}$ , and  $E_{0.27}$ .

Table 1-9. Identification of 2 MeV electron and proton irradiated induced defects in n-type Ge: Thermal activation energy level  $E_e$  (from  $E_c$  for electron traps, from  $E_v$  for hole traps), capture cross-section  $\sigma$ , annealing temperature, identifications, type of sample, and type of radiation particles are described [69].

Trap	$E_e$ (eV)	$\sigma$ ( $\text{cm}^{-2}$ )	Annealing ( $^{\circ}\text{C}$ ) <sup>a</sup>	Identification	Occurrence	
H <sub>0.30</sub>	0.30 <sup>b</sup>	$1.6 \times 10^{-13b}$	↑150	Sb related	Sb1, Sb2	H,e
E <sub>0.37</sub>	0.37	$1.1 \times 10^{-14}$	↓150	E center	Sb1, Sb2	H,e
E <sub>0.23</sub>	0.23	$2.0 \times 10^{-15}$	↑RT, ↓110	Sb and I related	Sb1, Sb2	H,e
E <sub>0.19</sub>	0.19	$1.5 \times 10^{-14}$	↑RT, ↓RT	Sb and I related	Sb1, Sb2	H,e
E <sub>0.13</sub>	0.13	$3.2 \times 10^{-15}$	↑RT, ↓RT	Sb and I related	Sb1, Sb2	H,e
E <sub>0.21</sub>	0.21	$7.1 \times 10^{-14}$	↑90, ↓180	Sb related?	Sb1, Sb2	H,e
E <sub>0.29</sub>	0.29	$2.1 \times 10^{-15}$	↓180	Divacancy	Sb1, Sb2 (,Ox?)	H
E <sub>0.30</sub>	0.30	$2.9 \times 10^{-14}$	↑RT, ↓110	I and impurity related?	Sb2	H,e
E <sub>0.28</sub>	0.28	$6.2 \times 10^{-15}$	↑190, ↓270	O-impurity complex?	Sb1	H,e
E <sub>0.27</sub>	0.27	$2.6 \times 10^{-15}$	↓150	A center	Sb1, Ox	H,e
E <sup>*</sup> <sub>0.19</sub>	0.19	$2.2 \times 10^{-15}$	↑130, ↓190	O related	Ox	H,e
E <sub>0.14</sub>	0.14	$1.3 \times 10^{-16}$	↑130, ↓190	O related	Ox	H,e

<sup>a</sup>After 2-MeV proton irradiation

<sup>b</sup> $E_{pa}$  and  $\sigma_{pa}$  at  $-1$  V bias.

### 1.3.3.3 Summary of defects in Ge

In summary, the defects which are present at room temperature with a large concentration are vacancy-related defects, associated with oxygen and with the doping impurity. Especially, there exist several oxygen related defects. The divacancy is also present: two localized levels are deep electron traps and one is shallow hole trap. The electron trap level M7 is not possible to be clearly identified since its peak temperature lies at its annealing temperature. In case of the electron irradiation of p-type Ge at low temperature, there has been identified two defect levels, one related to the vacancy and the other one related to the Ga interstitial, but these are completely annealed out once the cell is heat up to the room temperature. A simplified picture that shows positions of electron irradiation induced traps in the n- and p-type Ge forbidden gap is illustrated in Figure 1-9. According to the extensive research of Fage-Pedersen [69], defects introduced by 2 MeV electron and proton at room temperature are nearly identical except one kind of defect; divacancy. Furthermore, there are clear differences of defect generation, depending on the type and the concentration of n type dopant. The case of germanium exhibits a very wide annealing stage from nearly 0 to 500 K. Thus, knowing that which type of traps is remaining at certain working temperature of the solar cell could be a crucial importance to properly characterize the cell performance in relation to the nature of defect.

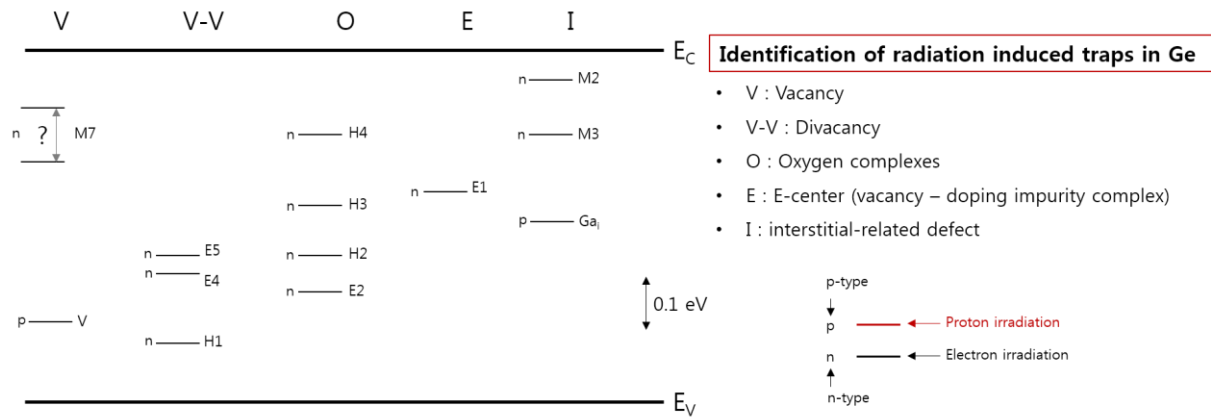


Figure 1-9. Tentative representation of identification of electron irradiation induced traps in Ge.

## 1.4 Mechanism of the degradation induced by the defects

### 1.4.1 Effects in carrier lifetime and diffusion length

The main effect of the displacements produced by irradiation is a disruption of the periodic lattice structure, resulting in a decrease of the minority carrier lifetime. Since, as we saw in Eq. (1-21), minority carrier lifetimes are inversely proportional to the recombination rates, the reciprocal lifetime contributions caused by various sets of recombination centers can be added to determine the inverse of the lifetime as follow:

$$\frac{1}{\tau} = \frac{1}{\tau_0} + \frac{1}{\tau_e} + \frac{1}{\tau_p} + \dots \quad (1-58)$$

where  $\tau$  = final minority carrier lifetime

$\tau_0$  = minority carrier lifetime before irradiation

$\tau_e$  = minority carrier lifetime due to electron irradiation

$\tau_p$  = minority carrier lifetime due to proton irradiation

One of the most commonly used analytical tools for the determination of the particle type and energy dependence of degradation in several types of solar cells including Si and GaAs has been developed from the basic relationship for lifetime degradation:

$$\frac{1}{\tau} = \frac{1}{\tau_0} + K_\tau \phi \quad (1-59)$$

where  $K_\tau$  is the damage coefficient (lifetime) and  $\phi$  is the radiation fluence.

However, minority carrier diffusion length is a more applicable and more easily determined parameter for solar cell analysis than minority carrier lifetime. The hole and electron currents,  $J_p$  and  $J_n$  are proportional to diffusion length  $L_p$  and  $L_n$ . Using  $L^2 = D\tau$ , the above expression becomes:

$$\frac{1}{L^2} = \frac{1}{L_0^2} + K_L \phi \quad (1-60)$$

Where  $L$  is the final minority carrier diffusion length and  $L_0$  is the minority carrier diffusion length before irradiation and  $K_L$  is the damage coefficient of diffusion length ( $= K_\tau/D$ ).

#### 1.4.2 Effects in properties of solar cells

In fact, the degradation of solar cells induced by radiation is most commonly measured in terms of the common electrical parameters such as  $I_{SC}$ ,  $V_{OC}$ , and  $P_{MAX}$ , since most laboratories are not equipped to measure lifetimes or diffusion lengths. The radiation damage in pn junction solar cells such as GaAs is actually even more complicated because the radiation degrades both the p and n-type layers of the cell. Thus, it requires that the diffusion length is measured in both parts to adequately characterize the damage to the cell.

Experience has shown that the degradation of solar cell electrical parameters due to radiation usually be expressed as follow for the case of  $I_{SC}$ :

$$I_{SC} = I_{SC,0} - C \log \left( 1 + \frac{\phi}{\phi_x} \right) \quad (1-61)$$

The  $\phi_x$  term represents the radiation fluence at which  $I_{SC}$  starts to change to a linear function of logarithm of the fluence. The degradation in  $I_{SC}$  may be expressed as a function of  $L$  (through  $K_L$ ) in an equation [70] which has the same form as Eq. (1-61) as follow:

$$I_{SC} = A - B \log(1 + K_L L_0^2 \phi) \quad (1-62)$$

Similar expressions may be obtained for  $V_{OC}$  and  $P_{MAX}$ , but their applicability to pn junction solar cells may be limited because their derivation rests on an expression between a single diffusion length and the short circuit current which has questionable validity for cells having diffusion lengths degrading at different rates on each side of the junction.

## 1.5 Simulation of radiation effects in solar cells

### 1.5.1 The concept of equivalent damage (JPL method)

Accurate calculation of the solar cell degradation due to the radiation effect is one of key element in the design of solar array for a successful mission. Degradation characteristics of solar cells are typically evaluated by irradiating the solar cells with mono-energetic electrons or protons normally incident on the solar cell. However, since the degradation of the solar cell performance is a function of the incident particle and the energy of the particle, significant number of irradiation tests with electrons and protons with various energies would be required to plot a predictable degradation curve of solar cell parameters. (typically 4 for electrons and 8 for protons) This approach has been already done by Jet propulsion laboratory (JPL), so this method is often referred as JPL method [70], [71]. From the experimental results, so-called the relative damage coefficients (RDCs) are derived from the ratios of particle fluences at which a certain level of solar cell degradation is reached. The RDCs are typically obtained by normalizing the critical fluences of electrons and protons separately to reference energies of 1 MeV and 10 MeV, respectively:

$$\begin{aligned} RDC(Z, e, E) &= \frac{\phi_{crit}(Z, e, 1 \text{ MeV})}{\phi_{crit}(Z, e, E)} \\ RDC(Z, p, E) &= \frac{\phi_{crit}(Z, p, 10 \text{ MeV})}{\phi_{crit}(Z, p, E)} \end{aligned} \quad (1-63)$$

where  $Z$  is a photovoltaic parameter such as  $P_{MAX}$ ,  $V_{OC}$  or  $I_{SC}$ ,  $E$  is the energy of the particle and  $\phi_{crit}$  is the critical fluence. Then, finally, the damage coefficient  $RDC_{p \rightarrow e}(Z)$  of 10 MeV protons relative to the 1 MeV electrons can be obtained by respective ratio:

$$RDC_{p \rightarrow e}(Z) = \frac{\phi_{crit}(Z, e, 1 \text{ MeV})}{\phi_{crit}(Z, p, 10 \text{ MeV})} \quad (1-64)$$

### 1.5.2 The concept of displacement damage dose (NRL method)

Recently, scientists from the Naval Research Laboratory (NRL) have developed a much simpler way of deriving an equivalent quantity to the RDCs. They showed that the RDCs for electrons and protons are proportional to the non-ionizing energy loss (NIEL). This quantity can be mathematically calculated for a given material applying the Coulomb scattering theory. The calculated NIEL (in unit of MeV cm<sup>2</sup>/g) is given by following equation:

$$-\left(\frac{dE}{d\chi}\right)_{NIEL} = \frac{N}{A} \int_{E_R}^{E_R^{max}} E_R L(E_R) \frac{d\sigma(E, E_R)}{dE_R} dE_R \quad (1-65)$$

where  $\chi = x\rho_A$ ,  $\rho_A$  is the absorber density in  $\text{g/cm}^3$ ,  $x$  is the penetration depth of the particle in the material,  $N$  is Avogadro constant and  $A$  is the atomic weight of the medium.  $E$  is the kinetic energy of the incident particle;  $E_R$  and  $E_R^{max}$  are the recoil kinetic energy and the maximum energy transferred to the recoil nucleus, respectively.  $E_d$  is the displacement energy,  $L(E_R)$  is the Lindhard partition function [72], [73] and  $d\sigma(E, E_R)/dE_R$  is the differential cross section for elastic Coulomb scattering for incoming particles on nuclei[74].

Degradation data obtained by NRL method is not plotted against fluence but against the product of fluence and NIEL. This quantity has a dimension of a dose and is then called as displacement damage dose (DDD or  $D_d$ ):

$$D_d = NIEL \cdot \phi \quad (1-66)$$

When calculating the NIEL for electrons and protons, one has to make sure that the NIEL calculation was carried out using a correct value of the displacement energy  $E_d$  of a material. Once the NIEL is calculated for the target material, only two proton energies and one electron energy are required to predict the degradation plot of solar cell parameters.

## Conclusion of the chapter 1

In this chapter, we have covered basic, but essentially important knowledge which we thought necessary before entering into the next chapters of my thesis. Starting from the diode equation of the solar cell, we derived each term of current and deepened the understanding of the diode equation; effect of dark saturation current to the light I-V characteristics, temperature dependence of solar cell operation and etc. Then, moved to the theoretical part of displacement damage by incident particle, we understood the concept of collisions and several mechanisms of the energy transfer from the incident particle to the lattice atom.

To correlate the theoretical knowledge of the defect creation by atomic displacement to our actual used materials, we summarized extensive data of irradiation induced defects of GaAs, GaInP and Ge from the literature. The summary of defects in each material will be a handful source to interpret the behavior of our solar cell under very special space conditions. However, as it is noted in the section of nature of defects in semiconductors, those defects are limited to measurable single defects (including primary and secondary defects) and they have been possible to be characterized. In actual radiated materials, there could exist more defects not reacting to the paramagnetic or the electrical way of measurement. There could be other single defects or more complex defects. So, by considering this, we should approach to the correlation of defects created by irradiation and electrical degradation of the solar cell with a conservative point of view.

Next, the influence of defect in the solar cell is briefly discussed, mainly focusing on the aspect of the decrease of carrier diffusion length due to traps in the forbidden gap. Finally, we have also discussed the simulation method of electron and proton irradiation of solar cells in space.

We are now ready to move forward to discuss the new findings in irradiation effect on the lattice matched GaInP/GaAs/Ge triple junction solar cell for space applications.

## Reference

- [1] M. A. Green, Y. Hishikawa, E. D. Dunlop, D. H. Levi, J. Hohl-Ebinger, and A. W. Y. Ho-Baillie, “Solar cell efficiency tables (version 51),” *Prog. Photovolt. Res. Appl.*, vol. 26, no. 1, pp. 3–12, Dec. 2017.
- [2] W. Shockley and H. J. Queisser, “Detailed Balance Limit of Efficiency of p-n Junction Solar Cells,” *J. Appl. Phys.*, vol. 32, no. 3, pp. 510–519, Mar. 1961.
- [3] Ben G Streetman and S. K. Banerjee, *Solid State Electronic Devices*, 6 ed. Pearson Education, 2006.
- [4] C. T. Sah, R. N. Noyce, and W. Shockley, “Carrier Generation and Recombination in P-N Junctions and P-N Junction Characteristics,” *Proceedings of the IRE*, vol. 45, no. 9, pp. 1228–1243, Jan. 1957.
- [5] H. J. Hovel, “The effect of depletion region recombination currents on the efficiencies of Si and GaAs solar cells,” presented at the Photovoltaic Specialists Conference, 10 th, Palo Alto, Calif, 1974, pp. 34–39.
- [6] S. C. Choo, “Carrier generation-recombination in the space-charge region of an asymmetrical p-n junction,” *Solid-State Electronics*, vol. 11, no. 11, pp. 1069–1077, 1968.
- [7] S. M. Sze and K. K. Ng, *Physics of Semiconductor Devices*. Hoboken, NJ, USA: John Wiley & Sons, Inc., 2006.
- [8] C. D. Thurmond, “The standard thermodynamic functions for the formation of electrons and holes in Ge, Si, GaAs, and GaP,” *Journal of The Electrochemical Society*, vol. 122, no. 8, pp. 1133–1141, 1975.
- [9] J. J. Wysocki and P. Rappaport, “Effect of Temperature on Photovoltaic Solar Energy Conversion,” *J. Appl. Phys.*, vol. 31, no. 3, pp. 571–578, Mar. 1960.
- [10] W. Shockley and J. W T Read, “Statistics of the Recombinations of Holes and Electrons,” *Physical Review*, vol. 87, no. 5, pp. 835–842, Sep. 1952.
- [11] R. N. Hall, “Electron-Hole Recombination in Germanium,” *Physical Review*, vol. 87, no. 2, pp. 387–387, Jul. 1952.
- [12] H. J. Hovel and J. M. Woodall, “Theoretical and experimental evaluations of Ga<sub>1-x</sub>Al<sub>x</sub>As-GaAs solar cells,” presented at the Photovoltaic Specialists Conference, 10 th, Palo Alto, Calif, 1974, pp. 25–30.
- [13] G. J. Dienes and G. H. Vineyard, “Radiation Effects in Solids (Interscience, New York, 1957),” *Google Scholar*, p. 129, 1962.
- [14] N. Bohr, *The penetration of atomic particles through matter*, vol. 18. I kommission hos E. Munksgaard, 1948.
- [15] D. Pons and J. Bourgoin, “Anisotropic-defect introduction in GaAs by electron irradiation,” *Physical Review Letters*, vol. 47, no. 18, pp. 1293–1296, 1981.
- [16] N. F. Mott, “The Scattering of Fast Electrons by Atomic Nuclei,” presented at the Proceedings of the Royal Society of London. Series A, 1929, vol. 124, no. 7, pp. 425–442.
- [17] N. F. Mott, “The Polarisation of Electrons by Double Scattering,” presented at the Proceedings of the Royal Society of London. Series A, 1932, vol. 135, no. 8, pp. 429–458.
- [18] W. A. McKinley and H. Feshbach, “The coulomb scattering of relativistic electrons by nuclei,” *Physical Review*, vol. 74, no. 12, pp. 1759–1763, Dec. 1948.
- [19] F. Seitz, “Displacement of atoms during irradiation,” *Solid State Phys.*, vol. 2, pp. 305–449, 1956.
- [20] G. H. Kinchin and R. S. Pease, “The Displacement of Atoms in Solids by Radiation,” *Rep. Prog. Phys.*, vol. 18, no. 1, pp. 1–51, 1955.
- [21] M. J. Berger, J. S. Coursey, M. A. Zucker, and J. Chang, “ESTAR, PSTAR, and ASTAR: Computer Programs for Calculating Stopping-Power and Range Tables for Electrons, Protons, and Helium Ions (version 1.2.3) [Online] Available: <http://physics.nist.gov/Star> [2018, March 13]. National Institute of Standards and Technology, Gaithersburg, MD.” PHYSICAL MEASUREMENT LABORATORY.
- [22] J. Bourgoin and M. Lannoo, *Point Defects in Semiconductors II*, vol. 35. Berlin, Heidelberg: Springer Berlin Heidelberg, 1983.
- [23] D. V. Lang, R. A. LOGAN, and L. C. Kimerling, “Identification of the defect state associated

- with a gallium vacancy in GaAs and  $\text{Al}_x\text{Ga}_{1-x}\text{As}$ ,” *Phys. Rev. B*, vol. 15, no. 10, pp. 4874–4882, Jan. 1977.
- [24] D. Pons and J. C. Bourgoin, “Irradiation-induced defects in GaAs,” *J. Phys. C: Solid State Phys.*, vol. 18, no. 20, pp. 3839–3871, 1985.
- [25] D. V. Lang and L. C. Kimerling, “Observation of recombination-enhanced defect reactions in semiconductors,” *Physical Review Letters*, vol. 33, no. 8, pp. 489–492, Jan. 1974.
- [26] D. Pons, A. Mircea, and J. Bourgoin, “An annealing study of electron irradiation-induced defects in GaAs,” *J. Appl. Phys.*, vol. 51, no. 8, pp. 4150–4157, Aug. 1980.
- [27] D. Stievenard and J. C. Bourgoin, “Defect-enhanced annealing by carrier recombination in GaAs,” *Phys. Rev. B*, vol. 33, no. 12, pp. 8410–8415, Jun. 1986.
- [28] T. I. Kolchenko and V. M. Lomako, “Introduction and annealing of defects in n-type GaAs following irradiation with electrons and gamma rays,” *Radiation Effects*, vol. 37, no. 1, pp. 67–72, Sep. 2006.
- [29] S. Loualiche, A. Nouailhat, G. Guillot, M. Gavand, A. Laugier, and J. C. Bourgoin, “Electron irradiation effects in p-type GaAs,” *J. Appl. Phys.*, vol. 53, no. 12, pp. 8691–8696, Dec. 1982.
- [30] L. C. Kimerling and D. V. Land, “Recombination-enhanced defect reactions in semiconductors,” presented at the Lattice defects in semiconductors, 1974. Invited and contributed papers from the international conference on lattice defects in semiconductors held in Freiburg, 22–25 July 1974, 1975.
- [31] D. Pons, “Anisotropic defect introduction in n and p-GaAs by electron irradiation,” *Physica B+C*, vol. 116, no. 1, pp. 388–393, Jan. 1983.
- [32] H. J. von Bardeleben, D. Stievenard, J. C. Bourgoin, and A. Huber, “Identification of EL2 in GaAs,” *Appl. Phys. Lett.*, vol. 47, no. 9, p. 970, 1985.
- [33] C. Delerue, C. Delerue, M. Lannoo, D. Stievenard, H. J. von Bardeleben, and J. C. Bourgoin, “Metastable State of EL2 in GaAs,” *Physical Review Letters*, vol. 59, no. 25, pp. 2875–2878, Dec. 1987.
- [34] P. N. Brunkov, V. S. Kalinovsky, V. G. Nikitin, and M. M. Sobolev, “Generation of the EL2 defect in n-GaAs irradiated by high energy protons,” *Semicond. Sci. Technol.*, vol. 7, no. 10, pp. 1237–1240, Jan. 1999.
- [35] G. Guillot, A. Nouailhat, G. Vincent, M. Baldy, and A. Chantre, “Caractérisation des défauts produits dans GaAs irradié aux protons par analyse des transitoires thermiques et optiques de capacité,” *Rev. Phys. Appl. (Paris)*, vol. 15, no. 3, pp. 679–686, 1980.
- [36] A. Sibille, “Electronically stimulated deep-center reactions in electron-irradiated InP: Comparison between experiment and recombination-enhancement theories,” *Phys. Rev. B*, vol. 35, no. 8, pp. 3929–3936, Mar. 1987.
- [37] B. Massarani, B. Massarani, and J. C. Bourgoin, “Threshold energy for atomic displacement in InP,” *Phys. Rev. B*, vol. 34, no. 4, pp. 2470–2474, Aug. 1986.
- [38] M. Yamaguchi, C. Uemura, and A. Yamamoto, “Radiation damage in InP single crystals and solar cells,” *J. Appl. Phys.*, vol. 55, no. 6, pp. 1429–1436, Mar. 1984.
- [39] J. Suski, J. C. Bourgoin, and H. Lim, “Defects induced by electron irradiation in InP,” *J. Appl. Phys.*, vol. 54, no. 5, pp. 2852–2854, May 1983.
- [40] T. A. Kennedy and N. D. Wilsey, “Identification of the isolated Ga vacancy in electron-irradiated GaP through EPR,” *Physical Review Letters*, vol. 41, no. 14, pp. 977–980, Jan. 1978.
- [41] D. V. Lang and L. C. Kimerling, “Observation of athermal defect annealing in GaP,” *Appl. Phys. Lett.*, vol. 28, no. 5, pp. 248–250, Mar. 1976.
- [42] E. Y. Brailovskii, I. D. Konozenko, and V. P. Tartachnik, “Defects in Electron-irradiated GaP,” *SOVIET PHYSICS SEMICONDUCTORS-USSR*, vol. 9, no. 4, pp. 505–506, 1975.
- [43] M. A. Zaidi, M. Zazoui, and J. C. Bourgoin, “Defects in electron irradiated GaInP,” *J. Appl. Phys.*, vol. 73, no. 11, pp. 7229–7231, 1993.
- [44] A. Khan, M. Yamaguchi, J. C. Bourgoin, J. C. Bourgoin, and T. Takamoto, “Thermal annealing study of 1 MeV electron-irradiation-induced defects in n+p InGaP diodes and solar cells,” *J. Appl. Phys.*, vol. 91, no. 4, pp. 2391–2397, 2002.
- [45] K. Ando, M. Yamaguchi, and C. Uemura, “Nonradiative-recombination-enhanced defect-structure transformation in low-temperature  $\gamma$ -ray-irradiated InP,” *Phys. Rev. B*, vol. 34, no. 4, pp. 3041–3044, Aug. 1986.

- [46] A. Khan, M. Z. Iqbal, U. S. Qurashi, M. Yamaguchi, N. Zafar, A. Dadgar, and D. Bimberg, "Characteristics of Alpha-Radiation-Induced Deep Level Defects in p-Type InP Grown by Metal-Organic Chemical Vapor Deposition," *Jpn. J. Appl. Phys.*, vol. 37, no. 1, pp. 4595–4602, Aug. 1998.
- [47] S. L. Feng, J. C. Bourgoin, F. Omnes, and M. Razeghi, "Defects in organometallic vapor-phase epitaxy-grown GaInP layers," *Appl. Phys. Lett.*, vol. 59, no. 8, p. 941, 1991.
- [48] J. Krynicki, M. A. Zaidi, M. Zazoui, J. C. Bourgoin, M. DiForte-Poisson, C. Brylinski, S. L. Delage, and H. Blanck, "Defects in epitaxial Si-doped GaInP," *J. Appl. Phys.*, vol. 74, no. 1, p. 260, 1993.
- [49] E. C. Paloura, A. Ginoudi, G. Kiriakidis, N. Frangis, F. Scholz, M. Moser, and A. Christou, "Electrical and structural properties of Ga 0.51In 0.49P/GaAs heterojunctions grown by metalorganic vapor-phase epitaxy," *Appl. Phys. Lett.*, vol. 60, no. 22, pp. 2749–2751, Jun. 1992.
- [50] N. Dharmarasu, M. Yamaguchi, J. C. Bourgoin, T. Takamoto, T. Ohshima, H. Itoh, M. Imaizumi, and S. Matsuda, "Majority- and minority-carrier deep level traps in proton-irradiated n+/p-InGaP space solar cells," *Appl. Phys. Lett.*, vol. 81, no. 1, pp. 64–66, Jul. 2002.
- [51] J. R. Dekker, A. Tukiainen, and R. Jaakkola, "Majority carrier traps in proton-irradiated GaInP," *Applied physics ...*, vol. 73, no. 24, p. 3559, 1998.
- [52] J. Dekker, J. Oila, K. Saarinen, A. Tukiainen, W. Li, and M. Pessa, "Cation and anion vacancies in proton irradiated GaInP," *J. Appl. Phys.*, vol. 92, no. 10, p. 5942, 2002.
- [53] J. A. Baldwin Jr., "Electron Paramagnetic Resonance in Irradiated Oxygen-Doped Germanium," *J. Appl. Phys.*, vol. 36, no. 3, pp. 793–795, Mar. 1965.
- [54] D. L. Trueblood, "Electron paramagnetic resonance in electron-irradiated germanium," *Physical Review*, vol. 161, no. 3, pp. 828–833, Dec. 1967.
- [55] R. E. Whan, "Investigations of Oxygen-Defect Interactions between 25 and 700°K in Irradiated Germanium," *Physical Review*, vol. 140, no. 2, pp. A690–A698, Oct. 1965.
- [56] S. R. Morrison and R. C. Newman, "The question of divacancies in germanium," *J. Phys. C: Solid State Phys.*, vol. 6, no. 11, pp. 1981–1988, Jun. 1973.
- [57] H. J. Stein, "Localized vibrational modes for implanted oxygen in germanium," *J. Appl. Phys.*, vol. 44, no. 6, pp. 2889–2890, Jun. 1973.
- [58] J. C. Bourgoin, P. M. Mooney, and F. Poulin, "Defects and Radiation Effects in Semiconductors," presented at the Inst. Phys. Conf. Ser, 1980, vol. 59, p. 33.
- [59] F. Poulin and J. C. Bourgoin, "Threshold energy for atomic displacement in electron irradiated germanium," *Rev. Phys. Appl. (Paris)*, vol. 15, no. 1, pp. 15–19, 1980.
- [60] F. Poulin and J. C. Bourgoin, "Characteristics of the electron traps produced by electron irradiation in n-type germanium," *Phys. Rev. B*, vol. 26, no. 12, pp. 6788–6794, Dec. 1982.
- [61] T. A. Callcott and J. W. Mackay, "Irradiation Damage in n-Type Germanium at 4.2°K," *Physical Review*, vol. 161, no. 3, pp. 698–710, Sep. 1967.
- [62] J. Bourgoin and F. Mollot, "Behaviour of Primary Defects in Electron-Irradiated Germanium," *physica status solidi (b)*, vol. 43, no. 1, pp. 343–355, Jan. 1971.
- [63] J. E. Whitehouse, "Electron Irradiation of p-Type Germanium at 4.2°K," *Physical Review*, vol. 143, no. 2, pp. 520–525, Mar. 1966.
- [64] C. E. Lindberg, J. L. Hansen, P. Bomholt, A. Mesli, K. B. Nielsen, A. N. Larsen, and L. Dobaczewski, "The antimony-vacancy defect in p-type germanium," *Appl. Phys. Lett.*, vol. 87, no. 17, pp. 172103–4, Oct. 2005.
- [65] A. Mesli, L. Dobaczewski, K. B. Nielsen, V. Kolkovsky, M. C. Petersen, and A. N. Larsen, "Low-temperature irradiation-induced defects in germanium: In situ analysis," *Physical Review B - Condensed Matter and Materials Physics*, vol. 78, no. 16, p. 165202, Oct. 2008.
- [66] J. Zizine, "Radiation Effects in Semiconductors," presented at the Proceedings of the Conference, Santa Fe, USA, Plenum Press, New York, 1968.
- [67] I. Arimura, "Photoabsorption effects in low temperature electron-irradiated Germanium," *IEEE Trans. Nucl. Sci.*, vol. 21, no. 6, pp. 21–25, 1974.
- [68] J. M. Meese, "Low-temperature recovery of irradiation defects in n-type germanium," *Phys. Rev. B*, vol. 9, no. 10, pp. 4373–4391, Jan. 1974.
- [69] J. Fage-Pedersen, A. N. Larsen, and A. Mesli, "Irradiation-induced defects in Ge studied by

- transient spectroscopies,” *Phys. Rev. B*, vol. 62, no. 15, pp. 10116–10125, Oct. 2000.
- [70] H. Y. Tada, J. R. J. Carter, B. E. Anspaugh, and R. G. Downing, *Solar cell radiation handbook*. Pasadena, CA: JPL Publication, 1982.
- [71] B. E. Anspaugh, *GAAS Solar Cell Radiation Handbook*. Pasadena, CA: JPL Publication, 1996.
- [72] I. Jun, “Effects of secondary particles on the total dose and the displacement damage in space proton environments,” presented at the IEEE Transactions on Nuclear Science, 2001, vol. 48, no. 1, pp. 162–175.
- [73] P. R. Hobson, “Principles of Radiation Interaction in Matter and Detection, 3rd edn., by Claude Leroy and Pier-Giorgio Rancoita,” *Contemporary Physics*, vol. 53, no. 6, pp. 544–544, Nov. 2012.
- [74] C. Baur, M. Gervasi, P. Nieminen, S. Pensotti, P. G. Rancoita, and M. Tacconi, “NIEL Dose Dependence for Solar Cells Irradiated with Electrons and Protons,” *arXiv.org*, vol. astro-ph.IM. WORLD SCIENTIFIC, pp. 692–707, 02-Dec-2013.

## *2 Experimental details and Materials*

2.1	Low Intensity Low Temperature (LILT) measurement system setup .....	59
2.1.1	Irradiation Facilities.....	60
2.1.2	Solar Simulator.....	64
2.1.3	Cryostat Chamber and measurement units .....	67
2.2	Structure of lattice matched GaInP/GaAs/Ge triple junction solar cell .....	69
2.3	Photon recycling effect in a component cell.....	71
2.4	In-situ characterization of TJ cells and its component cells .....	74
2.4.1	Indirect temperature measurement .....	75
2.4.2	Beginning Of Life performance of the cells .....	79
2.4.3	Electron and proton irradiation campaigns.....	83
	References .....	89

In this chapter, we introduce the concept of in-situ characterization of solar cell in low intensity low temperature (LILT) conditions under the electron or proton irradiations. The system is composed of mainly four major parts: irradiation facilities, solar simulator, cryostat chamber, and measurement units. First, electron and proton accelerator facilities that have been essential for the JUICE irradiation campaign are briefly presented. Subsequently, the solar simulator and the configuration of the cryostat chamber with electrical measurement units will be shown. Then, the structure of solar cells used in this study is presented. In addition, the test readiness review and preparations before the irradiation campaign are described. This includes temperature cycling test, calibration and stability test of solar simulator, and BOL cell performances. Finally, the photon recycling effect, which inherently exists in BOL component cells (mainly the bottom component cell), will be discussed.

## 2.1 Low Intensity Low Temperature (LILT) measurement system setup

This thesis is directly related to the Jupiter and its moons exploration mission of European Space Agency (ESA). This mission has an official name: JUPITER ICy moon Explorer (JUICE). When the spacecraft travels in space, we must consider its hazard conditions due to the extreme change of temperature, different solar irradiance with respect to the distance from the Sun, and space radiation (including high energy particle radiations). In this respect, the solar cell which generates electricity from the sunlight must be working within these specific mission conditions and the changes in solar cell properties must be carefully predicted and evaluated from experiments on the ground. When the spacecraft will be approaching Jupiter, a giant magnetic field traps highly charged particles travelling the orbit around Jupiter (as it does around Earth). Incident particles on the surface of the solar panel are generally omnidirectional and consist of wide range of energy. As it has been already discussed in the chapter 1, there exists a simulation technique to normalize these variations to conduct the minimum number of experiments in order to reproduce space irradiation conditions. Another important point is that the light intensity is very weak compared to that for GEO satellites. For irradiation study of GEO satellites, we normally take 1 AM0 (which corresponds to the solar irradiance of  $1356 \text{ W/m}^2$ ). On the other hand, when the spacecraft is in the orbit around Jupiter, the solar irradiance drops down to 0.037 AM0 ( $50 \text{ W/m}^2$ ). Furthermore, the temperature becomes also extremely low. According to the analysis performed by ESA [1], during the mission, the spacecraft will be exposed to temperature around 120 K. Thus, we have performed a majority of irradiation tests at 120 K. So, the terminology Low Temperature Low Intensity (LILT) in this thesis refers the condition of temperature 120 K and light intensity 0.037 AM0. The LILT conditions for the experiment can be achieved thanks to the solar simulator technology and the cryostat chamber system. Once the LILT system is prepared, it must be directly connected to the beam line of the accelerator so that the sample is exposed to the high energy particle bombardment. A

simple configuration of the in-situ measurement system of LILT solar cell performance adapted for irradiation facilities is shown in Figure 2-1.

The system is composed of four key parts: a) solar simulator which conveys a relevant AM0 solar spectrum into the cryostat chamber, b) cryostat chamber which is fully conductive (Faraday cage) with a temperature controllable sample support and a quartz window where the light comes in, c) measurement units to characterize the solar cell performance under illumination and in dark, together with the temperature control and monitor, and lastly d) irradiation facilities which are possible to be connected to the cryostat chamber through the beam line. Following subchapters will describe each of these key parts one by one.

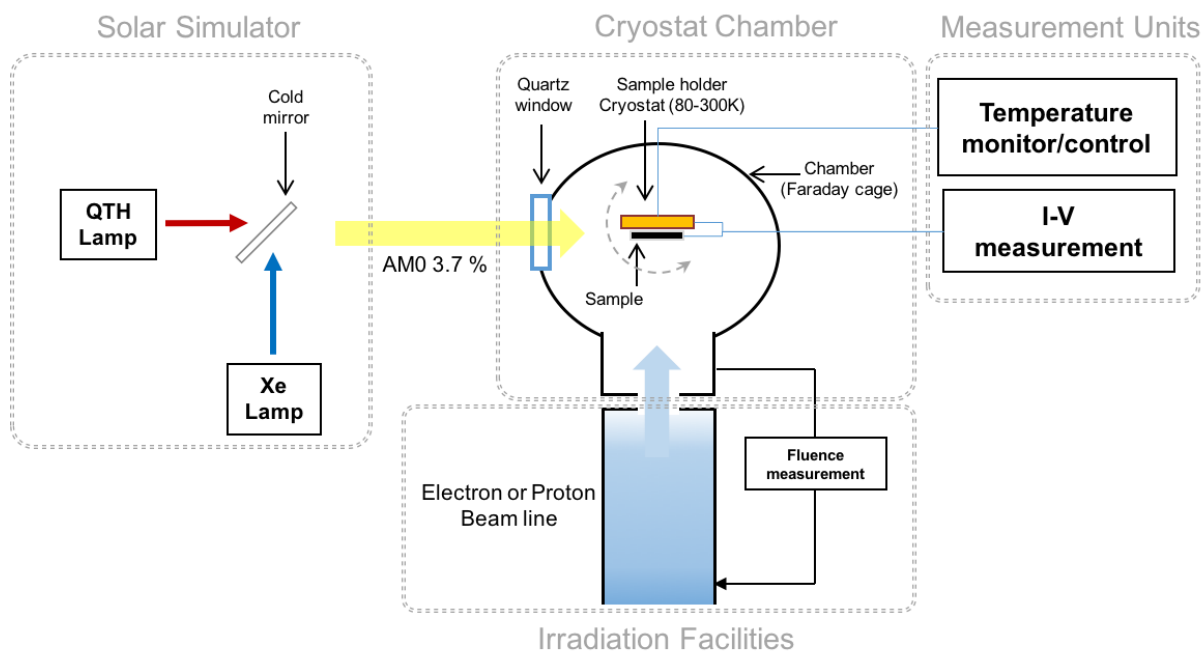


Figure 2-1. Simple configuration of in-situ LILT measurement system set up for solar cells under irradiation.

## 2.1.1 Irradiation Facilities

### 2.1.1.1 Electron irradiation

A pelletron type electron accelerator which was fabricated by National Electronics Corporation (NEC) and is being operated by SIRIUS team at LSI has been used for the electron irradiation. Figure 2-2 shows views of the electron accelerator at several positions. The energy for the electron can be modulated in the range of 150 keV – 2.5 MeV and the amount of current is of 150 nA – 50  $\mu$ A. The pelletron is a type of electrostatic charge generator which is similar to the Van de Graaff generator. The principle of the pelletron technology is to generate electrostatic charge by using a mechanical transport chain system composed of pellets (short conductive tubes connected by links made of insulating material), inductors with power supply and high voltage terminals where the transferred charges are finally built up. The advantage of using the pelletron type as replacement of the Van de Graaff type is that the pellet chains

can operate at a higher voltage than the rubber belt of Van de Graaff type and voltage and current can be achieved far higher. Thus, in the respect of the stability and range of operation energy, the pelletron has a lot of advantages compared to the Van de Graaff type accelerator.

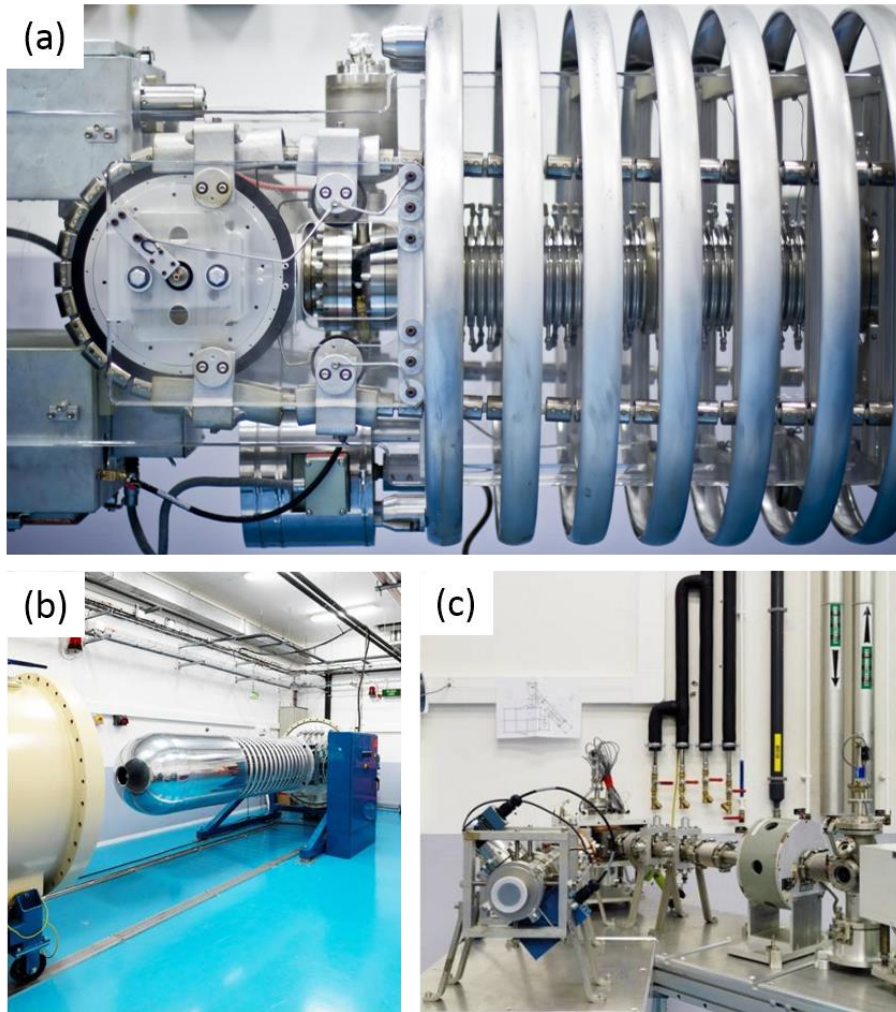


Figure 2-2. View of the pelletron type NEC electron accelerator at SIRIUS: (a) close view of inside – pelletron charging system, (b) accelerator tank, and (c) irradiation beam lines.<sup>6</sup>

The system of pelletron accelerator is surrounded by a pressure vessel filled with insulating sulfur hexafluoride ( $\text{SF}_6$ ) gas and equipped with an evacuated beamline. The acceleration of electron is done between the high voltage terminal and the ground. The accelerated electrons come out from the accelerator tank (see Figure 2-2 (b)) and their trajectories can be controlled by a magnetic field to guide the electrons to the end of beamline.

Typically, the high vacuum level less than  $10^{-7}$  Torr is required in the accelerator to achieve a stable electron beam current from a cathode emitter of the accelerator. The cathode emitter is extremely sensitive to the presence of  $\text{O}_2$  and  $\text{H}_2\text{O}$  molecules, at pressures higher than  $1.5 \times 10^{-7}$  Torr. Under the direct connection of the cryostat chamber and the beamline of the accelerator, it is not possible to achieve such a high vacuum level due to the outgassing from the cryostat chamber. Therefore, it is necessary to

<sup>6</sup> Reference of images: (a) <https://en.wikipedia.org/wiki/Pelletron> (b) and (c) <https://portail.polytechnique.edu/lsi/fr/equipements/linstallation-sirius>

put a stainless thin film (window) in a vacuum tube to isolate the beamline from the cryostat chamber. Maintaining a high vacuum level in the beamline of the accelerator, the cryostat chamber is separately pumped out by using a primary rotary pump to achieve a vacuum level of around  $10^{-3}$  Torr, in which the mean free path of the electron is long enough ( $\sim 10$  cm) to arrive to the solar cell. One consequence of adding the window is the scattering of electrons when they enter into the cryostat chamber (see Figure 2-3 (a)). As a result, the current density decreases with respect to the distance of the target from the window because the electrons are diffused. The fluence integrated in the solar cell is indirectly determined by measuring the current collected in an isolated thick copper which has a same shape as the solar cell samples ( $2 \times 2 \text{ cm}^2$ ). At the same time, the current collected from the Faraday cage is then measured. In this way, the ratio of two current is obtained (see Figure 2-3 (b)) and later the fluence integrated in the solar cell is calculated.

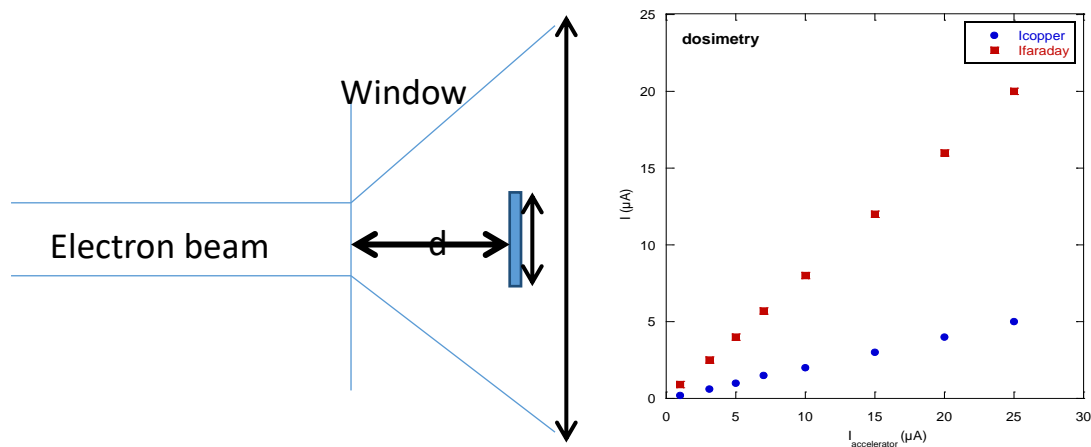


Figure 2-3. Scattering of electrons by the window and fluence calibration procedure.

### 2.1.1.2 Proton irradiation

For the proton irradiation, we have used a tandem type 2MV accelerator ARAMIS of Centre de Sciences Nucléaires et de Sciences de la Matière (CSNSM), a joint research unit belonging to both CNRS/IN2P3 and Université Paris-Sud. Two ion sources (Penning and Middleton) are used for the two working modes of the device:

- 1) Tandem mode is used with a sputtering negative ion source. Current by high negative ions is generated from the sputtering ion source. The ions are injected into the accelerator with an energy of 150 keV. In the center of the accelerator, a nitrogen stripper changes the ion charge sign and multiplies the charge. The ions then receive a second acceleration proportional to its charge.
- 2) With Van de Graaff mode the ion beam is produced from a Penning ion source, placed at the high voltage terminal of the accelerator. Ion ranges are varied depending on the type of gaseous elements such as hydrogen, helium, nitrogen and oxygen. The ion beam accelerated in the ARAMIS acceleration chamber is then extracted to the beamline.

By the switching magnet, the trajectory of the ion beam can be controlled. The configuration of ARAMIS accelerator is described in Figure 2-4. For the proton irradiation of the solar cell in this facility,

the cryostat chamber is directly connected to an interconnect chamber of the implantation beamline. Through the turbo pump of this chamber, the vacuum level of the cryostat chamber is achieved down to around low  $10^{-5}$  Torr. Once the required vacuum pressure is ready, the throat gate of the beamline is open so that the proton beam arrives directly to the solar cell mounted on the support of the cryostat chamber.

The calibration of the proton fluence is carried out by measuring the current density of protons which hit the conductive metal in the form of a circular frame installed between the cryostat chamber and the beamline. Since this circular frame has a hole (radius of 8 cm), the rest of protons can pass through this hole to arrive to the cryostat chamber.

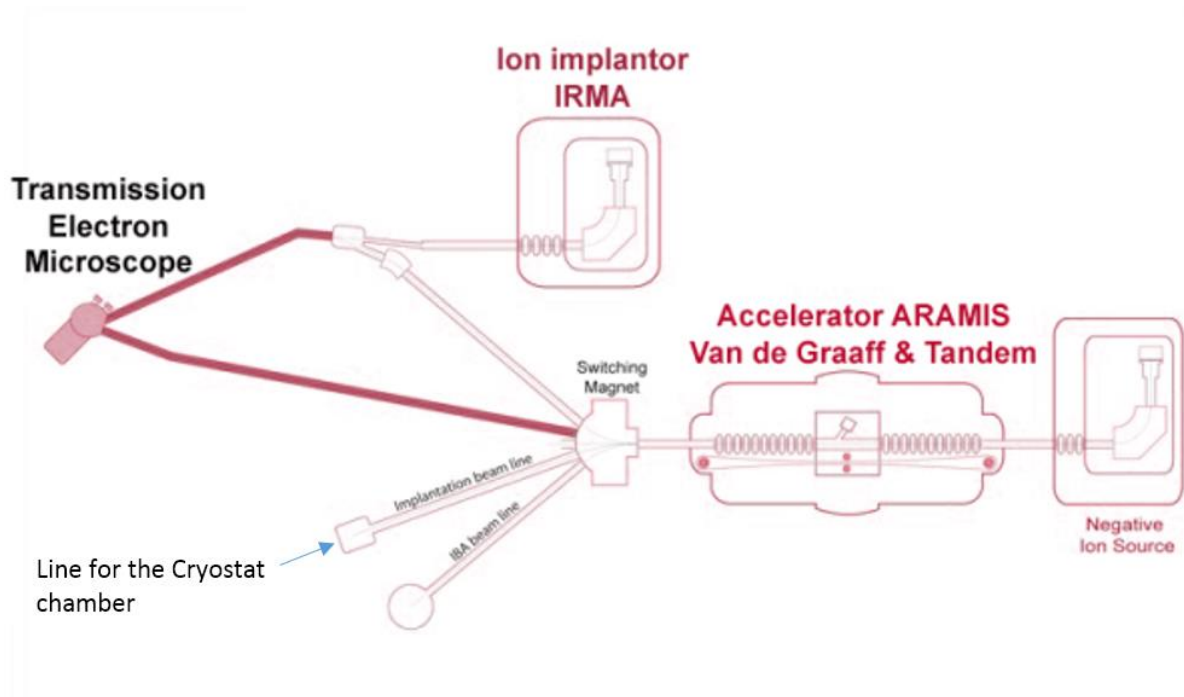


Figure 2-4. Representative configuration of Irradiation facility of Centre de Sciences Nucléaires et de Sciences de la Matière (CSNSM).<sup>7</sup>

<sup>7</sup> Reference of image: <http://jannus.in2p3.fr/spip.php?rubrique14>

## 2.1.2 Solar Simulator

The solar simulator consists of a Xenon (Xe) lamp and a Quartz Tungsten Halogen (QTH) lamp separated by a cold filter. The filter allows transmission of the high energy part (by reflection) of the Xe spectrum and of the low energy part (by transmission) of the QTH spectrum. The intensities of the two lamps must be balanced in order to reproduce the solar spectrum and to obtain an intensity of 3.7% AM0. The solar simulator adjustments and stability as a function of time are therefore critical parameters for a precise analysis of the influence of irradiation on the BOL and EOL electrical properties of TJ solar cells.

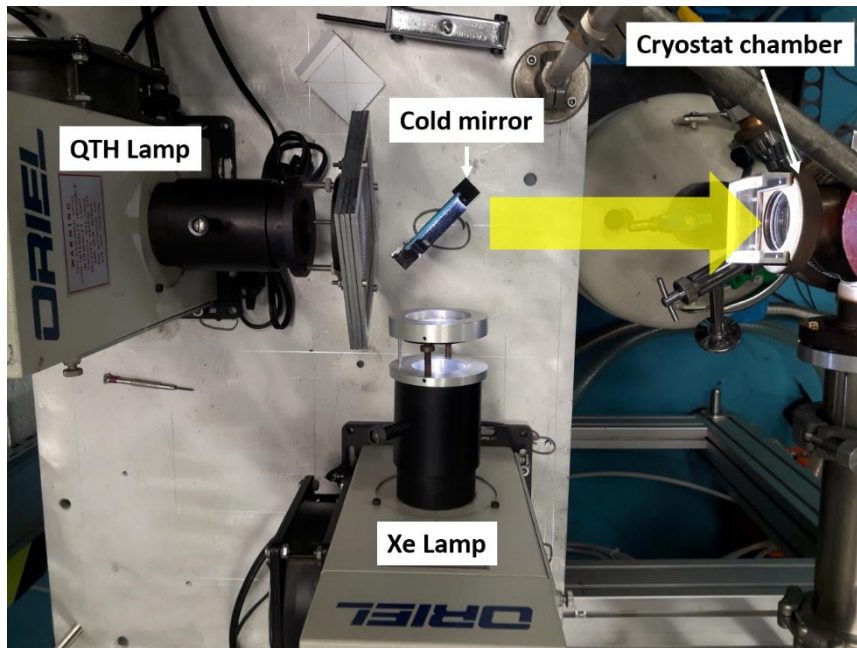


Figure 2-5. Vertical view of the solar simulator.

Figure 2-5 shows a vertical view of the solar simulator. The intensity of two light sources is individually controlled by the power supplies. For the longer spectrum, QTH lamp is too strong to precisely control for 3.7% AM0 condition, in this respect, a metal grid is added between the focal lens of the QTH lamp and the cold mirror to decrease light intensity from the QTH lamp.

Since the intensity and the balance of light from two lamps are extremely sensitive, the position of solar simulator table and the cryostat chamber must be fixed after a calibration.

One of the most important aspect for the solar simulator is a stability of spectrum and intensity. For the acceptable reliability of the solar simulator, the intensity of light should not exceed  $\pm 2\%$  of change during a day and the spectrum itself must be stable within a minimum deviation, if not, it may result in the change of current generation in the solar cell. Therefore, before the irradiation campaign, the stability test has been conducted carefully.

The first test was to record the spectra of the lamps used to simulate the illumination of the solar cells as a function of time with a Shamrock SR-303i-A spectrometer (Andor) coupled with an iSTAR DH734-18F 03 CCD camera (Andor). Figure 2-6 presents the result obtained during 24 hours

experiment with a typical spectrum of the Xe lamp, the maximal deviation from the average value at each wavelength and a line showing the stability goal for the solar simulator. In terms of stability of the Xe lamp, this experiment shows that the 2% goal is achieved for this part of the solar simulator. For the QTH lamp, it was not possible to measure the spectrum using the spectrometer of our laboratory since the measurement range was limited to 800 nm.

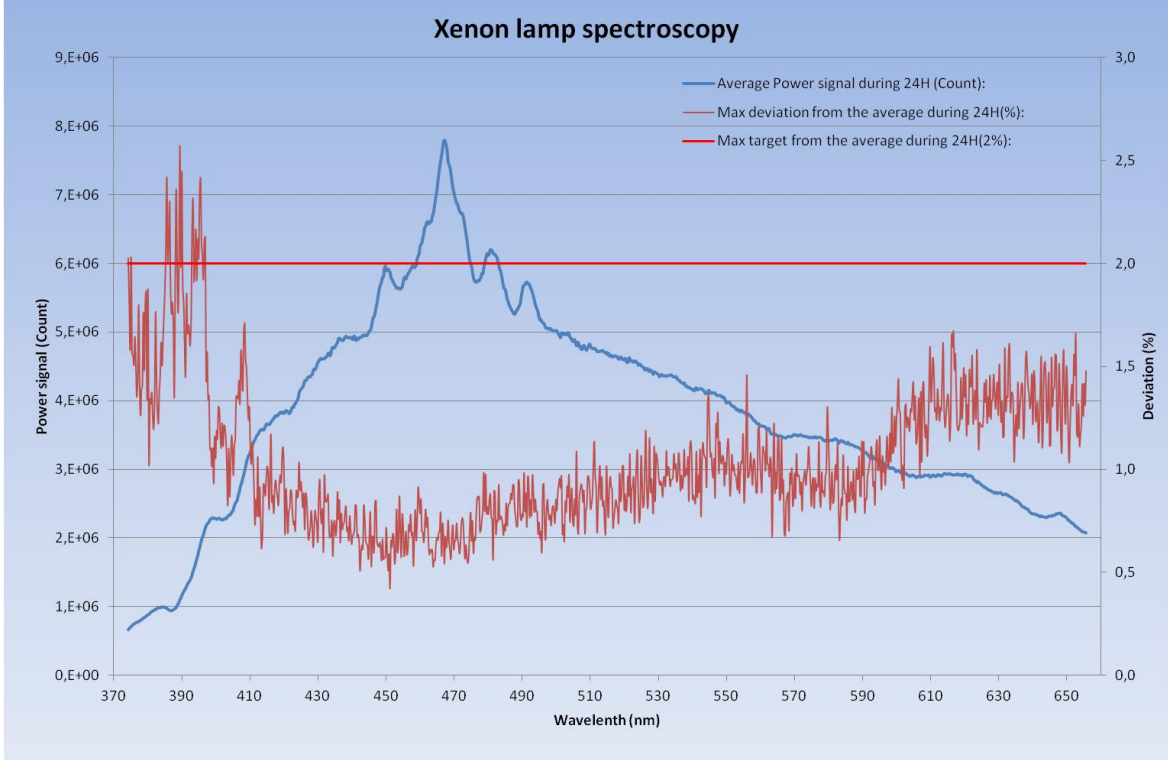


Figure 2-6. Evolution of the Xenon lamp spectrum recorded during 24 hours.

The second test was therefore to record the  $I_{SC}$  stability of three reference component cells as a function of time with a 3.7 % AM0 adjustment of the solar simulator. Figure 2-7 shows a test result made during 24 hours with the solar simulator. We can see that the current of three cells is well maintained within the margin of 2 %. This  $I_{SC}$  measurement shows also a good stability of our solar simulator during 24 hours.

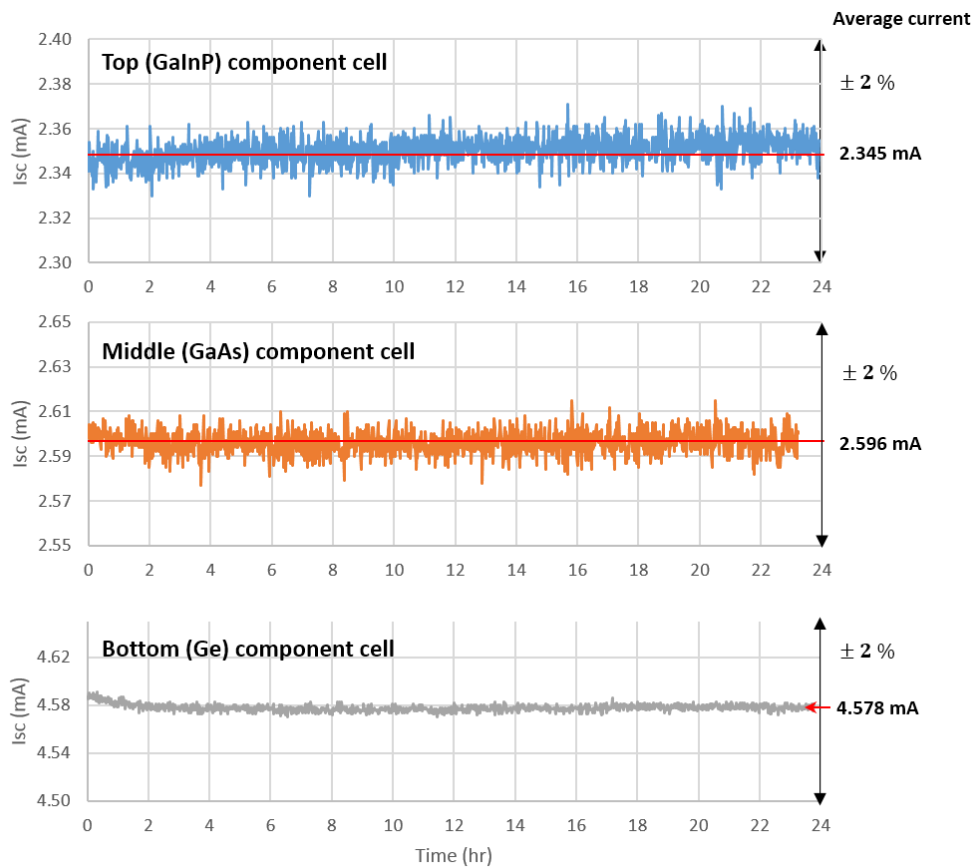


Figure 2-7. Evolution of  $I_{SC}$  measurement of three reference component cells during 24 hours.

The last point is to verify absolute current value of reference component cells. This step is essential to calibrate the solar simulator. By doing this test, the spectrum balance between two lamps can be precisely controlled. First, we have developed a support for component cells (see Figure 2-8 (a) and (b)). For, each reference cell, we measure their  $I_{SC}$  value inside of the cryostat chamber and outside of the cryostat chamber as shown in Figure 2-8 (c) and (d). In this way the correlation of  $I_{SC}$  measured inside and outside of the cryostat chamber can be obtained. For further irradiation tests, we simply verify the stability of the solar simulator by checking  $I_{SC}$  values of reference cells at outside of the cryostat chamber. The steps are described below:

- 1) Calibrate the distance and the intensity of two lamps of the solar simulator by monitoring  $I_{SC}$  values of reference cells mounted inside of the cryostat chamber. The calibrated  $I_{SC}$  must be within 2 % of margin for the top and middle cells and 10 % for the bottom reference cell. The reference values are given from the measurement performed by AZUR Space when the cells were just manufactured.
- 2) Put the sample holder of the reference cells in front of the window of the cryostat chamber as represented in Figure 2-8 (d), then measure  $I_{SC}$  of reference cells, illuminating the light from the solar simulator in dark ambient.
- 3) Verify  $I_{SC}$  value of each reference cell at outside of the cryostat chamber before and after the irradiation test. If  $I_{SC}$  values are out of the margin, control the power of two lights individually.

- 4) Do not adjust the placement of the cryostat chamber and the solar simulator unless the system configuration is modified.

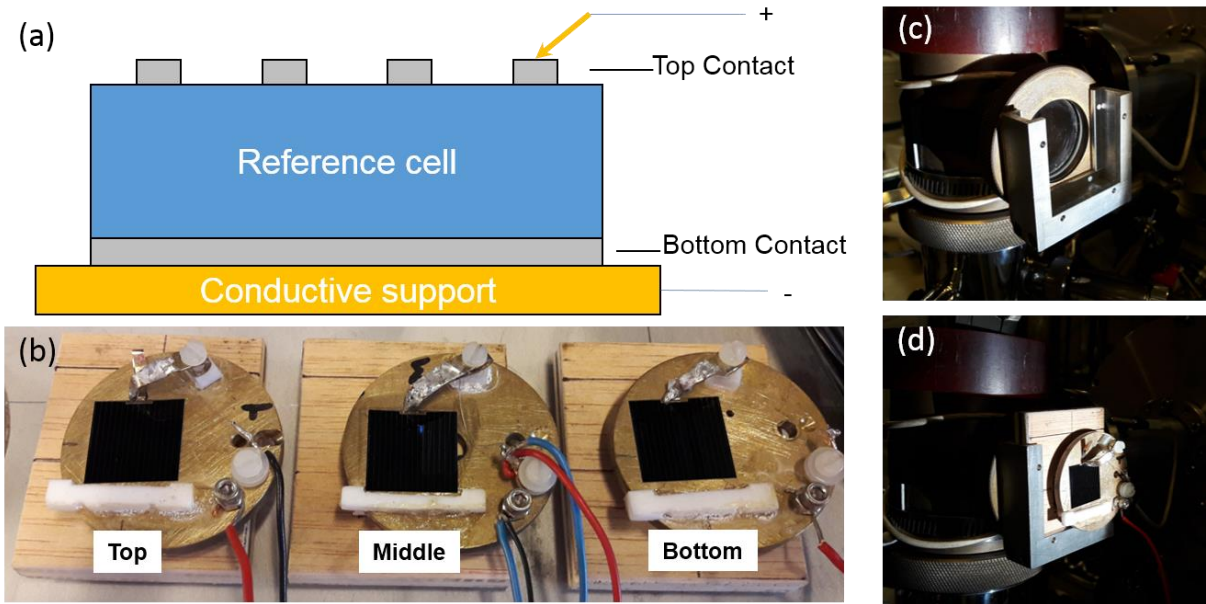


Figure 2-8. Reference component cells and the placements for the stability verification of the solar simulator.

The adjustment has been carried out, for the distance corresponding to the adaptation on the cryostat, for intensities of the power supplies of the QTH and Xe lamps, respectively. These data are reproducible after several days of interruption. An example of measurement is given in Table 2-1. Dedicate care must be concerned when the system is installed next to the accelerator beamline to set aside sufficient distance between the cryostat chamber and the solar simulator.

Table 2-1. Calibration of the solar simulator using  $I_{SC}$  measurement.

Cell	Reference $I_{SC}$ (mA)	Calibrated $I_{SC}$ (mA)	Error (%)	Calibrated $I_{SC}$ (outside) (mA)
Top	2.33	2.34	0.5	4.46
Middle	2.55	2.54	0.5	4.86
Bottom	4.64	4.64	0.0	7.74

### 2.1.3 Cryostat Chamber and measurement units

A cryostat chamber is composed of a temperature regulator and a conductive support system of which we can perform electrical and thermal measurements. The temperature can be controlled by pumping liquid nitrogen ( $LN_2$ ) and heating a thermal resistor.  $LN_2$  passes through the sample holder to decrease the temperature of a cell. A thermal resistor is also installed into the sample holder to precisely adjust the temperature. The minimum temperature of the sample holder is about 80 K, which is close to the

boiling point of LN<sub>2</sub>. Thus, it is possible to achieve the temperature down to 80 K. The temperature of the cell is not exactly the same because the contact between the sample and the support is not ideal, so it is also necessary to measure a temperature of the cell with respect to the temperature of the support. The temperature is measured through temperature probes (PT100) connected to the sample holder: one adhered to the bottom contact part (sample support) and the other adhered to the socle of the cryostat (see Figure 2-9 (a)). When we measure the temperature of the cell, we can detach the thermal gauge of the socle to adhere it to the sample.

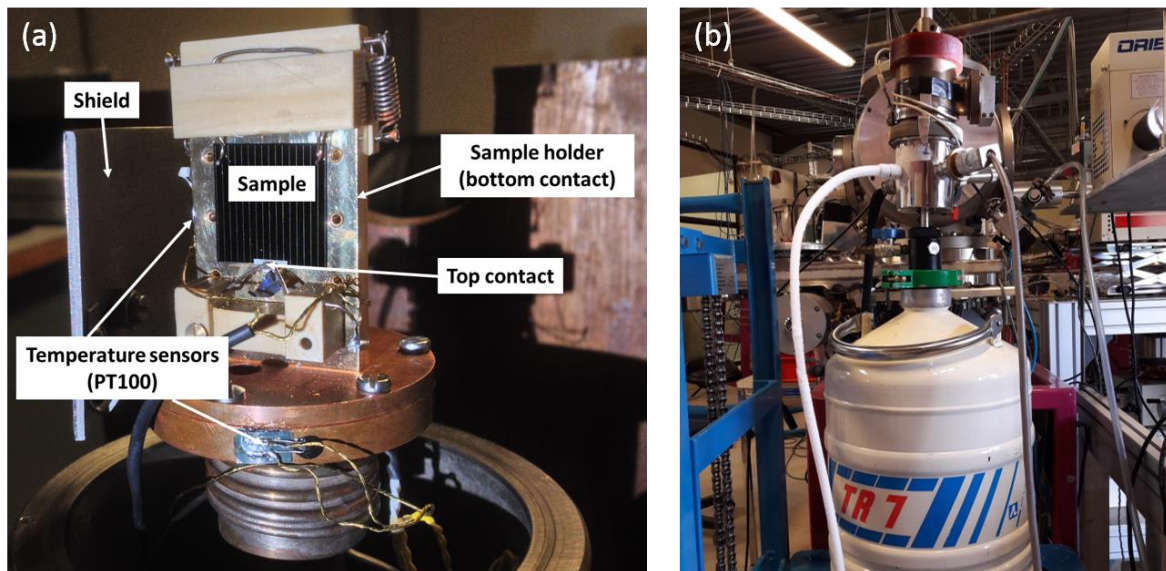


Figure 2-9. (a) Inside view of the cryostat chamber and (b) total view of the cryostat system.

The sample holder can also be rotated by 360 degrees. It is designed to perform both the irradiation with the particles and illumination after irradiation the TJ cells with the solar simulator through the quartz window. The cryostat chamber head is used as a faraday cage so that charged ions from the irradiation are extracted out from the chamber. The Faraday cage guarantees a continuous irradiation with accurate electrical measurement by discharging charged particles in the cryostat chamber coming from the accelerator. Electrical-temperature (I-V-T) measurements can be simultaneously carried out using a temperature controller (LakeShore 336 Temperature Controller) and multimeters (Hewlett Packard 34401A Multimeter and Keithley 2401 Sourcemeter). Temperature data is received by the temperature controller and electrical data is firstly acquired by the multimeters. The temperature and the voltage at zero current ( $V_{OC}$ ) are transferred together to a computer through a GPIB. Then they are registered with a certain period of time. Therefore, all history of the temperature of the sample holder and  $V_{OC}$  can be saved before, during, and after the irradiation. In the meantime, I-V characteristics of a cell are measured during the process at certain points: for example, before the irradiation and after the irradiation. Since this measurement is independent from the temperature and  $V_{OC}$  recording, we can obtain I-V data of the cell. In addition, 4 wire connection has been applied to minimize electrical noise produced from internal circuit. A noise problem is critical in low intensity of light conditions. Under illumination,  $I_{SC}$  is relatively too small compared to that at 100 % AM0 condition. Weak current signal can therefore be

interrupted by the noise signal. So, it is important to minimize those noises to obtain precise data in LILT conditions. For the I-V measurement, the setup can be varied with respect to the type of the cell (top, middle, bottom, and TJ cells) and the temperature ( $V_{OC}$  is temperature dependent parameter). Interval of measurement is normally set from 100 to 200 points depending on the voltage range (see Table 2-2).

Table 2-2. Set of the range of voltage used for I-V measurement of cells at different temperatures.

Cell	Range of voltage (V)	
	RT (300 K)	LT (80 or 120 K)
Top	0 to 1.5	0 to 2
Middle	0 to 1	0 to 1.5
Bottom	0 to 0.5	0 to 1
TJ	0 to 2.5	0 to 4

The light from the Xe lamp flickers in low intensity like 3.7 % AM0 condition. This feature is observed in  $I_{SC}$  of the top and middle cells (not in the bottom cells) in few hundreds micro ampere levels since the most of Xe light is absorbed by the top and middle cells. Therefore, we have applied the integration time of signal at each data point to improve the quality of data.

In summary, I-V-T measurements can be conducted in parallel in a very wide temperature range. Depending on a type of irradiation, the chamber is connected to the electron accelerator or the proton accelerator.

## 2.2 Structure of lattice matched GaInP/GaAs/Ge triple junction solar cell

The lattice matched GaInP/GaAs/Ge triple junction solar cell is one of the solar cells most used in terrestrial and in space industries today. This solar cell is fabricated on the p-type Ge substrate. First, bottom junction is created by As diffusion into the p-type Ge substrate forming a charge neutral region between n-GaAs and p-Ge layers. Then, in a reverse direction, a tunnel junction is formed to make generated carriers in sub-cells flow. The middle cell is composed of two barrier layers of highly doped (Al) GaInP at the edges, one back surface field layer (Al) GaAs at p-side, and p- and n- GaAs layers. Typically, p-doped layers are bases and n-doped layers are emitters. With the other tunnel junction between the top and middle sub-cells, the top sub-cell consists of a window layer n-doped AlInP, n-doped GaInP (emitter), p-doped GaInP (base), and highly p-doped GaInP as a back-surface field. On the surface of the solar cell, thin metal contact layers are welded and anti-reflection coating (ARC) is applied to maximize the light absorption in the cell. A complete diagram of the structure of the studied triple junction solar cell is presented in Figure 2-10 (b). The thickness of sum of all layers on the p-type

Ge substrate is only a few  $\mu\text{m}$  scale while the thickness of the Ge substrate is of around 140 or 80  $\mu\text{m}$  (depending on the batch). Thus, typically the thickness of the cell indicates an approximate thickness of the Ge substrate.

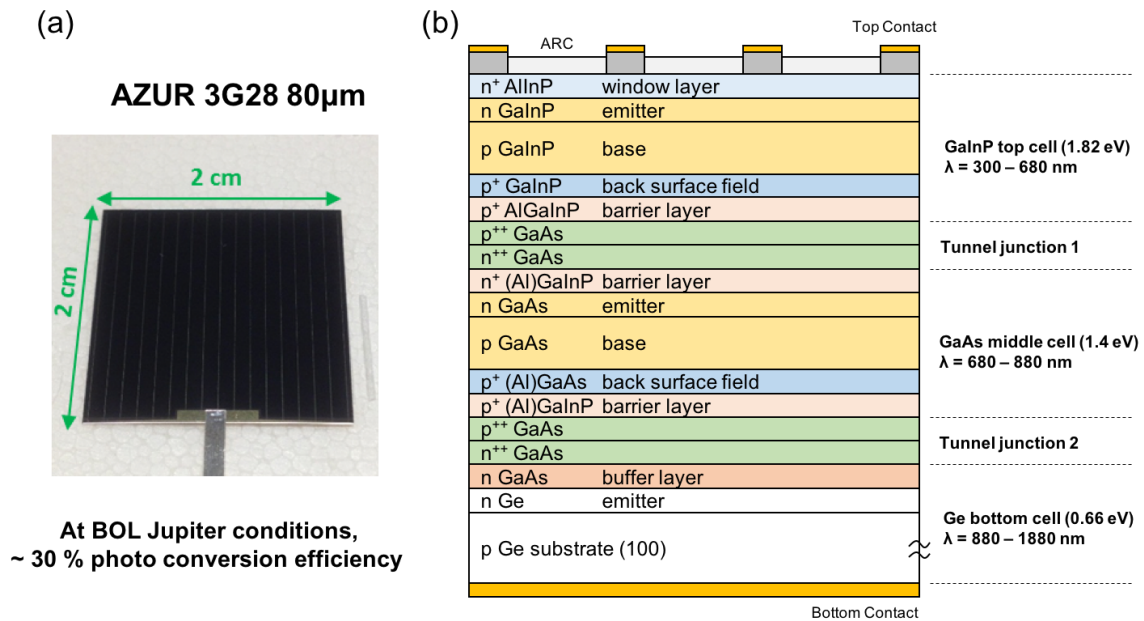


Figure 2-10. (a) 2x2 cm<sup>2</sup> AZUR 3G28 GaInP/GaAs/Ge triple junction solar cell (Ge substrate 80  $\mu\text{m}$ ) and (b) Layer composition of the lattice matched GaInP/GaAs/Ge triple junction solar cell grown on the p-type Ge substrate.

For the analysis of sub-cells of triple junction solar cells, we have used component cells of the triple junction solar cells. The component cell indicates the cell which have optically the same structure as the triple junction solar cell but electrically have only one junction among three sub-cells; top, middle or bottom junction. In other word, only one junction is electrically active owing to the pn junction while other sub-cells do not have any doped layer. Therefore, these layers can optically absorb light in accordance with their band gap energy but the excess carriers are not collected since there is no internal electric field to accelerate the carriers.

The top component cell is composed of the active GaInP pn junction layers and p-type GaAs buffer on the p-type Ge substrate. The middle component cell consists of the n-type GaInP filter layer, the active GaAs pn junction on the p-type Ge substrate. Last, the bottom component cell has two n-doped filter layer; GaInP (top) and GaAs (middle) on the active Ge pn junction. The absorbed light from the upper filter layer can be re-emitted in the form of a radiative recombination of excess carriers. This phenomenon is often referred as a photon recycling effect. It will be discussed in detail at the next section.

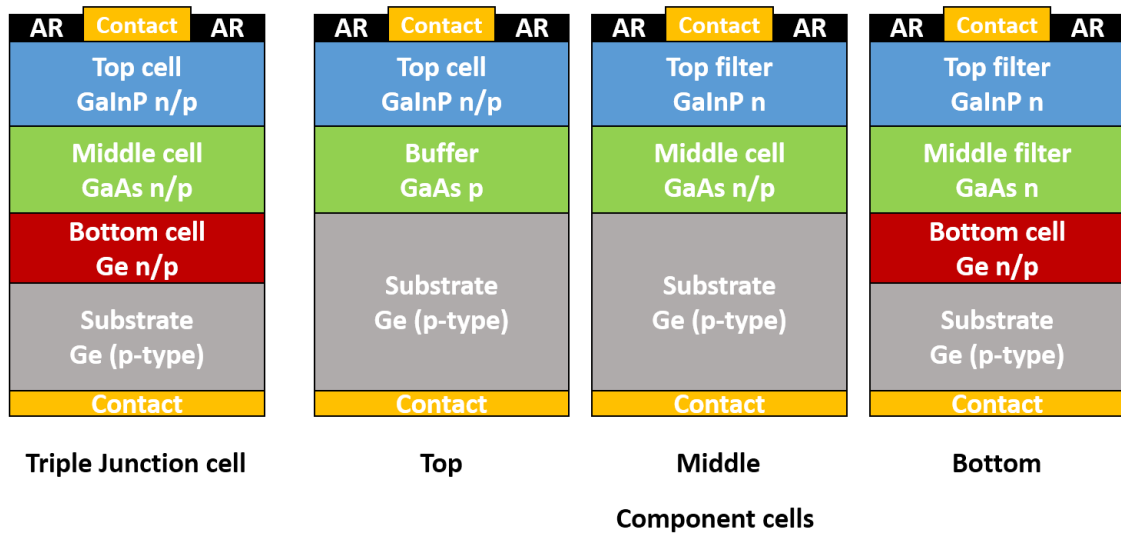


Figure 2-11. Simplified representation of structures of a TJ and its component cells.

### 2.3 Photon recycling effect in a component cell

The photon recycling effect (PRE or called as self-excitation) in semiconductor was first observed by Moss and Landsberg in 1957 [2], [3] and has been studied theoretically and experimentally for the minority carrier lifetime, carrier diffusion coefficients, and for overall lifetime. When this effect occurs in a semiconducting material, for instance, in wide bandgap semiconductors like GaAs which has a long enough carrier lifetime (SRH and/or radiative), photons emitted from a recombination of carriers can then be reabsorbed and create another electron-hole pair near the recombination site.

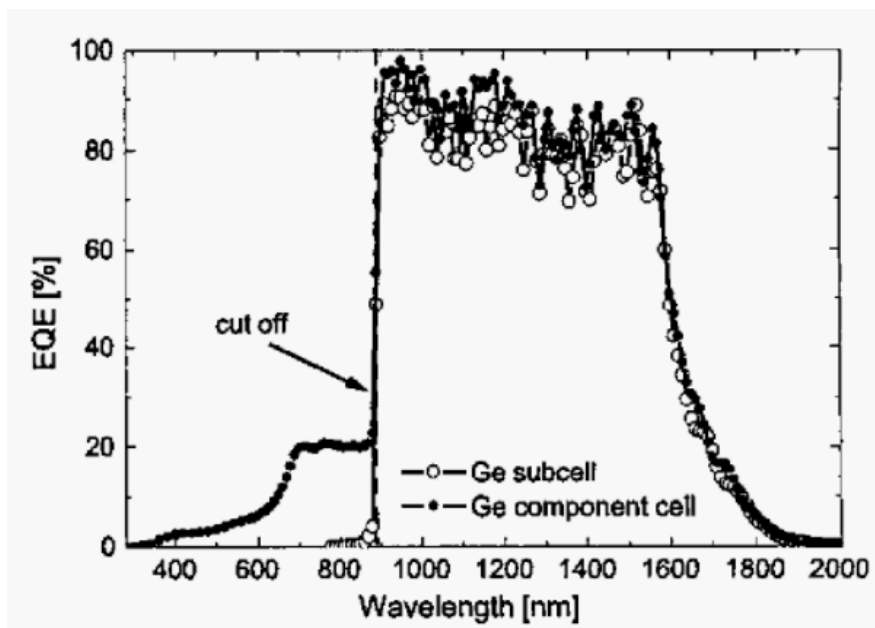


Figure 2-12. EQE of the Ge sub-cell and component cell [4].

The PRE is more frequently observed in the material which has larger thickness than its carrier diffusion length. It is also possible to observe the PRE between two neighboring layers, that is, one layer emits photons and these photons are absorbed by the other adjacent layer creating the electron hole pair. In the component cell structure, it is indeed probable that the PRE is detected from a middle (GaAs) or a bottom (Ge) component cells by EQE measurement [4]-[6]. Concerning the triple junction structure that we have used for the study, the amount of the PRE in the GaAs component cell is not significant. On the other hand, it is not negligible for the Ge component cells as shown in Figure 2-12. When the EQE of Ge component cell is directly compared to that of the Ge subcell, it is clear that additional photons from lower wavelength ranges, which are emitted in a form of radiative recombination from upper layers (top and middle optical filter layers), are absorbed at Ge cell, all parts of Ge cells (from the emitter to the base) can potentially absorb those emitted lights. As a consequence, the Ge component cell has higher photo generated current than the actual current value of the Ge subcell. Therefore, it was necessary to correct this current mismatch between the subcell and the component cell to directly consider the analysis of the component cell as the one of the subcell in the triple junction structure. Baur et al. have proposed to irradiate them with a small amount of dose like a radiation treatment on the Ge component cell. By doing so, most of radiative recombination centers in the GaInP and GaAs filters seem to disappear while the Ge cell is electrically hardly affected by the irradiation. Figure 2-13 shows an EQE measurement data of a Ge component cell before and after irradiations. It is clearly seen that the EQE of a Ge component cell at the range of 400 to 850 nm is completely suppressed by an electron irradiation with a fluence of  $2 \times 10^{14} \text{ cm}^{-2}$ . By eliminating this part of photon absorption in the Ge component cell, the created photo current can be decreased down to the level of that of the Ge subcell. The right-side y axis (relation EOL/BOL) indicates that the irradiation does not degrade photo generated current of the Ge junction (except less than 10 % at long wavelength ranges of 1600 – 1900 nm).

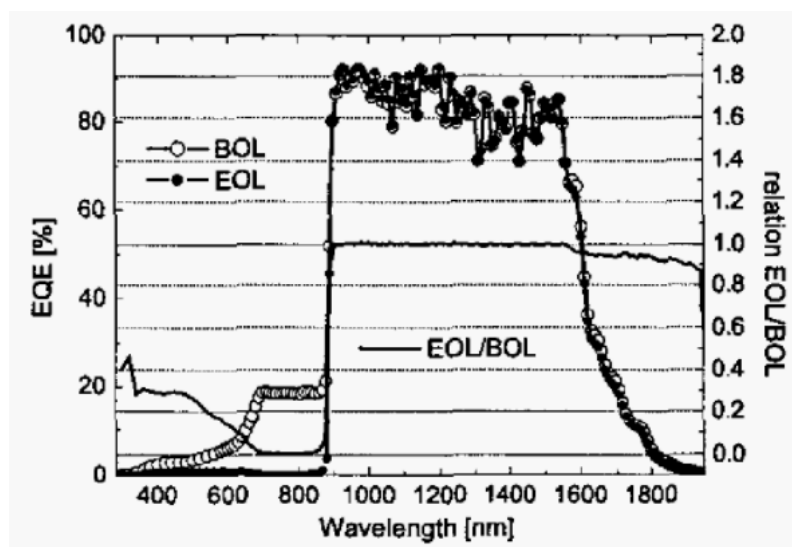


Figure 2-13. EQE of a Ge component cell before and after irradiation. The photon cycling from the upper layers is suppressed due to the degradation of the material quality after irradiation the sample [4].

During the JUICE mission, once the spacecraft is left to the Jupiter system, all of scientific activities are totally dependent on the electric supply from the solar panel. Therefore, the pre-evaluation of electricity generation from the solar energy must be correct when it is done in the lab scale since it is impossible to turn it back to Earth. Thus, a precise analysis of the TJ and its component cells under the irradiation test in LILT conditions is one of the primary importance. In this respect, irradiation test of TJ cells and its component cells must be accurate to give a correct evaluation of EOL performance of the TJ cells. For the irradiation test of Ge bottom component cells (hereafter we call them simply Ge cell or bottom cell unless specifically mentioned), we have added an additional irradiation step as a PRE removal step with a small fluence in both electron and proton irradiations. An example of the electron irradiation of a Ge cell at room temperature (RT) is presented in Figure 2-14.

A Ge cell has been cumulatively irradiated with 1 MeV electrons, fluences ranging from  $5 \times 10^{14}$  to  $2 \times 10^{15}$   $\text{cm}^{-2}$  at room temperature. The first irradiation with a fluence of  $5 \times 10^{14}$   $\text{cm}^{-2}$  decreased  $I_{SC}$  of the bottom cell from 5.1 to 4.4 mA. For further irradiation,  $I_{SC}$  of the bottom cell was not changed at all as known to be a radiation hardness at room temperature. This result proves that once the PRE is suppressed by an initial irradiation with a certain amount of electron fluence, later irradiations do not attribute to decrease  $I_{SC}$  of the Ge cells. Detailed discussions of electron irradiated cells' properties are in the chapter 4.

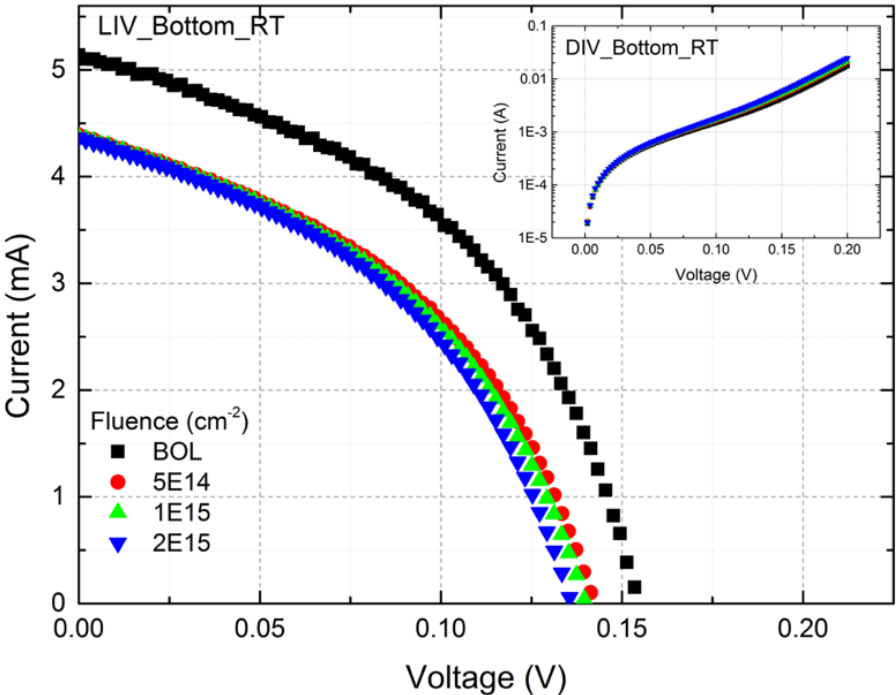


Figure 2-14. I-V characteristics of an electron irradiated Ge bottom component cell at room temperature under illumination and in dark (inset).

However, our interests are mainly focused on LILT conditions, i.e. the low temperature. Not like the case of room temperature irradiation, further decreases of  $I_{SC}$  of Ge cells at low temperature have been detected. Therefore, a test sequence has been applied to distinguish the decrease of the current due to

the cancellation of the PRE and due to the degradation of the Ge cell. The test sequence is described below:

- 1) Observe  $I_{SC}$  of a Ge cell while decreasing the temperature from 300 to 100 K before irradiation.
- 2) Irradiate the Ge cell at 100 K with a fluence of  $1 \times 10^{14} \text{ cm}^{-2}$  which is considered as the PRE removal fluence at RT.
- 3) Warm up the cell to 300 K, measuring its  $I_{SC}$  at the same temperature intervals as the step 1.
- 4) Cool down the cell to 100 K again, measuring its  $I_{SC}$  at the same temperature intervals as above.
- 5) Repeat steps 1 to 4 with the fluence  $1 \times 10^{14} \text{ cm}^{-2}$  or higher.

From this test, we have found that a clear difference occurs between the first and the second cycles as shown in Figure 2-15. Once Ge component cell is irradiated for the first time, significant amount of  $I_{SC}$  is erased even if the fluence is very small compared to the nominal fluence ( $1.5 \times 10^{15} \text{ cm}^{-2}$ ) which is applied for the JUICE irradiation test. When the cell is annealed at 300 K and cooled down again to 100 K, no recovery is observed. The fact that there is no recovery of  $I_{SC}$  from the first irradiation confirms that this degradation is related to the PRE. The difference between EOL ( $1 \times 10^{14} \text{ cm}^{-2}$ )  $I_{SC}$  values and BOL ones of Figure 2-15 (a) is the amount of PRE, which is cancelled from the bottom component cell after the irradiation. On the other hand, when the irradiated cell was again irradiated with the same amount of fluence, we observed a relatively smaller  $I_{SC}$  degradation compared to the first irradiation. In addition, this degraded  $I_{SC}$  was almost recovered after the RT annealing. As a consequence, the defects which induce the recombination of photo generated current are almost recovered after the room temperature annealing, which is also relevant to the result of the room temperature irradiation.

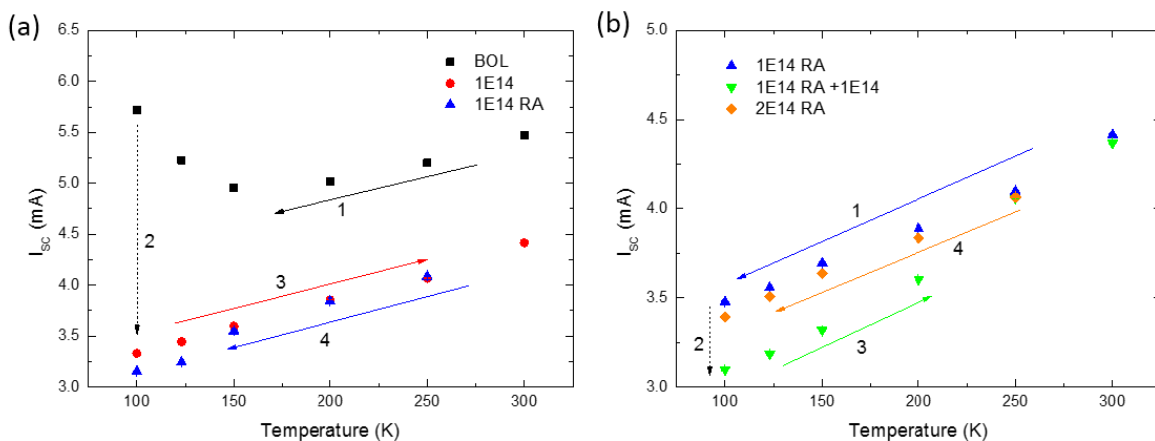


Figure 2-15. Evolution of  $I_{SC}$  of a bottom component cell at temperature ranging from 100 to 300 K. (a) 1 – decrease of temperature before irradiation, 2 – irradiation with a fluence of  $1 \times 10^{14} \text{ cm}^{-2}$ , 3 – increase of temperature after irradiation, 4 – decrease of temperature after room temperature annealing. (b) Same procedure as (a), except the fact that the cell is irradiated once again with the same fluence as conducted at (a).

## 2.4 In-situ characterization of TJ cells and its component cells

At the past, most of irradiation tests of solar cells were conducted at room temperature and their electrical properties were subsequently measured at room temperature since the most of studies were oriented to evaluate their EOL performance in orbits of the Earth [7], [8]. However, as demands of low temperature irradiation test have risen in terms of deep space missions, researchers have started to irradiate solar cells at low temperatures. But, most of measurements were conducted at room temperature except a few attempts [9]-[13]. Since defects created in semiconductors have more chances to be annealed at higher temperatures, heating the sample from its originally irradiated temperature can cause a loss of defect information which is formed at lower temperature. It is frequently observed as a recovery of the solar cell's performance. In this regard, to keep the temperature of the cell same during irradiation and measurement is essential to give correct EOL efficiency of TJ cells at LILT conditions. In order to do that, in-situ characterization system of the solar cell at low temperature has been developed in LSI. As discussed in the chapter 1, solar cell has temperature dependent properties such as  $V_{OC}$  and  $I_{sc}$ . Therefore, measuring correct temperature of a cell is very important.

### 2.4.1 Indirect temperature measurement

Inside the cryostat chamber, two temperature probes (PT100) have been installed in order to monitor the temperature in different areas of the cryostat chamber. Positions of these temperature probes are already marked in Figure 2-9 (a). But these probes do not directly measure the temperature of the cell on the sample holder. For this reason, it is obliged to attach another temperature probe on the surface of the solar cell to directly measure the temperature of the solar cell.

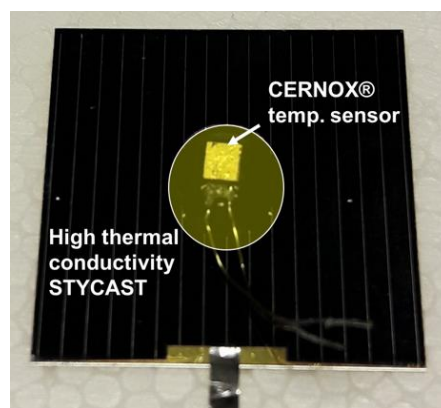


Figure 2-16. A picture of a 2x2 cm<sup>2</sup> solar cell with CERNOX® temperature sensor glued on the surface of the cell using high thermal conductivity STYCAST.

A calibrated CERNOX® temperature sensor (CX-1080-SD-HT-20L) has been used as a probe attached to the solar cell (see Figure 2-16). With the CERNOX® sensor, we measure therefore the reference temperature of the solar cell and compare it with the temperature measured by PT100 probes attached on the support and embedded in the socle and then, make a table to find a target temperature of the solar cell by just monitoring the temperature of the support of the socle.

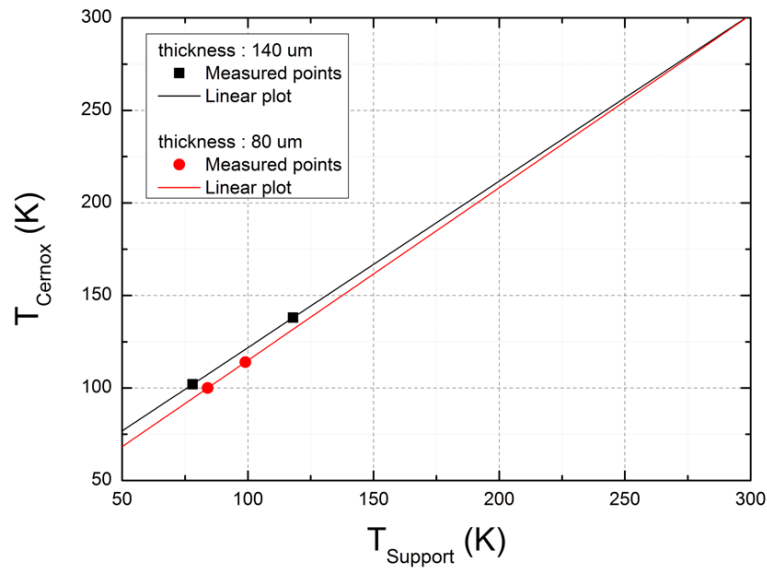


Figure 2-17. Temperature of the support versus temperature of the cell measured with the CERNOX sensor.

Figure 2-17 shows the difference of temperature measured on the surface of the cell and the sample supporter. The test was performed with two TJ cells; one is of 80 μm and the other is of 140 μm, respectively. For each TJ cell, measurement was carried out at two different low temperatures. The temperature of the cell with the CERNOX® sensor ( $T_{\text{Cernox}}$ ) and the temperature of the support using PT100 probe ( $T_{\text{Support}}$ ) were individually recorded. Then, two linear plots for different cell thicknesses were plotted from those measured points. Two plots met at the same point near room temperature (RT, 298 K). In addition,  $T_{\text{Cernox}}$  is nearly same as  $T_{\text{Support}}$  at RT. On the other hand, when decreasing  $T_{\text{Support}}$ , one can observe that the different between  $T_{\text{Cernox}}$  and  $T_{\text{Support}}$  becomes larger. For the cell with a thickness of 140 μm,  $T_{\text{Cernox}}$  is 120 K when  $T_{\text{Support}}$  is around 98 K ( $\Delta T_{140} = 22$  K), while  $T_{\text{Cernox}}$  of 80 μm cell becomes 120 K when  $T_{\text{Support}}$  is around 105.5 K ( $\Delta T_{80} = 14.5$  K). The temperature difference of the cell occurring especially at low temperature can originate from several factors:

- 1) The quality of contact between the sample and the support. In fact,  $V_{\text{OC}}$  measurement as a function of  $T_{\text{Support}}$  has been performed using a number of cells (both of 80 and 140 μm). The cells mostly exhibit identical  $V_{\text{OC}}$  at the same  $T_{\text{Support}}$ , indicating that the temperature of the cell is precisely controlled by  $T_{\text{Support}}$ . This observation proves that the contact quality is more or less the same for all cells.
- 2) Then, the other reason may be the thickness of Ge substrate, that is, in a thicker cell, more thermal exchange occurs resulting in a larger  $\Delta T$ .

This procedure must be carried out before irradiation because during the irradiation test, the surface of the cell must be completely exposed to precisely calculate irradiation dose damage in the cell. If the CERNOX® sensor is still attached on the surface of the cell, the surface will be partially covered and this will increase the uncertainty of measurement.

As already mentioned above, the temperature of the solar cell can also be estimated by the  $V_{OC}$  of the TJ or its component top, middle and bottom cells measured during this experiment. The point is therefore first to determine the relationships between the temperature of the solar cell and the temperature of the two PT100 sensors that will be always measured during experiments.

Another important aspect is to consider the increase of temperature of the cell during the irradiation. During JUICE mission, the solar cell will be exposed in low flux radiation conditions, i.e. the fluence that has been calculated from ESA is an estimated summation of fluence which will be cumulated during its entire mission period. In the laboratory, realization of the exact same condition as the mission condition is impossible due to limited irradiation beam time. Therefore, the flux of irradiation set for irradiation tests is much higher than the actual flux in space. In space, increase of the cell temperature by particle radiation is negligible. On the other hand, it is not the case for the electron irradiation using an electron accelerator. Since the defect generation mechanism can be affected by the difference of the temperature, the temperature during the irradiation should be maintained like non-irradiation temperature to avoid any unwanted uncertainty. As shown in Figure 2-18, When the 80  $\mu\text{m}$  cell is irradiated with a nominal flux of  $5 \times 10^{11} \text{ cm}^{-2}\text{s}^{-1}$ , its temperature increases about 8 K at the temperature ranging 100 – 120 K. In the case of the electron irradiation of the 140  $\mu\text{m}$  cell with the same flux, an increase of around 12 K was observed. In order to compensate this increase of temperature during the electron irradiation, we cooled down the temperature of the support so that we could maintain the temperature of the cell near 120 K during low temperature test sequences.

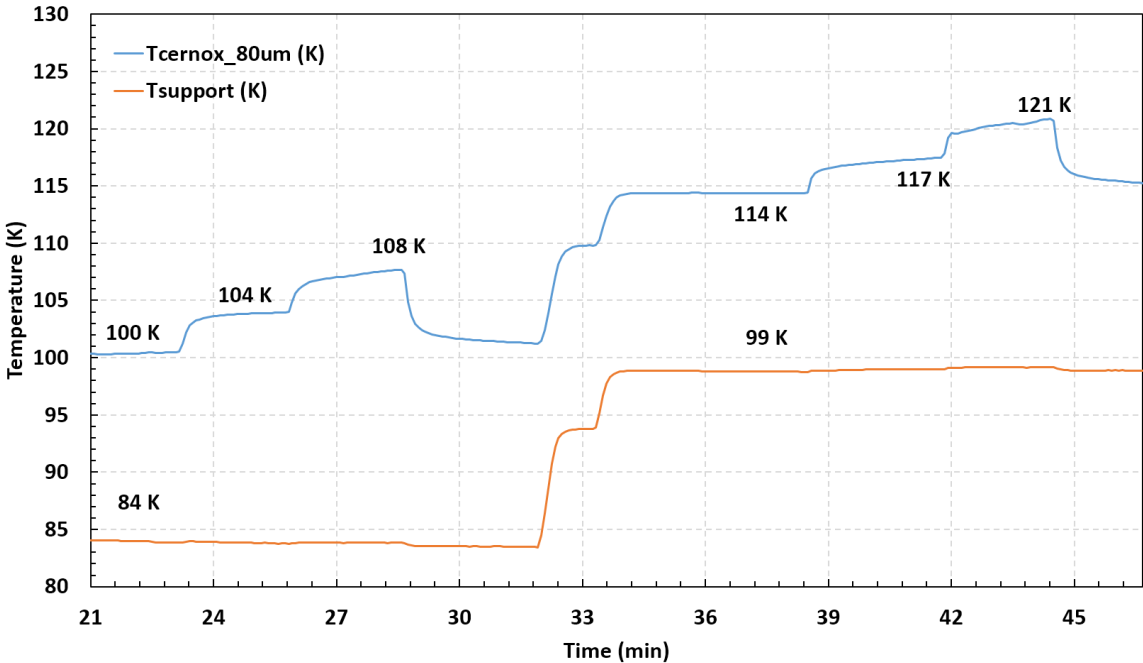


Figure 2-18. Measurement of  $T_{Support}$  and  $T_{Cernox}$  of a 3G28 80  $\mu\text{m}$  TJ cell at low temperatures during irradiation with fluxes of  $2.5 \times 10^{11}$  and  $5 \times 10^{11} \text{ cm}^{-2}\text{s}^{-1}$ .

In the meantime, proton irradiation does not increase the temperature of the cell since the proton flux is much less ( $\sim 10^9 \text{ cm}^{-2}\text{s}^{-1}$ ) than that of electron irradiation while the energy of particle is the same as 1 MeV. Since the flux of proton irradiation is about two orders of magnitudes smaller than that of electron irradiation. The energy dissipation occurred between proton particles and the solar cell is also hundreds of times less than the case of electron irradiation. Thus, it is not necessary to additionally decrease  $T_{\text{Support}}$  during proton irradiations.

#### 2.4.1.1 $V_{\text{OC}}$ as an indicator of temperature of the cell

$V_{\text{OC}}$  is a parameter which is temperature dependent as shown in Figure 2-19. It is therefore an indirect, but also good measurement technique of the bulk temperature of solar cell in conditions where we cannot glue directly a CERNOX® sensor upon the solar cell. Moreover, from the  $V_{\text{OC}}$  measurement, it is possible to determine the defects annealing processes occurring after irradiation. In this aspect, precise solar cell temperature measurements before, during and after irradiations are essential to discriminate between the influence of both temperatures decreases and the defect anneals processes after irradiation on the  $V_{\text{OC}}$  values. In addition, when decreasing  $T_{\text{Support}}$ , it takes more time to stabilize the temperature of the cell ( $T_{\text{Cell}}$ ). Generally, we wait for 5 to 10 minutes after  $T_{\text{Support}}$  arrives to the target temperature. To determine  $T_{\text{Cell}}$ , monitoring the  $V_{\text{OC}}$  value is the most effective way.

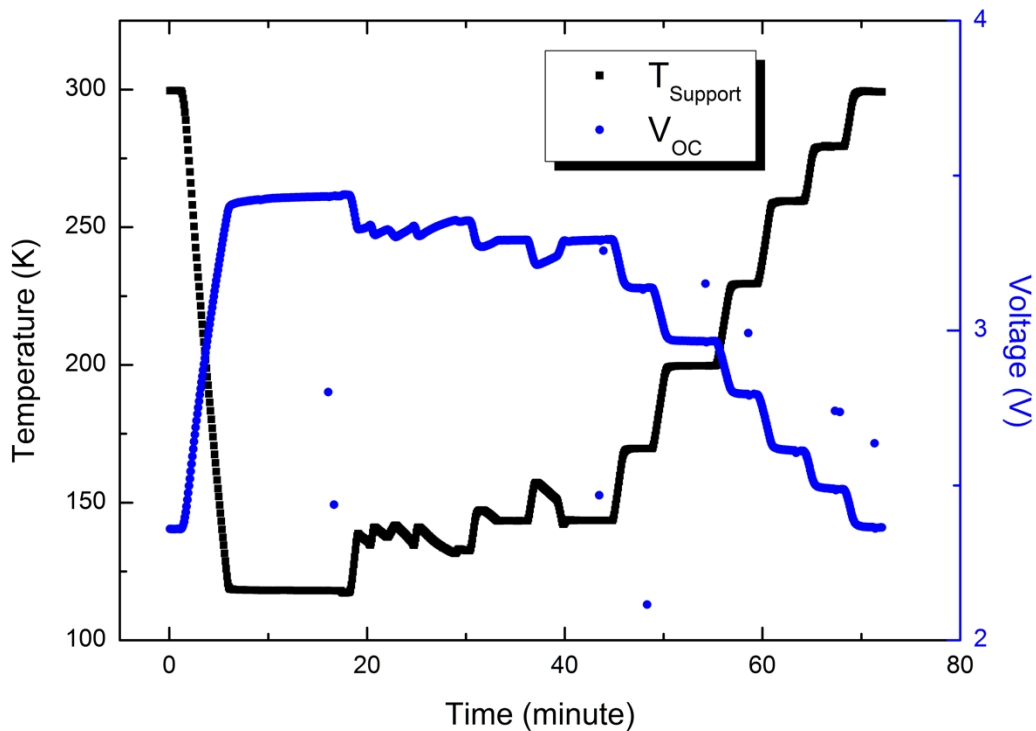


Figure 2-19. Measurement of  $V_{\text{OC}}$  of a TJ cell and  $T_{\text{Support}}$  during temperature control from 300 to 120 K.

## 2.4.2 Beginning Of Life performance of the cells

To confirm that there is no damage in the solar cell due to the mounting and during the thermal cycle, we have conducted a verification process with several TJ cells (1295-0980E-2, 1295-0980E-3 and 1295-4378E-5): total 3 times of mounting and dismounting, together with the entire LILT irradiation test sequence (assuming that the cell is irradiated at low temperature). Figure 2-20 describes how the thermal cycling test is performed with a TJ cell. The test is repeated three times per cell.

- 1) During the test 1, the cell is first mounted in the cryostat chamber (physical damage test during the mount) and once the vacuum is pumped out below to  $10^{-1}$  mbar, one can cool down the cell down to 120 K (as an accelerated annealing stage, 150 K is added in LILT test sequence). Light and dark I-V characteristics are then measured at each temperature.
- 2) Warm up the cell to the 300 K and cool it down again to 120 K to verify whether the cell has changed its I-V characteristics due to the thermal cycling.
- 3) Repeat the test sequence 1 and 2, then compare those three test results.

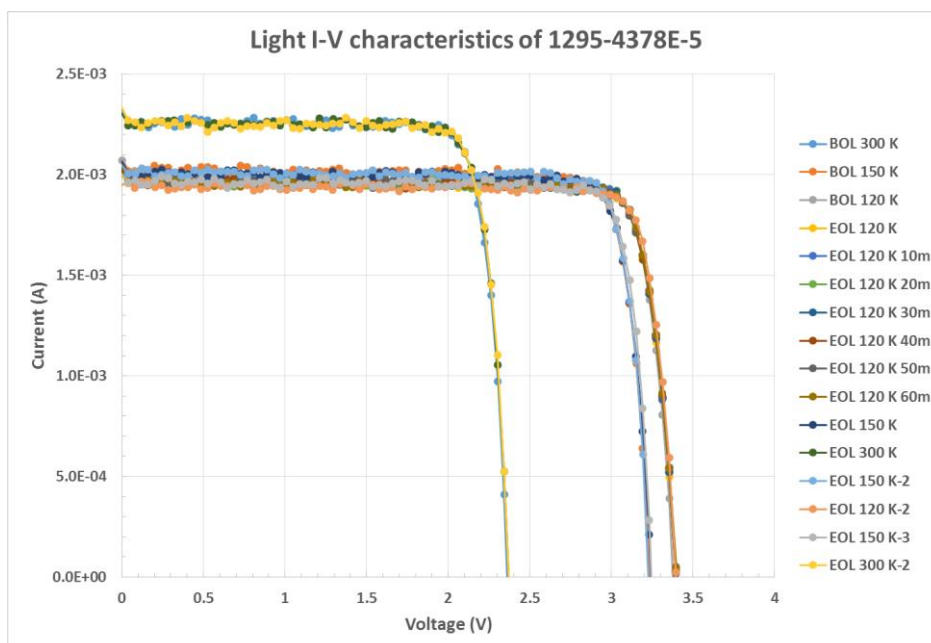


Figure 2-20. An example of thermal cycling test of the TJ solar cell (1295-4378E-5) as a part of test readiness review (TRR): I-V characteristics under illumination.

As one can find in Figure 2-20, the thermal cycling does not affect to the characteristics of the TJ cell. In addition, the mounting and dismounting by hands do not significantly influence the performance of the cells. We have summarized a test readiness review of three TJ cells performed before irradiation at 120 K. Three key solar cell parameters ( $I_{SC}$ ,  $V_{OC}$  and  $P_{MAX}$ ) measured at 120 K are noted in Table 2-3. In that testing phase, the coefficient of variation did not exceed 1, indicating the measurement is convincing and reproducible.

Table 2-3. Test readiness review (TRR) of three TJ solar cells at 120 K:  $I_{SC}$ ,  $V_{OC}$  and  $P_{MAX}$  were recorded during three times of tests: AVG means averaged values measured at different steps at 120 K. STDEV is a standard deviation of the average. CV, coefficient of variation, indicates the value of standard deviation divided by average.

120 K		1295-0980E-2			1295-0980E-3			1295-4378E-5		
		$I_{SC}$ (mA)	$V_{OC}$ (V)	$P_{MAX}$ (mW)	$I_{SC}$ (mA)	$V_{OC}$ (V)	$P_{MAX}$ (mW)	$I_{SC}$ (mA)	$V_{OC}$ (V)	$P_{MAX}$ (mW)
Test 1	AVG	1.95	3.385	5.752	1.97	3.435	6.190	1.94	3.435	6.046
	STDEV	0.0164	0.0170	0.0265	0.0074	0.0007	0.0305	0.0201	0.0006	0.0481
	CV (%)	0.84	0.50	0.46	0.37	0.02	0.49	1.03	0.02	0.80
Test 2	AVG	2.04	3.380	5.968	1.98	3.395	6.151	1.93	3.354	5.561
	STDEV	0.0192	0.0194	0.0502	0.0188	0.0011	0.0812	0.0153	0.0011	0.0489
	CV (%)	0.94	0.57	0.84	0.95	0.03	1.32	0.79	0.03	0.88
Test 3	AVG	1.97	3.349	5.716	1.98	3.385	5.935	1.97	3.395	5.765
	STDEV	0.0188	0.0127	0.0344	0.0212	0.0167	0.0383	0.0117	0.0008	0.0337
	CV (%)	0.96	0.38	0.60	1.07	0.49	0.64	0.59	0.02	0.58

Since June 2015, we have irradiated a lot of TJ and component cells. The detailed programs of each irradiation campaign will be described in the next section. In this section, we will be more focused on the BOL characteristics of a number of cells cumulated for irradiations performed from 2015 to 2017. I had first participated into the irradiation campaign at June 2015 for JUICE annealing verification test. At that time, we had two different test batches: 3G28 and 3G30 TJ cells. For each batch, there were 24 cells; total 48 cells to be irradiated. Their substrate thickness was about 140  $\mu\text{m}$ . Since the batch of 3G30 TJ cells exhibited a large kink effect on its I-V measurement under illumination at low temperature, the irradiation data of 3G30 TJ cells are excluded from analysis. For this reason, its BOL data is not included in this section.

## 3G28 140 $\mu\text{m}$ TJ cells for JUICE 2015

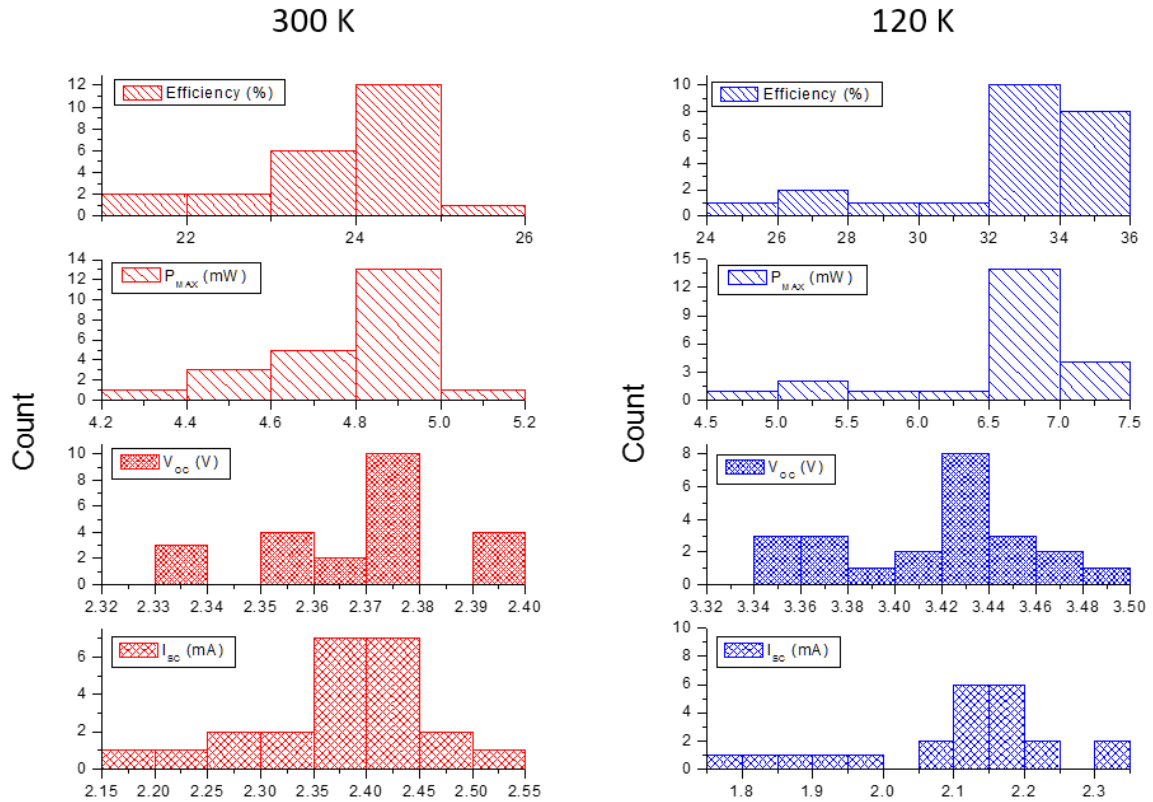


Figure 2-21. Histogram of BOL Efficiency,  $P_{MAX}$ ,  $V_{OC}$  and  $I_{SC}$  of 3G28 140  $\mu\text{m}$  TJ cells used for JUICE 2015 irradiation campaign: left side – measured at 300 K, right side – measured at 120 K. (Number of cells: 24 pcs)

Figure 2-21 presents distributions of solar cells key parameters (photo conversion efficiency (PCE),  $P_{MAX}$ ,  $V_{OC}$ , and  $I_{SC}$ ) of 3G28 140  $\mu\text{m}$  TJ cells before irradiation at 300 and 123 K. First, looking at the parameters at 300 K, the PCE of cells varies from 21 to 26 %, but most of cells have PCEs within the range of 23 – 25 %. For  $P_{MAX}$ , data are distributed from 4.2 to 5.2 mW. But, similar to the case of PCE, most of cells exhibit  $P_{MAX}$  between 4.6 and 5.0 mW. As to  $V_{OC}$ , data points appear more or less discretely from 2.33 to 2.40 V while the most frequent  $V_{OC}$  is positioned around at 2.37 – 2.38 V (10 cells).  $I_{SC}$  values are varied from 2.15 to 2.55 mA. Like there are some extreme cases in PCE,  $P_{MAX}$  and  $V_{OC}$ , the same cells exhibit either extremely low or high current. But most of cells (14 cells) show less distribution of  $I_{SC}$  values between 2.35 and 2.45 mA. It seems to be still a quite large distribution in comparison to the stability of one cell's  $I_{SC}$  value. Therefore, one should consider the fact that taking an average value of several samples would require a special care. At 120 K, the distribution of the BOL performance of cells becomes quite different. Generally, the data are more diversified at low temperature. PCE varies from 24 to 36 %,  $P_{MAX}$  from 4.5 to 7.5 mW,  $V_{OC}$  from 3.34 to 3.50 V, and  $I_{SC}$  from 1.75 to 2.35 mA.

To make more statistical analysis focusing on the batch of 3G28, and with thinner Ge substrate (~ 80  $\mu\text{m}$ ). We have increased the number of samples. Total 102 3G28 TJ cells have been prepared for the

2016 JUICE irradiation campaign. The same type of histogram analysis for 102 cells has been carried out as shown in Figure 2-22.

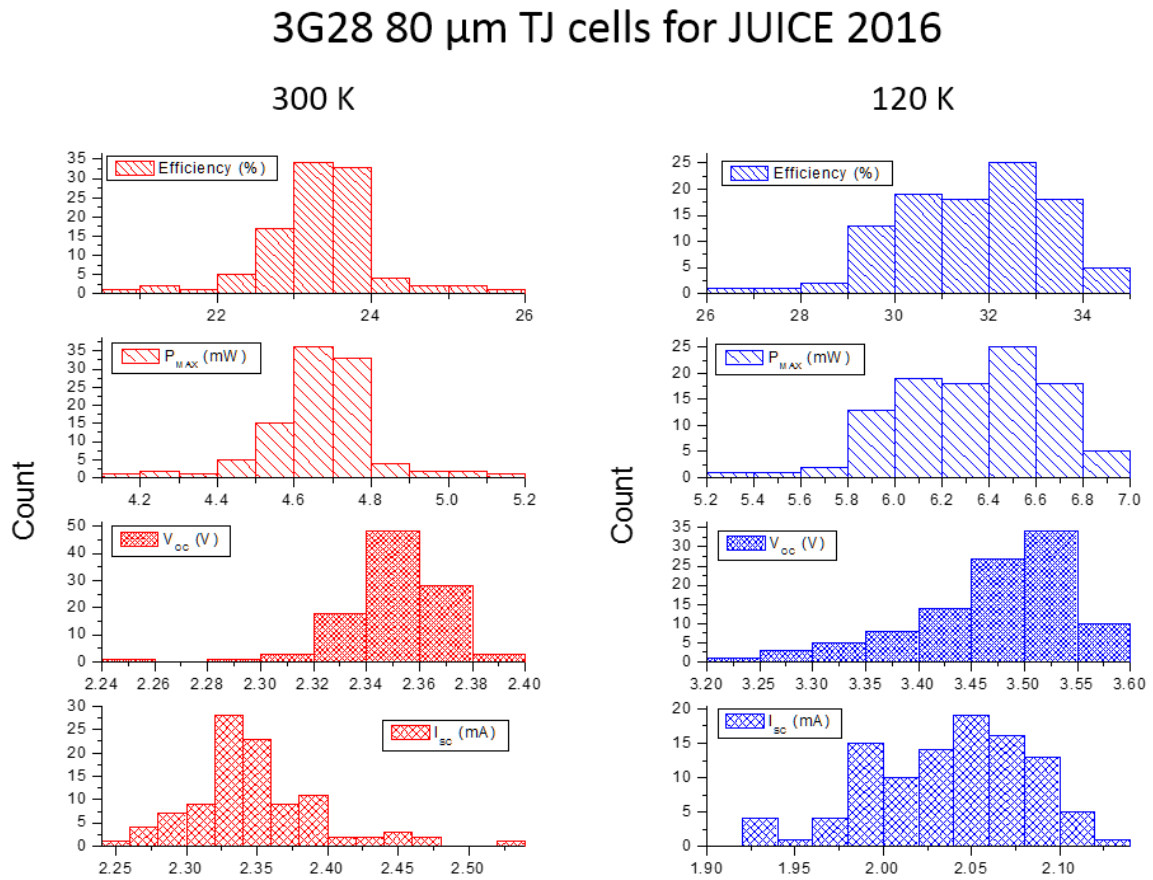


Figure 2-22. Histogram of BOL Efficiency,  $P_{MAX}$ ,  $V_{OC}$  and  $I_{SC}$  of 3G28 80  $\mu\text{m}$  TJ cells used for JUICE 2016 irradiation campaign: left side – measured at 300 K, right side – measured at 120 K. (Number of cells: 102 pcs)

With an increase number of cells, it seems that the data follow a normal distribution form compared to the case of JUICE 2015. For example, at 300 K, PCEs of 3G28 80 $\mu\text{m}$  TJ cells are mostly positioned at around 23.5 %, and compared to the case of JUICE 2015 cells, the extreme cases are much smaller than the frequently appeared values near the average. The similar conclusion can be applied to  $P_{MAX}$ ,  $V_{OC}$  and  $I_{SC}$  as well. In the meantime, by comparing the 3G28 140  $\mu\text{m}$  and the 3G28 80  $\mu\text{m}$  cells, one can find that the 3G28 140  $\mu\text{m}$  cells have slightly higher PCE than the 3G28 80  $\mu\text{m}$  cells. it is because the 3G28 140  $\mu\text{m}$  cells have, in general, higher current than the 3G28 80  $\mu\text{m}$  cells.

Came back to the analysis of 3G28 80  $\mu\text{m}$  cells, when they are measured at 120 K, the data are more distributed as it has been already observed in 3G28 140  $\mu\text{m}$  cells. the reason of this diversity at lower temperature originates from the temperature dependence of diode property of solar cells. The diode property of the solar cell is very sensitive to the temperature and moreover, the TJ cell is a device which is connected by three diodes in series. Thus, it is normal that the diversity of BOL performances of TJ cells becomes larger at low temperature.

Therefore, it is more reliable to take relative values for each cell when we compare the cell to other cells after irradiation. Furthermore, to take the average value of each parameter, we will first treat the data to make relative values and then calculate the average.

### 2.4.3 Electron and proton irradiation campaigns

We have used the electron and the proton irradiation facilities (SIRIUS at LSI and JANNUS at CSNSM) for JUICE irradiation campaigns and for scientific purposes related to the thesis. Depending on the fluence and in-situ measurement steps, the experimental time can be varied from ten minutes to several hours. If the irradiation is performed at low temperature like 120 K, one thermal cycle and stabilization process will add at least 30 minutes. Furthermore, the electron irradiation requires longer beam time than the proton irradiation since the equivalent electron fluence to be compared to the proton fluence is about 3 or 4 times larger. As a consequence, the electron irradiation could take several hours with low enough flux to not heat the sample too much. Considering these issues, the in-situ irradiation and measurement procedure should be properly planned.

#### 2.4.3.1 Test sequence

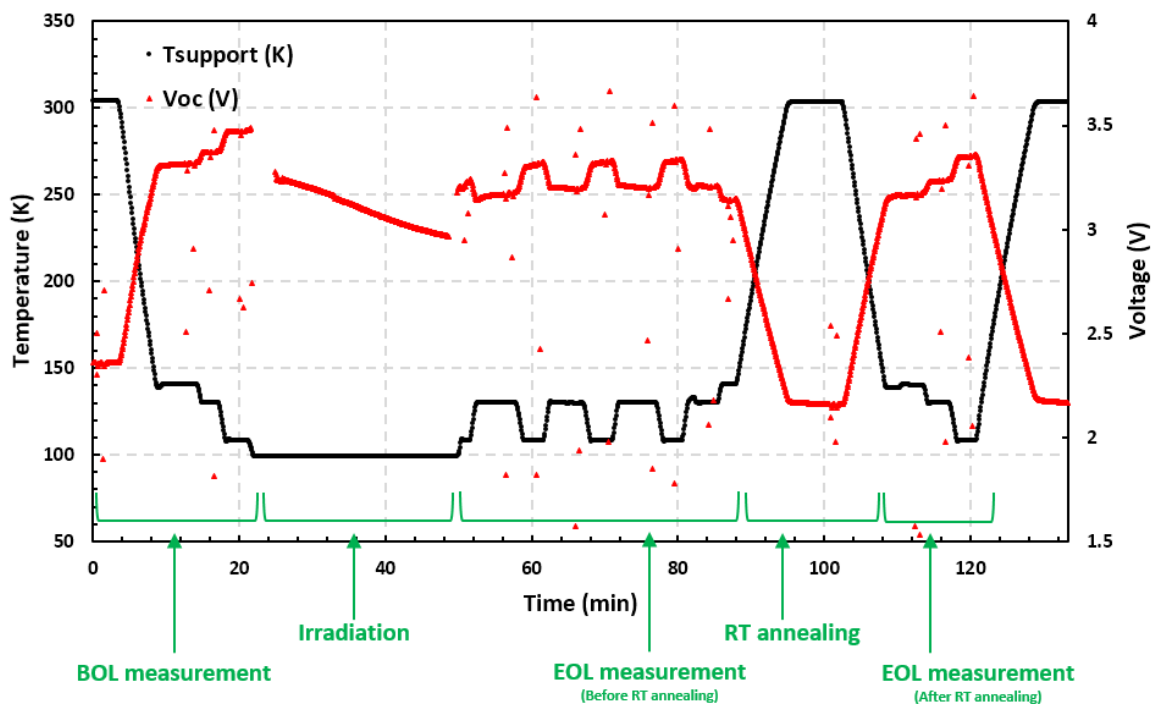


Figure 2-23. an example of in-situ test sequence of an electron irradiated TJ cell in LILT condition including an annealing process.

An example of valid test sequence for irradiations at LILT conditions is presented in Figure 2-23. First, a sample is mounted on the support of the cryostat chamber, and the vacuum is pumped out by the primary rotary pump. In the meantime, the calibration of solar simulator is carried out using reference component cells at outside of the cryostat chamber as already described in the section 2.1.2. Once the

vacuum is reached to a value lower than  $10^{-1}$  mbar, test sequences are followed as described in Table 2-4. In the table, the temperature RT corresponds to 300 K and -120, -130 and -150 °C correspond to roughly 150, 140 and 120 K, respectively. As shown, light and dark I-V measurements are conducted at each step. Cooling down the temperature from 300 to 120 K takes around 15 minutes if the temperature is directly cooled down without intermediate steps. When a cell is irradiated with the nominal flux ( $5 \times 10^{11} \text{ cm}^{-2}\text{s}^{-1}$ ) and the nominal fluence ( $1.5 \times 10^{15} \text{ cm}^{-2}$ ), the irradiation time is 3000 seconds (50 minutes). In the presented example, the irradiation condition was the nominal flux and the half of the nominal fluence (25 minutes of irradiation).

After the irradiation, EOL measurements are performed first during 30 minutes. This period is called as a LT annealing process (or a stabilization process). To accelerate the LT annealing process, 140 K intervals are inserted between 120 K intervals. I-V measurements are recorded at all temperature steps. Precise measurement points are described in Table 2-4.

Table 2-4. In-situ test sequence during the irradiation at low temperature

Step	Task	Conditions	Remarks
1	Light I-V/Dark I-V	25°C, 3.7% AM0	BOT RT
2	Light I-V/Dark I-V	-120°C, 3.7% AM0	BOT LT (-120°C)
3	Light I-V/Dark I-V	-130°C, 3.7% AM0	BOT LT (-130°C)
4	Light I-V/Dark I-V	-150°C, 3.7% AM0	BOT LT (-150°C)
5	Irradiation	Electrons/Protons	Standard/half dose
6	Light I-V/Dark I-V	-150°C, 3.7% AM0	EOT LT (-150°C)
7	Light I-V/Dark I-V	-130°C, 3.7% AM0	EOT LT (-130°C) + 5 minutes
8	Light I-V/Dark I-V	-150°C, 3.7% AM0	EOT LT (-150°C) + 10 minutes
9	Light I-V/Dark I-V	-130°C, 3.7% AM0	EOT LT (-130°C) + 15 minutes
10	Light I-V/Dark I-V	-150°C, 3.7% AM0	EOT LT (-150°C) + 20 minutes
11	Light I-V/Dark I-V	-130°C, 3.7% AM0	EOT LT (-130°C) + 25 minutes
12	Light I-V/Dark I-V	-150°C, 3.7% AM0	EOT LT (-150°C) + 30 minutes
13	Light I-V/Dark I-V	-130°C, 3.7% AM0	EOT LT (-130°C) LT anl
14	Light I-V/Dark I-V	-120°C, 3.7% AM0	EOT LT (-120°C) LT anl
15	Light I-V/Dark I-V	25°C, 3.7% AM0	EOT RT
16	Light I-V/Dark I-V	-120°C, 3.7% AM0	EOT LT (-120°C) RT anl
17	Light I-V/Dark I-V	-130°C, 3.7% AM0	EOT LT (-130°C) RT anl
18	Light I-V/Dark I-V	-150°C, 3.7% AM0	EOT LT (-150°C) RT anl
19	Light I-V/Dark I-V	25°C, 3.7% AM0	EOT RT - 2

Once the 30 minutes is passed, the cell is warmed up to RT (300 K) and wait for about 5 to 10 minutes until the  $V_{OC}$  of the cell is stabilized, and then, measure I-V characteristics at 300 K. This interval is considered as the RT annealing. Subsequently, the cell is again cooled down. Decreasing the temperature of the cell, record its I-V characteristics at 150, 140 and 120 K, respectively. Intermediate steps between 300 and 120 K can be skipped depending on the test sequence. The main interest is to compare the BOL and EOL performance of the cell at 300 K and 120 K. Once the EOL measurement at LT is finished after RT annealing, the temperature of the cell is again warmed up to RT. Finishing the last measurement at RT, take out the sample from the cryostat chamber, and change the sample to

irradiate the next one. In case of electron irradiation of JUICE 2016 irradiation campaign, the irradiation time could be varied from 25 minutes to 200 minutes. Including all steps, one test sequence in LILT condition is roughly between 2 to 5 hours per cell. This means that for JUICE 2016 irradiation campaign, several months of beamtime should be scheduled for 102 cells.

#### 2.4.3.2 Irradiations campaigns (JUICE 2015 – 2016 and components cells)

The aim of JUICE 2015 irradiation campaign was to evaluate the electron and proton radiation hardness of two batches (3G28 and 3G30 TJ cells) in LILT conditions and check the annealing coefficient of these TJ cells for electron and protons. The number of irradiated cells corresponding to the type of particle, energy of particle and fluences are described in Table 2-5.

Table 2-5. List of irradiated 3G28 and 3G 30 TJ cells during 2015 JUICE campaign.

Particle / Energy	Number of samples		Fluence (cm <sup>-2</sup> )
	3G28	3G30	
Electron / 1MeV	4	4	5.0x10 <sup>14</sup>
	4	4	1.0x10 <sup>15</sup>
	4	4	1.5x10 <sup>15</sup>
Proton / 1MeV	4	4	1.0x10 <sup>11</sup>
	4	4	2.0x10 <sup>11</sup>
	4	4	4.0x10 <sup>11</sup>

As already mentioned in the section 2.4.2, the batch 3G30 was finally excluded from the analysis since the 3G30 cells exhibited severe kink effect in light I-V characteristics at low temperature even before irradiation. The irradiation results of 2015 JUICE campaign showed an annealing in the order of 5 to 7 % for cells irradiated with  $4 \times 10^{11} \text{ cm}^{-2}$  1 MeV protons. On the other hand, results obtained on the cells irradiated with 1 MeV electrons are significantly distributed from cell to cell ranging from about 7 to 23 % (considering only the maximum fluence of  $2 \times 10^{15} \text{ cm}^{-2}$ ). These inconsistent results asked for additional test with the larger number of samples for a better understanding of the in-family behavior of electron and proton irradiation of TJ cells.

Therefore, in the frame work of JUICE irradiation campaign conducted in 2016, total 102 TJ solar cells have been irradiated under LILT conditions. Detailed irradiation conditions are described in Table 2-6. those irradiation data will be retreated in the chapter 3 for proton and in the chapter 4 for electron, together with additional irradiation data of component cells at various conditions.

Table 2-6. List of irradiated 3G28 TJ cells during 2016 JUICE campaign.

<b>Particle / Energy</b>	<b>Number of samples</b>	<b>Fluence (cm<sup>-2</sup>)</b>
<b>Electron / 1MeV</b>	12	7.5x10 <sup>14</sup>
	24	1.5x10 <sup>15</sup>
	12	3.0x10 <sup>15</sup>
<b>Electron / 2MeV</b>	6	6.5x10 <sup>14</sup>
	6	1.0x10 <sup>11</sup>
	6	1.35x10 <sup>11</sup>
<b>Proton / 1MeV</b>	13	2.0x10 <sup>11</sup>
	11	2.7x10 <sup>11</sup>
	3	4.0x10 <sup>11</sup>
	9	5.4x10 <sup>11</sup>
	6	7.5x10 <sup>14</sup>
<b>Electron / 1MeV (proton irradiated samples)</b>	6	7.5x10 <sup>14</sup>

In parallel, to build more concrete and detailed understanding of the degradation of TJ cells in LILT condition, a number of TJ and component cells have been irradiated. Variable parameters and/or measurement techniques are:

- 1) Type of particle: electron and proton
- 2) Energy of particle: 1 to 2 MeV
- 3) Irradiation temperature: 100 to 300 K
- 4) Isochronal annealing test: from 100 to 300 K
- 5) Cumulative radiation fluence: up to 6x10<sup>15</sup> electron.cm<sup>-2</sup> and up to 3.2x10<sup>12</sup> proton.cm<sup>-2</sup>
- 6) Orientation dependence of proton irradiation: Irradiation angle from 0 to 60 degrees

Apart from irradiation campaigns, 22 top, 15 middle, 32 bottom component cell and 24 TJ cells, total 93 cells have been irradiated for scientific studies.

#### 2.4.3.3 *Data treatment*

Once an irradiation test is finished for one TJ cell in JUICE 2016 irradiation campaign, nearly 40 I-V measurement data are created due to a number of steps per cell. This problem necessitated a semi automatized data treatment system. The automatization has been done using a VBA (Visual Basic for Applications) built in the Microsoft excel. As shown in Figure 2-24, follow the steps to automatically create an excel file which contains individual sheets (like in Figure 2-25) completed with calculated parameters, raw and converted light/dark I-V data, and created I-V graphs for each test sequence.

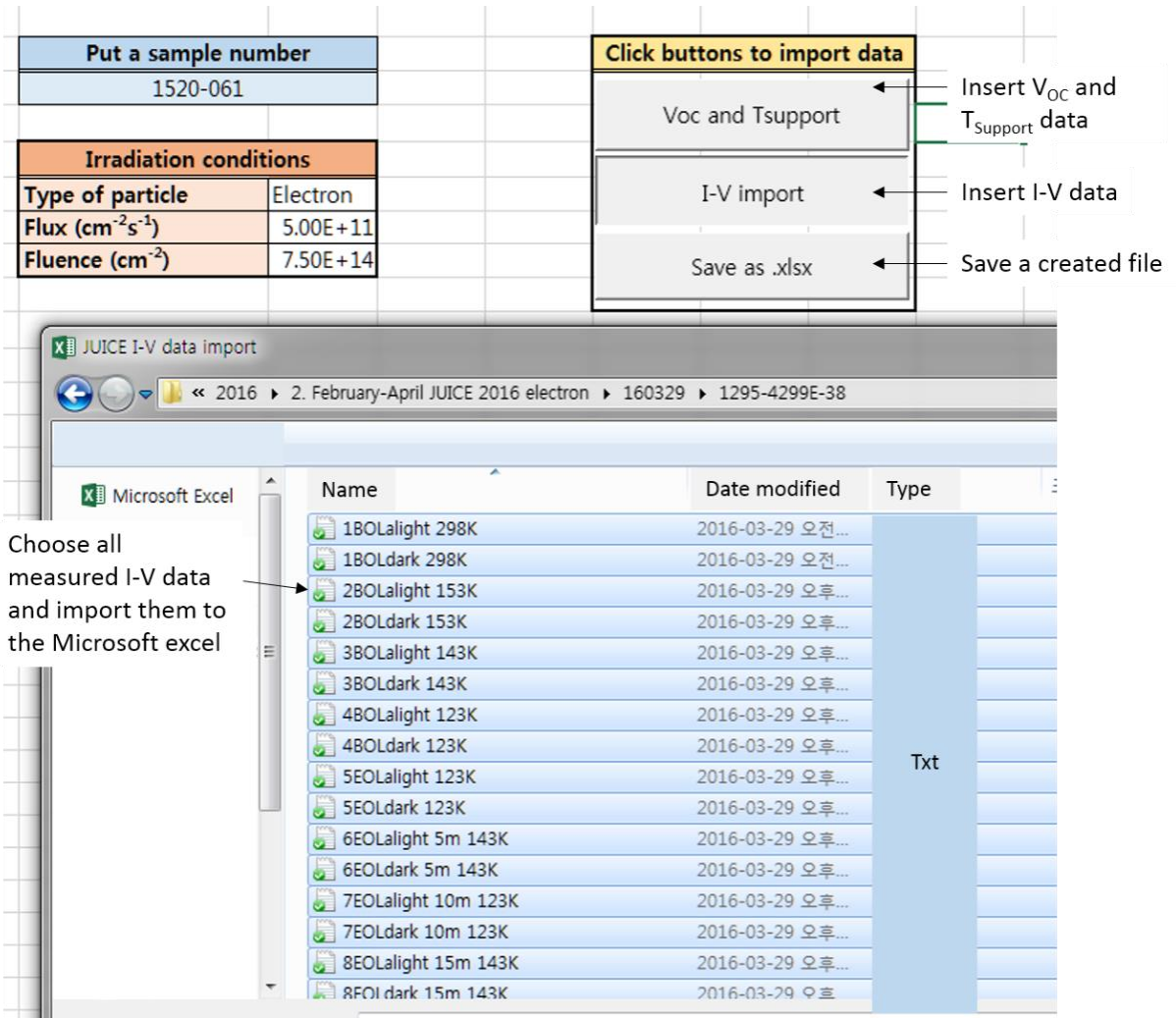


Figure 2-24. Import multiple data into an excel file to automatically create individual sheet containing all I-V information of related test sequence.

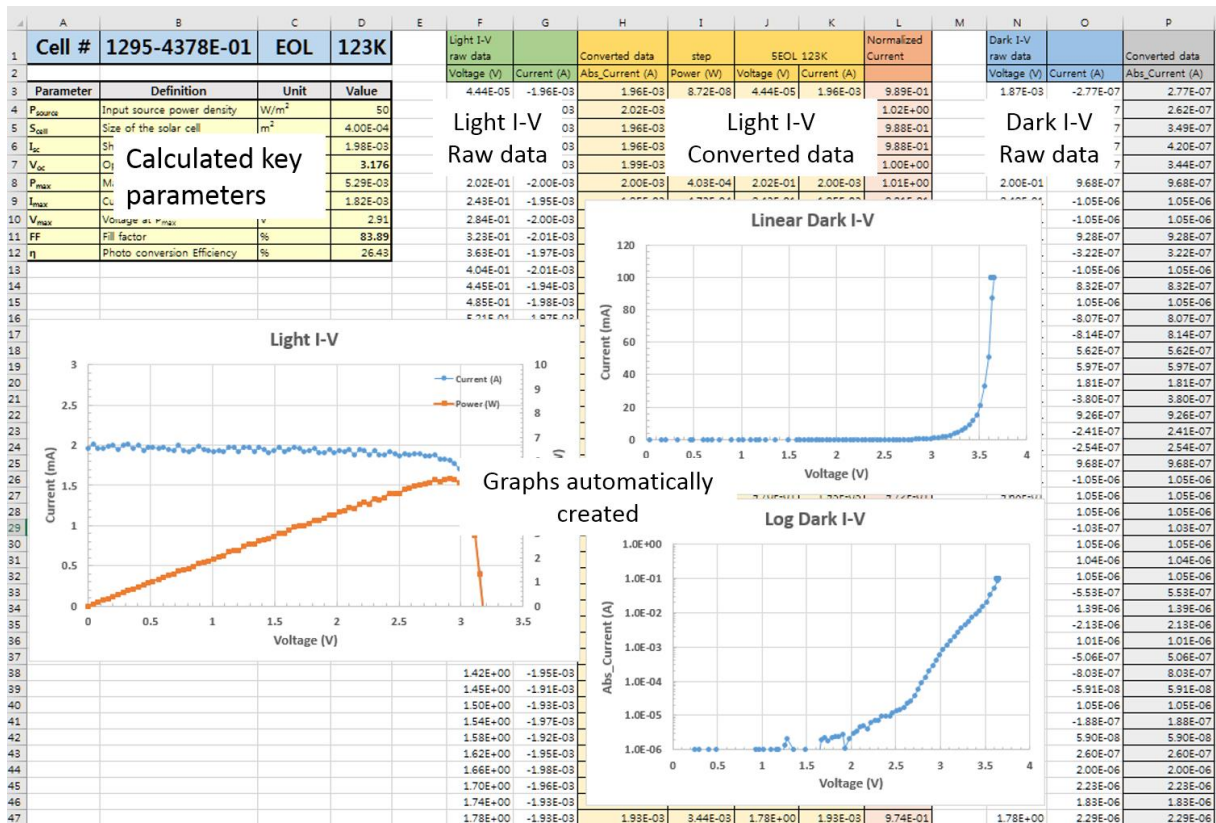


Figure 2-25. An example of the created excel sheet which contains calculated key parameters of solar cell, raw and converted I-V data, and automatically created light and dark I-V curves.

## References

- [1] O. Grasset and ESA, "Exploring the emergence of habitable worlds around gas giants," Nov. 2011.
- [2] T. S. Moss, "RESEARCH NOTES: Theory of the Spectral Distribution of Recombination Radiation from InSb," presented at the Proceedings of the Physical Society, 1957, vol. 70, no. 2, pp. 247–250.
- [3] P. T. Landsberg, "LETTERS TO THE EDITOR: Lifetimes of Excess Carriers in InSb," presented at the Proceedings of the Physical Society, 1957, vol. 70, no. 1, pp. 1175–1176.
- [4] C. Baur, M. Meusel, F. Dimroth, and A. W. Bett, "Investigation of Ge component cells," IEEE 31st Photovoltaic Specialists Conference (PVSC), pp. 675–678, 2005.
- [5] C. Baur, M. Hermle, F. Dimroth, and A. W. Bett, "Effects of optical coupling in III-V multilayer systems," *Appl. Phys. Lett.*, vol. 90, no. 19, p. 192109, 2007.
- [6] G. Siefer, C. Baur, and A. W. Bett, "External quantum efficiency measurements of Germanium bottom subcells: Measurement artifacts and correction procedures," presented at the 2010 35th IEEE Photovoltaic Specialists Conference (PVSC), 2010, pp. 000704–000707.
- [7] D. C. Marvin and J. C. Nocerino, "Evaluation of multijunction solar cell performance in radiation environments," presented at the Conference Record of the IEEE Photovoltaic Specialists Conference, 2000, vol. 2000, pp. 1102–1105.
- [8] B. E. Anspaugh, "Proton and electron damage coefficients for GaAs/Ge solar cells," presented at the Conference Record of the IEEE Photovoltaic Specialists Conference, 1992, vol. 2, pp. 1593–1598.
- [9] R. D. Harris, M. Imaizumi, R. J. Walters, J. R. Lorentzen, S. R. Messenger, J. G. Tischler, T. Ohshima, S. Sato, P. R. Sharps, and N. S. Fatemi, "In Situ Irradiation and Measurement of Triple Junction Solar Cells at Low Intensity, Low Temperature (LILT) Conditions," *IEEE Trans. Nucl. Sci.*, vol. 55, no. 6, pp. 3502–3507, Dec. 2008.
- [10] P. M. Stella, R. L. Mueller, R. L. Scrivner, and R. S. Helizon, "Preliminary low temperature electron irradiation of triple junction solar cells," 19th Space Photovoltaic Research and Technology, pp. 1–7, Feb. 2007.
- [11] C. Baur, V. Khorenko, G. Siefer, J. C. Bourgoin, M. Casale, R. Campesato, S. Duzellier, and Inguimbert V, "Development status of triple-junction solar cells optimized for low intensity low temperature applications," IEEE 39th Photovoltaic Specialists Conference (PVSC), pp. 3237–3242, 2013.
- [12] S. Park, J. C. Bourgoin, O. Cavani, V. Khorenko, C. Baur, and B. Boizot, "Origin of the Degradation of Triple Junction Solar Cells at low Temperature," E3S Web Conf., vol. 16, no. 1, pp. 04004–4, May 2017.
- [13] S. Park, J. C. Bourgoin, H. Sim, C. Baur, V. Khorenko, O. Cavani, J. Bourcois, S. Picard, and B. Boizot, "Space Degradation of 3J Solar Cells: I - Proton Irradiation," *Prog. Photovolt. Res. Appl.*, pp. 1–11, 2018.

# 3 Proton irradiation

3.1	Proton irradiation of TJ cells in LILT conditions .....	92
3.1.1	Analysis of I-V characteristics before and after 1 MeV proton irradiations .....	93
3.1.2	Degradation of key parameters in TJ cells .....	94
3.2	Approach to the component cells.....	95
3.2.1	Degradation of $I_{SC}$ and $V_{OC}$ at different temperatures .....	95
3.2.2	Electric field dependence of I-V characteristics .....	100
3.2.3	Orientation dependence of proton irradiation.....	102
3.2.4	Isochronal annealing in component cells.....	108
3.3	Discussion of the chapter 3 .....	110
3.3.1	Temperature and fluence dependences of the degradation.....	110
3.3.2	Recovery of proton irradiation-induced defects .....	113
3.3.3	Recombination of photo generated current by irradiation-induced defects.....	114
	Conclusion of the chapter 3.....	116
	Reference.....	117

Previously, in the chapter 2, we introduced the irradiation system setups and the preparation before the irradiation test for low temperature (LILT) conditions with lattice-matched GaInP/GaAs/Ge triple junction (TJ) solar cells. In this chapter, to understand the influence of proton irradiation on TJ solar cells under LILT conditions, we investigated its electrical behaviors Beginning Of Life (BOL) and End Of Life (EOL) I-V characteristics in dark (DIV) and under illumination (LIV), together with P-V characteristics (PV) of top, middle and bottom component cells in comparison to TJ cells under these conditions. Most of Proton irradiations were performed with 1 MeV energy and fluences ranging from  $2 \times 10^{10} \text{ cm}^{-2}$  to  $1.6 \times 10^{12} \text{ cm}^{-2}$  at temperatures ranging from 100 to 300 K, in the frame work of the JUICE annealing verification test followed by additional irradiation test for scientific analysis. A few 2 MeV irradiations were conducted for angular dependence test. The behavior of each parameter such as short circuit current  $I_{SC}$ , open circuit voltage  $V_{OC}$ , maximum power  $P_{MAX}$ , and fill factor FF will be presented. State-of-the-art lattice matched GaInP/GaAs/Ge triple junction (TJ) solar cells are now widely used for space missions because they have demonstrated the highest efficiency so far [1], [2]. Moreover, they exhibit the best radiation resistance compared to other types of cells [3], [4]. Their behavior under proton irradiations at room temperature has been studied extensively [5- 11]. During the JUICE mission, these TJ cells will be used for interplanetary and deep space missions, whose typical environment is often referred to as LILT conditions. However, the understanding of their behavior under particle irradiation at low temperature is still in infancy. Because of the difficulty to perform irradiation testing at low temperature followed by in-situ electrical data acquisition under solar illumination, this understanding has been deduced from low temperature measurements performed after room temperature irradiation [12- 14]. With the exception of the attempt [15], [16], the only studies of low temperature irradiation with in-situ measurements have been performed on TJ cells produced by AZUR SPACE Solar Power GmbH [17- 20].

Preliminary results [17] suggested that the electrical behavior of these TJ cells at low temperature was independent from the temperature at which irradiations were performed. However, in-situ analysis of the data acquired at low temperature reveals that several phenomena such as defect annealing and electric field dependence of recombination current have to be taken into account, the phenomena which are not observable in case of room temperature irradiation. This motivated us to perform a detailed study of the degradation of TJ cells and their respective component cells at temperatures ranging from 100K to 300 K. The study presented here is limited to the case of proton irradiation; the case of electron irradiation will be presented in chapter 4.

### 3.1 Proton irradiation of TJ cells in LILT conditions

A second hypothesis made in the literature is that degradations of electrical properties after protons or electrons irradiations are correlated once relative damage coefficients (RDCs) are established from experimental data. Indeed, extensive studies have been done for Si and GaAs materials [21].

To establish RDCs of different particles or energies, the most straightforward way is to measure degradations directly and calculate coefficients for each solar cell parameters. Then, generally effect of proton irradiation with different energies is reduced to 10 MeV proton equivalence fluence which produces the same damage effect as an actual proton spectrum in space. Same procedure is applied to 1 MeV electron equivalence fluence. Finally, RDC of 10 MeV proton and 1 MeV electron is calculated. In this respect, same approach has been applied to some GaInP/GaAs/Ge TJ solar cells [22]. However, applying the same approach in LILT conditions requires a number of new irradiation tests to obtain RDCs of GaInP/GaAs/Ge TJ cell. The other possible issue is that 1 MeV electrons and 1 MeV protons have different energy losses within the different junctions of the solar cell. In case of electron irradiation, energy loss of particle is not varied along the path inside the cell. For protons around 1 MeV, it is not the case.

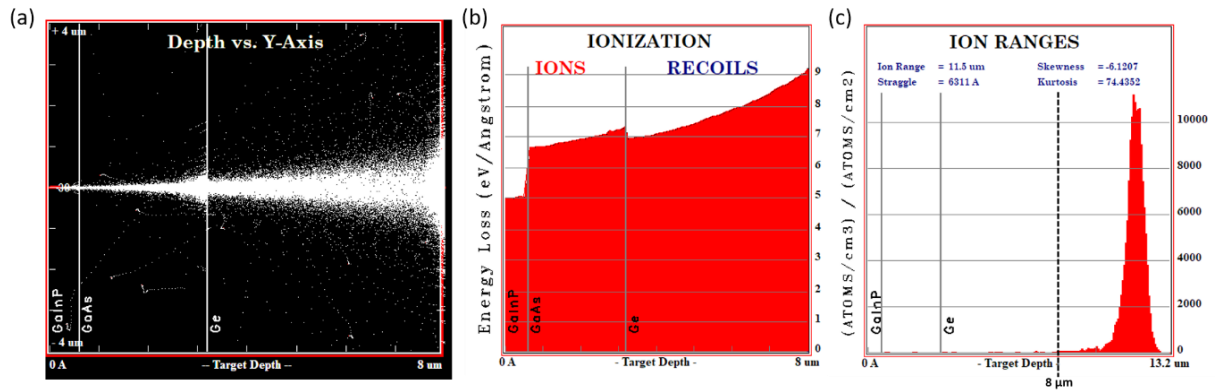


Figure 3-1. SRIM simulation with 1 MeV proton irradiation on the TJ cell used in this study. (a) Profile of ion propagation, (b) Ionization energy loss versus target depth and (c) Ion ranges. Displacement energy ( $T_D$ ) of 21 eV is applied for three materials.

Considering a triple junction structure of  $\text{Ga}_{0.51}\text{In}_{0.49}\text{P}$  ( $0.6 \mu\text{m}$ )/GaAs ( $2.6 \mu\text{m}$ )/Ge ( $140 \mu\text{m}$ ), a SRIM simulation has been carried out as represented in Figure 3-1 (SRIM-2013 software developed by James F. Ziegler [23]). A depth profile and an energy loss of ions are plotted up to  $8 \mu\text{m}$  from the surface of the top sub-cell. The energy of incident Hydrogen ions (protons) was set as 1 MeV and the displacement energy ( $T_D$ ) was assumed as 21 eV for three materials. The average energy loss ( $E_{\text{Loss}}$ ) of the protons in top junction is about  $5 \text{ eV}/\text{\AA}$  and it is increased up to  $7 \text{ eV}/\text{\AA}$  in bottom junction which is placed closed GaAs/Ge interface. According to the SRIM coding, protons that have 1 MeV energy are stopped at a depth of  $11.5 \mu\text{m}$ , sufficiently far from the active p-n junction region of Ge bottom cell. Therefore, one should consider that the increase of energy loss along the path of proton is not negligible and it can be more critical when the irradiation is not unidirectional like in space.

### 3.1.1 Analysis of I-V characteristics before and after 1 MeV proton irradiations

BOL and EOL LIV and PV of a cell (#:1520-030) irradiated at 123 K for a fluence of  $4 \times 10^{11} \text{ cm}^{-2}$  are presented in Figure 3-2. The I-V characteristics of the TJ cell are measured at 123 and 300 K. Thanks to the in-situ measurement, we can track the I-V characteristics of irradiated cells immediately. This allows us to properly measure EOL performance when the cell is stabilized at low temperature. Then the cell is warmed up to 300 K, once the cell is stabilized, its EOL property is again measured, and we cool down the cell again down to 123 K to observe any room temperature annealing effect. Changes of key parameters of this cell by the proton irradiation are noted in Table 3-1. First, when the cell is cooled down from 300 to 123 K, its  $I_{SC}$  value is decreased from 2.34 to 2.07 mA. As we shall discuss later, this is because the current limiting cell, which is the top cell in BOL condition, flows less current at lower temperature than at room temperature. Then, when the cell was irradiated with a fluence of  $4 \times 10^{11} \text{ cm}^{-2}$ , its EOL  $I_{SC}$  value became 1.96 mA ( $\Delta I = 0.11 \text{ mA}$ , 5.3 %). At the same time, the  $V_{OC}$  value was changed from 3.556 to 3.309 V ( $\Delta V = 247 \text{ mV}$ , 6.9 %) and the FF was degraded from 91.17 to 83.11 %. When we compared BOL and EOL  $V_{OC}$  values at 300 K, it is found out that  $\Delta V$  at 300 K was much larger (453 mV) than that at 123 K while the change of  $I_{SC}$  is only 2 % which is much smaller than the case of measurement at low temperature. As a result,  $P_{MAX}$  at 300 K is significantly affected by the degradation of  $V_{OC}$ . EOL  $P_{MAX}$  is degraded by 30 % from its BOL one at 300 K while it is only decreased by 20 % at 123 K. Thus, at low temperature, it seems that a performance of TJ cells is less affected by irradiation.

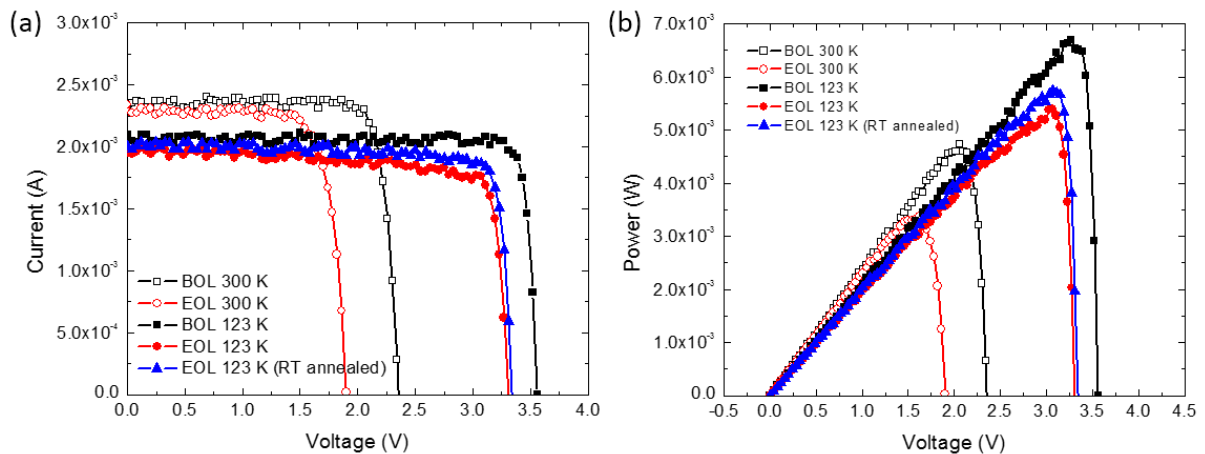


Figure 3-2. BOL and EOL (after 1 MeV proton irradiation at 123 K with  $4 \times 10^{11} \text{ cm}^{-2}$ ) electrical properties of 1520-030 TJ solar cell at 123 and 300 K under illumination: (a) I-V curves and (b) P-V curves.

Table 3-1. Electrical properties of 1520-030 TJ cell measured at 123 and 300 K before and after 1 MeV proton irradiation at 123 K (fluence =  $4 \times 10^{11} \text{ cm}^{-2}$ ).

	123 K (LT)			300 K (RT)	
	BOL	EOL	EOL RA	BOL	EOL
<b>I<sub>SC</sub> (mA)</b>	2.07	1.96	2.01	2.34	2.29
<b>V<sub>OC</sub> (mV)</b>	3.556	3.309	3.345	2.355	1.902
<b>FF (%)</b>	91.17	83.11	85.54	85.79	77.31
<b>P<sub>MAX</sub> (mW)</b>	6.70	5.39	5.75	4.73	3.37

In addition, we could also observe a recovery of solar cell performance after the room temperature annealing. The recovery of  $P_{MAX}$  originated from the recovery of  $I_{SC}$  (from 1.96 to 2.01 mA) and the recovery of FF (from 83.11 to 85.54 %). However, at this stage, we don't know which sub-cell contributes to degradation and recovery of each parameter, especially at in-situ LILT conditions. So, we will discuss in detail about this later in this chapter.

### 3.1.2 Degradation of key parameters in TJ cells

During JUICE annealing verification test which was performed during 2016, 48 pieces of 3G28 TJ cells were irradiated by 1 MeV protons with fluences varying from  $1 \times 10^{11}$  to  $5.4 \times 10^{11} \text{ cm}^{-2}$ . Irradiations and measurements were performed at 123 K. The number of cells irradiated in each condition varied from 3 to 13. Relative changes of  $I_{SC}$ ,  $V_{OC}$ , and  $P_{MAX}$  values after irradiation expressed as remaining factor (RF) are presented in Figure 3-3.

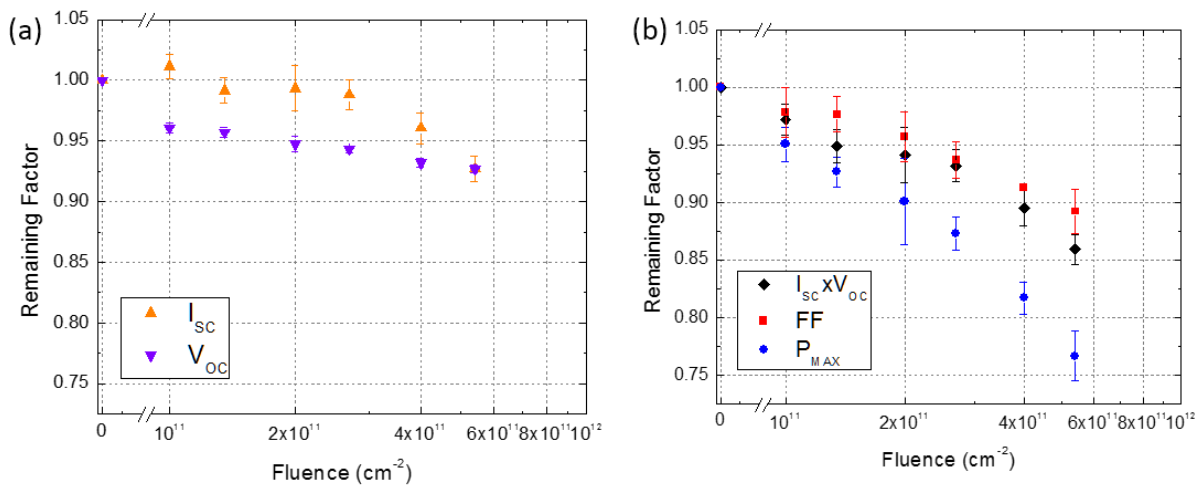


Figure 3-3. Remaining factor of key parameters of 1 MeV proton irradiated TJ solar cells at 123 K: (a) open-circuit voltage  $V_{OC}$ , short-circuit current  $I_{SC}$  and (b) product  $I_{SC} \times V_{OC}$ , fill factor FF and maximum power  $P_{MAX}$ .

The change of  $RF(I_{SC})$  versus fluence is small below typically  $2.7 \times 10^{11} \text{ cm}^{-2}$ , whereas it suddenly decreases reaching 0.93 at  $5.4 \times 10^{11} \text{ cm}^{-2}$ . This observation suggests that there could be a critical condition corresponding to a modification of the degradation mechanism inside the TJ cells components. As to  $RF(V_{OC})$ , it decreases regularly as a function of fluence, after an initial step for the lowest fluence used. However,  $RF(P_{MAX})$  decreases more rapidly than the product  $I_{SC} \times V_{OC}$ , as it should vary if the fill factor (FF) was independent of the fluence. At the highest fluence,  $RF(P_{MAX})$  is about 0.77 suggesting that there seems to be another source of degradation, besides  $I_{SC}$  and  $V_{OC}$ , affecting the fill factor FF.

Following this extensive irradiation test, more TJ cells together with its component cells were irradiated ranging temperature 100 to 300 K with fluence varying from  $10^{10}$  to  $10^{12} \text{ cm}^{-2}$ . Its analysis is discussed below.

## 3.2 Approach to the component cells

### 3.2.1 Degradation of $I_{SC}$ and $V_{OC}$ at different temperatures

The investigation of component cells was performed to determine the changes of the key parameters associated with each cell as a function of fluence in the temperature range 100 K - 300 K. Here, we focus on the changes of  $I_{SC}$  and  $V_{OC}$ . Accumulative irradiations were carried out on top, middle and bottom component cells at 100 K, 123 K, 200 K and 300 K. Figure 3-4 (a) shows the changes of  $I_{SC}$  as a function of fluence. The top cell appears to exhibit a smaller degradation than the middle cell. At room temperature, since BOL  $I_{SC}$  values of a top cell is slightly smaller than that of the middle cell, the top cell is actually the current limiting cell in the TJ cell. However, the middle cell becomes the current limiting cell after irradiation with a fluence of about  $10^{11} \text{ cm}^{-2}$  since its  $I_{SC}$  degradation is stronger than the  $I_{SC}$  of the top cell. For lower temperatures, the cells act differently: when the temperature decreases, in BOL conditions,  $I_{SC}$  of the top cell decreases while the middle cell  $I_{SC}$  apparently increases. As a result, a higher fluence of  $5 \times 10^{11} \text{ cm}^{-2}$  is required for changing the current limiting cell to the GaAs middle cell component. The bottom cell has a much higher BOL  $I_{SC}$  value compared to other two cells, so that, at 200 K and 300 K, in the TJ cell, the bottom cell does not become the current limiting cell even at the highest fluences considered in this work.

However, at 123K and 100 K, the value of  $I_{SC}$  of the bottom cell decreases abruptly. This strong effect of the bottom cell  $I_{SC}$  occurs for a very small fluence ( $2 \times 10^{10} \text{ cm}^{-2}$ ), partly at least because of the Photon Recycling Effect (PRE [24], [25]) (an effect not present in the TJ cell).

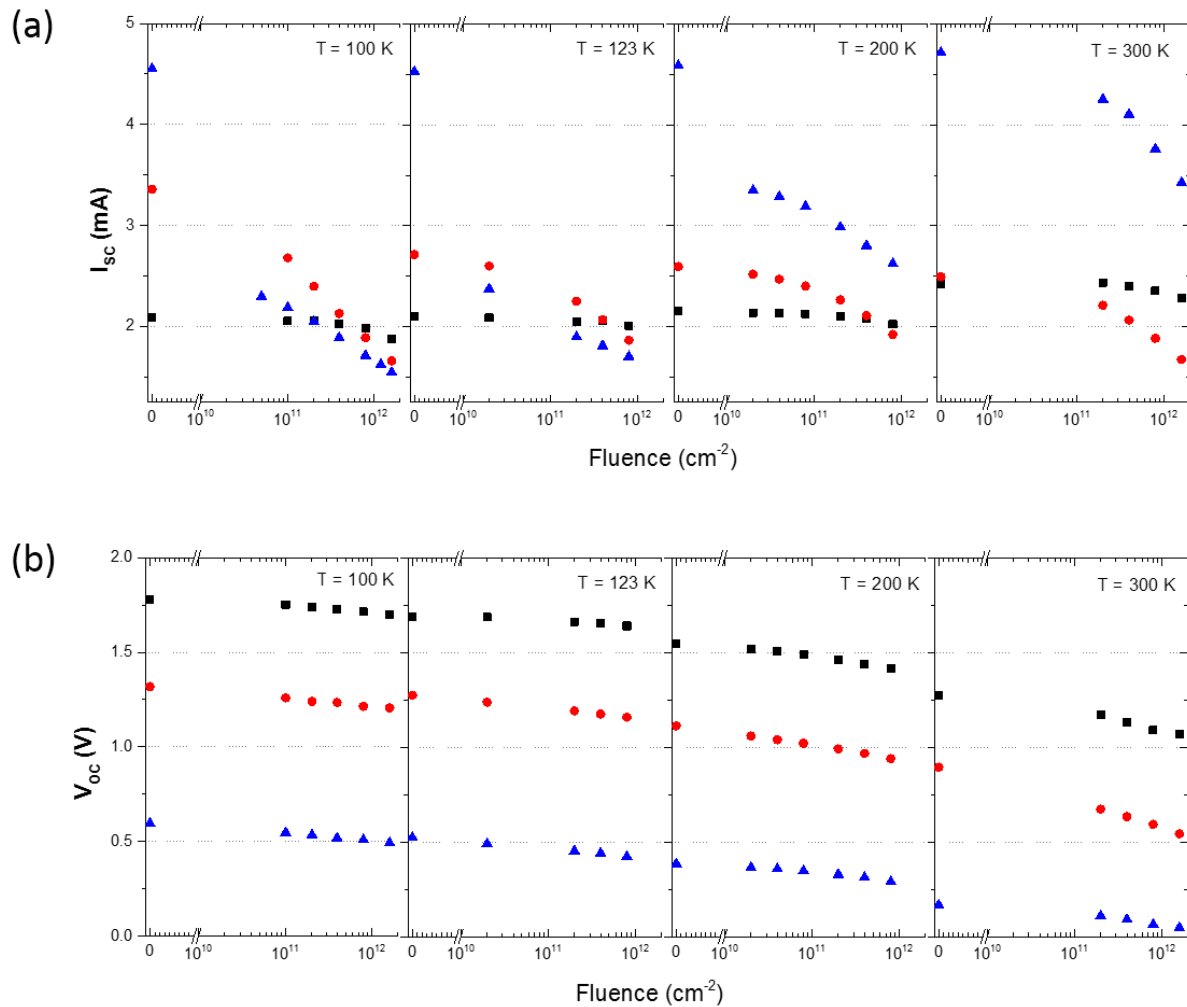


Figure 3-4. Fluence dependences of (a)  $I_{sc}$  and (b)  $V_{oc}$  of component cells at 100, 123, 200 and 300 K irradiated at 1 MeV with a flux  $4 \times 10^9 \text{ cm}^{-2}\text{s}^{-1}$ . Black square, red circle, and blue triangle indicate top, middle and bottom component cells, respectively.

The PRE is a phenomenon which describes re-absorption of radiative recombination from upper semiconductor layers to bottom layers, resulting in a higher  $I_{sc}$  than its intrinsic value (Detailed discussion of the PRE is in the chapter 2). In addition, the amount PRE is temperature dependent because the spectral response of each layer shifted by the change of bandgap of semiconductor, which is temperature dependent. In the bottom component cell, the portion of  $I_{sc}$  induced by the PRE becomes larger at lower temperature. Thus, we first needed to remove the PRE through a small amount of irradiation so that we can correctly observe the true degradation of  $I_{sc}$  due to the irradiation after removing the PRE. As a consequence, it is found that the bottom cell can become current limiting in the TJ cell if the bottom cell has a good shunt resistant. For the degradation of  $V_{oc}$  of the three component cells, it is presented in Figure 3-4 (b). In contrast with the case of  $I_{sc}$ ,  $V_{oc}$  is more gradually degraded for all three component cells. However, there was certainly temperature dependence. The more the temperature is lowered, the less degraded  $V_{oc}$  is. It is commonly observed for all three component cells. At 100 K, after the irradiation with a fluence of  $1.6 \times 10^{12} \text{ cm}^{-2}$ ,  $V_{oc}$  of top, middle and bottom component

cells were degraded as about 0.078, 0.112 and 0.102 V from its BOL values, respectively. While, at 300 K, degradations of  $V_{OC}$  were about 0.202, 0.352 and 0.120 V for top, middle and bottom component cells.

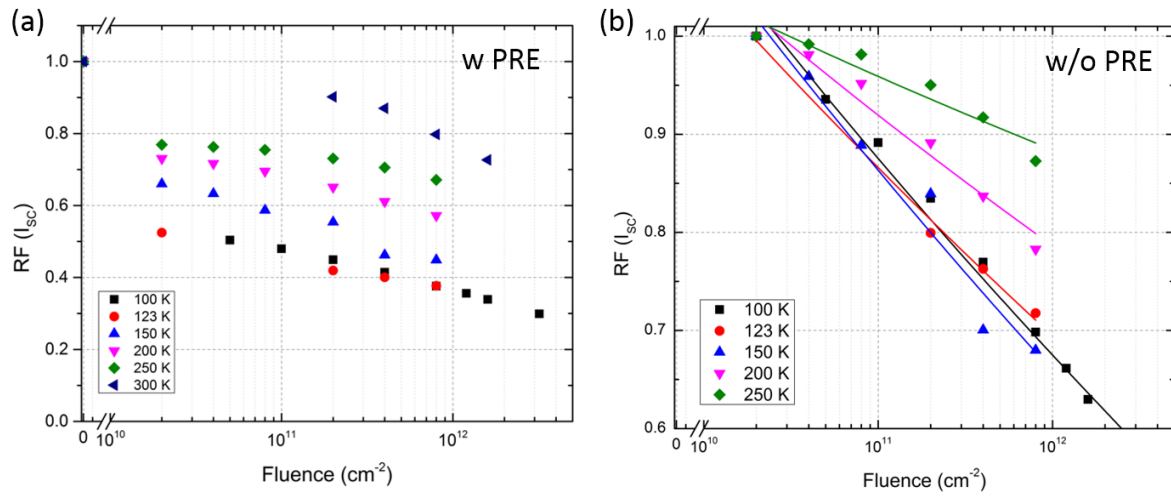


Figure 3-5.  $I_{sc}$  remaining factor of bottom component cells irradiated at various temperatures with a flux of  $4 \times 10^9 \text{ cm}^{-2} \text{ s}^{-1}$ : (a) before correction and (b) after corrections of the PRE.

Since the degradation of the bottom component cell appears to strongly depend on the irradiation temperature, we performed additional irradiations for the bottom component cell. The results are shown in Figure 3-5 (a). We consider here that the first irradiation with a fluence of  $2 \times 10^{10} \text{ cm}^{-2}$  is enough to remove the whole PRE in the bottom component cell, minimizing degradation of the cell by irradiation. Then, irradiations were accumulated at each irradiation temperature. I-V measurement was followed after irradiation at each fluence. However, when we irradiated the cell at 300 K, The PRE was not taken into account, so the first fluence was already much higher than that of other temperatures. The situation at 100 K was the same while the initial fluence was closer to  $2 \times 10^{10} \text{ cm}^{-2}$  and the degradation of  $I_{sc}$  at 100 K follows linear approximation when fluence is plotted in log scale. Thus, the approximate degradation point at  $2 \times 10^{10} \text{ cm}^{-2}$  could be reasonably predicted compared to the case of 300 K. Therefore, the case of 300 K was not included for further analysis after the PRE correction. The amount of  $I_{sc}$  degradation after the first irradiation with a fluence of  $2 \times 10^{10} \text{ cm}^{-2}$  tends to increase when the temperature decreases. As shown in Figure 3-5 (a), slopes of  $I_{sc}$  degradations at each temperature seem to be similar once the fluence exceeds  $10^{11} \text{ cm}^{-2}$  except the case of 300 K. At 200 and 250 K, the cells exhibit comparably smaller degradation than other cases. There is no data on that fluence for 300 K, so it is not clear to say whether this observation is still valid for 300 K or not. However, it is clearly seen that in the range between 123 and 250 K, we observe the drop of  $RF(I_{sc})$  from 0.52 to 0.78 (about 26 %). However, there is almost no difference of first drop of  $I_{sc}$  due to the removal of PRE and later degradation by proton irradiations between 100 and 123 K. Since the amount of PRE plays an important role for evaluating the  $RF(I_{sc})$ , it needed to be corrected to access a real degradation of  $I_{sc}$  which is directly related to the defects produced by proton irradiation. Considering the  $I_{sc}$  value after the

irradiation with a fluence of  $2 \times 10^{10} \text{ cm}^{-2}$  as a true BOL value,  $RF(I_{SC})$  is again calculated as a function of fluence at temperature ranging 100 to 250 K. Once it is corrected to remove the contribution of the PRE, they show that  $RF(I_{SC})$  is strongly temperature dependent between 150 and 250 K (see Figure 3-5 (b)). On the other hand, in the range of 100 and 150 K, we couldn't see its temperature dependence.

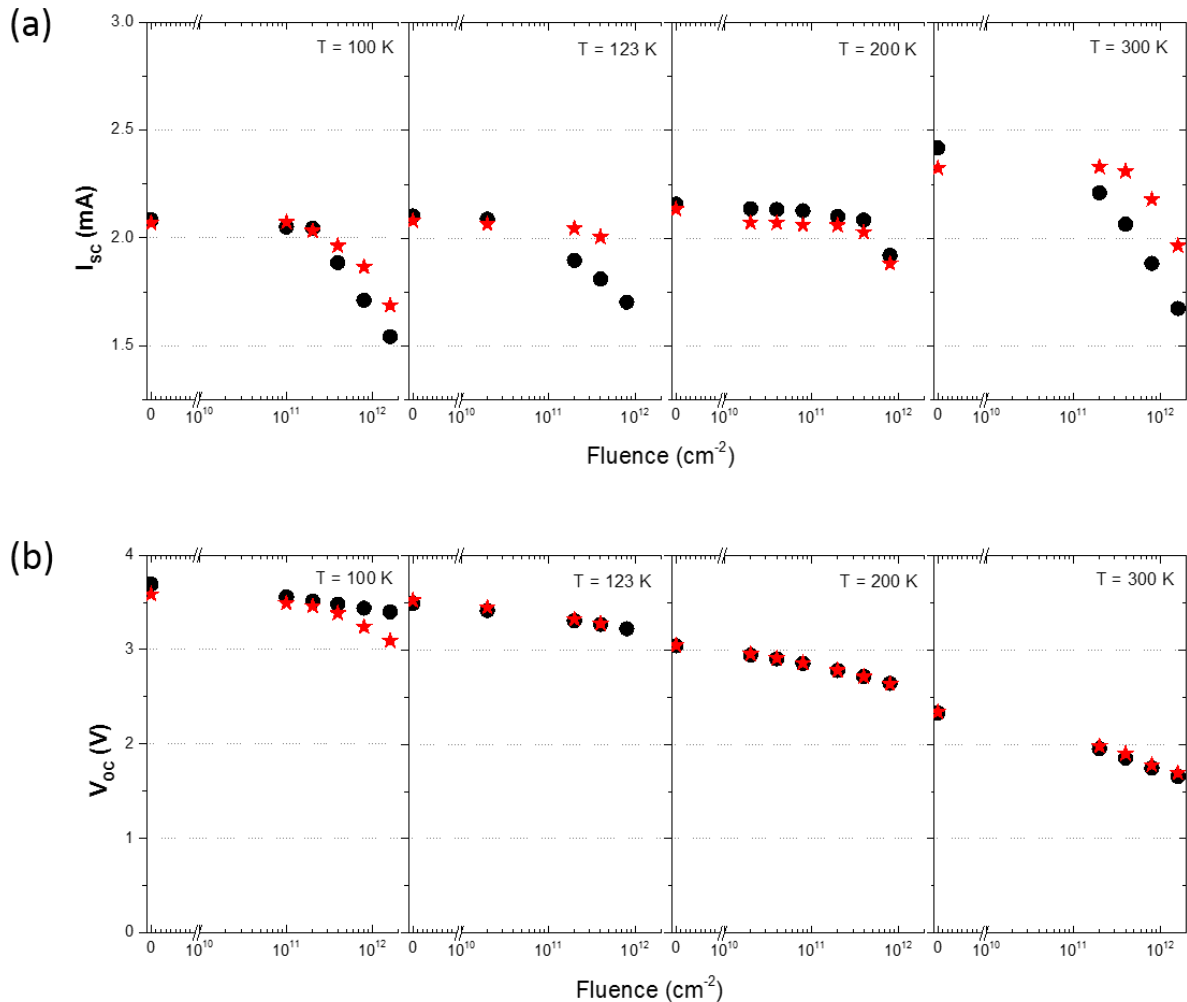


Figure 3-6. Comparison of the degradations of TJ cells with that deduced from the degradation of component cells: (a)  $I_{sc}$  and (b)  $V_{oc}$  at 100, 123, 200 and 300 K: Black circle and red star indicate data obtained from component cells and TJ cells, respectively.

The comparison between the degradations of  $I_{sc}$  and  $V_{oc}$  of the TJ cells with the ones deduced from the degradation of component cells (by selecting the minimum value of  $I_{sc}$  among the component cells and adding their  $V_{oc}$  values) is given in Figure 3-6. Note that the performance of each cell could vary from cell to cell. It shows that for  $V_{oc}$  (except 100 K) reasonable fits are obtained, which implies that the prediction of the  $V_{oc}$  degradation of TJ cells can be reasonably well deduced from that of the component cells. In the case of 100 K, the real  $V_{oc}$  of a TJ cell degrades faster than the reconstructed value from component cells as a function of irradiation. In fact, the cell 662E-84 TJ cell which was irradiated at 100 K exhibited a particular behavior in DIV measurement which is not observed in other TJ cells. As shown in Figure 3-7, its dark current property is significantly modified as it is irradiated especially at

higher fluence exceeded to  $4 \times 10^{11} \text{ cm}^{-2}$ . This fluence is where we can start to observe the discrepancy of  $V_{OC}$  from the simulation at 100 K.

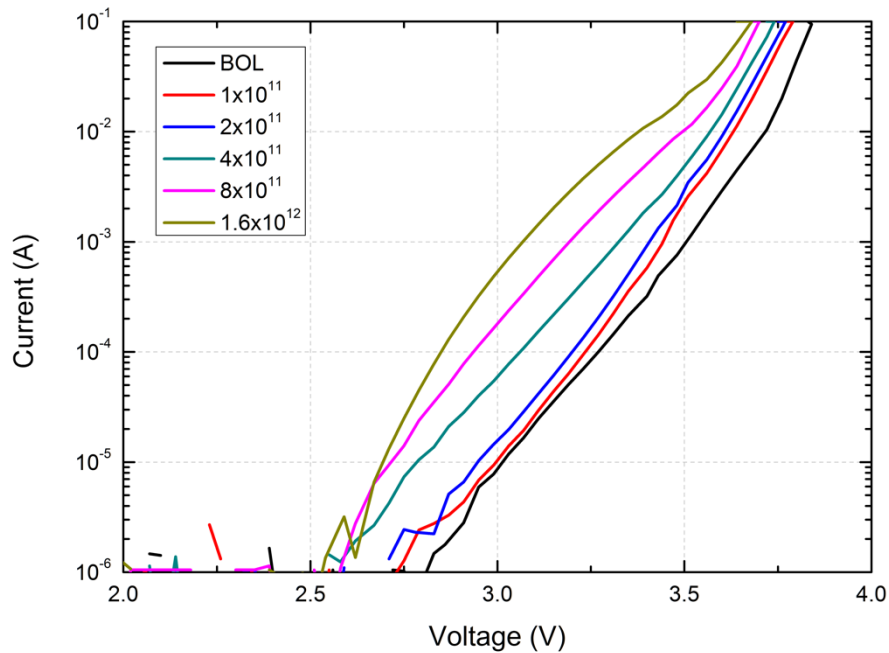


Figure 3-7. BOL and EOL I-V characteristics in dark of a proton irradiated TJ cell (662E-84) at 100 K. (fluence:  $\text{cm}^{-2}$ )

For the  $I_{SC}$  degradation, the fits are not satisfying except at 200 K. There is a clearly discrepancy between  $I_{SC}$  of TJ cell and simulated  $I_{SC}$  from component cells. At 100 K, it seems that the current is reasonably well matched when the cell is irradiated less than  $2 \times 10^{11} \text{ cm}^{-2}$ , and  $2 \times 10^{10} \text{ cm}^{-2}$  for 123 K. This is approximately the point where the  $I_{SC}$  of bottom component cells becomes smaller than that of top component cells (see the data points on 100 K and 123 K of Figure 3-4 (a)). Similar transition occurs from the top to the middle component cells during irradiation at 300 K. However, since BOL  $I_{SC}$  values of top and middle cells are similar, the transition occurs from the first irradiation with a fluence of  $2 \times 10^{11} \text{ cm}^{-2}$ . If the cell was irradiated with smaller fluence, the transition might happen earlier. Only at 200 K, the top component cell maintains its current limiting cell position up to  $4 \times 10^{11} \text{ cm}^{-2}$  and then the change from the top to the middle cell happened between  $4 \times 10^{11}$  and  $8 \times 10^{11} \text{ cm}^{-2}$ .

In fact, in the multi-junction solar cell, currents which flow in each sub-cell must be equal since the sub-cells are connected in series. Thus, the current measured in a TJ cell is highly dependent on the current limiting cell along the applied voltage. When 0 V is applied to a TJ cell, if the currents of sub-cells at 0 V are not equal, the current limiting cell will be driven in reverse at 0 V. For the top cell, the difference between its  $I_{SC}$  and the current in reverse until certain voltage is negligible since its shunt resistance is too high to introduce an increase of current. On the other hand, if the current limiting cell has a low shunt resistance so that the current in reverse is lowered than its  $I_{SC}$ , this reserve current can be a  $I_{SC}$  value in a TJ cell. Therefore, in this kind of situation, it is inevitable that the discrepancy between two

values is introduced in our simplified simulation. Examples showing the principle of  $I_{SC}$  measurement of triple junction solar cell in different current limiting situations are presented in Figure 3-8.

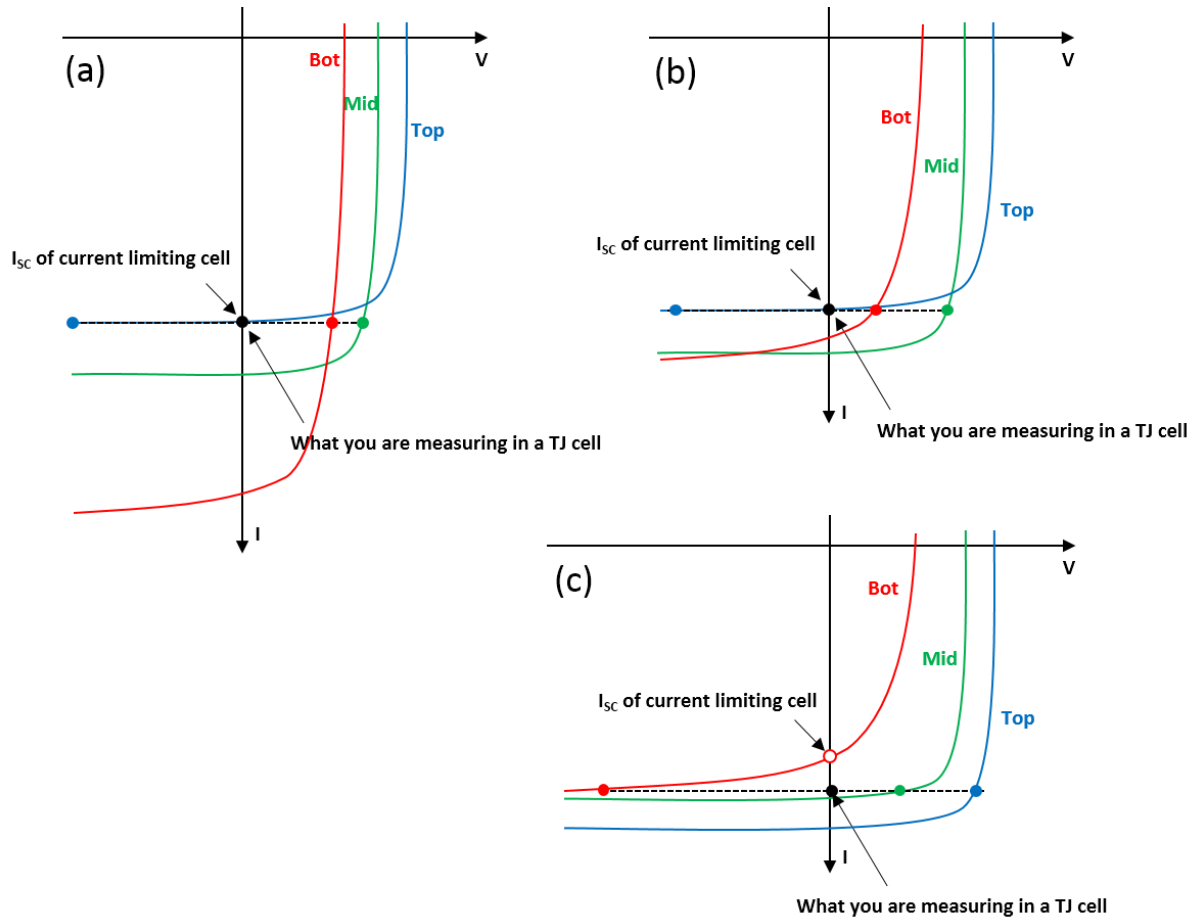


Figure 3-8. Diagram of light I-V measurement of a multi-junction solar cell composed of two sub-cells.

### 3.2.2 Electric field dependence of I-V characteristics

Besides usual degradations of  $I_{SC}$  and  $V_{OC}$ , TJ cells exhibit, in addition to the degradation induced by minority carrier recombination induced by the defects production, a degradation associated with another cell parameter, which is only observable under illumination. Figure 3-9 shows the comparison between I-V characteristics under illumination (LIV) and in dark (DIV) before and after irradiation with a fluence of  $1.6 \times 10^{12} \text{ cm}^{-2}$ . The DIV curve is shifted by  $I_{SC}$ , so that the DIV and LIV curves exhibit the same current at  $V = 0$ . Before irradiation, these two curves overlap perfectly from 0 to 2.8 V, then above to 2.8 V, the shifted DIV curve is decoupled from the LIV curve. This is because in BOL condition, the current mismatch of three sub-cells is large. Thus, the FF of LIV curve is higher than that of shifter DIV curve. After irradiation, this phenomenon almost disappeared in EOL measurement since the currents of sub-cells are not too much different from each other.

Our interest is on the region where the two curves are originally well overlapped in BOL condition. When the cell is irradiated, the current under illumination starts to increase as a function of voltage while the dark current maintains its original value. This phenomenon results in a significant decrease of FF of TJ cells after irradiation.

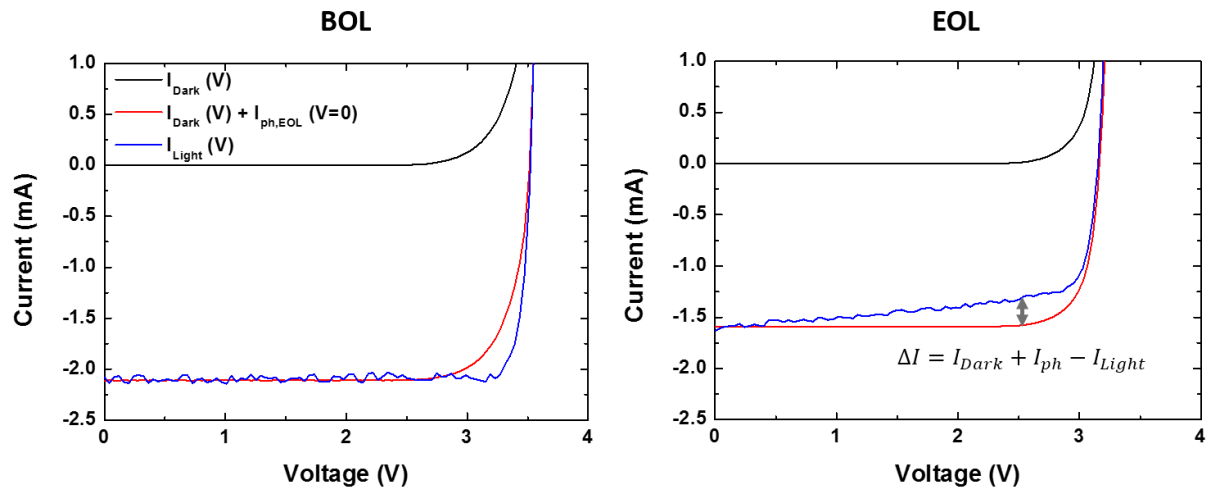


Figure 3-9. BOL and EOL I-V characteristics of a TJ cell irradiated with  $1.6 \times 10^{12} \text{ cm}^{-2}$  at 123 K (black curve: dark I-V, red curve: dark I-V +  $I_{sc}$  (EOL), blue curve: light I-V).

The same experiments have also been carried for all three component cells. As shown in Figure 3-10, the same result is observed like for the TJ cell in EOL conditions, we observe a discrepancy between LIV and shifted DIV curves for the top and middle cells. Within measurement accuracy, this effect is not observed for the bottom cell. Hence, the decrease of the photo current under illumination as a function of voltage in a TJ cell originates at least from the top and (or) middle sub-cells.

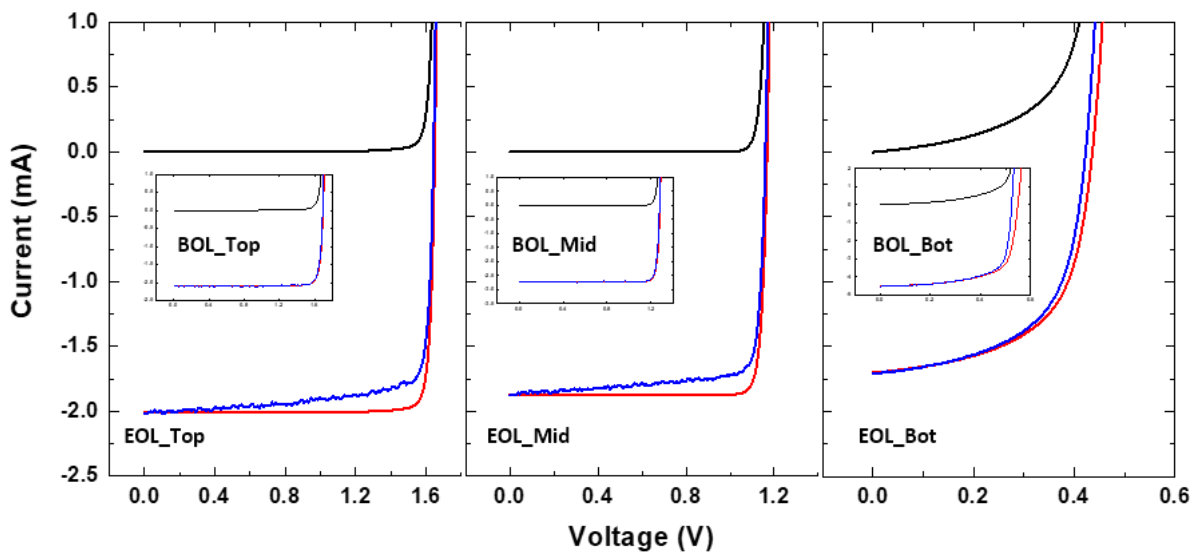


Figure 3-10. BOL and EOL I-V characteristics of top, middle, and bottom component cells irradiated at 123 K with  $8 \times 10^{11} \text{ cm}^{-2}$  (black curve: dark I-V, red curve: dark I-V +  $I_{sc}$  (EOL), blue curve: light I-V).

### 3.2.3 Orientation dependence of proton irradiation

One important result from this work considering low temperature proton irradiation is the significant temperature dependence of  $I_{SC}$  degradation inside the different component cells. This result is especially observed in the bottom component cell. This strong temperature dependence could be correlated to different defect nature and/or distributions inside the TJ solar cells as the function of irradiation temperature. If the assumption that the defects are less distributed at low temperature than at higher temperature is valid, we should observe the orientation effect of proton irradiation at different temperature. To study the orientation effect of proton irradiation, we also had to consider the effective penetration depth of proton at different incident angle.

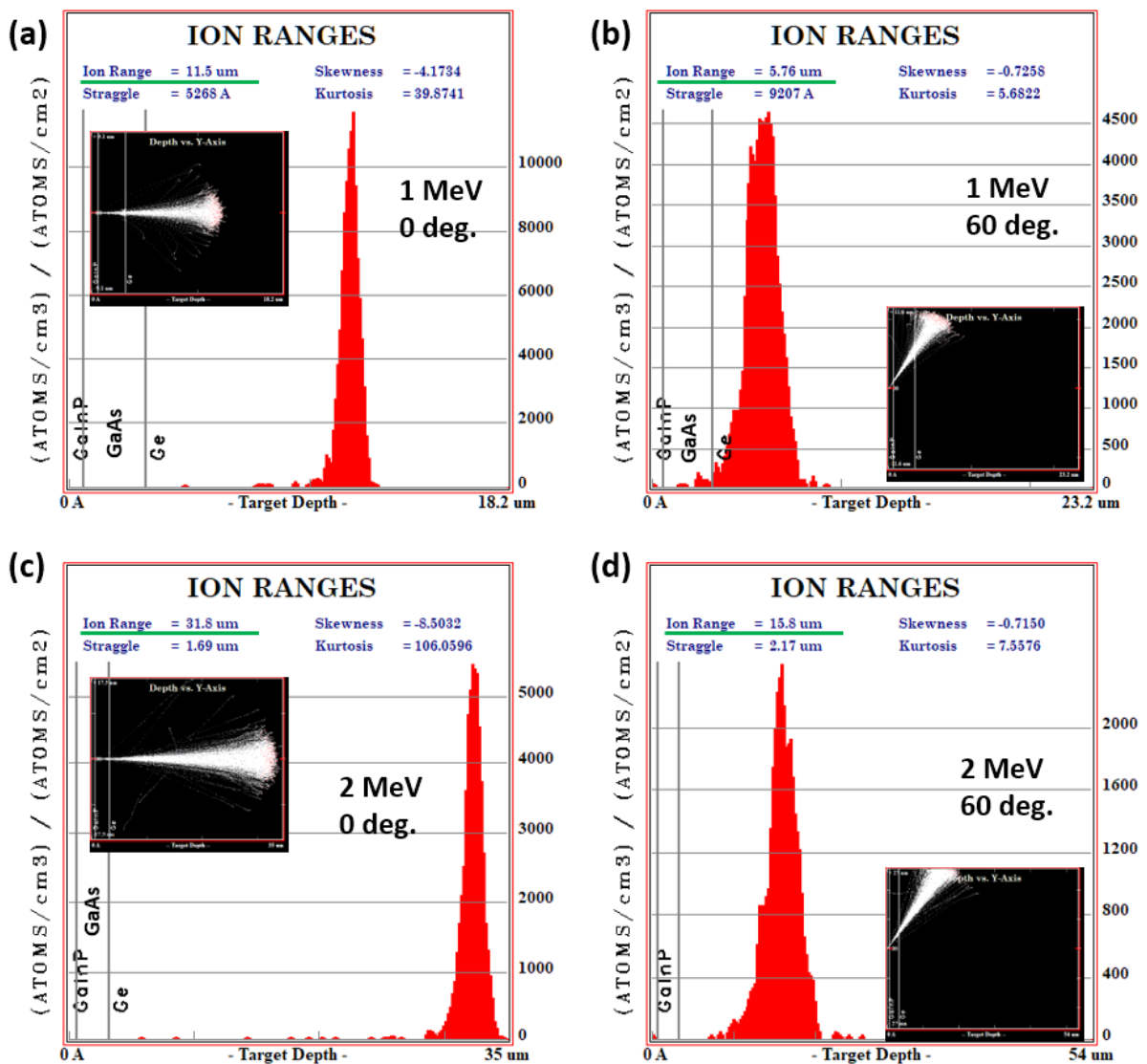


Figure 3-11. Penetration depth of 1 and 2 MeV proton irradiation (inset: ion profiles): (a) and (c) angle of incidence is 0 degree and (b) and (d) angle of incidence is 60 degrees.

When angle of incidence of proton is zero, the penetration depth of 1 MeV proton is about 11.5  $\mu\text{m}$  (see Figure 3-11 (a)). On the other hand, at 60 degrees of angle of incidence, the proton undergoes effectively

two times thicker cell thickness compared to the case of 0 degree. As a result, as shown in Figure 3-11 (b), 1 MeV protons are stopped at about 5.76  $\mu\text{m}$  of depth from the surface of TJ cell, closer to the Ge junction than the case of 0 degree, which possibly can induce unexpected additional degradation. When the energy of proton is 2 MeV, the penetration depth is increased almost 3 times compared to 1 MeV proton. Most of protons are stopped at 31.8  $\mu\text{m}$  (deep inside of p-type Ge substrate). Even at 60 degrees of angle of incidence, the proton ions are stopped far from the Ge junction.

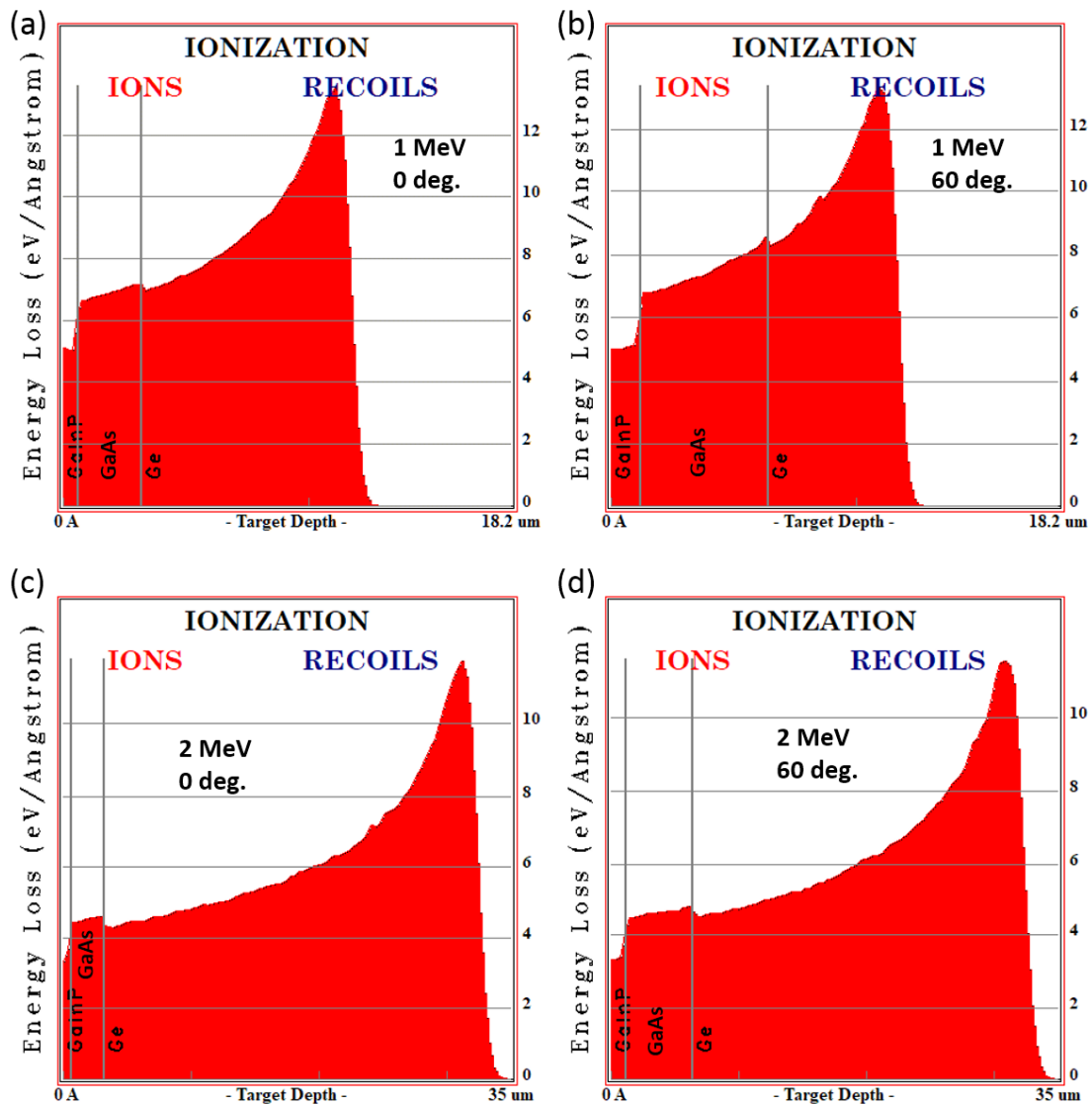


Figure 3-12. Ionization energy of 1 and 2 MeV proton in GaInP/GaAs/Ge TJ solar cell structure: (a) and (c) normal incident (angle is 0 degree) and (b) and (d) 60 degree of angle of incidence is applied to the structure; the effective thickness of all layers is doubled.

Furthermore, according to the SRIM results, when the irradiation angle of 1 MeV proton is tilted from 0 to 60 degrees (see Figure 3-12 (a) and (b)), the ionization energy near junctions becomes higher from 6.5 to 7 eV/A and from about 7 to 8.5 eV/A, in the middle and bottom sub-cells, respectively. On the other hand, the change of ionization energy due to angular modification of 2 MeV proton irradiation (Figure 3-12 (c) and (d)) is much smaller than the case of 1 MeV proton irradiation. Therefore, to

compare the energy effect on the angular dependence and to minimize unexpected effects due to the higher energy dissipation by angular dependence, we decided to perform 2 MeV proton irradiations for a longer penetration depth in order to minimize the influence of angular dependence on the ionization energy.

Before applying the different angle during the irradiation, the change of flux due to the tilted angle must be considered. When the sample is tilted by  $\theta$  from the initial condition as shown in Figure 3-13, actual flux which arrives to the surface of the sample is reduced by  $\cos \theta$ . Thus, this value should be compensated by dividing the fluence by  $\cos \theta$  when the angle is tilted by  $\theta$ .

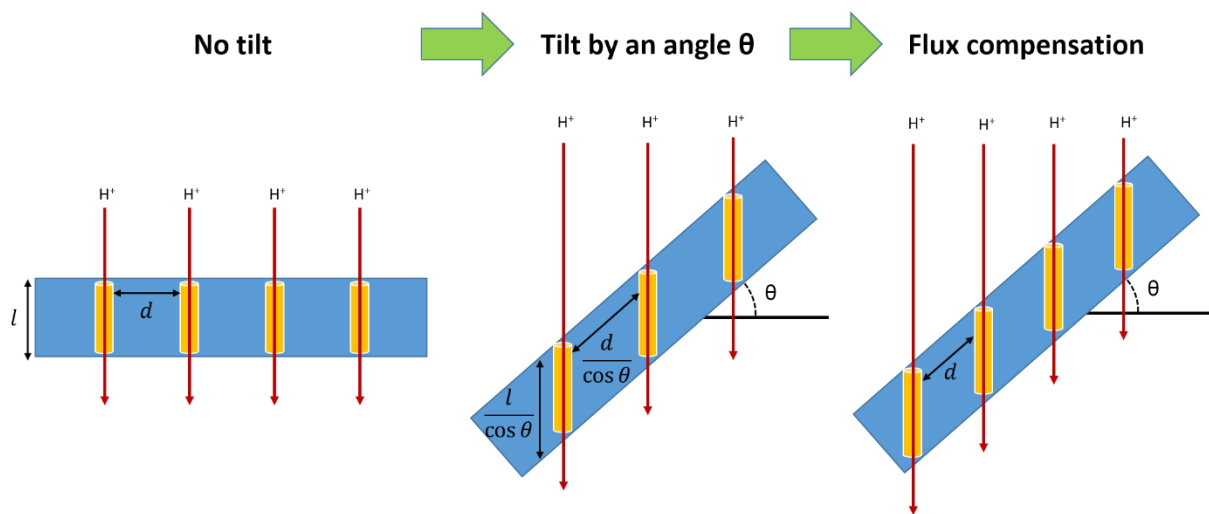


Figure 3-13. Simplified diagram showing an effect of change of the orientation of proton irradiation on the fluence.

Figure 3-14 shows the relative degradation of  $I_{SC}$  after 1 MeV proton in irradiated top and bottom component cells at 123 K with different angle of incidences (0, 30 and 60 degrees). As expected, the top cell exhibits small degradations. At a fluence of  $2 \times 10^{11} \text{ cm}^{-2}$ , relative degradation of  $I_{SC}$  was about 2 ~ 3 % for three incident angles and 2 ~ 6 % at  $4 \times 10^{11} \text{ cm}^{-2}$ . It is difficult to say that there is clear angular dependence of the degradation for the top component cell.

Concerning the bottom component cells, for removing the contribution of PRE on  $I_{SC}$ , a first irradiated with a fluence of  $2 \times 10^{10} \text{ cm}^{-2}$  has been performed and we assume that the  $I_{SC,0}$  at this dose corresponds to the BOL  $I_{SC}$  value for the Ge component cell. Then, the irradiation is accumulated up to  $4 \times 10^{11} \text{ cm}^{-2}$ . Then, we could observe that the relative degradation of  $I_{SC}$  of the bottom component cell was larger at higher degree of incident angle. But as mentioned above, with 1 MeV proton, the ionization energy in bottom layer is highly dependent on the incident angle. Thus, the change of energy dissipation at different angle should be taken into account when considering the orientation dependence of the proton irradiation. This will be treated with the result of 2 MeV irradiation of the bottom component cell.

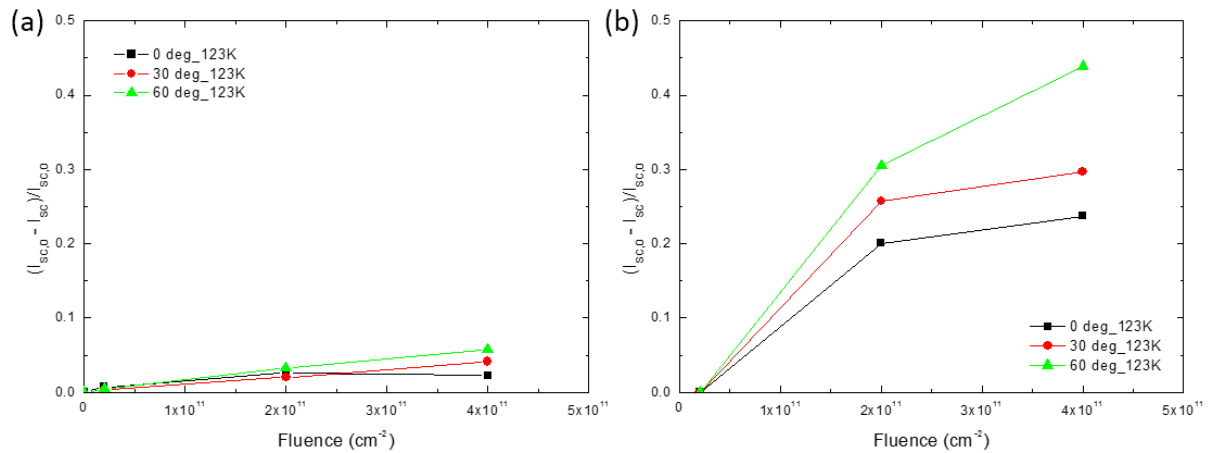


Figure 3-14. Relative degradation of  $I_{sc}$  of 1 MeV proton irradiated (a) top and (b) bottom component cells:  $(\text{BOL } I_{sc} - \text{EOL } I_{sc})/\text{BOL } I_{sc}$  at 123 K with different angles of incidence (0, 30 and 60 degrees).

After the test with 1 MeV proton irradiation only at 123 K, we realized that the temperature could play also an important role because the defect formation and mobility of defects can be influenced by temperature. We expected that a comparison of low temperature and room temperature irradiation results for the analysis of the orientation effect could be important in terms of defect analysis. Thus, for 2 MeV irradiation, we compared the irradiation at 300 K with the result of 123 K.

Figure 3-15 shows the relative degradations of  $I_{sc}$  of component cells at 123 and 300 K with different directions of 2 MeV proton irradiation. The maximum irradiation fluence for 123 K was set as  $4 \times 10^{11} \text{ cm}^{-2}$  since it was enough to see some changes. However, in the case of room temperature irradiation, the degradation of  $I_{sc}$  of middle and bottom cells was relatively smaller than at 123 K. Thus, we decided to irradiate with a fluence up to  $1.6 \times 10^{12} \text{ cm}^{-2}$  to observe some change more clearly. For the top component cells, first, the maximum relative degradation of  $I_{sc}$  is less than 5 % even after the irradiation with a fluence of  $4 \times 10^{11} \text{ cm}^{-2}$  at 123 K. Furthermore, the top cell doesn't exhibit a difference as a function of temperature. Since the degradation rate is very small, it is difficult to see any angular dependence. It seems to be related to the strong radiation hardness of this material; probably most of primary defects are easily annealed out. For the middle component cells, at 123 K, the degradation rate of  $I_{sc}$  is much larger than for the top component cells. At 0 degree, when fluence is the highest, a decrease of about 18 % on  $I_{sc}$  values is observed. When the cell is tilted by 30 and 60 degrees, the cells are more degraded than the case of 0 degree; however, results are almost identical between 30 and 60 degrees. At 300 K, the cells are in general less degraded than at 123 K. In the case of 300 K, only 60 degrees tilted cell showed more degradation than other cases. For the middle cell, it is not clear to conclude if the degradation of  $I_{sc}$  is clearly affected by the irradiation orientation. But at least, at 60 degrees, the middle cell is more degraded than at 0 degree. This result is observed for both irradiation temperatures except a lower degradation at room temperature.

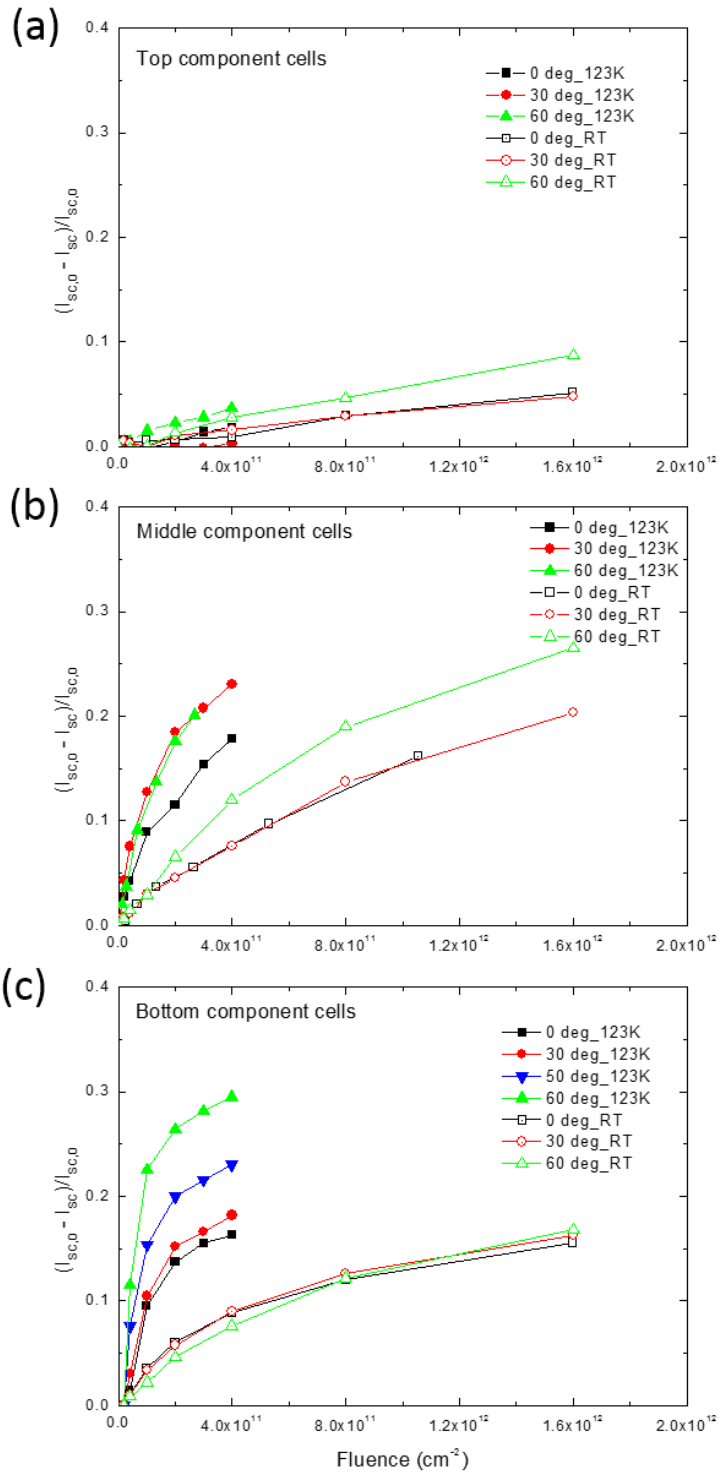


Figure 3-15. Relative degradation of  $I_{sc}$  of 2 MeV proton irradiated (a) top, (b) middle and (c) bottom component cells:  $(\text{BOL } I_{sc} - \text{EOL } I_{sc})/\text{BOL } I_{sc}$ , at 123 K and at 300 K (RT) with different angles of incidence (0, 30, 50 and 60 degrees).

As to the bottom component cell (see Figure 3-15 (c)), relative degradation of  $I_{sc}$  at 123 K increases slowly at higher fluence. However, the  $I_{sc}$  degradation is clearly a function of the angle. As the angle of incidence increases, more degradation of  $I_{sc}$  is observed. When the cell is perpendicularly placed (0

degree) to the proton beam line, only 15 % of  $I_{SC}$  is decreased by the fluence of  $4 \times 10^{11} \text{ cm}^{-2}$  while it is almost 30 % degradation at 60 degrees tilted irradiation.

Same experiments have been conducted at room temperature to compare with results at low temperature. As shown in Figure 3-15 (c), There is practically no angular dependence of the degradation of  $I_{SC}$  at room temperature which is a striking contrast from the low temperature irradiation results. To ensure if this is not a problem of low fluence, we irradiated the cell up to  $1.6 \times 10^{12} \text{ cm}^{-2}$  which is 4 times higher than the final fluence of the low temperature irradiation. Bottom component cells still didn't show angular dependence at room temperature. Furthermore, the relative degradation at room temperature is comparably smaller than the case of the low temperature.

From the observation that we have done by comparing the case of bottom cell at 123 and 300 K, we could assume that each proton entering to the Ge component cells introduces defects with a specific radius (maintaining the same defect area along its pathway, at a given depth). Then, the relative change of  $I_{SC}$  should be proportional to the actual length of the proton tracks where the defects are fixed and stabilized. Furthermore, the relationship between degradation of  $I_{SC}$  and the length of the proton track (damaged area) is directly related to the cosine of the angle of incidence ( $\cos \theta$ ). This means that, once we correct this parameter, the result should show the orientation independence.

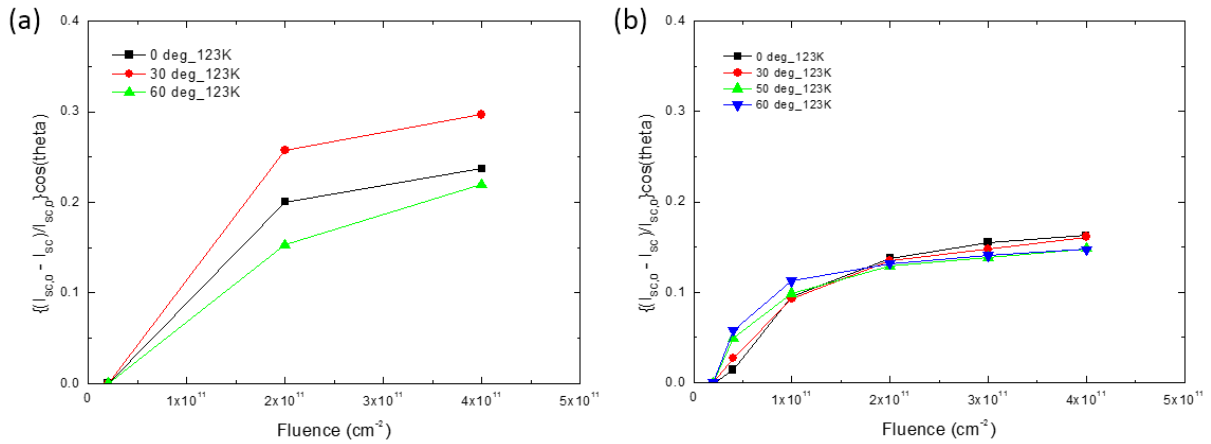


Figure 3-16. Compensated relative degradation of  $I_{SC}$  of bottom component cells at 123 K (angular coefficient is applied to compensate the effective thickness of the layers of the bottom component cell: (a) 1 MeV and (b) 2 MeV proton irradiations.

So, we applied the same correction for 1 MeV and 2 MeV irradiation of the bottom cell. Indeed, as shown in Figure 3-16, when the degradation of  $I_{SC}$  of the bottom component cell is corrected by  $\cos \theta$ , angular dependence apparently disappears in the case of 2 MeV proton irradiation. But, this is not the case for 1 MeV protons. From this comparison, we can find out the 1 MeV proton irradiation doesn't follow the angular dependence on the bottom component cell at 123 K. The reason could be that ionization energy of 1 MeV proton in Ge layers in TJ structure increases by 20 % when tilted by 60 degrees. However, the relationship of  $I_{SC}$  degradation and the angle at 1 MeV proton irradiation is not clear yet. Meanwhile, the result of 2 MeV irradiation at 123 K and 300 K indicates that degradation of

$I_{SC}$  at low temperature is linearly proportional to  $\cos \theta$  and this linear relationship is totally moved out when the cells are irradiated at 300 K.

From the analysis of orientation dependence in proton irradiated bottom component cell, we can conclude that the defects produce in the bottom cell have a highly temperature dependent mobility. At low irradiation temperatures, they are frozen (i.e. not uniformly distributed) so that the defects form like a cluster which is charged state along the proton path inside the cells, then it behaves as an insulating area which repels the minority carriers generated from the light absorption, resulting in a decrease of the photo generated current. In other words, this area can be considered as an electrically inactive area in the solar cell. However, when the temperature becomes higher, and eventually at room temperature, one can no more observe the angular dependence of  $I_{SC}$  degradation. This result indirectly proves that the defects are already homogeneously distributed; therefore, there is no more insulating area. In other words, the 2 MeV proton irradiation test with changing the angle of irradiation has permitted to verify that the non-uniformly distributed defects (i.e. clusters of defects) model along the proton tracks is valid at low temperature.

Concerning the top component cell, the angular dependence is much smaller than the case of the bottom component cell. Main reasons are first, GaInP is radiation hardness material compared to Ge, second, since the GaInP is used as a top layer, it receives less energy from the incident particle, that is, less ionization energy absorption ( $3 \text{ eV/m}^{-10}$  for 2 MeV proton). For the middle component cell, the amount of degradation of  $I_{SC}$  is not negligible compared to the case of the bottom component cell. There is an evident difference of degradation between 0 and 60 degrees. While the case at 30 degrees is still not clear. However, this difference exists at both low and room temperatures, indicating that this dependence is not able to be explained with the same model as the bottom one. Defects in GaAs material are known stable above 4 K after irradiation. Then, this relative difference of degradation doesn't come from recovery of defects. More detailed analysis will be needed to conclude the behavior of the middle cell.

### 3.2.4 Isochronal annealing in component cells

Since the component cells exhibit different temperature dependent behaviors, we performed isochronal annealing procedures following irradiations with a fluence of  $1.6 \times 10^{12} \text{ cm}^{-2}$  at 100 K. Figure 3-17 (a) shows the remaining factors of  $I_{SC}$ ,  $V_{OC}$  and  $P_{MAX}$  of the three component cells measured at 100 K after each annealing step. The annealing was carried out at 150, 190, 240 and 300 K during 5 minutes for the top and middle cells. For the bottom cell, the annealing temperature was increased by 18 K after the previous step. The annealing time was 5 minutes as well (see Figure 3-17 (b) and (c)).

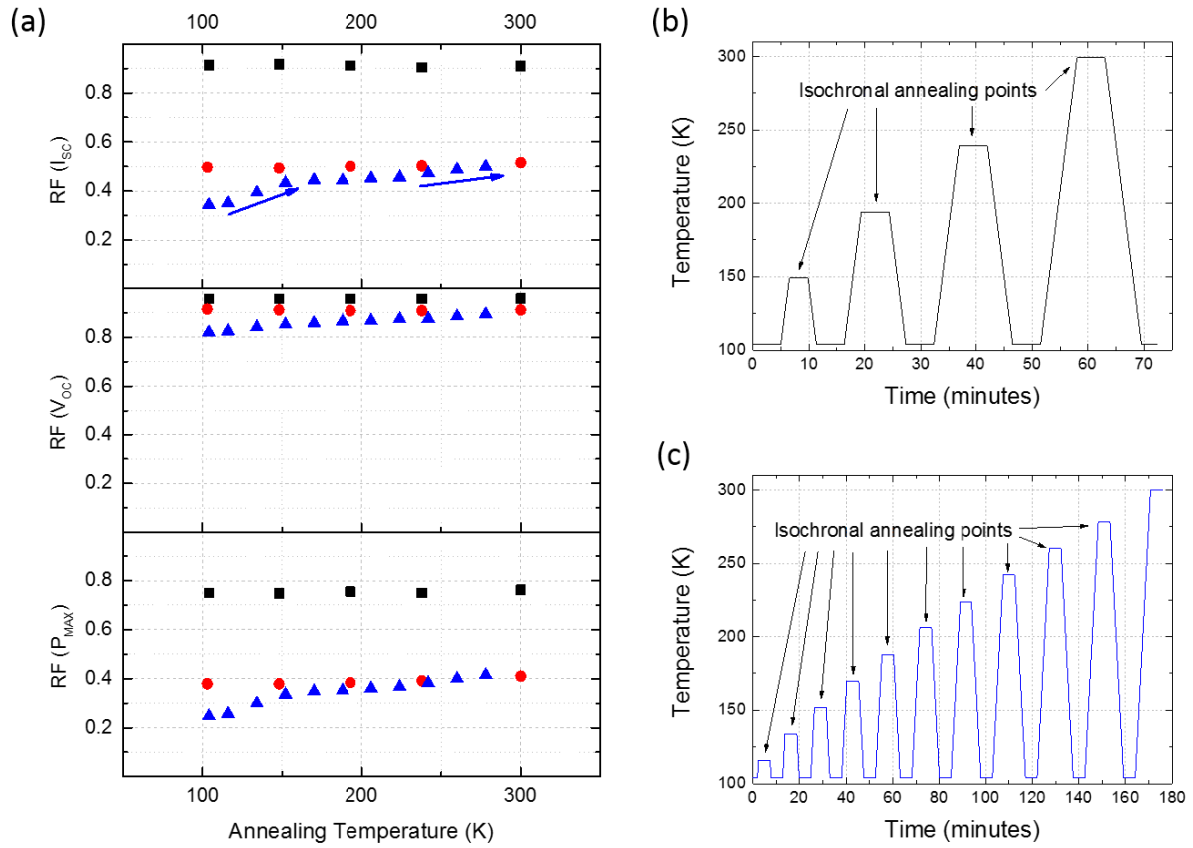


Figure 3-17. (a) Remaining factors of  $I_{SC}$ ,  $V_{OC}$  and  $P_{MAX}$  of proton irradiated ( $1 \text{ MeV}$ ,  $1.6 \times 10^{12} \text{ cm}^{-2}$ ) component cells during isochronal annealing stages: black square – top, red circle – middle, blue triangle – bottom cells, respectively. Temperature profile of isochronal annealing stages is represented: (b) top and middle cells and (c) bottom cell.

The top and middle cells did not show any significant recovery on  $I_{SC}$  and  $V_{OC}$  throughout the temperature range 100 K - 300 K. As a result, even if the cells are annealed at 300 K, RF ( $P_{MAX}$ ) of the top and the middle component cells were almost not improved (0.749 to 0.763 for the top, 0.379 to 0.410 for the middle component cell, respectively). Exact values are listed on Table 3-2.

However, changes of  $I_{SC}$  and  $V_{OC}$  values of the bottom cell result in a recovery of RF( $P_{MAX}$ ) from 0.247 to 0.415, especially, we could observe two stages centered at RF( $I_{SC}$ ) around 125 K and 250 K. Further annealing analysis related to the nature of defects is treated in the subchapter 3.3.2.

Table 3-2. Isochronal annealing of remaining factor of  $I_{SC}$ ,  $V_{OC}$  and  $P_{MAX}$  of 1 MeV proton irradiated top and middle component cells (measured at 100 K. irradiated with a fluence of  $1.6 \times 10^{12} \text{ cm}^{-2}$ )

Annealed Temp. (K)	Top			Middle		
	RF ( $I_{SC}$ )	RF ( $V_{OC}$ )	RF ( $P_{MAX}$ )	RF ( $I_{SC}$ )	RF ( $V_{OC}$ )	RF ( $P_{MAX}$ )
104	0.914	0.957	0.749	0.497	0.915	0.379
148	0.917	0.956	0.748	0.494	0.912	0.378
193	0.912	0.958	0.755	0.501	0.909	0.383
238	0.905	0.958	0.750	0.503	0.909	0.390
300	0.910	0.959	0.763	0.516	0.912	0.410

### 3.3 Discussion of the chapter 3

#### 3.3.1 Temperature and fluence dependences of the degradation

The rates of degradation of the components cells are different and depend on the temperature. Consider the  $I_{SC}$  values: the top cell exhibits a small degradation below  $10^{12} \text{ cm}^{-2}$ ; the middle cell exhibits a significant degradation from the lowest fluence: around 20 % at 300 and 200 K, increasing to about 50 %, at 100 K. As to the bottom cell, the sharp drop for the lowest fluence at low temperature must correspond partially to the cancellation of PRE, which is known to disappear after irradiation with the lowest fluence. However, as we shall now examine, the change of  $I_{SC}$  in the Ge bottom component cell is strongly temperature dependent, apparently more than expected when taking defect annealing into account. Figure 3-18 presents the temperature dependence of  $C = 1 - RF(I_{SC})$  (Data of Figure 3-5 (b) is re-treated to see an effect of temperature on defect concentration).  $C$  is a quantity directly correlated to the concentration of defects introduced by the irradiation.

As already observed in Figure 3-5 (b), decrease of  $RF(I_{SC})$  as a function of fluence was not different between 100 and 150 K, the temperature dependence starts to be expressed between 150 and 250 K. Through Figure 3-18, we can find that the quantity  $C$  is inversely proportional to the temperature in the range of 150 – 250 K, and the variation tends to be larger when the cumulated fluence is higher. This type of regular behavior in the range of 150 – 250 K is not expected to be related to the result of defect annealing [26]. In addition, the amplitude of the annealing stage of  $RF(I_{SC})$  around 125 K (between 100 and 150 K) observed in the isochronal annealing procedure (see Figure 3-17), of the order of 0.1, is not observed in this figure. This is strong evidence that the recovery of  $C$  is not related to the defect annealing.

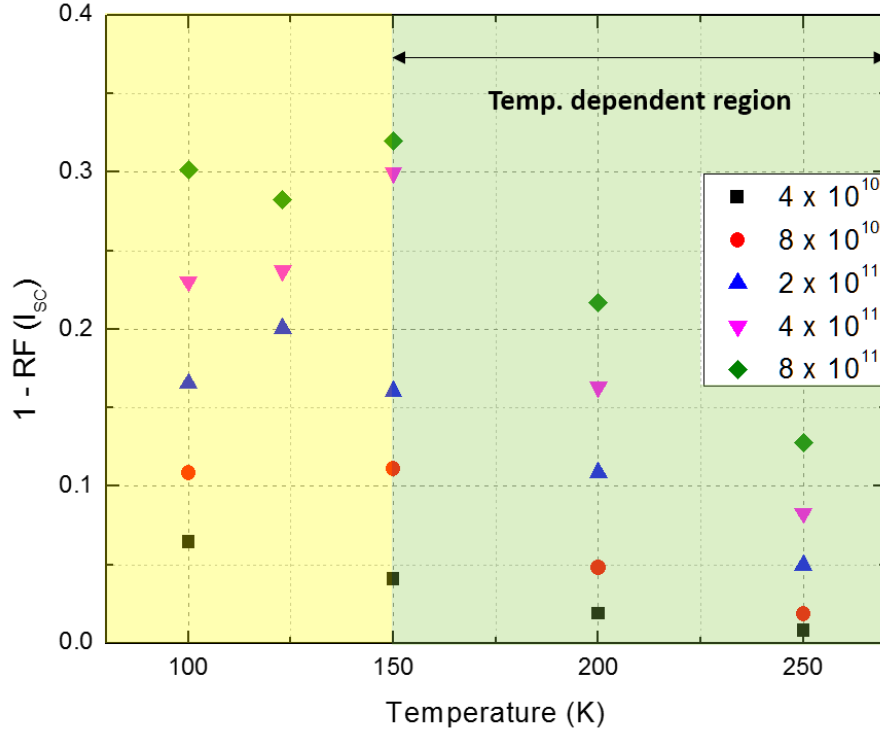


Figure 3-18.  $1 - RF(I_{sc})$  versus temperature in bottom component cells irradiated with various fluences (cm<sup>-2</sup>).

To explain this observation, the model could therefore be the following: an incoming proton produces atomic displacements, i.e. defects, along its track. Some of these defects are charged and consequently create a space charge region which can be approximated by a cylindrical volume  $V$  of radius  $r$  perpendicular to the surface of the cell. The radius  $r$  is a function of the charge  $Q$  trapped on the defects and of the doping concentration  $N$  in the material. Equality between the charge  $Q$  and the opposite charge  $NV$  developed in the space charge region makes that  $r$  is a function of  $Q$  and  $N$  at a given temperature. The space charge regions decorating the proton tracks repel the minority carriers generated by the illumination and, thus, reduce the effective active area  $S$  of the cell. Under the introduction of  $\varphi$  protons (per unit surface):

$$S = S_0 - \varphi S_0 \pi r^2 \quad (3-1)$$

where  $S_0$  the cell area, so that  $S$  can be expressed by:

$$\frac{S}{S_0} = 1 - \varphi \pi r^2 \quad (3-2)$$

The photocurrent being proportional to the active area of the cell degrades at the rate  $S/S_0$  such that:

$$1 - RF(I_{sc}) = 1 - \frac{S}{S_0} = \varphi \pi r^2 \quad (3-3)$$

The temperature dependence of  $RF(I_{sc})$  should reflect that of  $r^2$  which can be approximated by the fact that the carriers (of energy  $kT$ ) are repelled by the potential of the charge  $Q$  (proportional to  $r^{-1}$ ). Thus,  $RF(I_{sc})$  should (to first order) vary linearly with  $T^{-2}$ . Figure 3-19 illustrates that this is approximately the case when the temperature is large enough.

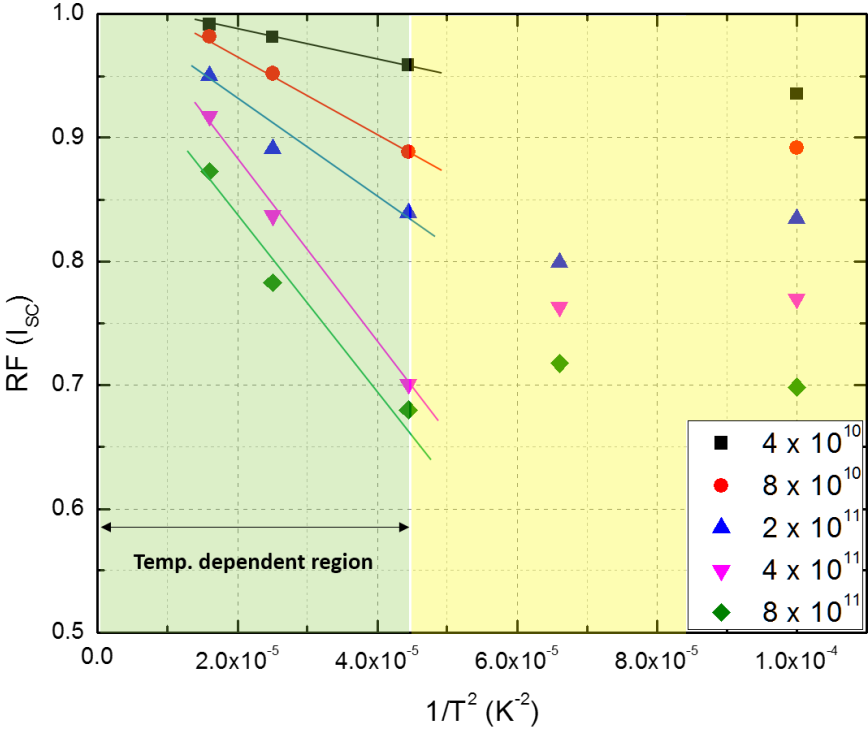


Figure 3-19.  $RF(I_{sc})$  versus  $T^{-2}$  of proton irradiated bottom component cells.

Finally, according to this picture, the degradation of  $V_{oc}$  is expected, as observed, to be small since it is not dependent on the cell area.

In conclusion, the experimental data concerning the bottom cell indicate that the degradation induced by proton irradiation at low temperature in Ge, is governed by space charged regions located around proton tracks, which implies that the resulting distribution of the induced defects is not uniform.

The bottom cell appears to become the current limiting cell below 123 K for a fluence larger than about  $10^{11} \text{ cm}^{-2}$ . Prediction of the nature of the current limiting cell versus temperature is not easy. In BOL triple – junction lattice matched cells, at 300 K and below, the top sub-cell is current limiting. Proton irradiation significantly degrade the  $I_{sc}$  of middle and bottom sub-cells resulting in the change of current limiting cell from top to middle or from top to bottom cell, depending on the temperature. The diagram of Figure 3-20 is an attempt to illustrate the expected temperature and proton fluence conditions indicating the nature of the limiting cell (note that Figure 3-20 necessitates considerably more data to be accurate).

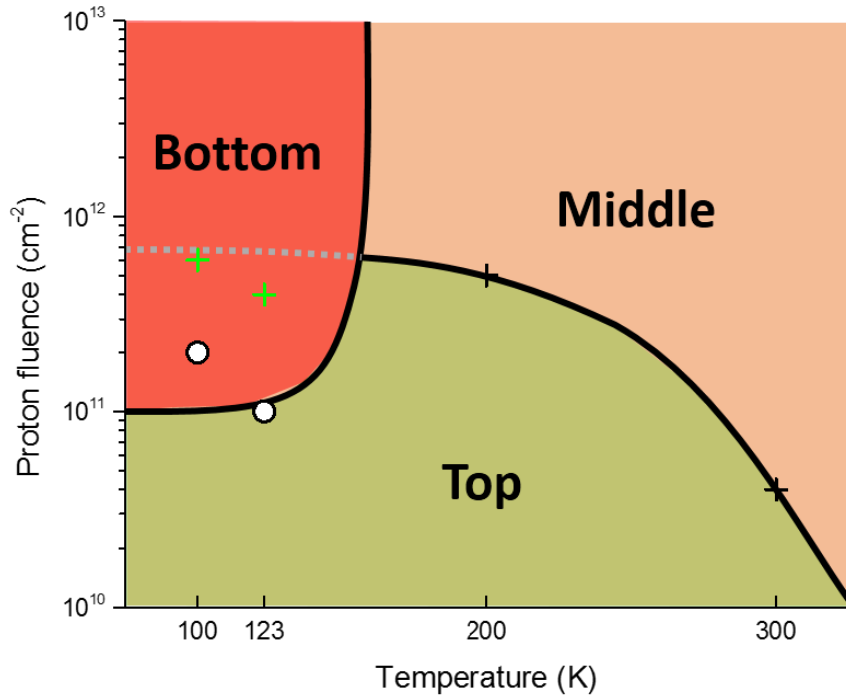


Figure 3-20. Fluence-temperature diagram indicating the regions in which a sub-cell is limiting the TJ cell: circle and cross symbols indicate transition points of current limiting from top to bottom and from top to middle sub-cell, respectively.

### 3.3.2 Recovery of proton irradiation-induced defects

The results describing the remaining factors of  $I_{SC}$ ,  $V_{OC}$  and  $P_{MAX}$  following isochronal steps are given in Figure 3-17. From the variations of  $I_{SC}$ , it can be concluded that no significant defect annealing occurs in top and middle sub-cells in the range 100 K to 300 K. Defects in top cells irradiated with protons below 300 K have not been previously investigated; only preliminary results exist for electron irradiations [27- 31]. As shown in Figure 3-4, at 100 K, decreases of 4 % of  $I_{SC}$  and few % of  $V_{OC}$  occur after the proton irradiation with a fluence of  $1.6 \times 10^{12} \text{ cm}^{-2}$ . As to the middle sub-cell, the conclusion is consistent with previous studies on electron induced defects in GaAs [32]. It has been established that in GaAs electron induced defects created at 4 K remain stable up to room temperature. No annealing stage should take place between 100 and 300 K. As to bottom cells, the annealing stages we observed could correspond to the defects detected following low temperature electron irradiation [26]. In addition, it should be noted that the proton irradiation can result in a proton implantation at the end of its trajectory, that is, 1 MeV proton is stopped in the p-type Ge bulk layer and it is possible to induce hydrogen related defects. M. Budde identified, in his thesis [33], these hydrogen related defects in Ge by means of an Infrared Absorption Spectroscopy. Three types of defects were classified:  $H_2^*$  defect, vacancy-hydrogen complexes and hydrogen-saturated self-interstitials. Among them, the  $H_2^*$  defect could be measured after the proton implantation at  $\sim 30$  K. On the other hand, the other two defects could only be observable after the sample was annealed at room temperature. The insulating area model which we have proposed

in this chapter seems to not be correlated to these hydrogen related defects since they are in principle formed at the end of proton track (no angular dependence on its size) and vacancy-hydrogen complexes and hydrogen-saturated self-interstitials are formed after room temperature annealing. Thus, at LILT condition, only possible candidate which can affect to the electrical degradation of the Ge cell is the  $H_2^*$  defect. However, it is still unclear whether the  $H_2^*$  defect is electrically active or inert.

### 3.3.3 Recombination of photo generated current by irradiation-induced defects

Besides the degradation induced by recombination of carriers generated by the illumination on the traps associated with the created defects, another type of degradation is observed, associated with the decrease of the photocurrent with increasing forward bias (see Figure 3-9 and Figure 3-10).

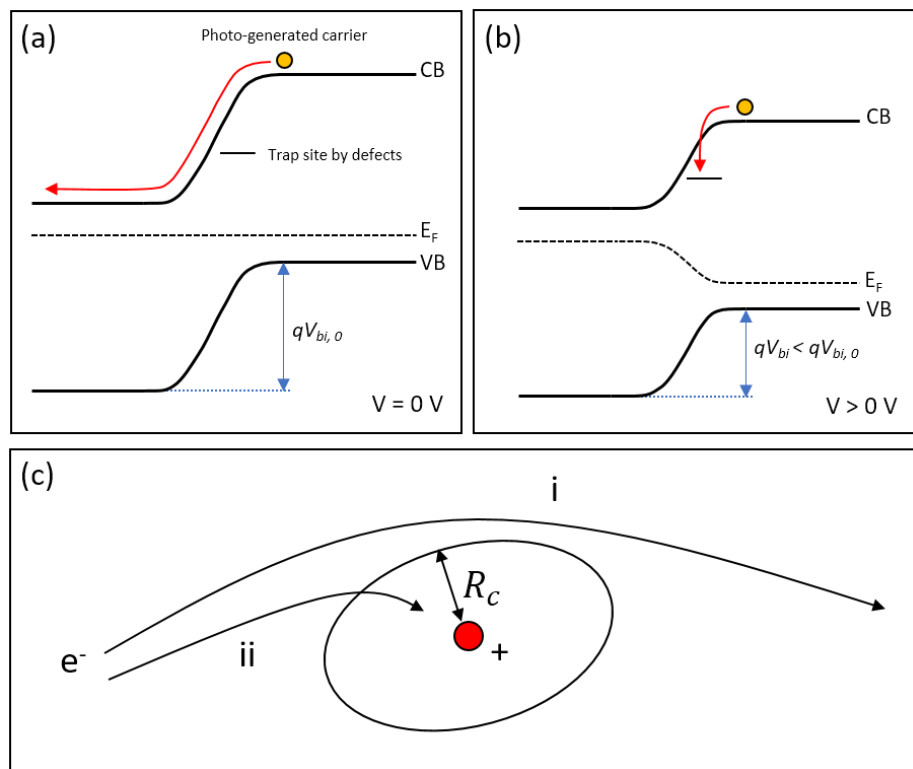


Figure 3-21. Simplified description of the electric field dependence of trap assisted recombination current ( $I_{tr}$ ) – band diagram (a) without bias, (b) positive bias and (c) a simple diagram of the electric field dependent capture rate of carriers on defects.

We understand this phenomenon as being related to the effect of electric field on the capture rate of free carriers by defects, a consequence of the increase of the capture rate of carriers on the defects via the Poole-Frenkel effect [34]. In other words, the photo-generated carrier has an enough kinetic energy to resist the coulombic attraction of a trap (defect site) induced by the irradiation when no external bias is applied ( $V = 0$  V). On the other hand, in positive biased conditions ( $V > 0$  V), the carrier contains less kinetic energy compared to the zero-biased condition (see Figure 3-21 (a) and (b)). Therefore, the

capture cross section of a minority carrier on a defect site, which results in carrier recombination and thus governs the collected photocurrent, depends on the electric field in the junction, i.e. on the applied voltage. This phenomenon, which has been treated rigorously [35], can be illustrated schematically in the following way: free carriers in a depletion region, have an energy which depends on temperature and electric field; they are captured by a defect when their energy becomes smaller than the attractive defect potential as illustrated in Figure 3-21 (c). For a Coulomb potential, the capture cross-section varies as  $V^{-2}$  so that the trap assisted recombination current  $I_{tr}$  increases with  $V$ .

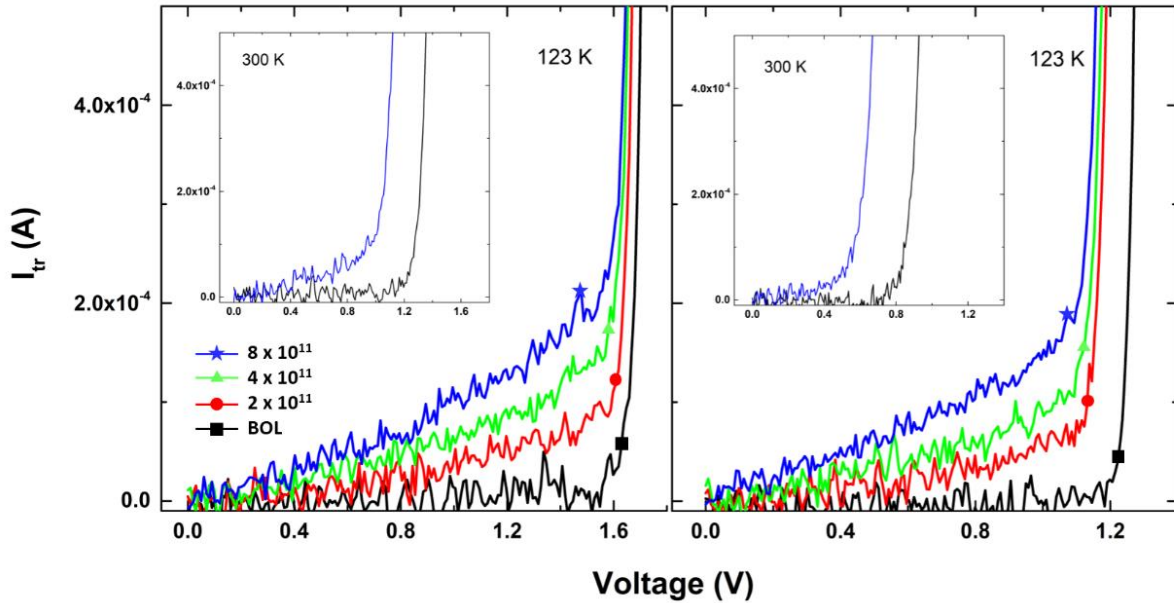


Figure 3-22. Voltage dependence of  $I_{tr}$  of top (left) and middle (right) component cells at 123 and 300 K (inset) for different fluences ( $\text{cm}^{-2}$ ).

The variation of trap assisted recombination current ( $I_{tr}$ ) as a function of  $V$  can be extracted from Figure 3-10 by subtracting a shifted DIV curve ( $I_{Dark} + I_{SC}$ ) from LIV one ( $I_{Light}$ ). We can evaluate the degradation factor induced by  $I_{tr}$  at the point where the power is maximum. The effect of irradiation fluence and temperature are shown in Figure 3-22. Apparently, the amount of  $I_{tr}$  depends on the fluence and the effect becomes smaller as the temperature increases. In the case of irradiation with a fluence of  $8 \times 10^{11} \text{ cm}^{-2}$ ,  $P_{MAX}$  predicted from the shifted DIV curve and measured from the LIV curve are about 3.00 mW and 2.71 mW for the top component cell, and 1.98 mW and 1.79 mW for the middle cell. Therefore, the degradation factor of the  $P_{MAX}$  due to this effect is about 9.7 % for the top cell and 9.6 % for the middle cell, respectively. This electric field effect is only observed in top and middle cells. This effect is not present in bottom cells since the irradiation induced defects are located in regions (cylinders around proton tracks) which do not participate to the active part of the cell.

## Conclusion of the chapter 3

We irradiated a number of TJ cells in LILT conditions to evaluate its EOL behavior for JUICE mission and associated component cells with various fluences of 1 and 2 MeV protons in the range of 100 – 300 K. Typical degradation characteristics of TJ cells in LILT conditions were described in I-V characteristics and its electrical parameters such as  $I_{SC}$ ,  $V_{OC}$ , FF and  $P_{MAX}$  were analyzed as a function of fluence.

The degradation of the current induced by the irradiation is generally due to the introduction of recombination centers but also, at low temperature, it is due to the degradation of the fill factor as a result of the electric field dependence of the capture rates of minority carriers on the defects.

From this study, we reveal that any of the three sub-cells can become the current limiting cell in the TJ cell, depending on temperature and fluence. Especially, the high degradation of the current in the bottom (Ge) cells can result in the TJ cell becoming bottom cell limited in certain EOL LILT conditions. It is the consequence of the fact that the distribution of the defects is not uniform because they are decorating the proton tracks. The result is the formation of space charge regions, repelling free carriers and the degradation is primarily due to the reduction in the active area of the cell. In addition, when the current limiting cell is switched from the top to other sub-cells due to irradiation, one should consider that the measured  $I_{SC}$  of TJ cell could be larger than the actual  $I_{SC}$  of current limiting cell since the current limiting cell in TJ cell functions in reverse voltage. Therefore, taking the minimum  $I_{SC}$  value of component cells to reconstruct the  $I_{SC}$  of TJ cell is not always consistent if the shunt resistance of current limiting cell is low.

Even though this model explains well the case of the bottom component cell, applying this model to other component cells still remains in difficulty since the angular dependence was not clear as observed from the bottom cell. Further study will be required to accomplish a concrete model explaining the degradation induced by proton at LILT conditions.

## Reference

- [1] A. W. Bett, F. Dimroth, W. Guter, R. Hoheisel, and E. Oliva, "Highest efficiency multi-junction solar cell for terrestrial and space applications," *24th European Photovoltaic Solar Energy Conference (EUPVSEC)*, Sep. 2009.
- [2] M. A. Green, K. Emery, Y. Hishikawa, W. Warta, and E. D. Dunlop, "Solar cell efficiency tables (Version 45)," *Prog. Photovolt. Res. Appl.*, vol. 23, no. 1, pp. 1–9, Dec. 2014.
- [3] M. Yamaguchi, T. Okuda, S. J. Taylor, T. Takamoto, E. Ikeda, and H. Kurita, "Superior radiation-resistant properties of InGaP/GaAs tandem solar cells," *Appl. Phys. Lett.*, vol. 70, no. 12, pp. 1566–1568, Mar. 1997.
- [4] N. Dharmarasu, M. Yamaguchi, A. Khan, T. Yamada, T. Tanabe, S. Takagishi, T. Takamoto, T. Ohshima, H. Itoh, M. Imaizumi, and S. Matsuda, "High-radiation-resistant InGaP, InGaAsP, and InGaAs solar cells for multijunction solar cells," *Appl. Phys. Lett.*, vol. 79, no. 15, pp. 2399–2401, Oct. 2001.
- [5] M. Imaizumi, T. Takamoto, and T. Sumita, "Study of radiation response on single-junction component sub-cells in triple-junction solar cells," *rd World Conference on Photovoltaic Solar Energy Conversion*, Osaka, Japan, pp. 599–602, 2003.
- [6] A. Gauffier, A. Gauffier, J. P. David, O. Gilard, J. P. David, and O. Gilard, "Analytical model for multi-junction solar cells prediction in space environment," *Microelectron. Reliab.*, vol. 48, no. 8, pp. 1494–1499, 2008.
- [7] W. Rong, L. Yunhong, and S. Xufang, "Effects of 0.28–2.80MeV proton irradiation on GaInP/GaAs/Ge triple-junction solar cells for space use," *Nucl. Instrum. Methods Phys. Res., Sect. B*, vol. 266, no. 5, pp. 745–749, 2008.
- [8] S.-I. Sato, T. Ohshima, and M. Imaizumi, "Modeling of degradation behavior of InGaP/GaAs/Ge triple-junction space solar cell exposed to charged particles," *J. Appl. Phys.*, vol. 105, no. 4, p. 044504, 2009.
- [9] D. Elfiky, M. Yamaguchi, T. Sasaki, T. Takamoto, C. Morioka, M. Imaizumi, T. Ohshima, S.-I. Sato, M. Elnawawy, T. Eldesuky, and A. Ghitas, "Study the effects of proton irradiation on GaAs/Ge solar cells," *IEEE 35th Photovoltaic Specialists Conference (PVSC)*, pp. 002528–002532, 2010.
- [10] G. Xin, F. Zhan-zu, C. Xin-yu, Y. Sheng-sheng, and Z. Lei, "Performance Evaluation and Prediction of Single-Junction and Triple-Junction GaAs Solar Cells Induced by Electron and Proton Irradiations," *IEEE Trans. Nucl. Sci.*, vol. 61, no. 4, pp. 1838–1842, Aug. 2014.
- [11] R. Hoheisel, D. Scheiman, S. Messenger, P. Jenkins, and R. Walters, "Detailed Characterization of the Radiation Response of Multijunction Solar Cells Using Electroluminescence Measurements," *IEEE Trans. Nucl. Sci.*, vol. 62, no. 6, pp. 2894–2898, Oct. 2016.
- [12] C. J. Gelderloos, K. B. Miller, R. J. Walters, G. P. Summers, and S. R. Messenger, "Low intensity low temperature performance of advanced solar cells," *IEEE 29th Photovoltaic Specialists Conference (PVSC)*, pp. 804–807, 2002.
- [13] P. Stella, G. Davis, R. Mueller, and S. Distefano, "The environmental performance at low intensity, low temperature (LILT) of high efficiency triple junction solar cells," *2nd International Energy Conversion Engineering Conference*, 2004.
- [14] P. M. Stella, R. L. Mueller, R. L. Scrivner, and R. S. Helizon, "Preliminary low temperature electron irradiation of triple junction solar cells," *th Space Photovoltaic Research and Technology*, pp. 1–7, Feb. 2007.
- [15] T. Ohshima, T. Sumita, and M. Imaizumi, "Evaluation of the electrical characteristics of III-V compounds solar cells irradiated with protons at low temperature," *IEEE 35th Photovoltaic Specialists Conference (PVSC)*, pp. 806–809, 2005.
- [16] R. D. Harris, M. Imaizumi, R. J. Walters, J. R. Lorentzen, S. R. Messenger, J. G. Tischler, T. Ohshima, S. Sato, P. R. Sharps, and N. S. Fatemi, "In Situ Irradiation and Measurement of Triple Junction Solar Cells at Low Intensity, Low Temperature (LILT) Conditions," *IEEE Trans. Nucl. Sci.*, vol. 55, no. 6, pp. 3502–3507, Dec. 2008.
- [17] C. Baur, V. Khorenko, G. Siefer, J. C. Bourgoin, M. Casale, R. Campesato, S. Duzellier, and Inguimbert V, "Development status of triple-junction solar cells optimized for low intensity

- low temperature applications,” *IEEE 39th Photovoltaic Specialists Conference (PVSC)*, pp. 3237–3242, 2013.
- [18] J. C. Bourgoin, B. Boizot, K. Khirouni, and V. Khorenko, “On the Prediction of Solar Cell Degradation in Space,” *10th European Space Power Conference (ESPC)*, vol. 719, p. 1, Aug. 2014.
- [19] S. Taylor, C. Baur, T. Torunski, V. Khorenko, G. Strobl, R. Campesato, R. Hoheisel, M. Hermle, F. Dimroth, D. Stetter, K. Dettlaff, J. Bourgoin, S. Makham, and G. Sun, “Performance of European Triple-Junction Solar Cells for Deep Space Missions,” vol. 661, pp. 34–39, Sep. 2008.
- [20] C. Baur, V. Khorenko, G. Siefer, V. Inguibert, S. Park, B. Boizot, J. C. Bourgoin, M. Casale, R. Campesato, H.-G. Schnell, A. Gerhard, P. Zanella, E. Ferrando, X. Reutenauer, E. Bongers, and A. Gras, “Status of Solar Generator Related Technology Development Activities Supporting the Juice Mission,” *E3S Web Conf.*, vol. 16, no. 8, pp. 04005–8, May 2017.
- [21] G. P. Summers, E. A. Burke, P. Shapiro, S. R. Messenger, and R. J. Walters, “Damage correlations in semiconductors exposed to gamma, electron and proton radiations,” *IEEE Trans. Nucl. Sci.*, vol. 40, no. 6, pp. 1372–1379, 1993.
- [22] D. C. Marvin and J. C. Nocerino, “Evaluation of multijunction solar cell performance in radiation environments,” presented at the Conference Record of the IEEE Photovoltaic Specialists Conference, 2000, vol. 2000, pp. 1102–1105.
- [23] J. F. Ziegler, M. D. Ziegler, and J. P. Biersack, “SRIM – The stopping and range of ions in matter (2010),” *Nuclear Inst. and Methods in Physics Research, B*, vol. 268, no. 11, pp. 1818–1823, Jun. 2010.
- [24] C. Baur, M. Meusel, F. Dimroth, and A. W. Bett, “Investigation of Ge component cells,” *IEEE 31st Photovoltaic Specialists Conference (PVSC)*, pp. 675–678, 2005.
- [25] P. Singh and N. M. Ravindra, “Temperature dependence of solar cell performance—an analysis,” *Sol. Energy Mater. Sol. Cells*, vol. 101, no. C, pp. 36–45, Jun. 2012.
- [26] J. C. Bourgoin, P. M. Mooney, and F. Poulin, “Defects and Radiation Effects in Semiconductors,” presented at the Inst. Phys. Conf. Ser., 1980, vol. 59, p. 33.
- [27] M. A. Zaidi, M. Zazoui, and J. C. Bourgoin, “Defects in electron irradiated GaInP,” *J. Appl. Phys.*, vol. 73, no. 11, pp. 7229–7231, 1993.
- [28] A. Khan, A. Khan, M. Yamaguchi, M. Yamaguchi, T. Takamoto, N. de Angelis, T. Takamoto, and J. C. Bourgoin, “Recombination centers in electron irradiated GaInP: application to the degradation of space solar cells,” *J. Cryst. Growth*, vol. 210, no. 1, pp. 264–267, 2000.
- [29] A. Khan, M. Yamaguchi, J. C. Bourgoin, J. C. Bourgoin, and T. Takamoto, “Thermal annealing study of 1 MeV electron-irradiation-induced defects in n+p InGaP diodes and solar cells,” *J. Appl. Phys.*, vol. 91, no. 4, pp. 2391–2397, 2002.
- [30] A. Khan, M. Yamaguchi, N. Dharmaso, J. Bourgoin, K. Ando, and T. Takamoto, “Deep Level Transient Spectroscopy Analysis of 10 MeV Proton and 1 MeV Electron Irradiation-Induced Defects in p-InGaP and InGaP-based Solar Cells,” *Jpn. J. Appl. Phys.*, vol. 41, no. 3, pp. 1241–1246, Mar. 2002.
- [31] N. Dharmarasu, M. Yamaguchi, J. C. Bourgoin, T. Takamoto, T. Ohshima, H. Itoh, M. Imaizumi, and S. Matsuda, “Majority- and minority-carrier deep level traps in proton-irradiated n+/p-InGaP space solar cells,” *Appl. Phys. Lett.*, vol. 81, no. 1, pp. 64–66, Jul. 2002.
- [32] D. Pons and J. C. Bourgoin, “Irradiation-induced defects in GaAs,” *J. Phys. C: Solid State Phys.*, vol. 18, no. 20, pp. 3839–3871, 1985.
- [34] M. Budde, “Hydrogen-related defects in proton-implanted silicon and germanium”, PhD thesis at Aarhus Center for Atomic Physics, Institute of Physics and Astronomy, University of Aarhus, Denmark, 1998.
- [33] M. A. Zaidi, J. C. Bourgoin, and H. Maaref, “Poole-Frenkel-assisted emission from deep levels in electron-irradiated germanium,” *Semicond. Sci. Technol.*, vol. 4, no. 9, pp. 739–742, Sep. 1989.
- [34] G. Vincent, A. Chantre, and D. Bois, “Electric field effect on the thermal emission of traps in semiconductor junctions,” *J. Appl. Phys.*, vol. 50, no. 8, pp. 5484–5487, 1979.

# ***4 Electron irradiation***

4.1	Irradiation of TJ cells in LILT conditions.....	120
4.1.1	Analysis of I-V characteristics before and after 1 MeV electron irradiations .....	121
4.1.2	Degradation of key parameters in TJ cells .....	125
4.2	Approach to the component cells.....	126
4.2.1	Degradation of $I_{SC}$ and $V_{OC}$ at different temperatures .....	126
4.2.2	The excess leakage current in dark I-V characteristics.....	128
4.3	Annealing effect of electron irradiated cells .....	133
4.4	Discussion of the chapter 4 .....	134
4.4.1	Uncertainty of the TJ cell degradation induced by electron irradiations .....	134
4.4.2	Origin of the excess current.....	135
	Conclusion of the chapter 4.....	136
	Reference.....	138

Previously, in the chapter 3, we have mainly focused on the proton irradiation effect on TJ cells and its component cells. In this chapter, we will present the analysis of electrical properties of TJ cells and its component cells under 1 MeV electron irradiation at different temperatures. Beginning Of Life (BOL) and End Of Life (EOL) I-V characteristics in dark (DIV) and under illumination (LIV) at different temperatures will be described, together with P-V characteristics (PV). Furthermore, fluence dependences of electrical parameters (short circuit current  $I_{SC}$ , open circuit voltage  $V_{OC}$ , maximum power  $P_{MAX}$ , and fill factor FF) and annealing properties of each component cell will be described. Especially in this chapter, we will discuss the distribution of EOL performance of TJ cells which is not observed in the case of proton irradiation.

## 4.1 Irradiation of TJ cells in LILT conditions

Solar cells degrade in space because they are submitted to irradiation with energetic particles, mostly electrons and protons. Especially, the electrons with more than several MeV of the energy can easily penetrate the cover glass and induce a damage in active regions of the solar cells. These electrons produce lattice displacements, resulting in the creation of electrically active defects [1]. Some of these defects play the role of minority carriers traps, thus inducing the recombination of electron-hole pairs [2] which are then not collected by the junction and consequently decrease the cell efficiency [3]. Defect introduction is well documented for irradiations performed at room temperature for most of the materials such as Si [4], GaAs [5], [6], GaInP [7], [8] and Ge [9]-[11], which are used in the production of solar cells. Concerning low temperature irradiations, information exists on defects in GaAs [5], to a less extent in Ge and practically none in GaInP.

Meanwhile, in a device level, as we discussed briefly in the previous chapter, dealing degradation induced by proton irradiation, the past studies of the degradation of these cells have been limited to irradiations around room temperature [12]-[14] and extrapolations in LILT conditions were obtained by measuring at low temperature cells irradiated at room temperature, with the exception of one attempt [15], [16]. Preliminary results [17]-[20] seemed to suggest that the behavior at low temperature of these cells was rather similar for irradiations performed at low temperature and for room temperature irradiations. However, recent observations showed that the degradation by electron irradiation of TJ cells is larger than expected if it was only ascribed to the introduction of recombination centers by the irradiation.

#### 4.1.1 Analysis of I-V characteristics before and after 1 MeV electron irradiations

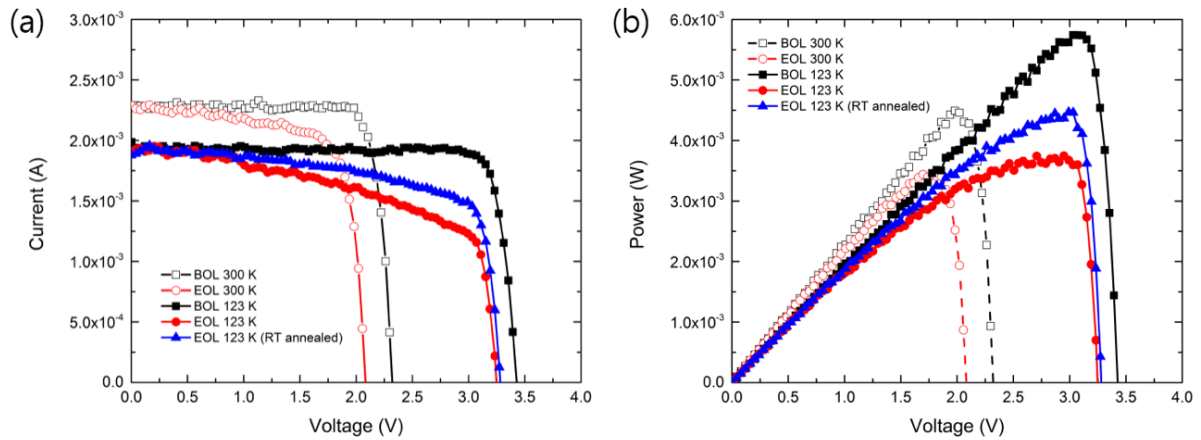


Figure 4-1. BOL and EOL (after 1 MeV electron irradiation at 123 K with  $3 \times 10^{15} \text{ cm}^{-2}$ ) electrical properties of 1295-0443E-26 TJ solar cell at 123 and 300 K under illumination: (a) I-V curves and (b) P-V curves.

Figure 4-1 shows BOL and EOL LIV and PV of a cell (#:1295-0443E-26) irradiated at 123 K for a fluence of  $3 \times 10^{15} \text{ cm}^{-2}$ , measured at 123 and 300 K. The measurement was carried out right after the irradiation, then we measured LIV and DIV at different 5 minutes steps to verify whether the cell was stabilized or not. Most of cells showed any changes of the electrical performance after 30 minutes of stabilization at 123 K. In this work, the EOL values represent the values measured after 30 minutes annealing at LILT conditions (also called as low temperature annealing, LA). At 123 K, as shown in Table 4-1, at 123 K,  $I_{SC}$  value wasn't changed before and after irradiation at  $3 \times 10^{15} \text{ cm}^{-2}$ . But as we will discuss later, the degradation of  $I_{SC}$  could occur in particular TJ cells. The change of  $I_{SC}$  changes after 1 MeV electron irradiation was also observed from certain TJ cells during the measurements at 300 K. By contrast,  $V_{OC}$  values decreased from 3.427 to 3.247 V at 123 K, and when the TJ solar cells were annealed at room temperature (RA), we observed that the  $V_{OC}$  value was recovered up to 3.281 V ( $dV = 34 \text{ mV}$ ). The annealing of  $V_{OC}$  at 300 K was too small to increase  $P_{MAX}$  of the cell (expected around 1 % of contribution to the recovery). Meanwhile, one can observe that, in general,  $V_{OC}$  degraded more at 300 K than at 123 K. If we consider now the FF and  $P_{MAX}$  changes in the TJ cells after 1 MeV electron irradiation (see Figure 4-1 (b)), it is clearly seen that more important changes occurred in both LT (123 K) and RT (300 K) measurements. Especially, the contribution of FF to the degradation of  $P_{MAX}$  was bigger at 123 K than at 300 K. Moreover, after RT annealing, we could see that the  $P_{MAX}$  was recovered by 20 % at 123 K, which is mainly the result of the FF recovery (18 %). (Here, the recovery was calculated by dividing  $EOL - EOL \text{ RA}$  into EOL value.) This observation implies that the in-situ measurement at 123 K after electron irradiation is important to correctly measure the performance of the cell at LILT conditions.

Table 4-1. Degradation measured at 123 and 300 K of  $I_{SC}$ ,  $V_{OC}$ , FF,  $P_{MAX}$  of 1 MeV electron irradiated TJ cell at 123 K ( $3 \times 10^{15} \text{ cm}^{-2}$ ).

	123 K (LT)			300 K (RT)	
	BOL	EOL	EOL RA	BOL	EOL
$I_{SC}$ (mA)	1.93	1.93	1.93	2.28	2.27
$V_{OC}$ (mV)	3.427	3.247	3.281	2.321	2.083
FF (%)	86.9	59.8	70.7	85.0	72.7
$P_{MAX}$ (mW)	5.74	3.75	4.47	4.49	3.44

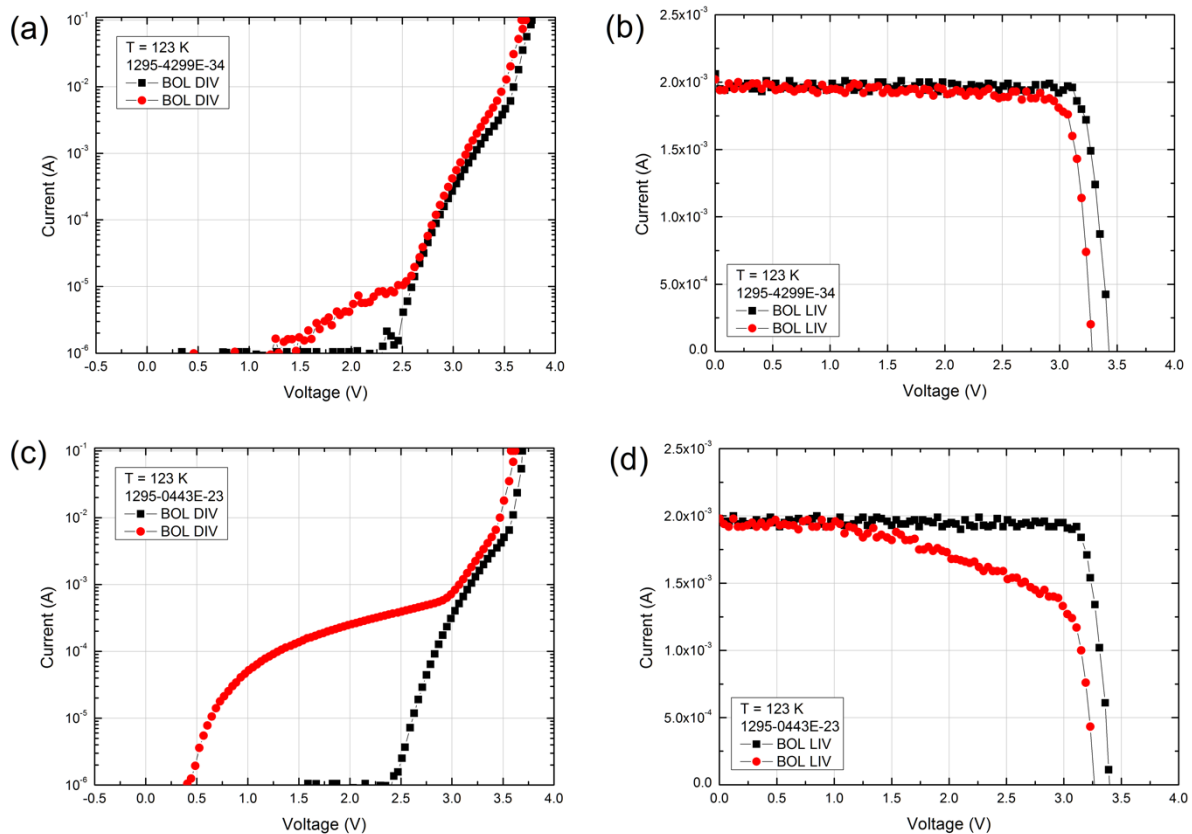


Figure 4-2. BOL and EOL I-V characteristics in dark (log scale) and under illumination of two TJ cells at 123 K: 1295-4299E-34 (a and b) and 1295-0443E-23 (c and d).

To investigate the origin of this effect, we analyzed LIV and DIV of TJ cells (#: 1295-4299E-34 and 1295-0443E-23) which were irradiated with a fluence of  $1.5 \times 10^{15} \text{ cm}^{-2}$  at 123 K (see Figure 4-2). The DIV graphs are described in  $\log(I)$  versus  $V$  to check a change of diode property of the cells more easily after the irradiation. Due to the sensitivity limit, we could only measure the dark current above the  $10^{-6}$  A. In case of the cell 1295-4299E-34, we observed that the dark current is increased nearly up to  $10^{-5}$  A at 2 V. Such kind of increase in dark current now will be called as excess (leakage) current or excess dark current. However, the amount of the excess current in the cell 1295-4299E-34 is too low to affect to the degradation of LIV characteristics of the cell. On the other hand, even though the cells were irradiated with smaller amount of fluence ( $1.5 \times 10^{15} \text{ cm}^{-2}$ ) than the cell #: 1295-0443E-26 (the fluence

of  $3 \times 10^{15} \text{ cm}^{-2}$ ), a significant amount of an excess current was measured in EOL DIV compared to the BOL one of the cell 1295-0443E-23 as shown in Figure 4-2 (c). Within our measurement limit, we started to observe the difference between BOL and EOL DIV from 0.5 V, and this excess dark current rapidly increased. When this current passed the current level of  $10^{-4} \text{ A}$  at around 1.3 V, the effect of excess dark current was actually reflected to the LIV curve. Since this excess current kept increasing nearly to  $10^{-3} \text{ A}$ , it resulted in a significant  $P_{\text{MAX}}$  degradation near at 2.8 V. In this kind of case, the excess current on the DIV curves could have a significant role of the deterioration of solar cell performance because it induces additional degradation in the LIV results.

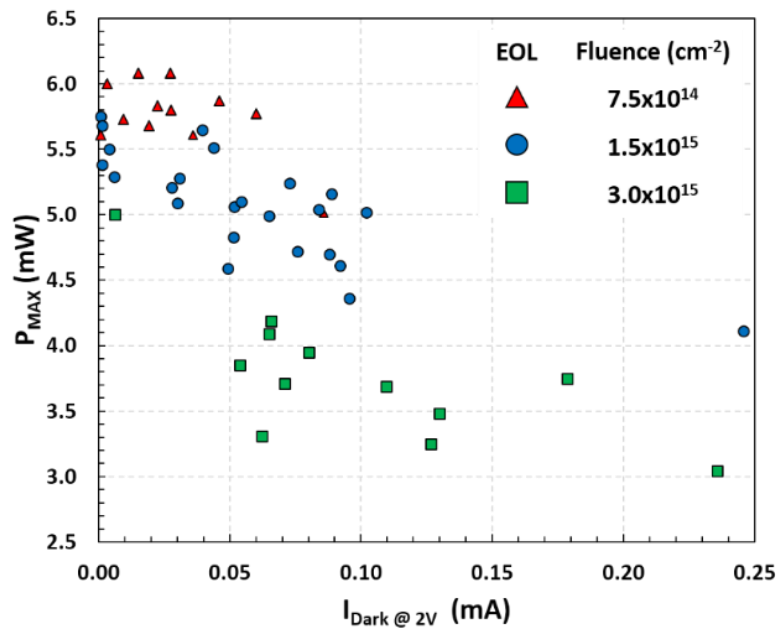


Figure 4-3. Relationship between  $I_{\text{Dark}}$  at 2 V and  $P_{\text{MAX}}$  of each electron irradiated TJ cell at 123 K

In fact, through a number of irradiation test at three different fluences, we found that the distribution of excess current in dark is from few  $10^{-6}$  to  $10^{-4} \text{ A}$  (two order of magnitude) in case of electron irradiation, which was not observed from the proton irradiation test. Since  $P_{\text{MAX}}$  value was directly affected by the amount of the excess current, a quantitative analysis was additionally carried out. Figure 4-3 shows the relationship between excess leakage current in dark measured at 2 V ( $I_{\text{Dark}}$ ) and  $P_{\text{MAX}}$  of entire electron irradiated TJ cells. The cells were irradiated and measured at 123 K. The cells irradiated with a fluence of  $7.5 \times 10^{14} \text{ cm}^{-2}$  have  $P_{\text{MAX}}$  value between 5.5 to 6 mW (except for one cell of 5 mW with 0.9 mA of excess current). We can see that the  $P_{\text{MAX}}$  is not directly influenced by the excess current even if it exceeds 0.05 mA since the amount of the excess current is still too small compared to the photo current. However, for the cells irradiated with a fluence of  $1.5 \times 10^{15} \text{ cm}^{-2}$ , we could see a larger spread of  $P_{\text{MAX}}$  (from 4.1 to 5.8 mW). The spread of data became even worse in the case of the fluence of  $3 \times 10^{15} \text{ cm}^{-2}$ . The amount of  $I_{\text{Dark}}$  varied from 0.01 to 0.24 mA. As a result, the variation of  $P_{\text{MAX}}$  value was also huge from 3 to 5 mW. We found that normally the degradation of  $P_{\text{MAX}}$  due to the distortion of I-V curve occurs from certain amount of fluence (in case of our study, this was  $1.5 \times 10^{15} \text{ cm}^{-2}$ ). Furthermore, Uncertainty of the prediction of the EOL performance is increased as we increased the fluence.

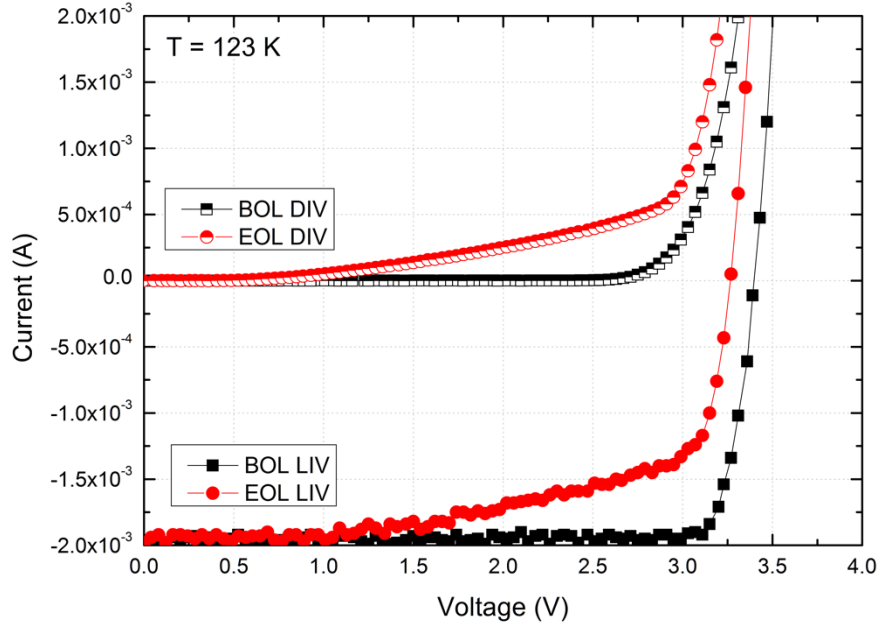


Figure 4-4. BOL and EOL I-V characteristics in dark and under illumination of a 1295-0443E-23 TJ cell at 123 K, irradiated with 1MeV electrons.

Figure 4-4 shows BOL and EOL I-V characteristics in dark and under illumination of a TJ cell (1295-0443E-23) at 123 K in linear scale. As shown, the shape of BOL and EOL curve looks similar each other. It is because the solar cell approximately follows the superposition principle (only when the voltage dependence of photo generated current is small). Thus, we can simply assume that the photo generated current is equally added to the dark current. An increase of the slope of EOL dark current from around 0.7 V is therefore the reason of the degradation of the TJ cell because the dark current corresponds to a decrease of the photocurrent in the voltage region where the power is maximum. Thus, when the excess leakage current becomes higher than the current of  $10^{-4}$  A, one can start to observe non-negligible decrease of the photocurrent in the linear scale LIV resulting in a significant degradation of  $P_{MAX}$ .

Indeed, the BOL and EOL  $P_{MAX}$  of the 1295-0443E-23 TJ cell are  $P_{MAX,BOL} = 5.98$  mW and  $P_{MAX,EOL} = 4.11$  mW, respectively. If we assume that  $P_{MAX,EOL}$ , corresponding to minority carrier recombination, is only deduced (assuming no change in the fill factor) from the small  $I_{SC}$  and  $V_{OC}$  changes after irradiation, it is of the order of 5.7 mW. Indeed, the dark current significantly affects the maximum power. According to K. C. Reinhardt et al. [21],  $P_{MAX}$  is related to the short circuit current ( $I_{SC}$ ) and the dark current at maximum power ( $I_{dMAX}$ ) through the following relation:

$$P_{MAX} = (I_{SC} - I_{dmax}) \left( \frac{nk_B T}{q} \right) \ln \left( \frac{I_{dMAX}}{I_0} \right) \quad (4-1)$$

where  $n$  and  $I_0$  are ideality factor and reverse saturation current, respectively. By this equation, as the cell exhibits higher  $I_{dMAX}$ , its maximum power will be smaller. And the effect of  $I_{dMAX}$  is especially

critical when  $I_{SC}$  is sufficiently small like in the LILT conditions where the light intensity is extremely low. Therefore, the control of this excess current is of prime importance for mastering the degradation since the maximum power is directly related to its amplitude.

### 4.1.2 Degradation of key parameters in TJ cells

In the LILT conditions (AM0 3.7 %, 123 K), 48 TJ cells were irradiated varying fluences from  $7.5 \times 10^{14}$  to  $3 \times 10^{15} \text{ cm}^{-2}$ . From each sample, main parameters such as  $I_{SC}$ ,  $V_{OC}$ ,  $I_{SC} \times V_{OC}$ , FF, and  $P_{MAX}$  were extracted and then average values and standard deviations were calculated. In fact, BOL characteristics can be slightly different from cell to cell due to the homogeneity issue as already discussed in the chapter 2. So, the absolute comparison can induce some errors. Thus, to analyze the relative change by the irradiation, we calculated so called remaining factors RF (divide EOL values by BOL ones) for  $I_{SC}$ ,  $V_{OC}$ ,  $I_{SC} \times V_{OC}$ , FF, and  $P_{MAX}$ . The RF of each parameter versus fluence is presented in Figure 4-5.

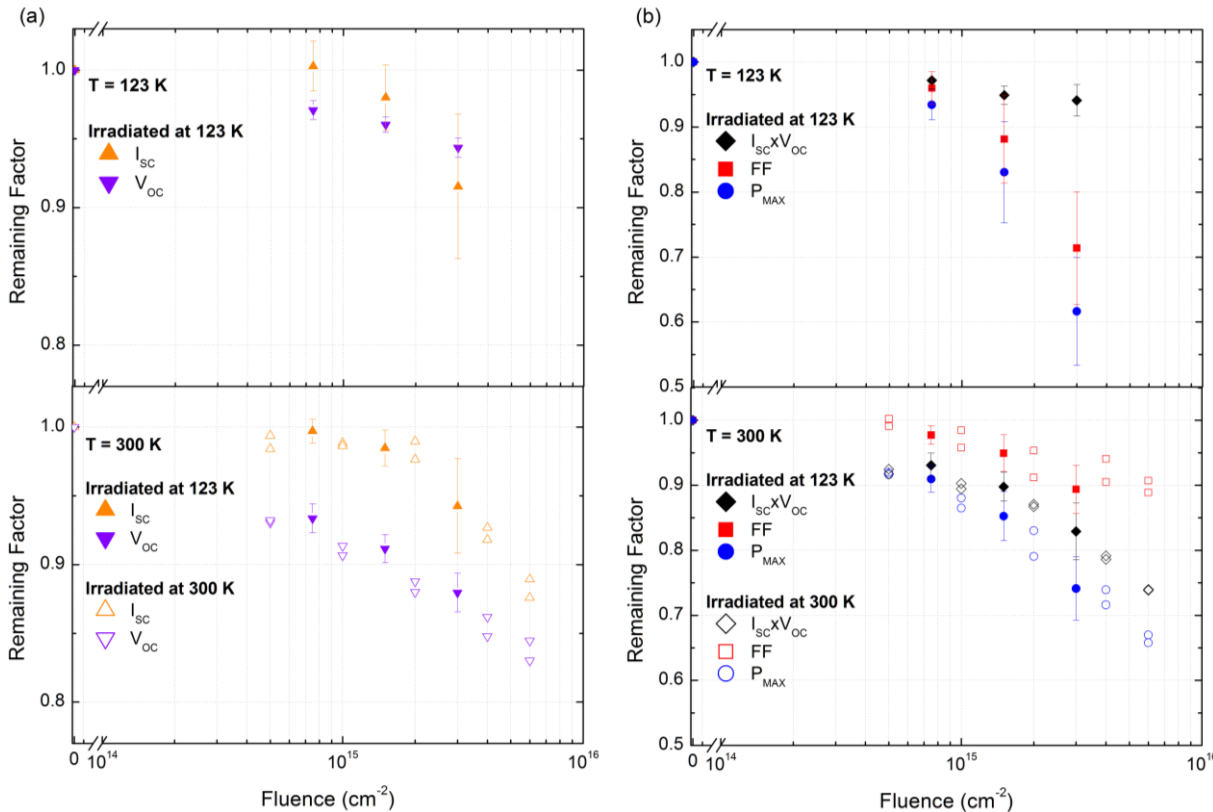


Figure 4-5. Remaining factor of (a)  $I_{sc}$ ,  $V_{oc}$ , (b)  $I_{sc} \times V_{oc}$ , FF,  $P_{MAX}$  of TJ solar cells at 123 and 300 K.

The data measured at 300 K from the same cells are also presented. In addition, data from two TJ cells irradiated at 300 K at different fluences are added to compare with LT irradiated, but RT measured ones. As one can see, either the cell is irradiated at LT or at RT, once the cell is measured at RT at the end, the cell exhibits a similar degradation trend. This result implies that when the cell is heated up, it loses its intrinsic property which can only be observed at LT. Therefore, measuring the I-V characteristics of a cell at higher temperature than the temperature where the cell is irradiated can cause a

misunderstanding of the cell electrical properties. In this regard, the in-situ LILT measurement is important for the analysis of irradiation effects for a deep space mission.

At 123 K, when the cells are irradiated with the lowest fluence of  $7.5 \times 10^{14} \text{ cm}^{-2}$ , average  $I_{SC}$  value does not change. It seems that the fluences less than about  $7.5 \times 10^{14} \text{ cm}^{-2}$  are too low to create a significant number of defects leading to minority carrier recombination. However, as one can see the error margin of the value, the degradation of  $I_{SC}$  depends much on the cell number. There is a certain amount of uncertainty in the EOL performances. In addition, this error margin becomes higher at higher fluences. Meanwhile, the rate of degradation of  $I_{SC}$  seems to increase for a fluence of about  $3 \times 10^{15} \text{ cm}^{-2}$ , suggesting that the mechanism of degradation has been changed. On the contrary,  $V_{OC}$  is in average degraded down to 96 % from its BOL value even after the irradiation with a fluence of  $7.5 \times 10^{14} \text{ cm}^{-2}$ , and the overall degradation trend is similar from cell to cell. Thus, we observe relatively low error margins than the case of  $I_{SC}$ . Beside the degradation of  $I_{SC}$  and  $V_{OC}$ , the degradation of  $P_{MAX}$  appears larger than the product  $I_{SC} \times V_{OC}$  (see Figure 4-5 (b)), which implies that an additional phenomenon, other than the recombination of photo-carriers on the defects [22], [23], participates to the degradation. Owing to the large scatter of this effect induced on  $P_{MAX}$ , it seems to be not well controlled. In fact, the degradation behavior of  $P_{MAX}$  mostly originates from the degradation of FF. We can clearly see the effect of FF on  $P_{MAX}$ , that is, as the fluence increases, the both of FF and  $P_{MAX}$  exhibits significant drop of RF and the error margin becomes larger.

However, when the temperature goes up to 300 K, TJ cells behave differently. First, the rate of degradation of  $V_{OC}$  becomes higher at 300 K compared to at 123 K and therefore to an increase of the degradation due to  $I_{SC} \times V_{OC}$ . On the other hand, the relative FF degradation at 300 K is less than the one observed at 123 K, and it shows a smaller scatter at 300 K. However, the degradation under electron irradiation of  $P_{MAX}$  at 300 K remains smaller than the one analyzed in LILT conditions. Real Predictions of solar cells in space conditions around Jupiter must take therefore into account both irradiation and IV measurements at low temperature.

## 4.2 Approach to the component cells

### 4.2.1 Degradation of $I_{SC}$ and $V_{OC}$ at different temperatures

To understand the results of electron irradiated TJ cells with more details, especially for the low temperature, we performed additional irradiations with GaInP, GaAs and Ge component cells in the same way of the case of the proton irradiation. Figure 4-6 shows the dependences of  $V_{OC}$  and  $I_{SC}$  measured as a function of the integrated fluence for irradiations performed at temperatures ranging from 100 to 300 K (the cells were measured at its irradiation temperature).

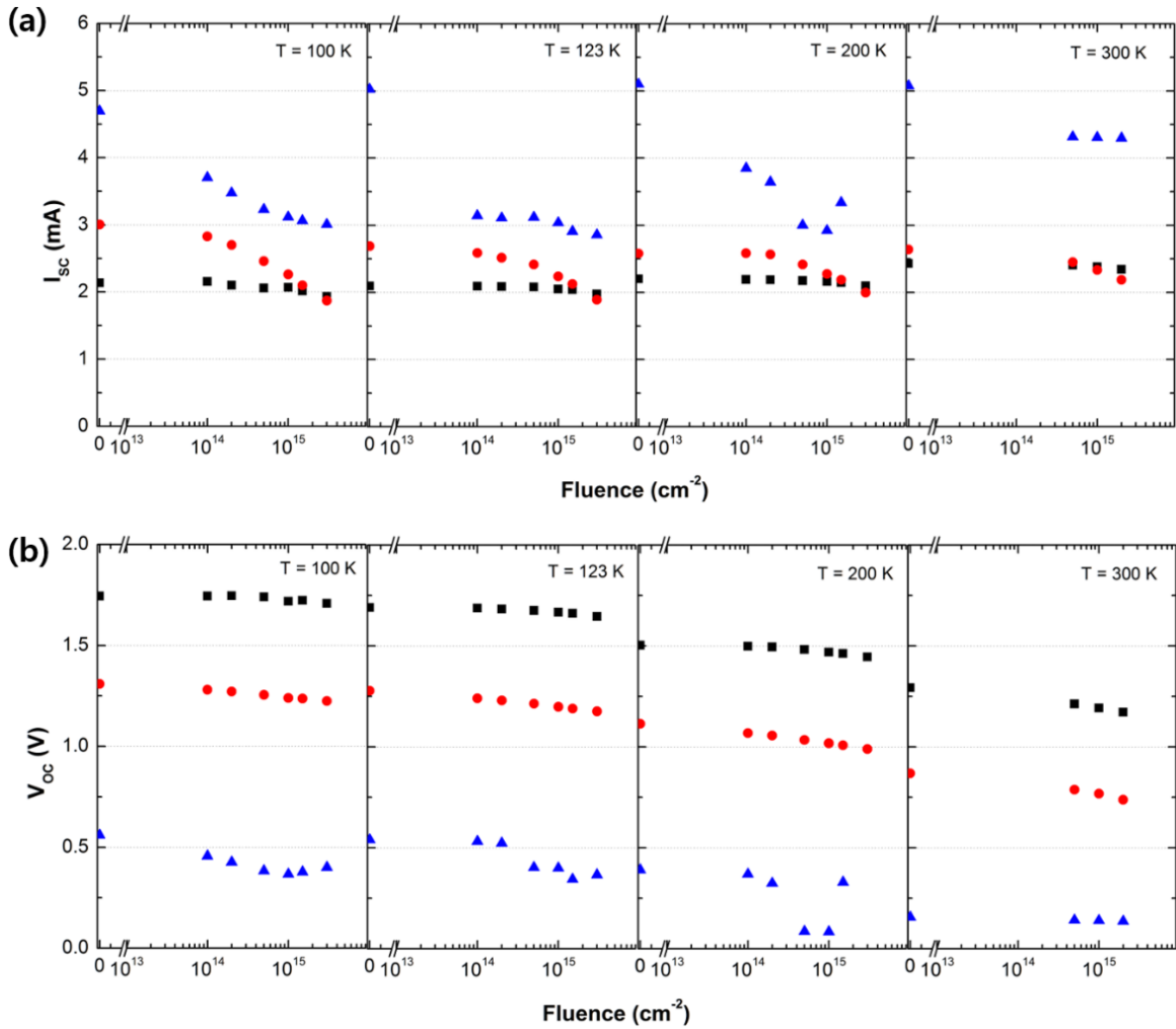


Figure 4-6.  $I_{sc}$  and  $V_{oc}$  versus fluence of top (black square), middle (red circle), bottom (blue triangle) component cells at 100, 123, 200 and 300 K.

In BOL condition, GaInP top cell exhibits a steady decrease of its  $I_{sc}$  value approximately from 2.43 to 2.14 mA when temperature decreases from 300 to 100 K. Meanwhile, the  $I_{sc}$  of top cell shows strong radiation hardness at all fluences and irradiation temperatures. Comparing BOL values to last EOL ones ( $2$  or  $3 \times 10^{15}$   $\text{cm}^{-2}$ ), the change of  $I_{sc}$  is only 4 to 10 %. For the middle GaAs cell, BOL  $I_{sc}$  increases from around 2.64 to 3.0 mA when the cell is cooled down from 300 to 100 K. Different from the case of top cell, the rate of  $I_{sc}$  degradation becomes higher as the irradiation temperature decreases. For example, at 200 K,  $I_{sc}$  of middle cell became 2 mA from 2.58 mA when irradiated with a fluence of  $3 \times 10^{15}$   $\text{cm}^{-2}$  while it decreased from 3 to 1.87 mA at 100 K. As a consequence, even though the BOL  $I_{sc}$  value becomes high at low temperature, change of the current limiting cell occurs always between fluences of  $1.5$  and  $3 \times 10^{15}$   $\text{cm}^{-2}$ . Meanwhile,  $I_{sc}$  of a BOL Ge bottom cell is about 5 mA at 300 K, and the  $I_{sc}$  value is decreased to about 4.3 mA after a first irradiation with a fluence of  $5 \times 10^{14}$   $\text{cm}^{-2}$ . Once the first irradiation is finished, the  $I_{sc}$  values don't decrease further even if the cell is again irradiated until  $2 \times 10^{15}$   $\text{cm}^{-2}$ . However, in case of low temperature irradiations 100, 123 and 200 K considered in our study,  $I_{sc}$  value of bottom cell starts to degrade as a function of fluence. In fact, we irradiated bottom

cells from two different batches; one for 100 K, the other for other temperatures. Besides, bottom cells exhibited instant recovery after irradiation. This fast recovery required us to stabilize the EOL bottom cells after each irradiation step at each temperature (100, 123, and 200 K) for 10 minutes.

At 300 K, it is clear that the degradation of  $V_{OC}$  values of TJ cell is mainly due to the top cell (1.293 to 1.172 V,  $dV = 121$  mV) and the middle cell (0.869 to 0.737,  $dV = 132$  mV). The  $V_{OC}$  value of bottom cell is changed only from 0.156 to 0.136 V,  $dV = 20$  mV (Cells were irradiated with a fluence of  $2 \times 10^{15}$   $\text{cm}^{-2}$ ). However, as the temperature becomes lower,  $V_{OC}$  value of top and middle cells degrades less than at the higher temperature. In addition, contribution of the bottom cell to the degradation of  $V_{OC}$  increases at lower temperature. At 100 K,  $dV$  values of  $3 \times 10^{15}$   $\text{cm}^{-2}$  EOL top, middle and bottom cells are 36, 84 and 159 mV, respectively. This result corresponds to the fact that TJ cells exhibit less degradation of  $V_{OC}$  at 123 K (3.45 V  $\rightarrow$  3.25 V) than at 300 K (2.6 V  $\rightarrow$  2.1 V) as already presented in Figure 4-5 (a). As previously mentioned, the bottom component cell exhibits unstable electrical characteristics at low temperature, especially when it is just irradiated. The phenomenon which is typically observed after the electron irradiation is the recovery of  $V_{OC}$ . Detailed analysis on the recovery of the electrical performance will be discussed in the chapter 4.3.

#### 4.2.2 The excess leakage current in dark I-V characteristics

Like we already observed the appearance of excess current in the DIV curves of electron irradiated TJ cells, the same phenomenon occurred from all types of component cells as shown in Figure 4-7. In general, the bottom component cell has already three or four order of magnitude greater amount of dark current than other two component cells even in BOL condition. (But BOL performance of bottom cells is different depending from batch to batch and from cell to cell as discussed in the chapter 2.) The BOL bottom cells appear to have the dark current from  $10^{-6}$  to  $10^{-4}$  A (depending on its working voltage) before the thermal current starts to increase. When the bottom cell is irradiated with a fluence of  $3 \times 10^{15}$   $\text{cm}^{-2}$ , the EOL dark current is one order of magnitude greater than its BOL value while the degradation of the thermal current is relatively small. As to the top and middle component cells, BOL dark current of two cells is in the level of  $10^{-9}$  A at close to  $V = 0$ , then it goes up to  $10^{-7}$  A as the voltage increases.

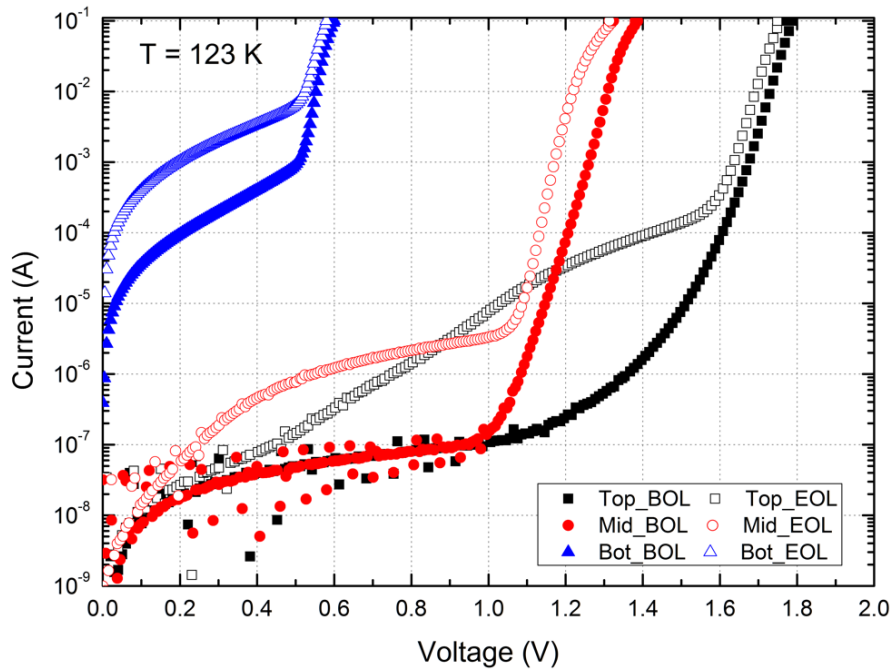


Figure 4-7. I-V characteristics of component cells before and after electron irradiation at 123 K. Appearance of excess currents from all component cell after irradiation with a fluence of  $3 \times 10^{15} \text{ cm}^{-2}$ .

When the component cells were irradiated, one can typically observe the degradation of thermal current. The middle cell showed more degradation of the thermal current. This results from that defects, which act as compensating centers in each doping layer and junction, reduce the doping effect so that the built-in voltage which is directly related to  $V_{OC}$  is decreased. At 123 K, the top cell is less affected than the middle and the bottom cells. In addition, one can also observe the excess dark current from the top and the middle cells. However, the extent of increase of the excess current was higher in the top cell than in the middle cell. The magnitude of the excess current of top cell increased up to near  $10^{-4} \text{ A}$  where it can affect to the  $P_{MAX}$  degradation whereas that of the middle cell is generally limited under  $10^{-5} \text{ A}$ .

Overall, this observation shows that any sub-cell could cause the degradation of fill factor of TJ cells. This excess current in dark can significantly affect the performance of solar power generation when it exceeds a current level of  $10^{-4} \text{ A}$  (cell area:  $4 \text{ cm}^2$ ) in LILT conditions since the photo generated current in this condition is only few mA scales. As to the TJ cell, one should consider which sub-cell is the current limiting cell concerning temperature, irradiation, and applied voltage. As we already discussed in the chapter 4.2.1, when the TJ cell is irradiated with electrons, the bottom cell never becomes a current limiting cell even at 100 K. Thus, the effect of high excess current in the bottom cell is not reflected in the LIV of TJ cells until a certain level of voltage (typically 3 V at 123 K) since the current is limited by the current of top or middle sub-cell. Whereas, it affects to the  $V_{OC}$  drop of TJ cells. Therefore, the FF degradation of the TJ cell can be easily detected when the excess leakage current in dark of its current limiting cell is high enough.

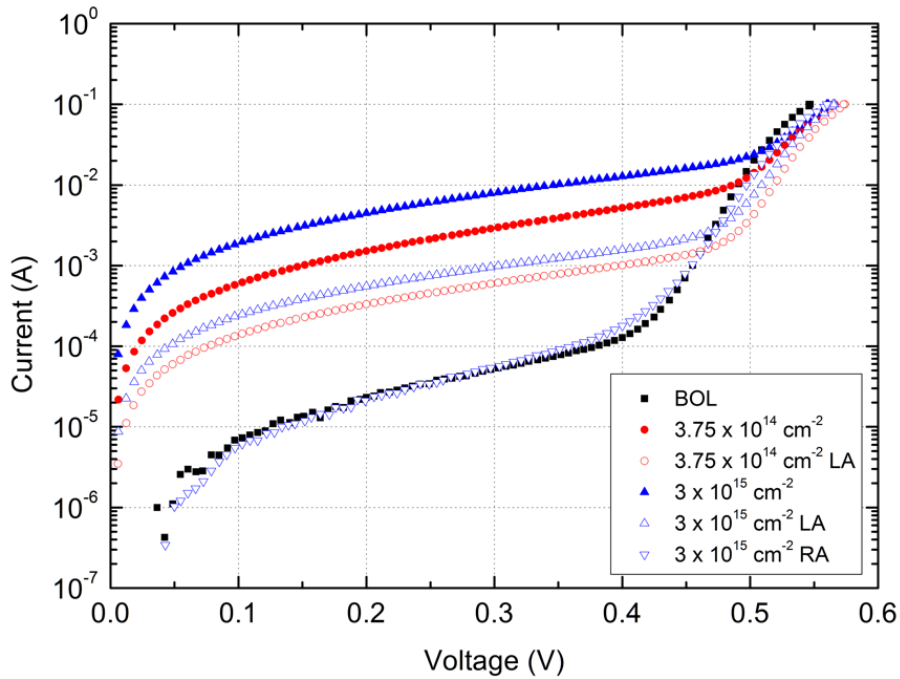


Figure 4-8. BOL and EOL dark I-V characteristics of a bottom component cell (0399-B) cumulatively irradiated up to a fluence of  $3 \times 10^{15} \text{ cm}^{-2}$  at 123 K. After each step of irradiation, annealing at 143 K (LA) for 10 minutes was carried out for an accelerated defect annealing at low temperature. RT annealing (RA) result is included for comparisons.

To analyze the nature and the property of the excess leakage current in dark, we designed an experiment with a bottom component cell:

1. Accumulative irradiation test including 10 minutes annealing at 143 K: fluence variation from  $3.75 \times 10^{14}$  to  $3 \times 10^{15} \text{ cm}^{-2}$  (Figure 4-8 and Figure 4-9).
2. Measuring DIV at different temperatures (temperature increasing from 123 to 300 K)
3. Measuring DIV at different temperatures (temperature decreasing from 300 to 123 K)

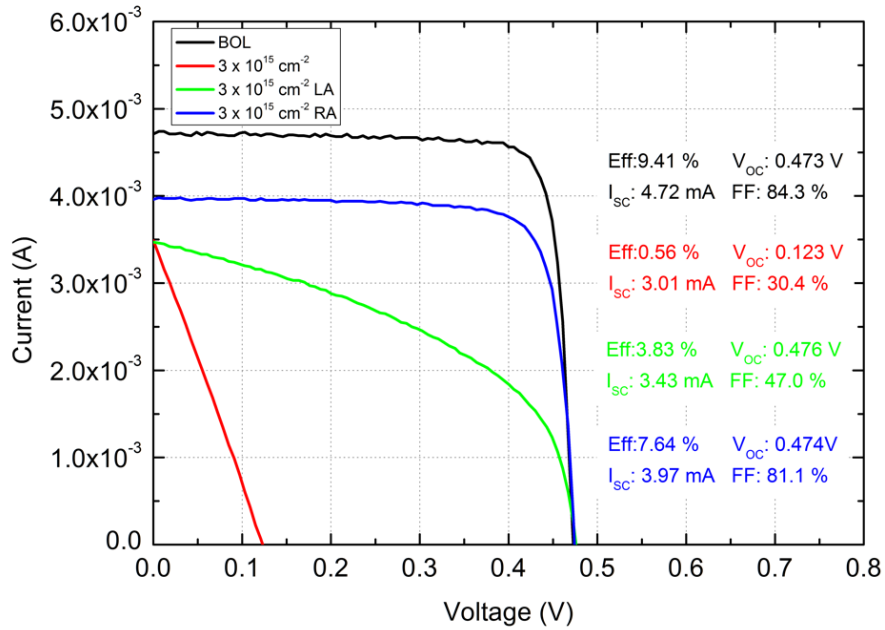


Figure 4-9. LA and RA annealing effects on light I-V characteristics of an electron irradiated bottom component cell (0399-B) at a fluence of  $3 \times 10^{15} \text{ cm}^{-2}$ .

Even when the bottom cell is irradiated even with a small amount of fluence ( $3.75 \times 10^{14} \text{ cm}^{-2}$ ), its  $I_{\text{Dark}}$  became almost two orders of magnitude greater ( $2 \times 10^{-3} \text{ A}$  at  $0.3 \text{ V}$ ) than in the BOL conditions ( $5 \times 10^{-5} \text{ A}$  at  $0.3 \text{ V}$ ). After the low temperature annealing (LA) at  $143 \text{ K}$  for 10 minutes, the  $I_{\text{Dark}}$  at  $0.3 \text{ V}$  became  $5 \times 10^{-4} \text{ A}$ . This fast recovery of  $I_{\text{Dark}}$  at LT is directly related to the recovery of  $V_{\text{OC}}$  of TJ cell during the stabilization at low temperature after the irradiation. At the fluence of  $3 \times 10^{15} \text{ cm}^{-2}$ ,  $I_{\text{Dark}}$  of the bottom cell at  $0.3 \text{ V}$  is close to  $10^{-2} \text{ A}$ . Due to the high excess current, the bottom cell acts like an ohmic register even under illumination as we can see the red curve in Figure 4-9. However, this state is very unstable; hence the bottom cell quickly recovers its FF and  $V_{\text{OC}}$  values. While  $V_{\text{OC}}$  is nearly returned close to the BOL value, FF is not fully recovered due to the excess leakage current in dark. Even though, since the amount of excess current decreases fast, less and less photo generated currents are canceled by the excess current resulting in the recovery of the FF. On the other hand, when the cell is annealed at  $300 \text{ K}$  and measured again at  $123 \text{ K}$ , the increase of its dark current becomes practically zero. As a result, the FF is recovered up to 81 %.

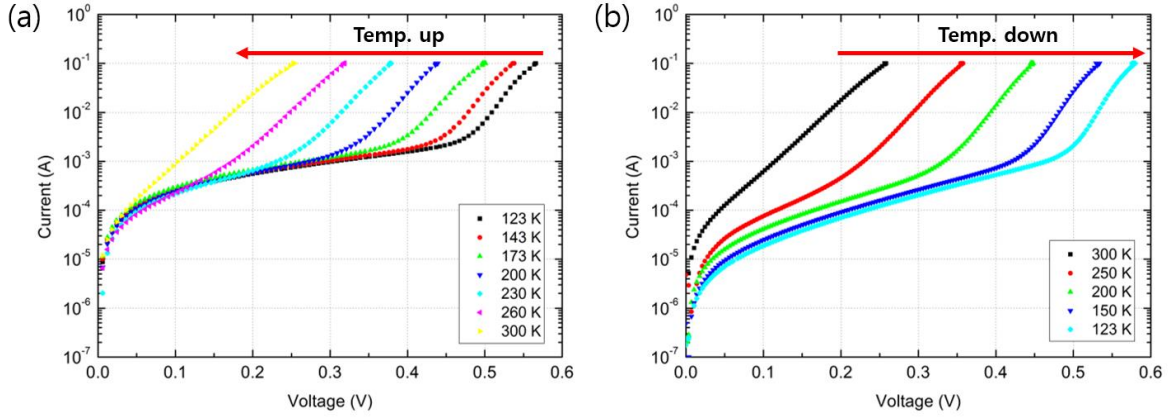


Figure 4-10. EOL dark I-V characteristics of an electron irradiated bottom component cell at different temperatures: the measurement (b) is performed after the measurement (a).

When the temperature increases from 123 to 300 K, we can expect that some defects induced by the electron irradiation might be annealed (step 2 of the experiment). In sequence 3, the cell is again measured in reverse direction, i.e. decreasing the temperature from 300 to 123 K. Thus, if there are defects which were engaged to the excess leakage current, the result would show a diminution of this current. Indeed, we observed a clear difference between the experiment step 2 and step 3 as presented in Figure 4-10. While the temperature goes up, the amount of excess leakage current seems to remain on the same current level. However, when the cell is measured again while cooling down, the excess current level becomes lower at lower temperature.

Eventually, the RT annealed (RA) bottom cell exhibits about one order smaller amount of excess current in dark compared to the case before annealing. In fact, the excess current consists of several components which is complicated to analyze. However, through this observation, we could find an annealing feature of the excess current, implying that some defects in the bottom cell, which have been induced by the electron irradiation are recovered. These defects act as traps where the majority carriers (either electrons or holes) can pass in the way of indirect tunneling. The excess current related to the impurity states in the forbidden gap induced by bombardments was already observed by D. Meyerhofer et al. [24]. This current is called as an exponential excess current. Chyoweth et al. [25] have proposed the equation of the exponential excess current which depends on the doping and the bombardment as below:

$$J_{exc} = D' \exp \left[ -\beta' m^* \frac{1}{2} n^{*-1/2} (E_G - eV + Q) \right] \quad (4-2)$$

where  $D'$  is the variation of the density of impurity states with energy,  $m^*$  is a reduced mass of electron,  $n^*$  is a reduced doping concentration,  $Q$  is a function of the sum of the Fermi level penetrations.

As described, this current is different from the band-to-band tunneling, but still has a tunneling feature through impurity states (traps) in the forbidden gap. Furthermore, this excess current is temperature dependent even though it is due to the tunneling. According to Figure 4-10 (b), when the cell is again cooled down, the cell exhibits less amount of excess leakage current than at higher temperature. To sum

up, the concentration of related defects has been changed between the step 2 and step 3 due to the annealing. As a consequence, once a cell is already annealed at higher temperature (for example, at 300 K), at least we can assume that an unwanted variable (change of defect concentration due to the annealing) is eliminated so that the dark current can be measured more accurately at lower temperatures. Likewise, we observed that the excess leakage current is temperature dependent. The excess current becomes smaller at lower temperatures.

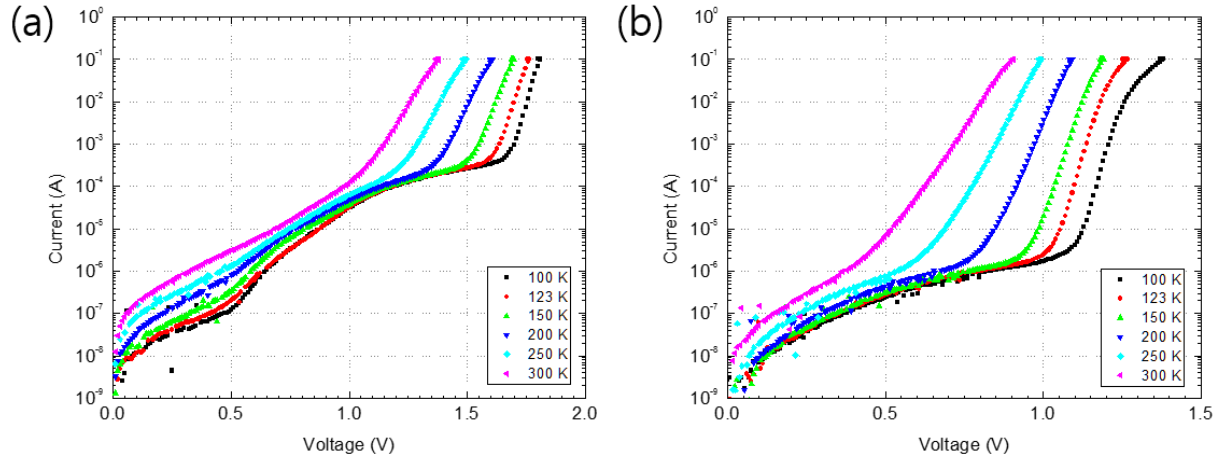


Figure 4-11. EOL Dark I-V characteristics of top (a) and middle (b) component cells irradiated with a fluence of  $3 \times 10^{15} \text{ cm}^{-2}$  at 123 K. The DIV measurements are realized increasing the temperature from 100 to 300 K after annealing at 300 K.

Similar observation was obtained from the top and the middle component cells as well. Figure 4-11 shows EOL dark I-V characteristics of top and middle component cells varying temperature from 100 to 300 K. As discussed above for the bottom cell, when the component cells are irradiated, typically top cells exhibit larger excess current than the middle cells. In summary, in a TJ cell, the excess current occurs in any kind of sub-cell. However, the prediction of exact amount and the shape of the excess current seems to be quite challenging since it really appears with various forms and there could be other kinds of unknown components. Even sometimes, there is almost no additional excess current. More detailed research should be undertaken, but it seems to be also related to the initial condition of the cells.

### 4.3 Annealing effect of electron irradiated cells

After the irradiation, we carried out the isochronal annealing for the top and bottom component cells. Cells used for the annealing procedure have been irradiated at 96 K with a fluence of  $1 \times 10^{15} \text{ cm}^{-2}$ . Figure 4-12 (a) and (b) show changes of remaining factor of  $I_{SC}$ ,  $V_{OC}$ ,  $P_{MAX}$ , FF of top and bottom cells respectively, as a function of annealing temperature.

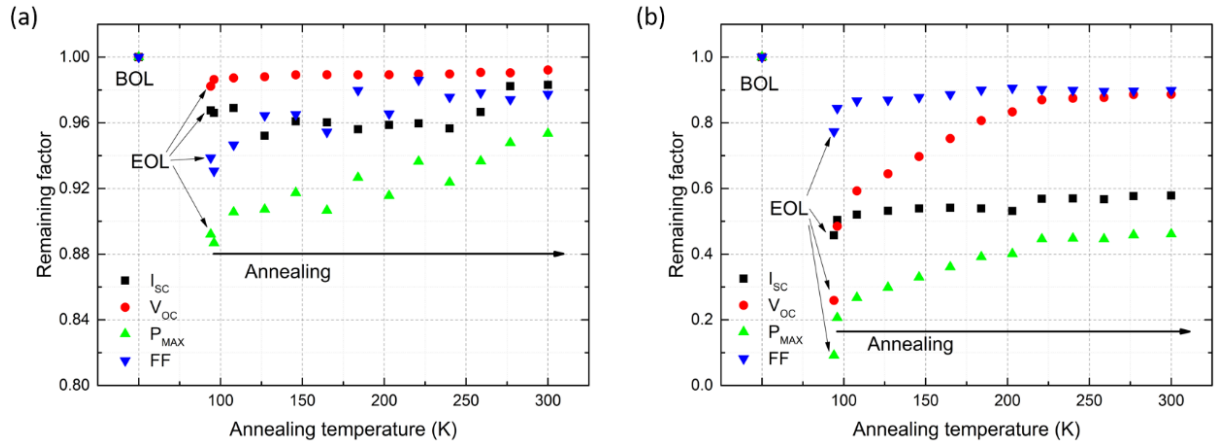


Figure 4-12. Changes of  $I_{SC}$ ,  $V_{OC}$ ,  $P_{MAX}$ , FF Remaining factors of electron irradiated (a) top and (b) bottom component cells during isochronal annealing (measured at 96 K: the lowest cell temperature that can be achieved using liquid nitrogen pumping). Cells irradiated with a fluence of  $1 \times 10^{15} \text{ cm}^{-2}$  at 96 K.

For the top cell (Figure 4-12 (a)), the degradation of  $V_{OC}$  is small compared to its other parameter such as  $I_{SC}$ , FF, and we can hardly see its recovery. The recovery of  $I_{SC}$  is not clear since the values during the annealing is not steadily increased. Change of  $RF(I_{SC})$  through all annealing temperature is about 2 %. The tendency of FF recovery is clearer than a  $I_{SC}$  one. However, it also shows an unstable variation during the annealing, especially at the temperature ranging between 150 and 250 K. Due to the fact that FF recovery is not steady,  $P_{MAX}$  shows same phenomenon during the annealing stage, even though it recovers of about 6 %. Bottom cell exhibits a totally different behavior (Figure 4-12 (b)). First, the degradation of  $V_{OC}$  is drastic.  $RF(V_{OC})$  value is equal to 0.25 immediately after the irradiation. The  $RF(V_{OC})$  is recovered from 0.25 to 0.5 in 5 minutes. After the first significant recovery at the irradiated temperature (96 K), we could measure a steady recovery of  $V_{OC}$  at the range between 116 and 240 K, and the rate of recovery became smaller at higher temperatures. Second, the  $I_{SC}$  value decreased significantly as well after irradiation (PRE included). But there are two sharp recovery points at around 100 and 210 K. The recovery of FF is not remarkable.  $RF(FF)$  remains near  $0.9 \pm 0.02$  during the annealing procedure.  $P_{MAX}$  of the bottom cells decreases down to 10 % from its BOL value after the irradiation. The reason is mainly due to the degradation of  $V_{OC}$ . However, the recovery rate is also very significant. The final  $RF(P_{MAX})$  value is 0.47 (recovered by 0.37 from 0.1).

## 4.4 Discussion of the chapter 4

### 4.4.1 Uncertainty of the TJ cell degradation induced by electron irradiations

As found out in this chapter, the main reason of the deterioration of the TJ cell performance is the appearance of an excess tunneling current in the different component cells. Apart from the degradation of  $I_{SC}$  and  $V_{OC}$ , this appears by deforming the shape of I-V curve under illumination by a decreasing of the FF. In general, this significant degradation seems to originate from the top cell. In some rare cases,

the middle cell can be severely deteriorated as well. Since the bottom cell is not close to the current limiting cell of the TJ cell, its excess tunneling current does not affect to the actual degradation of TJ cell performance even if the actual amount of excess tunneling current of the bottom cell is the biggest among the different sub-cells.

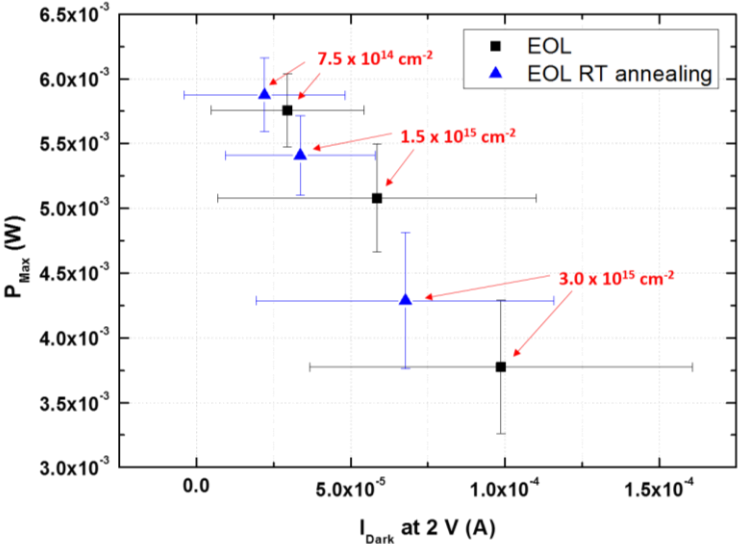


Figure 4-13. P<sub>MAX</sub> versus I<sub>Dark</sub> at 2 V of electron irradiated TJ cells at 123 K.

One of main difficulties for interpreting our observations is correlated to the fact that the amount and the spreading of excess tunneling current are unpredictable. This is not what has been observed in the case of the proton irradiation in the previous chapter. Figure 4-13 simply shows how the solar cell power generation under illumination is affected by the amount of the excess tunneling current. As shown, the amount of tunneling current becomes bigger and more spread when the cell is irradiated at higher fluences. On the other hand, when the irradiated cells are annealed at RT, the excess tunneling current can be significantly reduced. The effect of annealing was higher for the irradiated cells with high fluences.

In fact, the amplitude of the tunneling current is different from cell to cell and from batch to batch. Even though the cells are from the same batch, due to the inhomogeneity of doping concentration or material quality, the EOL characteristics of the cells can be different. And this becomes more obvious when comparing different batches. If inherent cell’s detailed property isn’t emerged in I-V measurements, the electrical performance of the cells might not be affected by the inhomogeneous BOL conditions. Nonetheless, they can still act as triggers for excess tunneling current.

#### 4.4.2 Origin of the excess current

First, as we proved through the experiment using a bottom cell, the cause of the excess current induced by electron irradiation originates from the tunneling through trap sites in forbidden gap. More precisely, this tunneling current seems to occur from the interaction between majority carriers and localized trap

levels with defects located in the space charge region of the junction. A simplified diagram in Figure 4-14 illustrates a trap assisted indirect tunneling of an electron from the conduction band of n-doped side to the valence band of p-doped side in the junction. This excess current is proportional to the density of occupied states in the conduction band. When the temperature is lower, the density of occupied states with electrons in the conduction band will decrease resulting in the less amount of excess current. In addition, the tunneling probability can be also dependent on the concentration and the trap level of defects located in the space charge region. Especially, Ge bottom cell has a narrow bandgap than other two component cells. The bottom cell is therefore more sensitive to the tunneling current. Likewise, the internal electric field (band bending) that is formed between n-doped and p-doped layers can play an important role to the dark current. When the external field with positive bias is applied to the pn junction, the sum of two field will result in diminution of the bending of the junction. Thus, the more carriers in occupied states will be able to hop to trap levels in the localized state until before the thermal current starts to increase drastically.

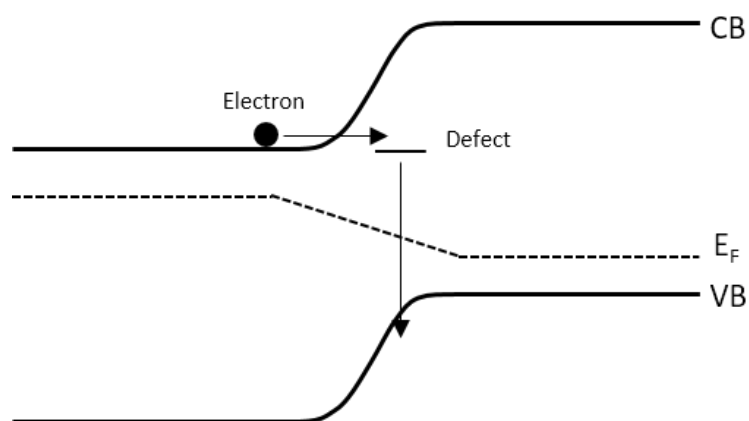


Figure 4-14. Tunneling current at defect created by irradiation in depletion zone.

## Conclusion of the chapter 4

In this chapter, we have studied the influence of 1 MeV electron irradiation on the electrical properties of TJ cells in LILT condition. We have observed in this work a severe degradation of FF at various range of fluences (from  $10^{14}$  to  $10^{15}$   $\text{cm}^{-2}$ ) from triple junction solar cells, which was not observed previously during 1 MeV proton irradiations. This FF degradation is due to the high excess current which can be measured in dark, and this appears at EOL conditions. The dark excess current originated from the trap assisted indirect tunneling (observed in all sub-cells).

In the Ge component bottom cell, significant recovery of the excess tunneling current was observed after low temperature annealing. In addition, in some cases, most of tunneling effect was vanished after a room temperature annealing. It is correlated to the removal of defects localized in the space charge region of the junction by annealing processes. However, it was not the case for the top and middle component cells. This tunneling seems to be induced by homogeneously distributed primary defects in active regions of the junction.

A huge difference of degradation under the same conditions was observed from cell to cell. This seems to originate from initial inhomogeneity of TJ cells (not electrically measured) which can induce defects when the irradiation is done. Suppress the dark excess current of sub-cells is the way to improve TJ cell performance at LILT electron irradiation conditions.

Through the vast investigation of electron irradiated component cells at different temperatures, we found out:

- that the bottom sub-cell doesn't become a current limiting cell in the triple junction structure since its current remains much higher than that of other two sub-cells in the temperature range of 100 to 300 K.
- that the top cell exhibits the best radiation hardness concerning  $I_{SC}$  among three sub-cells. However, since the significant excess tunneling current can be induced in the top cell by irradiation, this cell becomes the main source of degradation of FF of the TJ cell, especially at low temperature.

Therefore, the control of this excess current is of prime importance for mastering the degradation since the maximum power is directly related to its amplitude and the scatter in  $P_{MAX}$  reflects that of the excess current.

## Reference

- [1] J. W. Corbett, J. C. Bourgoin, and C. Weigel, "Radiation damage and defects in semiconductors," J. E. Whitehouse, Ed. 1973, pp. 1–16.
- [2] J. Bourgoin and M. Lannoo, *Point Defects in Semiconductors II*, vol. 35. Berlin, Heidelberg: Springer Berlin Heidelberg, 1983.
- [3] H. Y. Tada, J. R. J. Carter, B. E. Anspaugh, and R. G. Downing, *Solar cell radiation handbook*. Pasadena, CA: JPL Publication, 1982.
- [4] R. C. Newman, "Defects in silicon," *Rep. Prog. Phys.*, vol. 45, no. 10, pp. 1163–1210, Nov. 2000.
- [5] D. Pons and J. C. Bourgoin, "Irradiation-induced defects in GaAs," *J. Phys. C: Solid State Phys.*, vol. 18, no. 20, pp. 3839–3871, 1985.
- [6] D. Stievenard, X. Boddaert, J. C. Bourgoin, and H. J. von Bardeleben, "Behavior of electron-irradiation-induced defects in GaAs," *Phys. Rev. B*, vol. 41, no. 8, pp. 5271–5279, Mar. 1990.
- [7] M. A. Zaidi, M. Zazoui, and J. C. Bourgoin, "Defects in electron irradiated GaInP," *J. Appl. Phys.*, vol. 73, no. 11, pp. 7229–7231, 1993.
- [8] J. Dekker, J. Oila, K. Saarinen, A. Tukiainen, W. Li, and M. Pessa, "Cation and anion vacancies in proton irradiated GaInP," *J. Appl. Phys.*, vol. 92, no. 10, p. 5942, 2002.
- [9] P. M. Mooney, M. Cherki, and J. C. Bourgoin, "Energy levels in electron irradiated n-type germanium," *J. Physique Lett.*, vol. 40, no. 2, pp. 19–22, 1979.
- [10] P. M. Mooney, F. Poulin, and J. C. Bourgoin, "Annealing of electron-induced defects in n-type germanium," *Phys. Rev. B*, vol. 28, no. 6, pp. 3372–3377, Sep. 1983.
- [11] C. A. Ferreira Lima and A. Howie, "Defects in electron-irradiated germanium," *Philosophical Magazine*, vol. 34, no. 6, pp. 1057–1071, Aug. 2006.
- [12] M. Imaizumi, T. Takamoto, and T. Sumita, "Study of radiation response on single-junction component sub-cells in triple-junction solar cells," *3rd World Conference on Photovoltaic Solar Energy Conversion*, Osaka, Japan, pp. 599–602, 2003.
- [13] G. Xin, F. Zhan-zu, C. Xin-yu, Y. Sheng-sheng, and Z. Lei, "Performance Evaluation and Prediction of Single-Junction and Triple-Junction GaAs Solar Cells Induced by Electron and Proton Irradiations," *IEEE Trans. Nucl. Sci.*, vol. 61, no. 4, pp. 1838–1842, Aug. 2014.
- [14] R. Hoheisel, D. Scheiman, S. Messenger, P. Jenkins, and R. Walters, "Detailed Characterization of the Radiation Response of Multijunction Solar Cells Using Electroluminescence Measurements," *IEEE Trans. Nucl. Sci.*, vol. 62, no. 6, pp. 2894–2898, Oct. 2016.
- [15] T. Ohshima, T. Sumita, and M. Imaizumi, "Evaluation of the electrical characteristics of III-V compounds solar cells irradiated with protons at low temperature," *IEEE 35th Photovoltaic Specialists Conference (PVSC)*, pp. 806–809, 2005.
- [16] R. D. Harris, M. Imaizumi, R. J. Walters, J. R. Lorentzen, S. R. Messenger, J. G. Tischler, T. Ohshima, S. Sato, P. R. Sharps, and N. S. Fatemi, "In Situ Irradiation and Measurement of Triple Junction Solar Cells at Low Intensity, Low Temperature (LILT) Conditions," *IEEE Trans. Nucl. Sci.*, vol. 55, no. 6, pp. 3502–3507, Dec. 2008.
- [17] C. Baur, V. Khorenko, G. Siefer, J. C. Bourgoin, M. Casale, R. Campesato, S. Duzellier, and Inguibert V, "Development status of triple-junction solar cells optimized for low intensity low temperature applications," *IEEE 39th Photovoltaic Specialists Conference (PVSC)*, pp. 3237–3242, 2013.
- [18] J. C. Bourgoin, B. Boizot, K. Khirouni, and V. Khorenko, "On the Prediction of Solar Cell Degradation in Space," *10th European Space Power Conference (ESPC)*, vol. 719, p. 1, Aug. 2014.
- [19] S. Taylor, C. Baur, T. Torunski, V. Khorenko, G. Strobl, R. Campesato, R. Hoheisel, M. Hermle, F. Dimroth, D. Stetter, K. Dettlaff, J. Bourgoin, S. Makhm, and G. Sun, "Performance of European Triple-Junction Solar Cells for Deep Space Missions," vol. 661, pp. 34–39, Sep. 2008.
- [20] C. Baur, V. Khorenko, G. Siefer, V. Inguibert, S. Park, B. Boizot, J. C. Bourgoin, M. Casale, R. Campesato, H.-G. Schnell, A. Gerhard, P. Zanella, E. Ferrando, X. Reutenauer, E. Bongers,

- and A. Gras, "Status of Solar Generator Related Technology Development Activities Supporting the Juice Mission," *E3S Web Conf.*, vol. 16, no. 8, pp. 04005–8, May 2017.
- [21] K. C. Reinhardt, C. S. Mayberry, B. P. Lewis, and T. L. Kreifels, "Multijunction solar cell iso-junction dark current study," presented at the Conference Record of the Twenty-Eighth IEEE Photovoltaic Specialists Conference - 2000 (Cat. No.00CH37036), 2000, pp. 1118–1121.
- [22] M. A. Zaidi, J. C. Bourgoin, and H. Maaref, "Poole-Frenkel-assisted emission from deep levels in electron-irradiated germanium," *Semicond. Sci. Technol.*, vol. 4, no. 9, pp. 739–742, Sep. 1989.
- [23] G. Vincent, A. Chantre, and D. Bois, "Electric field effect on the thermal emission of traps in semiconductor junctions," *J. Appl. Phys.*, vol. 50, no. 8, pp. 5484–5487, 1979.
- [24] D. Meyerhofer, G. A. Brown, and H. S. Sommers, "Degenerate Germanium. I. Tunnel, Excess, and Thermal Current in Tunnel Diodes," *Physical Review*, vol. 126, no. 4, pp. 1329–1341, 1962.
- [25] A. G. CHYNOWETH, W. L. FELDMANN, and R. A. LOGAN, "Excess tunnel current in silicon Esaki junctions," *Physical Review*, vol. 121, no. 3, pp. 684–694, Dec. 1961.

# 5 *General discussion*

5.1	Comparison of electron and proton irradiation in LILT conditions.....	141
5.2	Distribution of BOL and EOL data set: Case of electron and proton irradiated TJ cells.....	149
5.3	Correlation of radiation induced defects with electrical property of the solar cell. ....	151
	Conclusion of the chapter 5.....	153
	Reference.....	154

In this chapter, we will compare the electron irradiated cells with the proton irradiated ones in LILT conditions. As an analytical method, displacement damage dose (DDD) analysis has been adapted, which is now widely being used for correlating electron and proton irradiations with various energies and eventually for the prediction of degradation of solar cell performances in space. Direct comparison of BOL and EOL values of some key parameters will be presented to discuss the large distribution of EOL  $P_{MAX}$  of electron irradiated TJ cells in LILT condition. Lastly, we try to correlate the electrical degradation of TJ and its component cells with the defects induced by irradiation in LILT conditions.

### 5.1 Comparison of electron and proton irradiation in LILT conditions

Before to start to compare the electron and proton irradiated TJ and its component cells, it should be noticed that the proton particle loses its kinetic energy through its path due to the coulombic reaction with atoms of medium. It is especially significant for low energy proton from few hundred keV to few MeV scale. As already discussed in the chapter 3, 1 and 2 MeV protons are stopped in the middle of Ge substrate, penetrating up to around 12 and 32  $\mu\text{m}$ , respectively. As it is already shown using SRIM in the chapter 3, average energy loss of 1 MeV proton in top layer is  $5 \text{ eV/m}^{10}$ . Since the thickness of the top layer is about  $0.6 \mu\text{m}$ , a proton particle loses its energy of 30 keV when it passes through the top layer. In the middle layer, the proton loses about 18 % of its energy when it has initially the energy of 1 MeV. Therefore, when the particle enters into the bottom layer, 1 MeV proton will finally become about 790 keV instead of 1 MeV. In the case of 2 MeV proton, its energy loss is less than the case of 1 MeV. A simple diagram showing the change of energy of proton is described in Figure 5-1. Since the energy loss of proton for both 1 and 2 MeV protons is not significant when they pass the top layer, we will only apply the energy loss for the bottom component cell.

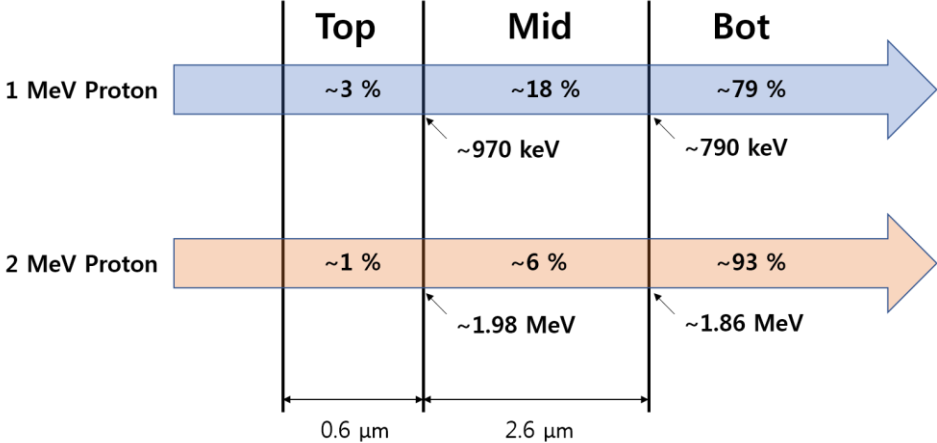


Figure 5-1. Representative diagram of approximate energy loss of incident 1 and 2 MeV proton in the studied TJ solar cell.

Empirically, it has been known that the GaAs junction in the triple junction solar cell is the primary cause of degradation by both electron and proton irradiation at room temperature. for this reason, the displacement damage dose (DDD) analysis, usually simulate the degradation of TJ cell with the data of

GaAs cell. Figure 5-2 shows electron and proton NIEL curves as a function of particle energy. For this calculation, we have selected the threshold displacement energy of GaAs as  $E_d = 21$  eV. This value is taken from Baur et al. [1]. With this value, they extracted a best fit for electron and proton irradiation with several energies at RT. NIELs of electron and proton at 1 MeV are  $\sim 1 \times 10^{-5}$  and  $5 \times 10^{-2}$  MeVcm<sup>2</sup>/g, respectively. Namely, by the NIEL calculation, we can deduce that 1 MeV proton can transfer about 5000 times larger energy than 1 MeV electron in GaAs.

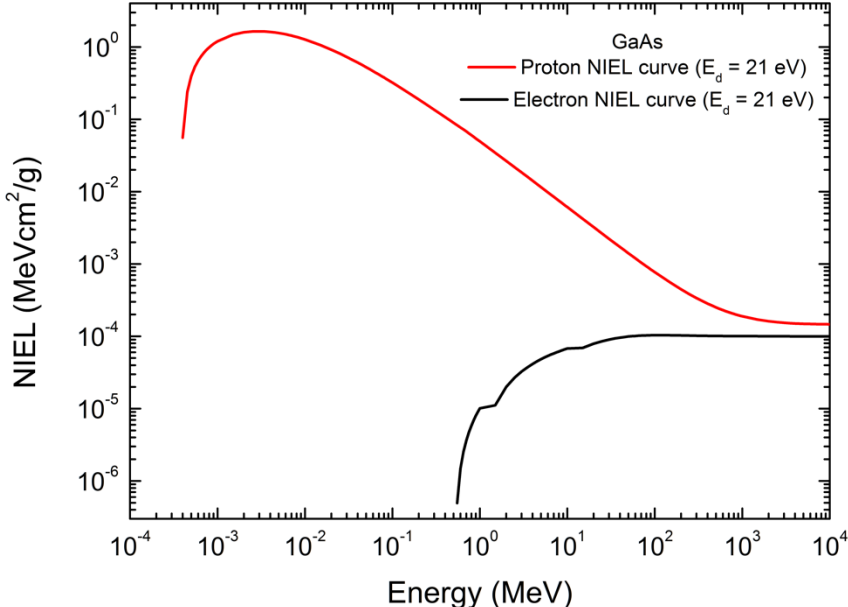


Figure 5-2. Non-Ionizing Energy Loss (NIEL) versus energy of proton (red) and electron (black) in GaAs ( $E_d = 21$  eV) calculated using Screen Relativistic (SR)[2].

As the energy gets larger, NIEL of protons becomes smaller while that of electrons increases and then at very high energy near GeV scale, both NIELs are saturated to near a low  $10^{-3}$  MeVcm<sup>2</sup>/g. Apart from the JUICE irradiation campaign, we have also irradiated more TJ cells at higher energy (2 MeV). 6 TJ cells were irradiated with a fluence of  $6.5 \times 10^{14}$  cm<sup>-2</sup> and an energy of 2 MeV electrons and 2 TJ cells with 2 MeV protons (fluences of  $2 \times 10^{11}$  and  $4 \times 10^{11}$  cm<sup>-2</sup> for each cell). For the irradiation conditions and details for 1 MeV proton and electron, please refer the chapter 3 and the chapter 4.

In order to compare all of electron and proton irradiated TJ cell in one graph, we converted the electron and the proton fluence to DDD using the conversion method (Eq. (1-66)) which is introduced in subchapter 1.5.2. In Figure 5-3, remaining factor (RF) of  $I_{SC}$ ,  $V_{OC}$ , FF and  $P_{MAX}$  of 3G28 TJ cells irradiated with 1 and 2 MeV electron and protons in LILT conditions are summarized. Irradiations and measurements were conducted at 123 K. To support the DDD analysis of 3G28 TJ cells, same methodology has been applied to top, middle and bottom component cells. Figure 5-4, Figure 5-5 and Figure 5-6 show RF( $I_{SC}$ ,  $V_{OC}$ , FF,  $P_{MAX}$ ) of top, middle and bottom component cells. For these experiments, much less number of cells have been irradiated due to the limited number of cells and beam time. Each symbol represents one cell but each cell has been irradiated cumulatively. For the top and middle component cells, 3 cells were used for 1 MeV electron and proton and 2 MeV proton irradiations.

For the bottom component cells, 5 cells were used (1 MeV proton – 2 cells, 1 MeV electron – 1 cell, 2 MeV proton – 2 cells).

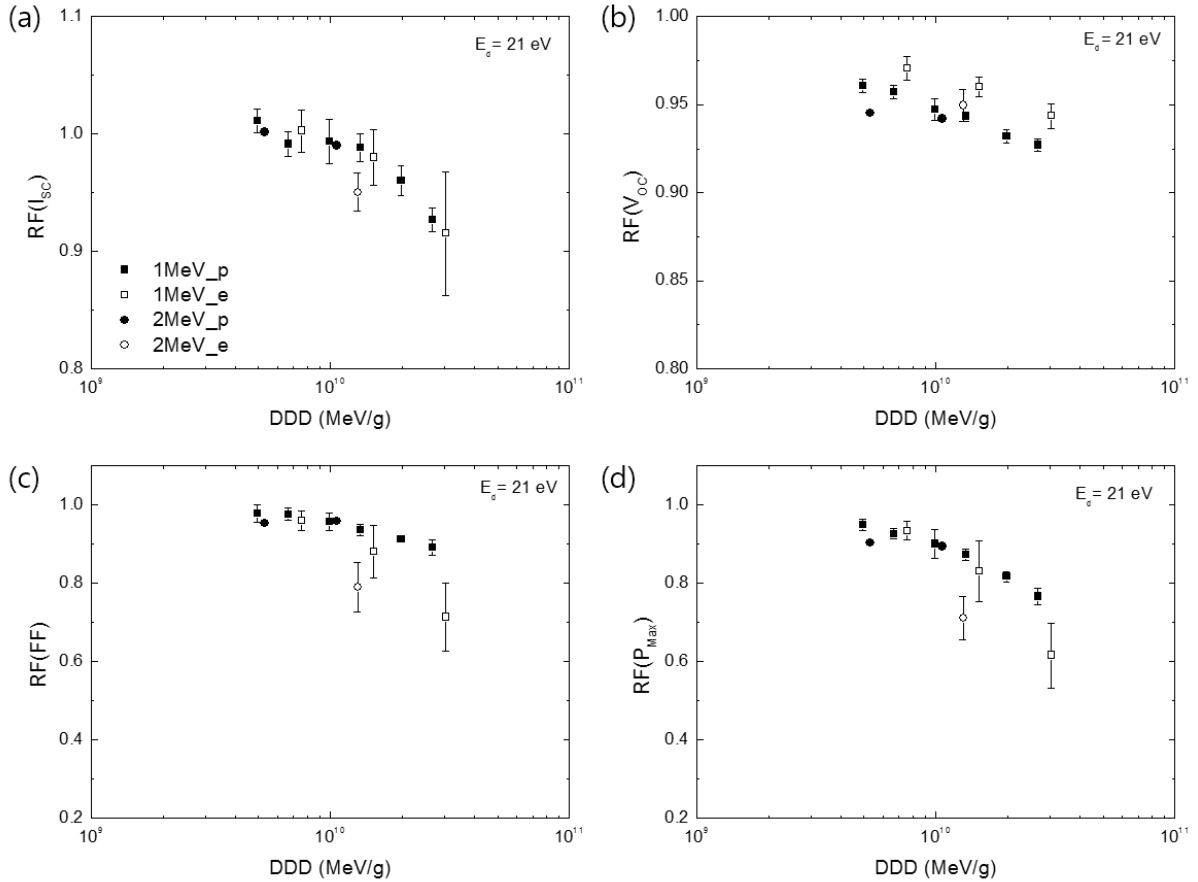


Figure 5-3. Relative degradation of (a)  $I_{SC}$ , (b)  $V_{OC}$ , (c) FF and (d)  $P_{MAX}$  of the 3G28 TJ solar cell as a function of displacement damage dose converted from electron and proton fluences based on the NIEL calculation on an atomic displacement energy of  $E_d = 21$  eV (the value used for the NIEL calculation of GaAs solar cell [1]). Black square – 1 MeV proton, white square – 1 MeV electron, black circle – 2 MeV proton, and white circle – 2 MeV electron. Represented data are average values with standard deviation.

When comparing the  $RF(I_{SC})$  of 1 MeV electron and proton irradiated TJ cells, it seems that their average values follow the same degradation curve. However, there is a huge difference between electron and proton irradiated TJ cells. We can notice that there are much larger variations of  $RF(I_{SC})$  of electron irradiated cells than that of the proton ones. Moreover, the  $RF(I_{SC})$  values are more and more spread as the electrons fluence increases. This means that, for the electron irradiation, the uncertainty of EOL performance of TJ cell becomes higher. The reason of this large distribution on  $I_{SC}$  is still unclear, but it may come from the competition of current limiting between top and middle sub-cells. Another possible explanation is that EOL  $I_{SC}$  of electron irradiated top or middle sub-cell is intricately related to the defects and carrier life time. Meanwhile, it seems that  $RF(I_{SC})$  of 2 MeV proton irradiated TJ cells lies on the prediction curve of 1 MeV proton ones. However, the cells irradiated with 2 MeV electron exhibit stronger degradation on  $I_{SC}$  than 1 MeV electron irradiated cells. The same trend is observed from Figure 5-3 (b), (c) and (d) which represent  $V_{OC}$ , FF and  $P_{MAX}$  versus DDD, respectively.

For  $V_{OC}$  degradation, first, we can see that values are less distributed compared to the case of  $I_{SC}$ . One important thing is that 1 MeV electron induces less damage to the TJ cell than 1 MeV proton while it is not the case for other parameters such as FF and  $P_{MAX}$ . The  $V_{OC}$  of TJ cell is simply a series sum of that of sub-cells when the current is zero. Thus, simulating EOL  $V_{OC}$  value of a TJ cell from the component cells is quite simple; just adding  $V_{OC}$  of component cells at the same EOL condition. More detailed discussion of the  $V_{OC}$  of TJ cell will be continued after discussing all component cells.

Concerning 2 MeV proton data, the left dark-circle point (fluence of  $2 \times 10^{11} \text{ cm}^{-2}$ ) is placed about 1 % below from the 1 MeV proton data points while the right one ( $4 \times 10^{11} \text{ cm}^{-2}$ ) seems to be well fit with other proton points. The reason of this difference is not clear. It could be from an abnormal property of the TJ cell irradiated with 2 MeV,  $2 \times 10^{11} \text{ cm}^{-2}$  proton or some unknown reason.

The RF(FF) values of 1 MeV electron and proton irradiated TJ cells are similar when DDD is smaller than  $10^{10} \text{ MeV/g}$ . However, they are decoupled at larger DDD. The RF(FF) of electron irradiated one starts to decrease more rapidly than that of proton one. At the highest irradiation condition, the difference between two average RF(FF) values are about 0.2, that is, 20%. Furthermore, like the case of  $I_{SC}$  of electron irradiated cells, the standard deviation of RF(FF) is also very large. Considering the scale of Figure 5-3 (c), the distribution of EOL FF is even more severe than for EOL  $I_{SC}$ . As it has been already mentioned in the chapter 3, the origin of the huge drop of FF is a large dark excess current. When this dark current is higher than the level of  $10^{-4} \text{ A}$ , it starts to decrease the light current in generation region (fourth quadrant of LIV) under illumination of 3.7 % AM0. The influence of the excess dark current on the LIV characteristics can be significantly dependent on the intensity of light. In LILT conditions, the intensity of light is weak, therefore, even small amount of excess dark current like the case above can induce a huge drop of FF and this also results in the drop of  $P_{MAX}$ . In this point of view, by looking at Figure 5-3 (d), it is reasonable for us to observe a similar decoupling behavior of RF( $P_{MAX}$ ) degradation by 1 MeV electron and proton irradiation at higher DDD, also with a large distribution.

For more structural approach, we have correlated these degradations of remaining factors to those of component cells at the same LILT conditions. First, for DDD analysis of the top component cells, the NIEL values for electron and proton in GaInP were calculated based on the displacement threshold energy taken from the recent work by Okuno et al. [3]. Remaining Factors of  $I_{SC}$ ,  $V_{OC}$ , FF and  $P_{MAX}$  of the top cell are presented in Figure 5-4 as a function of DDD. The extent of degradation of RF( $I_{SC}$ ) of the top cells is similar with that of TJ cells. The relative degradation is typically less than 5 % when the DDD is less than  $10^{10} \text{ MeV/g}$ . Indeed, at smaller fluences, it is difficult to confine a specific degradation level. However, it seems that the electron irradiated top component cells degrades less than the component cell irradiated with protons. The same observation is still valid for  $V_{OC}$ . With equal amount of DDD, electron irradiated top cell exhibited higher RF( $V_{OC}$ ) compared to the case of proton irradiation. In a TJ structure, the portion of top sub-cell on  $V_{OC}$  of TJ cell is the largest. Thus, this is probably one of reasons of the less  $V_{OC}$  degradation of electron irradiation TJ cells (see Figure 5-3 (b)).

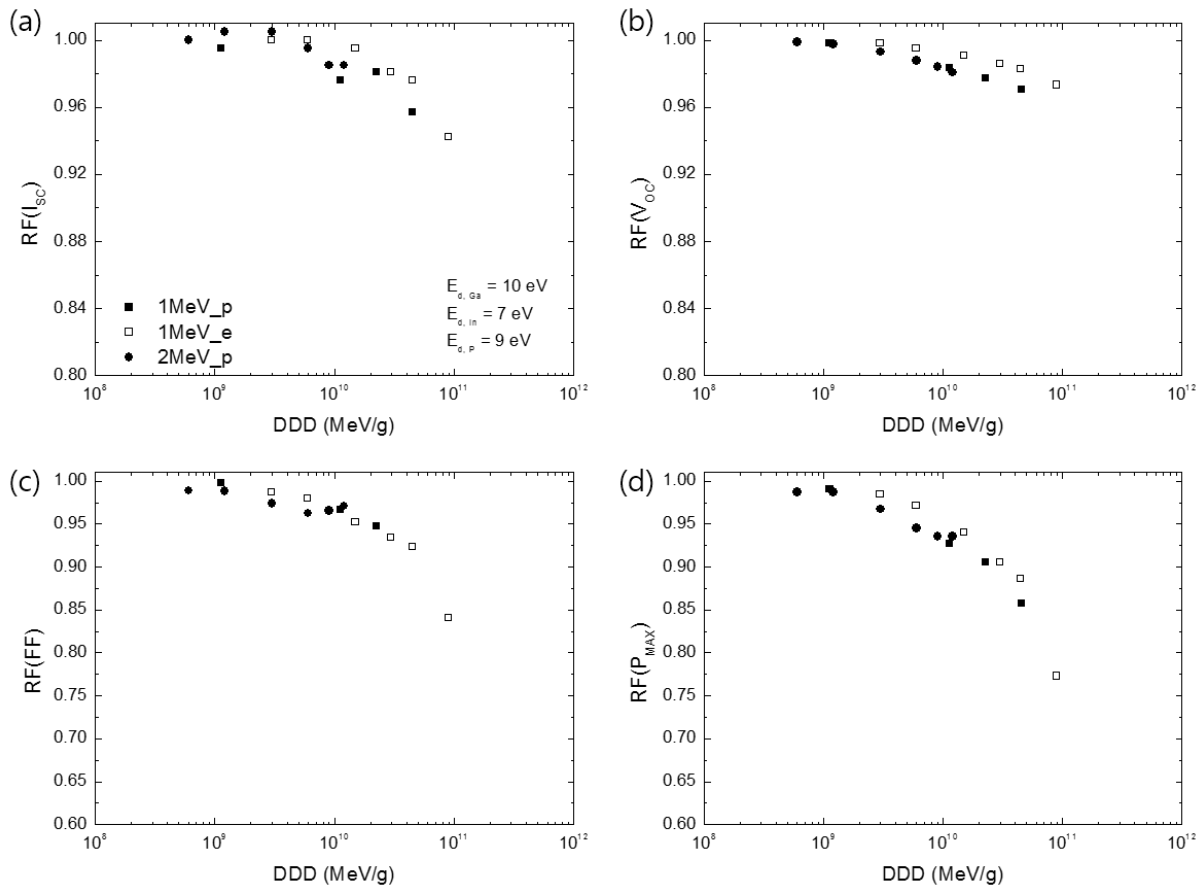


Figure 5-4. Relative degradation of (a)  $I_{SC}$ , (b)  $V_{OC}$ , (c) FF and (d)  $P_{MAX}$  of the top component cell as a function of displacement damage dose converted from electron and proton fluences based on the NIEL calculation on atomic displacement energies of  $E_d = 10, 7$  and  $9$  eV for Ga, In and P, respectively (values taken from the ref. [3]). Black square – 1 MeV proton, white square – 1 MeV electron, black circle – 2 MeV proton, and white circle – 2 MeV electron. Represented data are average values with standard deviation.

RF(FF) degradation under both electron and proton for the top component cells follow a single curve until the DDD level of  $10^{10}$  MeV/g. On the other hand, suddenly, at DDD of  $10^{11}$  MeV/g, the electron irradiated cells undergo a huge drop of FF (about 10 % of RF). For the proton irradiated cells, this type of decrease has not been observed. It doesn't seem to be related to the amount of dose since it is clearly related to the appearance of the excess dark current in top component cell after electron irradiation. As discussed already in the chapter 3, the excess dark current in TJ and all component cells appears only when the cell is irradiated by electrons. Due to this phenomenon, the top component cell exhibits a 'significant' FF degradation when the electron fluence is sufficiently high to make the dark excess current becomes higher than the level of  $10^{-4}$  A as shown in Figure 5-5. When the cumulated electron fluence is near  $3 \times 10^{15}$   $\text{cm}^{-2}$ , the FF of this top component cell decreased from 82.86 to 75.44 %. As mentioned above, the FF directly affects to the  $P_{MAX}$  of the cell. Therefore, as one can see in Figure 5-4 (d), the electron irradiated top cell with a DDD of  $10^{11}$  MeV/g has a RF( $P_{MAX}$ ) of 0.77 and it is expected to be even lower than RF( $P_{MAX}$ ) of proton irradiated one if the cell is irradiated with the same amount of DDD. These differences of electron and proton irradiation on the top component cell may explain

why the electron irradiated TJ cell exhibits a larger degradation of FF compared to the proton irradiated cells in LILT condition.

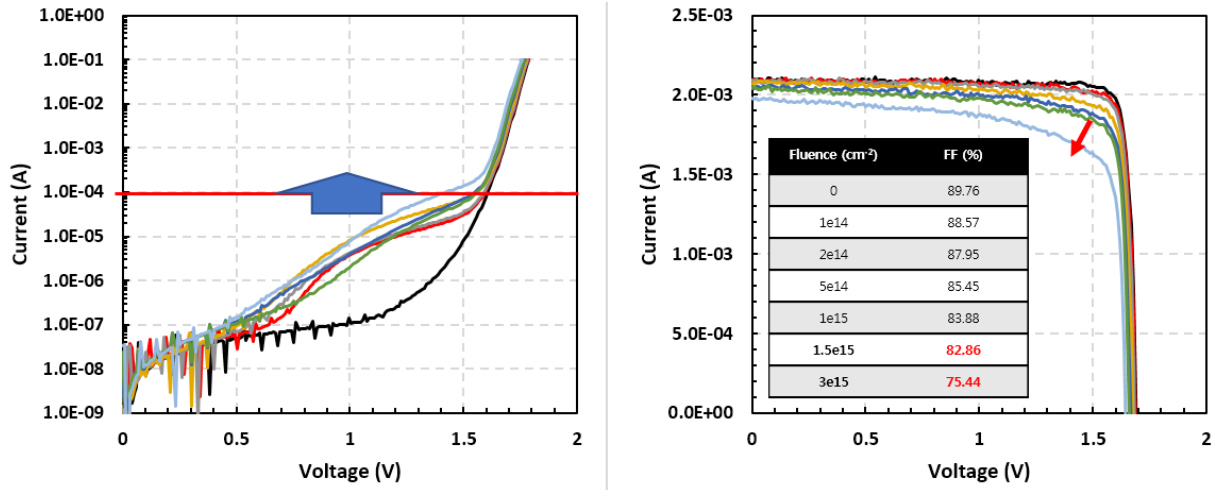


Figure 5-5. DIV (left) and LIV (right) of an electron irradiated top component cell at LILT conditions.

The DDD approach with  $E_d = 21$  eV was already applied to GaAs/Ge (substrate) single junction cells and the GaAs solar cell has proven its predictable degradation property in RT irradiation conditions. In a TJ structure for the GaAs middle component cell in LILT conditions, we were not sure if it could be still valid even if the structure is different (existence of GaInP top layer on top of GaAs junction). Furthermore, the irradiation temperature was different (300 K versus 120 K). Surprisingly, when applying same NIEL parameter as used for single junction GaAs cell at RT, the GaAs middle component cell has shown perfectly matched RF values for all four parameters even in LILT condition as shown in Figure 5-6.  $RF(I_{SC})$  of the middle cells decreased down to 0.7 at  $10^{11}$  MeV/g. The degradation of  $V_{OC}$  is analyzed larger previously for the top cell (more than the factor of 2) while FF of the middle cells exhibit more or less similar radiation hardness with the top cells. These all three parameters contribute to the degradation of  $P_{MAX}$  of the middle cell, but the main factor of degradation under irradiation is the  $I_{SC}$ . The degradation of the middle cell under electron and proton irradiations can be considered identical when DDD analysis is applied to the TJ cell. Therefore, the difference observed especially in FF degradation must be correlated to the behaviors of either top or bottom sub-cells.

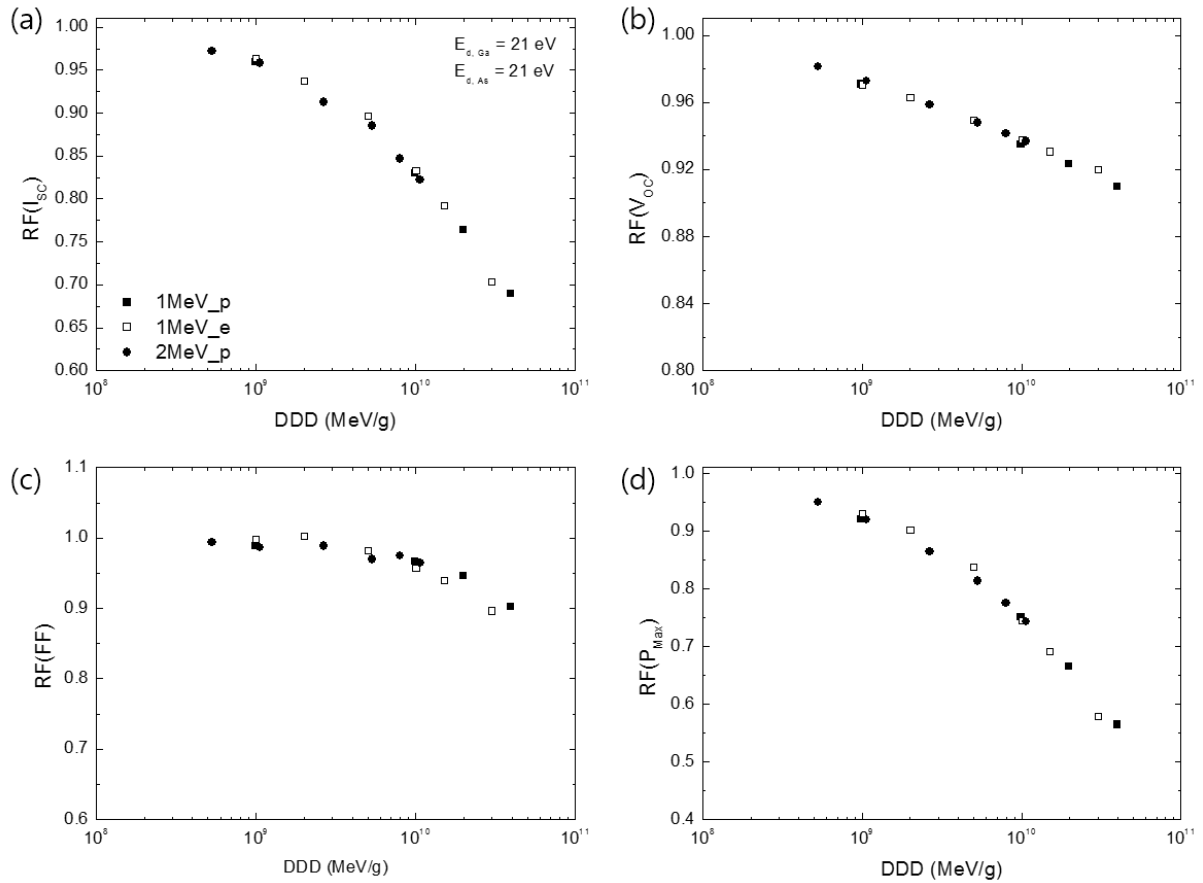


Figure 5-6. Relative degradation of (a)  $I_{SC}$ , (b)  $V_{OC}$ , (c) FF and (d)  $P_{MAX}$  of the middle component as a function of displacement damage dose converted from electron and proton fluences based on the NIEL calculation on an atomic displacement energy of  $E_d = 21$  eV (the value taken from the ref. [1]). Black square – 1 MeV proton, white square – 1 MeV electron, black circle – 2 MeV proton, and white circle – 2 MeV electron. Represented data are average values with standard deviation.

By contrast to other component cells, we have first to remove for the calculations of bottom component cell remaining factors the Photon Recycling (PRE) influence on electrical properties. It had to be carried out before measuring any relative degradation of electrical parameter of the bottom component cell. Thus, in Figure 5-7, we assume that the RF values have been obtained by dividing EOL values into BOL (w/o PRE). The Ge solar cell is known for having a good radiation hardness at RT. By contrary, the radiation hardness around 120 K is strongly decreasing. For the bottom cell  $RF(I_{SC})$ , within a boundary of 5 %, all the data points are placed on the single degradation prediction curve. However, having same  $RF(I_{SC})$  does not always mean that they have same absolute values. As already addressed in the chapter 3, at lower temperature, we have observed a larger first drop of  $I_{SC}$ . This result is not only correlated with the PRE but also related to some unique property of proton irradiation at low temperatures (frozen defect clusters acting as insulating columns along proton track) which is clearly different from electron irradiation. Apart from this detail, it seems possible to predict the degradation of  $RF(I_{SC})$  of electron and proton irradiated Ge component cell using one DDD curve.

In fact, when the bottom cell has just been irradiated, recovery of the cell FF and  $V_{OC}$  occurs during a low temperature annealing process. Here, all data of electron irradiated bottom cells are obtained after the stabilization. Even though,  $RF(V_{OC})$  of the electron irradiated cell shows much lower values

compared to that of proton irradiated ones. In fact, the degradation and recovery of  $V_{OC}$  is not independent on FF. In other word, if the FF hugely decreases, the  $V_{OC}$  will follow this degradation. As shown in Figure 5-7 (c), FF of proton irradiated cell does not almost decrease while the RF(FF) of electron irradiated cells decreases almost half from its original value down to almost 0.5 at  $3 \times 10^9$  MeV/g. Due to the low RF of  $V_{OC}$  and FF of electron irradiated Ge component cell, it exhibits also very low RF( $P_{MAX}$ ) lower than samples irradiated with protons. From these observations, one can now say that, together with the top cell, the bottom cell is another main reason of additional degradation of electron irradiated TJ cell.

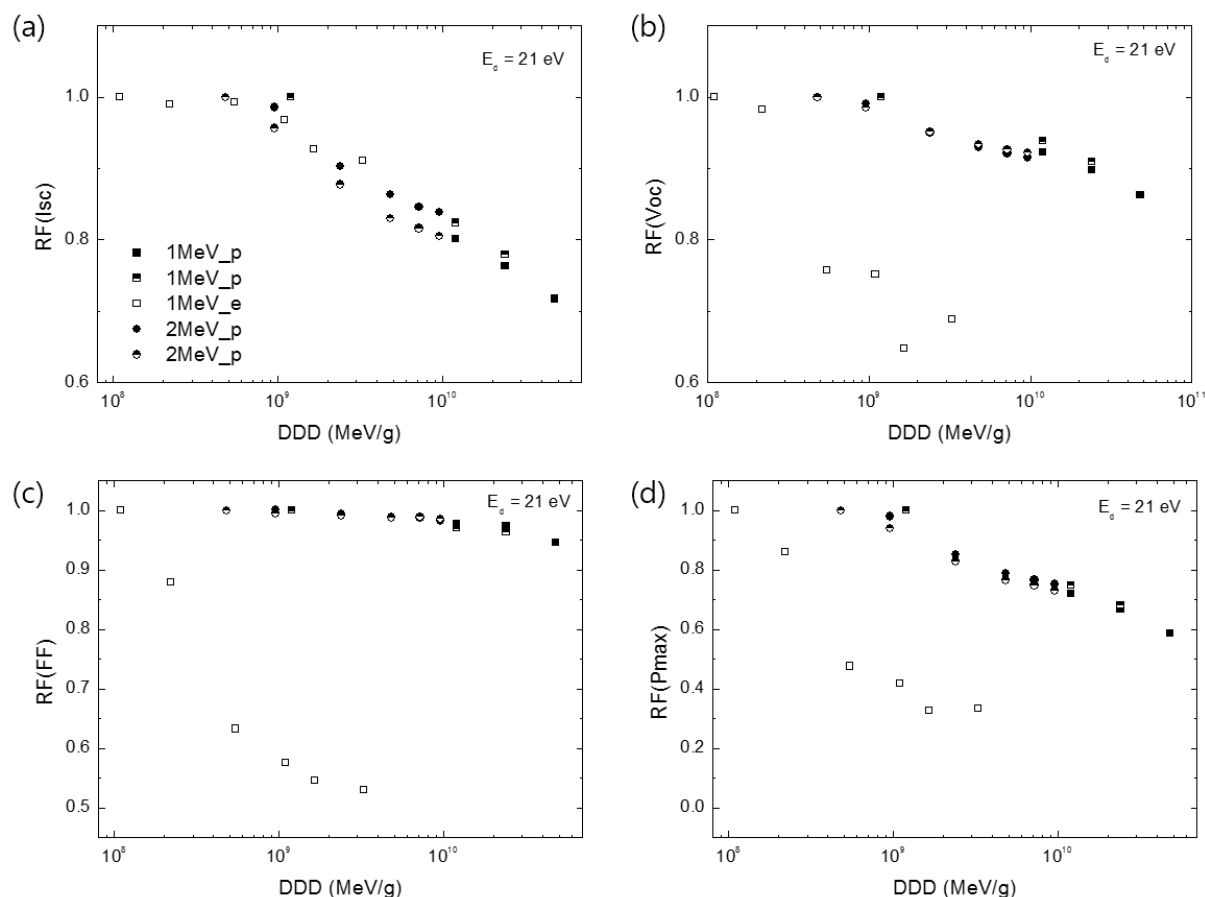


Figure 5-7. Relative degradation of (a)  $I_{sc}$ , (b)  $V_{oc}$ , (c) FF and (d)  $P_{MAX}$  of the bottom component cell as a function of displacement damage dose converted from electron and proton fluences based on the NIEL calculation on an atomic displacement energy of  $E_d = 21$  eV (the value taken from the ref. [4]). Black square – 1 MeV proton, white square – 1 MeV electron, black circle – 2 MeV proton, and white circle – 2 MeV electron. Represented data are average values with standard deviation.

Figure 5-8 shows the dark I-V (DIV) characteristics of Ge component cells before (BOL) and after (EOL) irradiation with 1 MeV protons and electrons at 123 K, with fluences of  $2 \times 10^{11}$  and  $3 \times 10^{15}$   $\text{cm}^{-2}$ , respectively (i.e. corresponding approximately to the same value of the NIEL). To plot the DIV, a log scale on y-axis is used to observe the low voltage component of the current, below thermionic emission. The degradation of the thermal current part is practically the same for proton and electron irradiated cells. On the other hand, an additional excess current is observed in the voltage range of 0 to 0.5 V where flat band is not reached. This excess current is associated with tunneling induced by the defects present

in the space charge region of the junction [5], and it's observed only for the electron irradiated cell. The insets of Figure 5-8 (a) and (b) show DIV characteristics of a Ge component cells as a function of the accumulated fluence. Obviously for electron irradiated samples, the tunneling current increases with fluence which is in good agreement with a classical phenomenon, i.e. radiation induced trap assisted tunneling current [6]: it is the result of the creation of electrically active defects in the space charge region of the junction. As shown in the inset of Figure 5-8 (a), the proton irradiation does not induce the tunneling current up to fluences of  $8 \times 10^{11} \text{ cm}^{-2}$ . Therefore, the absence of tunneling current in proton irradiated cells [7] is surprising since it implies that defects created in this space charge region may not act as traps assisting in tunneling.

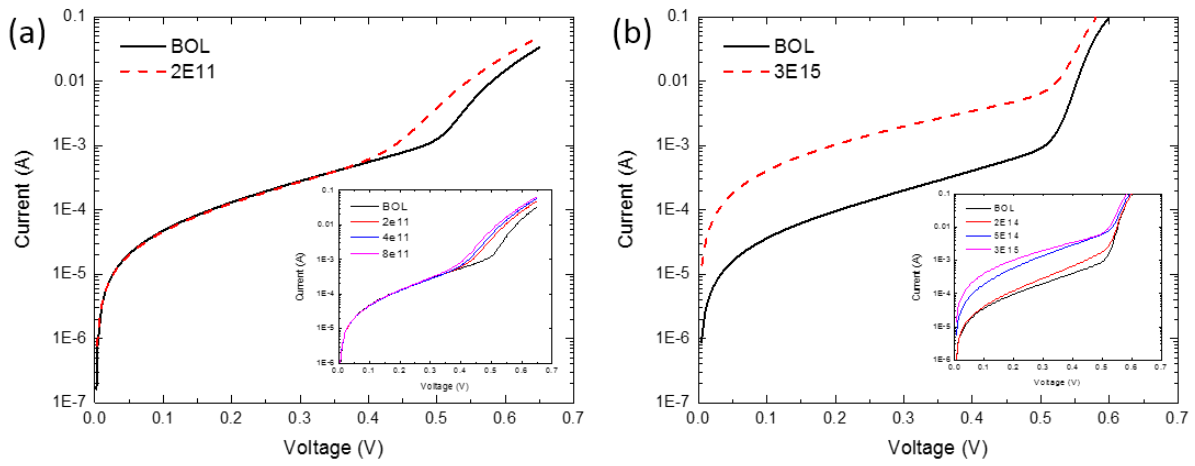


Figure 5-8. Dark I-V characteristics, measured at 123 K, of 1 MeV protons ( $2 \times 10^{11} \text{ cm}^{-2}$ ) (a) and 1 MeV electrons ( $3 \times 10^{15} \text{ cm}^{-2}$ ) (b) irradiated Ge component cells at 123 K.

## 5.2 Distribution of BOL and EOL data set: Case of electron and proton irradiated TJ cells

Figure 5-9 shows BOL and EOL FF and  $P_{\text{MAX}}$  values of all JUICE 3G28 TJ cells. Here we decided to show only FF and  $P_{\text{MAX}}$  because the FF has a direct correlation with the data distribution of  $P_{\text{MAX}}$  of electron irradiated TJ cell. Each of box type data, presented in this figure, is composed of a number of individual data in the same irradiation condition and the box sizes represents a standard deviation, min-max values and an average value. Before irradiation; i.e. in BOL condition, most of the cells have more or less identical FF values close to 90 %. However, this balance is then broken after electron irradiation with a fluence more than  $1.5 \times 10^{15} \text{ cm}^{-2}$ . As a consequence, we start to observe a significant data distribution on FF and  $P_{\text{MAX}}$  after irradiation and low temperature annealing (LA) processes (EOL 123K (LA)). The change is evident when comparing the black and the red box charts. Not even the average FF and  $P_{\text{MAX}}$  values are decreased, but their distributions become larger. The blue box represents data set when the cell is annealed at room temperature (RA) and then measured again at 123 K. Generally, for high dose irradiated cells, we observe more recovery in terms of both FF and  $P_{\text{MAX}}$ . But this does not

mean that the EOL FF and  $P_{MAX}$  data become always less distributed after the annealing. It does seem to be in the case of EOL with a fluence of  $1.5 \times 10^{15} \text{ cm}^{-2}$ , but not for the case of  $3 \times 10^{15} \text{ cm}^{-2}$ .

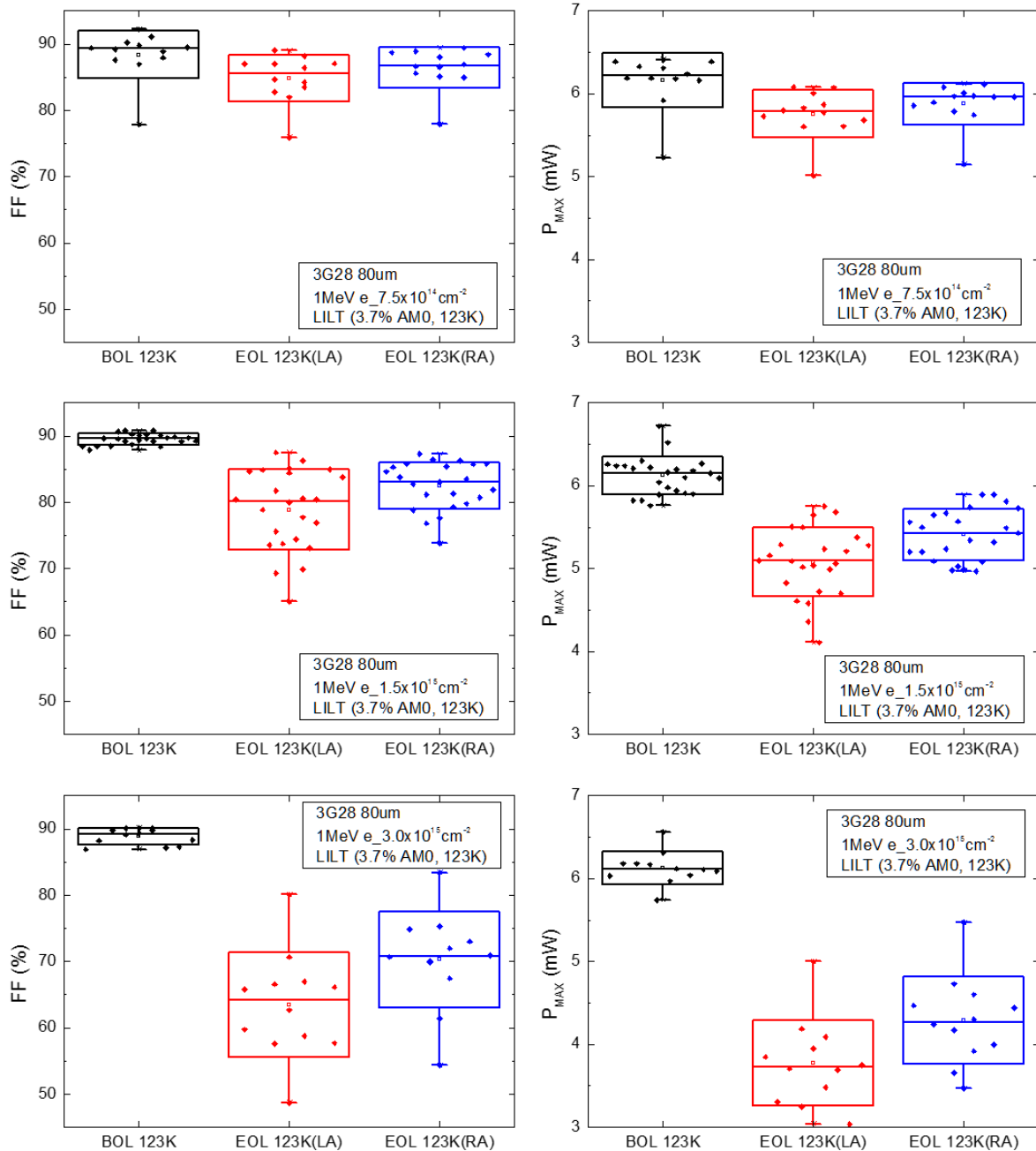


Figure 5-9. Distribution of absolute FF and  $P_{MAX}$  values (BOL, EOL and RT annealed EOL) of electron irradiated JUICE 3G28 TJ solar cells in LILT conditions.

On the other hand, as shown in Figure 5-10, proton irradiated TJ cells do not exhibit any increase of distribution of FF. All BOL FF values are close to 90 % and the EOL FF values are decreased by 10 % from their BOL values. Thus, the  $P_{MAX}$  exhibits the same behavior as FF. the RT annealing recovers the FF of cells by a few %, but still there is no effect on distribution of data. Naturally, the annealing does not affect to the distribution of  $P_{MAX}$ . The behavior of proton irradiated cells is therefore much more predictable without randomness. It is possible because the proton irradiation does not produce the excess dark current which is not very controllable in respect of the appearance and the amount.

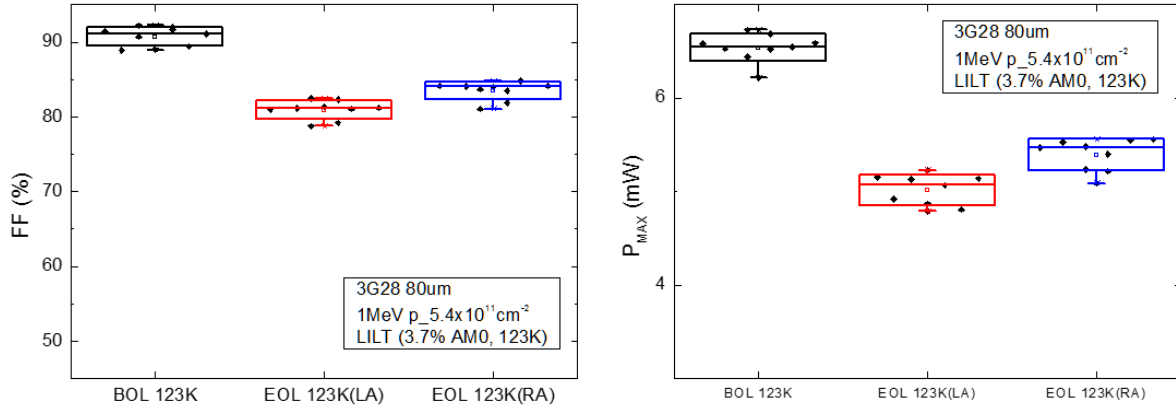


Figure 5-10. Distribution of absolute FF and  $P_{MAX}$  values (BOL, EOL and RT annealed EOL) of proton irradiated JUICE 3G28 TJ solar cells in LILT conditions. (maximum proton fluence only)

Then, now the question is how we can improve the uncertainty of EOL characteristics of electron irradiated TJ cell. To operate the cell in LILT conditions, we must decrease or remove the excess dark current from all sub-cell (mostly from top and bottom cell). Since these currents come from trap induced tunneling, one of possible and the easiest way to try is to change the doping concentration of each junction. By lowering the doping concentration in a material, we can expect that there will be less interaction between impurities and primary defects.

### 5.3 Correlation of radiation induced defects with electrical property of the solar cell

When a pn junction is irradiated, defects can be generated in the neutral regions (both n- and p- type regions) as well as in the space charge region. The defects can influence to the doping concentration level with their charged states or can affect the minority carrier lifetime resulting in a decrease of photo generated current of a solar cell. In the case of the GaAs component cell, these two major effects were clearly observed from both electron and proton irradiations at LILT condition. It is possible that one type of defects contributes to both phenomena or there exists several types of defects which behave for each phenomenon. Due to the limit of measurement techniques used for researches on materials, it is not possible to identify all types of defects created by irradiation. However, even limited information could be helpful to find a correlation between defects and the electrical degradation of the solar cell. In the GaAs, the defect generation is started from the displacement of As atoms. The detached As atom form a primary defect  $V_{As} - As_i$  as an initial stage. Some As can replace the Ga in the lattice forming the  $As_{Ga}$  antisite as well. The primary defect is known to be very stable up to 500 K. From the isochronal annealing test, we have verified that there is nearly no recovery of  $I_{SC}$  of both electron and proton irradiated GaAs cells. Therefore, it is highly probable that the primary defect act as a site where the minority carriers are captured and cause a decrease of carrier lifetime. Concerning the diode property of GaAs junction, it is simply evaluated by tracking the change of EOL  $V_{OC}$ . When the  $RF(V_{OC})$  were

analyzed in LILT condition, they exhibited almost identical degradation. However, it was not the case of the measurement at RT. The  $V_{OC}$  degradation of proton irradiated GaAs cell was larger than that of electron irradiated one. This implies that the charged defects in the neutral regions might not be the same inside electron and proton irradiated cells. These defects behave differently at different temperatures. More particularly, the defects in proton irradiated cells exhibit a bigger temperature dependence of charged state so that it results in the larger degradation of diode property of the junction.

On the other hand, the GaInP junction shows a bit different result. When this cell is irradiated at 123 K with a proton fluence of  $8 \times 10^{11} \text{ cm}^{-2}$ , the dark I-V curve at current level of  $10^{-3} \text{ A}$  is shifted to left by around 50 mV. By contrast, a left shift of 200 mV occurs at 300 K. This difference substantially suggests that the charged level of defects in GaInP is more temperature dependent, to be compared with the GaAs middle cell. There is a possibility that defects related to phosphorous Frenkel pair contributes to the doping concentration on p-side since these defect levels are relatively close to the band edge (valence band for p-doped material). On n-side, some secondary defects and impurity complex, or derivation from native defects can make the doping concentration smaller. As already discussed, these defects seem to have very strong temperature dependence on their charge state. Concerning the degradation of  $I_{SC}$ , as the GaInP cell is already well known for its strong radiation hardness, we have seen only small degradation. This means that the most of defects created by irradiation are not very active for capturing the minority carriers. It could be from low capture cross section of these defects or from low generation rate of defect. In GaInP cells, we could not observe any particular recovery of  $V_{OC}$ ,  $I_{SC}$  during the isochronal annealing.

Back to the discussion of defects in the GaAs cell (same for the GaInP cell), only electron irradiated cells exhibit an excess dark current. Its appearing condition and annealing property is very random in this moment. Many different defect levels are in forbidden gap of GaAs and GaInP cells. This can potentially make the indirect tunneling of majority or minority carriers.

Concerning the Ge component cell, the degradation of Ge at LILT condition is more significant than other two cells and by itself comparing to the result at RT. Furthermore, degradation profiles of electron irradiated and proton irradiated Ge cell and its annealing property are also significantly different.

When a Ge component cell is just irradiated by electrons, first it undergoes an immediate recovery on  $V_{OC}$  and FF while proton irradiated Ge cell does not show this behavior. It is directly related to the amount of the excess dark current. The defects which contribute to the indirect tunneling disappear even in LILT conditions. According to the literature, it can be related to the defects from oxygen complexes and/or interstitial-related defects. Furthermore, when the isochronal annealing is performed to electron irradiated Ge cell, a strong recovery of  $V_{OC}$  has been observed between 100 to 230 K ( $RF(V_{OC})$  from 0.5 to 0.9). It seems that most of defects from various origins such as E center, A center and divacancy are recovered throughout this temperature range. Even if there is significant recovery on  $V_{OC}$ , the  $I_{SC}$  value is not so much changing in this annealing study. About 5 % of  $I_{SC}$  is recovered at irradiated temperature (100 K), then one more recovery step has been observed between 200 and 220 K.

Interesting point is that the proton irradiated Ge cell exhibits significantly different characteristics compared to the electron irradiated one. First, the degradation of  $I_{SC}$  is more severe than the electron case, then its recovery is more dramatic. The  $RF(I_{SC})$  drops down to about 0.3 and there is no immediate recovery. Instead, we could observe a steady recovery of  $I_{SC}$  in two different temperature range. Low temperature range near 120 K is probably related to the recovery of A center and E center. Then near 260 K, this recovery could come from the O-impurity complex. Surprisingly, proton irradiated Ge cell does not have a large drop of  $V_{OC}$  and FF since it has no additional excess dark current despite of high proton irradiations. It seems that the proton irradiation does not create various level of defects which the carriers can jump from defect to defect to produce an indirect tunneling.

## Conclusion of the chapter 5

In this chapter, we tried to directly compare the electron and proton irradiations using the displacement damage dose (DDD) approach. As it has been already verified at RT, the GaAs component cell showed almost a perfect match of DDD between electron and proton irradiated cells in LILT condition. This can indicate that the final defects produced by electron and proton irradiations are perhaps the same. Concerning the GaInP top component cell, electron irradiated cells exhibited less degradation on  $V_{OC}$ . It can explain why the electron irradiated TJ cell shows less degradation on  $V_{OC}$  than the case of proton irradiation. For the Ge bottom component cell, the electron irradiation induced much larger downgrading of  $V_{OC}$ , FF and  $P_{MAX}$  compared to the proton irradiation. Especially, comparing the  $RF(FF)$  of proton and electron irradiated Ge cells, there is almost no drop of  $RF(FF)$  when irradiated by proton even with a very strong DDD (larger than  $10^{10}$  MeV/g) while  $RF(FF)$  rapidly decreased less than 0.6 at a DDD of  $10^9$  MeV/g. As a consequence, much larger degradation of  $P_{MAX}$  could be observed from electron irradiated Ge bottom cells.

The excess dark current has been found from all types of component cells only when they are irradiated with electrons. Since this excess current originates from the tunneling at high voltage regions and showing a quasi-temperature independent property, we correlate this phenomenon with indirect tunneling current through traps in the forbidden gap. In the case of electron irradiation, the electron can create more various level of defects in the junction, and if the current from this effect exceeds a certain amount ( $\sim 10^{-4}$  A for  $4\text{ cm}^2$  area), it significantly decreases a solar cell's performance in LILT conditions. The occurrence of this tunneling current is not coherent, i.e. it varies a lot from cell to cell.

A possible way to improve (or remove) this phenomenon is decrease a doping concentration. By doing that, it can be expected that the radiation induced defects less interact with dopants and impurities. Therefore, they will create less number of defects working as tunneling trap sites.

## Reference

- [1] C. Baur, M. Gervasi, P. Nieminen, P. G. Rancoita, and M. Tacconi, “Solar Cell Degradation Analysis Applying the Displacement Damage Dose Approach Using Appropriate NIEL Values,” *10th European Space Power Conference (ESPC)*, vol. 719, p. 3, Aug. 2014.
- [2] M. J. Boschini, P. G. Rancoita, and M. Tacconi, “SR-NIEL Calculator: Screened Relativistic (SR) Treatment for Calculating the Displacement Damage and Nuclear Stopping Powers for Electrons, Protons, Light- and Heavy- Ions in Materials (version 3.9.3).” Millano-Bicocca, Italy, Oct-2017.
- [3] Y. Okuno, S. Okuda, M. Akiyoshi, T. Oka, M. Harumoto, K. Omura, S. Kawakita, M. Imaizumi, S. R. Messenger, K. H. Lee, and M. Yamaguchi, “Radiation degradation prediction for InGaP solar cells by using appropriate estimation method for displacement threshold energy,” *J. Appl. Phys.*, vol. 122, no. 11, pp. 114901–8, Sep. 2017.
- [4] D. Pons and J. C. Bourgoin, “Irradiation-induced defects in GaAs,” *J. Phys. C: Solid State Phys.*, vol. 18, no. 20, pp. 3839–3871, 1985.
- [5] S. Park, J. C. Bourgoin, O. Cavani, V. Khorenko, C. Baur, and B. Boizot, “Origin of the Degradation of Triple Junction Solar Cells at low Temperature,” *E3S Web Conf.*, vol. 16, no. 1, pp. 04004–4, May 2017.
- [6] J. R. Srouf and J. M. McGarrity, “Radiation Effects on Microelectronics in Space,” *Proceedings of the IEEE*, vol. 76, no. 11, pp. 1443–1469, Jan. 1988.
- [7] S. Park, J. C. Bourgoin, H. Sim, C. Baur, V. Khorenko, O. Cavani, J. Bourcois, S. Picard, and B. Boizot, “Space degradation of 3J solar cells: I-Proton irradiation,” *Prog. Photovolt. Res. Appl.*, vol. 23, no. 1, p. 1, Apr. 2018.

# *General Conclusions*

The aim of thesis work was to understand the behavior of electron and proton irradiated GaInP/GaAs/Ge triple junction solar cell in LILT conditions. From these experiments using electrons and protons on a large number of TJ and component solar cells, we found that the degradation mechanisms under electron and proton irradiations in LILT conditions can be strongly different. First a very peculiar phenomenon in electron irradiated cells was observed: a large distribution of electrical properties data (especially, fill factor FF). This type of result has never been reported from past studies about the TJ cells since there were only few attempts of in-situ irradiation test in LILT conditions. Moreover, most of studies related to radiation effects of the solar cells were performed at room temperature. Realizing a lack of knowledge on this subject, we have irradiated a number of component cells in various temperatures with many different fluences. In addition, the annealing tests have been carried out to check the recovery of solar cell performance to be correlated to nature of radiation induced defects in each type of material.

The origin of large distribution of FF values (affecting to  $P_{MAX}$ ) of electron irradiated TJ cells was an excess current measured in dark I-V characteristics. Since the intensity of the light source is very weak in LILT conditions, small amount of current could significantly affect the degradation of cell performance. The excess current occurred from every component cells, while its intensity was different from cell to cell. Bottom Ge component cells were the most sensitive to the electron irradiation in LILT conditions, followed by top component cells. The excess current also appeared in middle component cells, but its amount was not too large to affect to the cell's performance. The difficult point of analyzing the excess current was that the occurrence of this excess current is very random. It was sure that at higher fluences, there was 'generally' larger excess current. However, it varied also from cell to cell even though all the other conditions were the same. Through the dark I-V measurement test, we have concluded that the excess current comes from indirect tunneling by defects created by electron irradiations.

On the other hand, proton irradiated cells did not show any particular increase of the excess current in dark I-V measurement. Due to this difference between electron and proton irradiation, the standard deviation of  $P_{MAX}$  proton irradiated TJ cells was much smaller than that of electron irradiated ones. The other meaningful finding from proton irradiated cells is that proton irradiated bottom cells showed much larger degradation of  $I_{SC}$  than in the case of electron irradiation. After removing the contribution of PRE from both electron and proton irradiated bottom component cells, the proton ones still had smaller  $I_{SC}$  values. Furthermore, the current drop of the proton case was too large to change the current limiting cell to the bottom sub-cell at the low enough temperature (approximately lower than 120 K). We concluded that the proton irradiation in low temperature can produce a frozen defect cluster along the proton path which behave like an insulating area. This phenomenon is well observed in bottom component cell since

parts of its defects are unstable in the temperature ranging 100 to 300. This observation implies that any of three sub-cells can be the current limiting cell in LILT conditions in a proton irradiation environment.

Due to these reasons, we need to have a special care when applying the displacement damage dose (DDD) analysis to the proton and electron irradiated cells in LILT conditions. In LILT conditions, DDD analysis is still perfectly well matched for the GaAs cell, not so well for the GaInP cell and not at all for the Ge cell. DDD analysis on  $I_{SC}$  seems to be well adapted for all three cells, but it is not the case for  $V_{OC}$  and  $P_{MAX}$ . As a consequence, it was the same for the TJ cells. Therefore, to make an appropriate prediction curve, it is necessary to apply a modification factor for  $V_{OC}$  and  $P_{MAX}$  values of the top and bottom cells.

## Perspectives

This thesis work was very unique but not easy to be reproduced since it needed irradiation facilities, a cryostat system and measurement instruments. Under the in-situ irradiation and measurement test, we could only perform electrical measurement varying the temperature of the cryostat chamber due to several reasons: spatial limit of installation, lost of information while heating up the sample. Furthermore, parallel analysis of defects induced by radiation was not available since the cell size was too large to be measured by DLTS or other technique such as PAC. As a result, our understanding of the irradiation effect of TJ solar cell in LILT conditions is still limited to the past research on the nature of defects performed in a material level, not a device level. Therefore, for deeper and more precise understanding, it will be necessary to analyze the defect production and the degradation of the cell performance using defect analysis techniques in parallel.

Meanwhile, to overcome a large degradation of TJ cell (part of Ge bottom cell) under the electron irradiation in LILT condition, there could be two big different approaches:

1. To improve the radiation hardness of the Ge cell by modifying the structure or the material quality.
2. To replace the Ge bottom cell to the other material such as Silicon or other III-V compounds to realize other type of triple or four junction cells.

# *Annexe – Résumé de thèse en français*

Aujourd'hui, la cellule multijonction de pointe est la cellule solaire à triple jonction, à base d'arséniure de gallium (GaAs), de phosphonium de gallium-indium (GaInP) et de germanium (Ge). Récemment, la NASA a lancé une sonde spatiale baptisée Juno en 2011 pour la mission d'exploration de Jupiter. La cellule solaire à triple jonction à base de GaInP / GaAs / Ge a été utilisée pour la première fois dans le cadre de cette mission d'exploration de l'espace profond. L'ESA lancera son vaisseau spatial en 2022. La mission JUICE est la première mission de grande envergure du programme Vision cosmique 2015-2025 de l'ESA visant à explorer la gigantesque planète gazeuse Jupiter et ses lunes, Ganymede, Callisto et Europa. L'environnement de Jupiter appelé "système jovien" est entouré d'un grand champ magnétique provenant de Jupiter. Les particules telles que les électrons et les protons qui sortent du Soleil sont capturées par le champ magnétique puis accélérées par la force de Lorentz. Jusqu'à présent, la situation semble similaire à celle de l'orbite terrestre. Cependant, il faut aussi considérer que Jupiter est très éloignée du Soleil et que l'intensité du spectre solaire diminue jusqu'au 3,7% de l'AM0. De plus, la température absolue moyenne près de Jupiter est d'environ 120 K, tandis que la température moyenne près de la Terre est supposée être de 300 K. Pour pouvoir mener à bien les missions de l'ESA, il est nécessaire d'évaluer les performances précises d'une cellule solaire en fin de vie qui sera équipée pour le vaisseau spatial, cela est de la plus haute importance. Dans ce cadre, le LSI a participé à l'étude de vérification du recuit des cellules solaires, réalisant l'irradiation des électrons avec l'accélérateur SIRIUS et l'irradiation des protons au CSNSM de l'Université Paris-Sud à Orsay. Lors du test d'irradiation de la cellule solaire à triple jonction (TJ) GaInP / GaAs / Ge, à la pointe de la technologie pour la mission JUICE, des questions scientifiques concernant leur comportement dans des conditions d'espace profond, comme près de Jupiter, ont été soulevées. Ainsi, à travers ce travail de thèse, nous tenterons de trouver des réponses à certaines questions telles que la génération de défauts dans les cellules solaires complexes TJ en fonction de la température d'irradiation, les fluences et la nature de la particule et l'influence de ces défauts sur les propriétés électriques des cellules TJ.

## **Cette thèse est composée de cinq chapitres avec des conclusions générales à la fin.**

Le but du **chapitre 1** est de comprendre le principe de fonctionnement de la cellule solaire et l'impact des défauts induits par le rayonnement sur ses propriétés physiques et électriques. Par conséquent, dans la physique du photovoltaïque, nous aborderons d'abord la description électrique du dispositif photovoltaïque en utilisant les connaissances des semi-conducteurs, puis nous décrirons la physique des dommages par rayonnement dans le semi-conducteur et la création de défauts dans certains matériaux de cellules solaires. Enfin, combinant tous ces aspects, nous décrirons des techniques de simulation actuellement bien adaptées à la recherche et à l'industrie de la cellule solaire spatiale.

Dans le **chapitre 2**, nous introduirons le concept de caractérisation *in-situ* de cellules solaires dans des conditions de basse intensité et basse température (LILT) sous irradiations aux électrons ou aux protons. Le système est composé de quatre parties principales:

1. Des installations d'irradiation : un accélérateur linéaire d'électrons ou de protons
2. Un simulateur solaire composé d'une lampe de Xenon et d'une lampe de Quartz Tungstène Halogène et sa table de positionnement
3. Une chambre de cryostat avec un support des échantillons, une vitre qui permet au faisceau de passer pour illuminer les cellules solaires, une pompe rotative à vide et un système de pompage d'azote liquide.
4. Des unités de mesure : un contrôleur de température et des multimètres pour la caractéristique électrique

Premièrement, seront brièvement présentées les installations d'accélérateurs d'électrons et de protons qui ont été essentielles pour la campagne d'irradiation, puis en second lieu le simulateur solaire et la configuration de la chambre du cryostat avec les unités de mesure électriques. Sera également introduit, la structure des cellules solaires utilisées dans cette étude. En outre, on décrira ensuite la revue de l'état du test et les préparatifs avant la campagne d'irradiation. Cela inclut le test de cyclage en température, le test de calibration et de stabilité du simulateur solaire et les performances de la cellule BOL. Enfin, nous traiterons de l'effet de recyclage des photons, qui existe de manière inhérente dans les cellules composantes en BOL (principalement la cellule composante du bas).

Au sein du **chapitre 3**, afin de comprendre l'influence de l'irradiation des protons sur les cellules solaires TJ dans des conditions LILT, nous avons examiné ses comportements électriques caractéristiques en début de vie (BOL) et en fin de vie (EOL) IV, dans l'obscurité (DIV) et sous illumination (LIV), ainsi que les caractéristiques P-V (PV) des cellules composantes du haut, du milieu et du bas par rapport aux cellules TJ dans ces conditions. La plupart des irradiations des protons ont été effectuées avec une énergie de 1 MeV et des fluences comprises entre  $2 \times 10^{10} \text{ cm}^{-2}$  et  $1,6 \times 10^{12} \text{ cm}^{-2}$  à des températures comprises entre 100 et 300 K, dans le cadre du test de vérification du recuit JUICE suivi d'un test d'irradiation supplémentaire pour des analyses scientifiques. Quelques irradiations de 2 MeV ont été effectuées pour le test de dépendance angulaire. Le comportement de chaque paramètre, tel que le courant de court-circuit  $I_{SC}$ , la tension de circuit ouvert  $V_{OC}$ , la puissance maximale  $P_{MAX}$  et le facteur de remplissage FF, sera présenté. Les cellules solaires à triple jonction (TJ) GaInP / GaAs / Ge à réseau à la fine pointe de la technologie sont maintenant largement utilisées pour les missions spatiales car elles ont démontré une efficacité maximale. De plus, elles présentent la meilleure résistance aux radiations par rapport aux autres types de cellules. Leur comportement sous irradiation de protons à température ambiante a été étudié de manière approfondie. Au cours de la mission JUICE, ces cellules TJ seront utilisées pour des missions interplanétaires et dans des espaces lointains, dont l'environnement typique est souvent appelé conditions LILT. Cependant, la compréhension de leur comportement sous

irradiation de particules à basse température en est encore à ses balbutiements. En raison de la difficulté d'effectuer des tests d'irradiation à basse température suivis par une acquisition de données électriques *in-situ* sous éclairage solaire, cette compréhension a été déduite des mesures à basse température effectuées après irradiation à la température ambiante. À l'exception de cette tentative, les seules études d'irradiation à basse température avec mesures *in-situ* ont été réalisées sur des cellules TJ produites par AZUR SPACE Solar Power GmbH.

Les résultats préliminaires suggèrent que le comportement électrique de ces cellules TJ à basse température est indépendant de la température à laquelle les irradiations ont été effectuées. Cependant, l'analyse *in-situ* des données acquises à basse température révèle que plusieurs phénomènes, tels que le recuit des défauts et la dépendance du courant de recombinaison au champ électrique, doivent être pris en compte, phénomènes qui ne sont pas observables en cas d'irradiation à la température ambiante. Cela nous a motivés à effectuer une étude détaillée de la dégradation des cellules TJ et de leurs cellules composantes respectives à des températures comprises entre 100 et 300 K.

De la même logique que le chapitre précédent, nous présenterons l'analyse des propriétés électriques des cellules TJ et de ses cellules constitutives sous irradiation d'électrons de 1 MeV à des différentes températures dans le **chapitre 4**. Les performances BOL et EOL dans l'obscurité (DIV) et sous illumination (LIV) à des différentes températures seront décrites, ainsi que les caractéristiques P-V (PV). En outre, les dépendances de fluence des paramètres électriques (courant de court-circuit  $I_{SC}$ , tension de circuit ouvert  $V_{OC}$ , puissance maximale  $P_{MAX}$  et facteur de remplissage FF) et les propriétés de recuit de chaque cellule composante seront décrites. En particulier dans ce chapitre, nous discuterons de la distribution de la performance EOL des cellules TJ qui n'est pas observée dans le cas de l'irradiation de protons.

Dans le **chapitre 5**, nous comparerons les cellules irradiées aux électrons avec celles qui ont été irradiées au proton dans des conditions LILT. En tant que méthode analytique, l'analyse de la densité de dommage par déplacement (DDD) a été adaptée. Elle est maintenant largement utilisée pour corrélérer les irradiations d'électrons et de protons avec diverses énergies et, éventuellement, pour la prévision de la dégradation des performances de cellules solaires dans l'espace. Une comparaison directe des valeurs de BOL et EOL de certains paramètres clés sera présentée afin de discuter de la large distribution de EOL  $P_{MAX}$  des cellules TJ irradiées par des électrons en condition LILT. Enfin, nous essayons de corrélérer la dégradation électrique de la TJ et de ses cellules constitutives avec les défauts induits par l'irradiation en conditions LILT.

## Conclusions générales

Le but de cette thèse était de comprendre le comportement de la cellule solaire à triple jonction GaInP / GaAs / Ge irradiée par des électrons et des protons dans des conditions de faible amplitude de rayonnement. À partir de ces expériences, en utilisant des électrons et des protons sur un grand nombre de cellules solaires TJ et ses cellules composantes, nous avons constaté que les mécanismes de dégradation sous irradiations aux électrons et aux protons dans des conditions LILT peuvent être très différents. Tout d'abord, un phénomène très particulier a été observé dans les cellules irradiées aux électrons : une large distribution de données de propriétés électriques (en particulier, le facteur de remplissage FF). Ce type de résultat n'a jamais été rapporté par des études antérieures sur les cellules TJ car il n'y a eu que peu de tentatives de test d'irradiation *in-situ* dans des conditions de LILT. De plus, la plupart des études relatives aux effets des cellules solaires sur les rayonnements ont été réalisées à la température ambiante. Conscient du manque de connaissances sur le sujet, nous avons irradié un certain nombre de cellules composantes à des températures variées et à des fluences très variées. De plus, des tests de recuit ont été effectués pour vérifier que la récupération des performances de la cellule solaire était corrélée à la nature des défauts induits par le rayonnement dans chaque type de matériaux.

L'origine d'une large distribution des valeurs de FF (affectant  $P_{MAX}$ ) des cellules TJ irradiées aux électrons était un courant en excès mesuré dans les caractéristiques I-V à l'obscurité. Étant donné que l'intensité de la source de lumière est très faible dans des conditions de faible intensité, une faible quantité de courant pourrait affecter de manière significative la dégradation des performances de la cellule. Le courant en excès est apparu dans chaque cellule, alors que son intensité était différente d'une cellule à l'autre. Les cellules composantes Ge au bas étaient les plus sensibles à l'irradiation des électrons dans des conditions de faible perte, suivies des cellules composantes du haut. Le courant en excès est également apparu dans les cellules composantes du milieu, mais sa quantité n'était pas trop importante pour affecter les performances de la cellule. Le point difficile de l'analyse du courant en excès était que l'apparition de ce courant en excès est très aléatoire. Il était certain qu'à des débits plus élevés, il y avait 'généralement' un excès de courant plus important. Cependant, cela variait aussi d'une cellule à l'autre même si toutes les autres conditions étaient identiques. Par le test de mesure I-V à l'obscurité, nous avons conclu que l'excès de courant provenait d'un effet tunnel indirect par des défauts créés par des irradiations d'électrons.

En revanche, les cellules irradiées aux protons n'ont montré aucune augmentation particulière du courant en excès lors de la mesure de l'I-V sombre. En raison de cette différence entre les irradiations par des électrons et par des protons, l'écart-type des cellules TJ irradiées par le  $P_{MAX}$  était beaucoup plus petit que celui des cellules irradiées par des électrons. L'autre découverte significative des cellules irradiées aux protons est que les cellules composantes du bas irradiées aux protons ont montré une dégradation de  $I_{SC}$  beaucoup plus importante que dans le cas de l'irradiation par des électrons. Après avoir éliminé la contribution de PRE des cellules composantes irradiées par des électrons et par des protons, les cellules irradiées aux protons avaient toujours des valeurs  $I_{SC}$  plus faibles. En outre, la chute

de courant d'une cellule composante du bas irradiée par des protons était trop importante pour modifier la cellule de limitation de courant en sous-cellule du bas à une température suffisamment basse (environ inférieure à 120 K). Nous avons conclu que l'irradiation de protons à basse température peut produire une grappe de défauts gelés le long du trajet de proton qui se comporte comme une zone isolante. Ce phénomène est bien observé dans la cellule du bas, car une partie de ses défauts est instable pour des températures comprises entre 100 et 300 K. Cette observation implique que l'une quelconque des trois sous-cellules peut être la cellule limitant le courant dans des conditions de LILT dans un environnement d'irradiation de protons.

Pour ces raisons, l'application de l'analyse de la dose de dommage par déplacement (DDD) aux cellules irradiées aux protons et aux électrons dans des conditions de faible amplitude (LILT) nécessite une attention particulière. Dans les conditions LILT, l'analyse DDD est toujours parfaitement adaptée pour la cellule GaAs, pas très bien pour la cellule GaInP et pas du tout pour la cellule Ge. L'analyse DDD sur  $I_{SC}$  semble être bien adaptée pour les trois cellules, mais ce n'est pas le cas pour  $V_{OC}$  et  $P_{MAX}$ . En conséquence, il en a été de même pour les cellules TJ. Par conséquent, pour créer une courbe de prédiction appropriée, il est nécessaire d'appliquer un facteur de modification pour les valeurs  $V_{OC}$  et  $P_{MAX}$  des cellules composantes du haut et du bas.

# *List of Publications*

## **Peer reviewed publications**

S. Park, J. C. Bourgoin, H. Sim, C. Baur, V. Khorenko, O. Cavani, J. Bourcois, S. Picard, and B. Boizot, “Space degradation of 3J solar cells: I-Proton irradiation,” *Prog. Photovolt. Res. Appl.*, vol. 23, no. 1, p. 1, Apr. 2018. DOI: 10.1002/pip.3016

S. Park, J. C. Bourgoin, H. Sim, C. Baur, V. Khorenko, O. Cavani, and B. Boizot, “Space degradation of 3J solar cells: II-Electron irradiation,” *to be submitted in 2018*.

S. Park, J. C. Bourgoin, C. Baur, and B. Boizot, “Solar cell degradation in space: electron/proton damage equivalence at low temperatures,” *to be submitted in 2018*.

## **Conference proceedings**

### **The 44<sup>th</sup> IEEE Photovoltaic Specialists Conference (PVSC 2017)**

S. Park, J. C. Bourgoin, O. Cavani, S. Picard, J. Bourcois, V. Khorenko, C. Baur, and B. Boizot, “Proton Irradiation of 3J Solar Cells at Low Temperature,” *the proceedings of the 44th IEEE PVSC*, Washington DC, Jun. 2017.

### **The 11<sup>th</sup> European Space Power Conference (ESPC 2016) – Published in E3S Web of Conferences**

S. Park, J. C. Bourgoin, O. Cavani, V. Khorenko, C. Baur, and B. Boizot, “Origin of the Degradation of Triple Junction Solar Cells at low Temperature,” *E3S Web Conf.*, vol. 16, no. 1, pp. 04004–4, May 2017

C. Baur, V. Khorenko, G. Siefer, V. Inguibert, S. Park, B. Boizot, J. C. Bourgoin, M. Casale, R. Campesato, H.-G. Schnell, A. Gerhard, P. Zanella, E. Ferrando, X. Reutenauer, E. Bongers, and A. Gras, “Status of Solar Generator Related Technology Development Activities Supporting the Juice Mission,” *E3S Web Conf.*, vol. 16, no. 8, pp. 04005–8, May 2017.

V. Khorenko, C. Baur, G. Siefer, M. Schachtner, S. Park, B. Boizot, J. C. Bourgoin, M. Casale, and R. Campesato, “BOL and EOL Characterization of AZUR 3G LILT Solar Cells for ESA JUICE Mission,” *E3S Web Conf.*, vol. 16, no. 8, pp. 03011–5, May 2017.

## **Awards**

Best student paper award from the 44<sup>th</sup> IEEE PVSC, Jun. 2016.

“Proton Irradiation of 3J Solar Cells at Low Temperature,” Area 7: Space Solar Cell Concepts

# List of Figures

Figure 0-1. the first solar powered satellite Vanguard 1. ....	9
Figure 0-2. Chart of best research-cell efficiencies updated by NREL at 25/04/2018. ....	10
Figure 0-3. Juno mission to Jupiter (2010 Artist's concept). ....	11
Figure 0-4. Artist's impression of JUICE mission. ....	12
Figure 1-1. Equivalent circuit diagram of an illuminated solar cell based on two diodes model. ....	15
Figure 1-2. Current-Voltage (I-V) curve of a solar cell in dark and under illumination. ....	16
Figure 1-3. Conventional I-V curve of an illuminated solar cell (effect of series and shunt resistances on electrical characteristics). ....	17
Figure 1-4. A pn junction in forward bias: (a) minority carrier distribution in two side of depletion region with a graphical instruction of distance $x_n$ and $x_p$ from the interface of depletion and charge neutral regions; (b) band banding diagram with variation of quasi-Fermi level with position[3]. ....	20
Figure 1-5. Representative figure of a structure of solar cell with a window layer on the top of junction. Current densities in window, emitter, depletion region, and base due to excess carriers are noted as $J_D$ , $J_{D+d}$ , $J_W$ , and $J_{D+d+W}$ , respectively. ....	27
Figure 1-6. The number of displacement by the cascade as a function of PKA energy (from K-P model). ....	33
Figure 1-7. Tentative representation of identification of radiation induced traps in GaAs. ....	40
Figure 1-8. Tentative representation of identification of radiation induced traps in GaInP. ....	44
Figure 1-9. Tentative representation of identification of electron irradiation induced traps in Ge. ....	49
Figure 2-1. Simple configuration of in-situ LILT measurement system set up for solar cells under irradiation. ....	60
Figure 2-2. View of the pelletron type NEC electron accelerator at SIRIUS: (a) close view of inside – pelletron charging system, (b) accelerator tank, and (c) irradiation beam lines. ....	61
Figure 2-3. Scattering of electrons by the window and fluence calibration procedure. ....	62
Figure 2-4. Representative configuration of Irradiation facility of Centre de Sciences Nucléaires et de Sciences de la Matière (CSNSM). ....	63
Figure 2-5. Vertical view of the solar simulator. ....	64
Figure 2-6. Evolution of the Xenon lamp spectrum recorded during 24 hours. ....	65
Figure 2-7. Evolution of $I_{SC}$ measurement of three reference component cells during 24 hours. ....	66
Figure 2-8. Reference component cells and the placements for the stability verification of the solar simulator. ....	67
Figure 2-9. (a) Inside view of the cryostat chamber and (b) total view of the cryostat system. ....	68
Figure 2-10. (a) $2 \times 2 \text{ cm}^2$ AZUR 3G28 GaInP/GaAs/Ge triple junction solar cell (Ge substrate $80 \mu\text{m}$ ) and (b) Layer composition of the lattice matched GaInP/GaAs/Ge triple junction solar cell grown on the p-type Ge substrate. ....	70
Figure 2-11. Simplified representation of structures of a TJ and its component cells. ....	71
Figure 2-12. EQE of the Ge sub-cell and component cell [4]. ....	71
Figure 2-13. EQE of a Ge component cell before and after irradiation. The photon cycling from the upper layers is suppressed due to the degradation of the material quality after irradiation the sample [4]. ....	72
Figure 2-14. I-V characteristics of an electron irradiated Ge bottom component cell at room temperature under illumination and in dark (inset). ....	73
Figure 2-15. Evolution of $I_{SC}$ of a bottom component cell at temperature ranging from 100 to 300 K. (a) 1 – decrease of temperature before irradiation, 2 – irradiation with a fluence of $1 \times 10^{14} \text{ cm}^{-2}$ , 3 – increase of temperature after irradiation, 4 – decrease of temperature after room temperature annealing. (b) Same procedure as (a), except the fact that the cell is irradiated once again with the same fluence as conducted at (a). ....	74
Figure 2-16. A picture of a $2 \times 2 \text{ cm}^2$ solar cell with CERNOX® temperature sensor glued on the surface of the cell using high thermal conductivity STYCAST. ....	75
Figure 2-17. Temperature of the support versus temperature of the cell measured with the CERNOX sensor. ....	76

Figure 2-18. Measurement of $T_{\text{Support}}$ and $T_{\text{Cernox}}$ of a 3G28 80 $\mu\text{m}$ TJ cell at low temperatures during irradiation with fluxes of $2.5 \times 10^{11}$ and $5 \times 10^{11} \text{ cm}^{-2}\text{s}^{-1}$ .....	77
Figure 2-19. Measurement of $V_{\text{OC}}$ of a TJ cell and $T_{\text{Support}}$ during temperature control from 300 to 120 K.....	78
Figure 2-20. An example of thermal cycling test of the TJ solar cell (1295-4378E-5) as a part of test readiness review (TRR): I-V characteristics under illumination.....	79
Figure 2-21. Histogram of BOL Efficiency, $P_{\text{MAX}}$ , $V_{\text{OC}}$ and $I_{\text{SC}}$ of 3G28 140 $\mu\text{m}$ TJ cells used for JUICE 2015 irradiation campaign: left side – measured at 300 K, right side – measured at 120 K. (Number of cells: 24 pcs).....	81
Figure 2-22. Histogram of BOL Efficiency, $P_{\text{MAX}}$ , $V_{\text{OC}}$ and $I_{\text{SC}}$ of 3G28 80 $\mu\text{m}$ TJ cells used for JUICE 2016 irradiation campaign: left side – measured at 300 K, right side – measured at 120 K. (Number of cells: 102 pcs).....	82
Figure 2-23. an example of in-situ test sequence of an electron irradiated TJ cell in LILT condition including an annealing process.....	83
Figure 2-24. Import multiple data into an excel file to automatically create individual sheet containing all I-V information of related test sequence. ....	87
Figure 2-25. An example of the created excel sheet which contains calculated key parameters of solar cell, raw and converted I-V data, and automatically created light and dark I-V curves.....	88
Figure 3-1. SRIM simulation with 1 MeV proton irradiation on the TJ cell used in this study. (a) Profile of ion propagation, (b) Ionization energy loss versus target depth and (c) Ion ranges. Displacement energy ( $T_{\text{D}}$ ) of 21 eV is applied for three materials.....	92
Figure 3-2. BOL and EOL (after 1 MeV proton irradiation at 123 K with $4 \times 10^{11} \text{ cm}^{-2}$ ) electrical properties of 1520-030 TJ solar cell at 123 and 300 K under illumination: (a) I-V curves and (b) P-V curves. ....	93
Figure 3-3. Remaining factor of key parameters of 1 MeV proton irradiated TJ solar cells at 123 K: (a) open-circuit voltage $V_{\text{OC}}$ , short-circuit current $I_{\text{SC}}$ and (b) product $I_{\text{SC}} \times V_{\text{OC}}$ , fill factor FF and maximum power $P_{\text{MAX}}$ .....	94
Figure 3-4. Fluence dependences of (a) $I_{\text{SC}}$ and (b) $V_{\text{OC}}$ of component cells at 100, 123, 200 and 300 K irradiated at 1 MeV with a flux $4 \times 10^9 \text{ cm}^{-2}\text{s}^{-1}$ . Black square, red circle, and blue triangle indicate top, middle and bottom component cells, respectively. ....	96
Figure 3-5. $I_{\text{SC}}$ remaining factor of bottom component cells irradiated at various temperatures with a flux of $4 \times 10^9 \text{ cm}^{-2}\text{s}^{-1}$ : (a) before correction and (b) after corrections of the PRE.....	97
Figure 3-6. Comparison of the degradations of TJ cells with that deduced from the degradation of component cells: (a) $I_{\text{SC}}$ and (b) $V_{\text{OC}}$ at 100, 123, 200 and 300 K: Black circle and red star indicate data obtained from component cells and TJ cells, respectively. ....	98
Figure 3-7. BOL and EOL I-V characteristics in dark of a proton irradiated TJ cell (662E-84) at 100 K. (fluence: $\text{cm}^{-2}$ ) .....	99
Figure 3-8. Diagram of light I-V measurement of a multi-junction solar cell composed of two sub-cells. ....	100
Figure 3-9. BOL and EOL I-V characteristics of a TJ cell irradiated with $1.6 \times 10^{12} \text{ cm}^{-2}$ at 123 K (black curve: dark I-V, red curve: dark I-V + $I_{\text{SC}}$ (EOL), blue curve: light I-V).....	101
Figure 3-10. BOL and EOL I-V characteristics of top, middle, and bottom component cells irradiated at 123 K with $8 \times 10^{11} \text{ cm}^{-2}$ (black curve: dark I-V, red curve: dark I-V + $I_{\text{SC}}$ (EOL), blue curve: light I-V).....	101
Figure 3-11. Penetration depth of 1 and 2 MeV proton irradiation (inset: ion profiles): (a) and (c) angle of incidence is 0 degree and (b) and (d) angle of incidence is 60 degrees. ....	102
Figure 3-12. Ionization energy of 1 and 2 MeV proton in GaInP/GaAs/Ge TJ solar cell structure: (a) and (c) normal incident (angle is 0 degree) and (b) and (d) 60 degree of angle of incidence is applied to the structure; the effective thickness of all layers is doubled. ....	103
Figure 3-13. Simplified diagram showing an effect of change of the orientation of proton irradiation on the fluence. ....	104
Figure 3-14. Relative degradation of $I_{\text{SC}}$ of 1 MeV proton irradiated (a) top and (b) bottom component cells: $(\text{BOL } I_{\text{SC}} - \text{EOL } I_{\text{SC}}) / \text{BOL } I_{\text{SC}}$ at 123 K with different angles of incidence (0, 30 and 60 degrees). ....	105

Figure 3-15. Relative degradation of $I_{SC}$ of 2 MeV proton irradiated (a) top, (b) middle and (c) bottom component cells: $(BOL I_{SC} - EOL I_{SC})/BOL I_{SC}$ , at 123 K and at 300 K (RT) with different angles of incidence (0, 30, 50 and 60 degrees). .....	106
Figure 3-16. Compensated relative degradation of $I_{SC}$ of bottom component cells at 123 K (angular coefficient is applied to compensate the effective thickness of the layers of the bottom component cell: (a) 1 MeV and (b) 2 MeV proton irradiations. ....	107
Figure 3-17. (a) Remaining factors of $I_{SC}$ , $V_{OC}$ and $P_{MAX}$ of proton irradiated (1 MeV, $1.6 \times 10^{12} \text{ cm}^{-2}$ ) component cells during isochronal annealing stages: black square – top, red circle – middle, blue triangle – bottom cells, respectively. Temperature profile of isochronal annealing stages is represented: (b) top and middle cells and (c) bottom cell. ....	109
Figure 3-18. $1 - RF(I_{SC})$ versus temperature in bottom component cells irradiated with various fluences ( $\text{cm}^{-2}$ ). ....	111
Figure 3-19. $RF(I_{SC})$ versus $T^{-2}$ of proton irradiated bottom component cells. ....	112
Figure 3-20. Fluence-temperature diagram indicating the regions in which a sub-cell is limiting the TJ cell: circle and cross symbols indicate transition points of current limiting from top to bottom and from top to middle sub-cell, respectively. ....	113
Figure 3-21. Simplified description of the electric field dependence of trap assisted recombination current ( $I_{tr}$ ) – band diagram (a) without bias, (b) positive bias and (c) a simple diagram of the electric field dependent capture rate of carriers on defects. ....	114
Figure 3-22. Voltage dependence of $I_{tr}$ of top (left) and middle (right) component cells at 123 and 300 K (inset) for different fluences ( $\text{cm}^{-2}$ ). ....	115
Figure 4-1. BOL and EOL (after 1 MeV electron irradiation at 123 K with $3 \times 10^{15} \text{ cm}^{-2}$ ) electrical properties of 1295-0443E-26 TJ solar cell at 123 and 300 K under illumination: (a) I-V curves and (b) P-V curves. ....	121
Figure 4-2. BOL and EOL I-V characteristics in dark (log scale) and under illumination of two TJ cells at 123 K: 1295-4299E-34 (a and b) and 1295-0443E-23 (c and d). ....	122
Figure 4-3. Relationship between $I_{Dark}$ at 2 V and $P_{MAX}$ of each electron irradiated TJ cell at 123 K. ....	123
Figure 4-4. BOL and EOL I-V characteristics in dark and under illumination of a 1295-0443E-23 TJ cell at 123 K, irradiated with 1MeV electrons. ....	124
Figure 4-5. Remaining factor of (a) $I_{SC}$ , $V_{OC}$ , (b) $I_{SC} \times V_{OC}$ , FF, $P_{MAX}$ of TJ solar cells at 123 and 300 K. ....	125
Figure 4-6. $I_{SC}$ and $V_{OC}$ versus fluence of top (black square), middle (red circle), bottom (blue triangle) component cells at 100, 123, 200 and 300 K. ....	127
Figure 4-7. I-V characteristics of component cells before and after electron irradiation at 123 K. Appearance of excess currents from all component cell after irradiation with a fluence of $3 \times 10^{15} \text{ cm}^{-2}$ . ....	129
Figure 4-8. BOL and EOL dark I-V characteristics of a bottom component cell (0399-B) cumulatively irradiated up to a fluence of $3 \times 10^{15} \text{ cm}^{-2}$ at 123 K. After each step of irradiation, annealing at 143 K (LA) for 10 minutes was carried out for an accelerated defect annealing at low temperature. RT annealing (RA) result is included for comparisons. ....	130
Figure 4-9. LA and RA annealing effects on light I-V characteristics of an electron irradiated bottom component cell (0399-B) at a fluence of $3 \times 10^{15} \text{ cm}^{-2}$ . ....	131
Figure 4-10. EOL dark I-V characteristics of an electron irradiated bottom component cell at different temperatures: the measurement (b) is performed after the measurement (a). ....	132
Figure 4-11. EOL Dark I-V characteristics of top (a) and middle (b) component cells irradiated with a fluence of $3 \times 10^{15} \text{ cm}^{-2}$ at 123 K. The DIV measurements are realized increasing the temperature from 100 to 300 K after annealing at 300 K. ....	133
Figure 4-12. Changes of $I_{SC}$ , $V_{OC}$ , $P_{MAX}$ , FF Remaining factors of electron irradiated (a) top and (b) bottom component cells during isochronal annealing (measured at 96 K: the lowest cell temperature that can be achieved using liquid nitrogen pumping). Cells irradiated with a fluence of $1 \times 10^{15} \text{ cm}^{-2}$ at 96 K. ....	134
Figure 4-13. $P_{MAX}$ versus $I_{Dark}$ at 2 V of electron irradiated TJ cells at 123 K. ....	135
Figure 4-14. Tunneling current at defect created by irradiation in depletion zone. ....	136
Figure 5-1. Representative diagram of approximate energy loss of incident 1 and 2 MeV proton in the studied TJ solar cell. ....	141

Figure 5-2. Non-Ionizing Energy Loss (NIEL) versus energy of proton (red) and electron (black) in GaAs ( $E_d = 21$ eV) calculated using Screen Relativistic (SR)[2].	142
Figure 5-3. Relative degradation of (a) $I_{SC}$ , (b) $V_{OC}$ , (c) FF and (d) $P_{MAX}$ of the 3G28 TJ solar cell as a function of displacement damage dose converted from electron and proton fluences based on the NIEL calculation on an atomic displacement energy of $E_d = 21$ eV (the value used for the NIEL calculation of GaAs solar cell [1]). Black square – 1 MeV proton, white square – 1 MeV electron, black circle – 2 MeV proton, and white circle – 2 MeV electron. Represented data are average values with standard deviation.	143
Figure 5-4. Relative degradation of (a) $I_{SC}$ , (b) $V_{OC}$ , (c) FF and (d) $P_{MAX}$ of the top component cell as a function of displacement damage dose converted from electron and proton fluences based on the NIEL calculation on atomic displacement energies of $E_d = 10, 7$ and $9$ eV for Ga, In and P, respectively (values taken from the ref. [3]). Black square – 1 MeV proton, white square – 1 MeV electron, black circle – 2 MeV proton, and white circle – 2 MeV electron. Represented data are average values with standard deviation.	145
Figure 5-5. DIV (left) and LIV (right) of an electron irradiated top component cell at LILT conditions.	146
Figure 5-6. Relative degradation of (a) $I_{SC}$ , (b) $V_{OC}$ , (c) FF and (d) $P_{MAX}$ of the middle component as a function of displacement damage dose converted from electron and proton fluences based on the NIEL calculation on an atomic displacement energy of $E_d = 21$ eV (the value taken from the ref. [1]). Black square – 1 MeV proton, white square – 1 MeV electron, black circle – 2 MeV proton, and white circle – 2 MeV electron. Represented data are average values with standard deviation.	147
Figure 5-7. Relative degradation of (a) $I_{SC}$ , (b) $V_{OC}$ , (c) FF and (d) $P_{MAX}$ of the bottom component cell as a function of displacement damage dose converted from electron and proton fluences based on the NIEL calculation on an atomic displacement energy of $E_d = 21$ eV (the value taken from the ref. [4]). Black square – 1 MeV proton, white square – 1 MeV electron, black circle – 2 MeV proton, and white circle – 2 MeV electron. Represented data are average values with standard deviation.	148
Figure 5-8. Dark I-V characteristics, measured at 123 K, of 1 MeV protons ( $2 \times 10^{11}$ cm <sup>-2</sup> ) (a) and 1 MeV electrons ( $3 \times 10^{15}$ cm <sup>-2</sup> ) (b) irradiated Ge component cells at 123 K.	149
Figure 5-9. Distribution of absolute FF and $P_{MAX}$ values (BOL, EOL and RT annealed EOL) of electron irradiated JUICE 3G28 TJ solar cells in LILT conditions.	150
Figure 5-10. Distribution of absolute FF and $P_{MAX}$ values (BOL, EOL and RT annealed EOL) of proton irradiated JUICE 3G28 TJ solar cells in LILT conditions. (maximum proton fluence only).	151

# List of Tables

Table 1-1. Identification of electron irradiated induced defects in n-type GaAs: Peak temperature $T_0$ (for an emission rate of $70 \text{ s}^{-1}$ ), introduction rate $\tau$ for 1 MeV electron irradiation, energy level $E_e$ (from the conduction band), capture cross-section $\sigma$ , annealing temperature $T_a$ , activation energy associated with the annealing $E_a$ , pre-exponential factor of the annealing rate $\nu$ [25], [26].	36
Table 1-2. Identification of electron irradiation induced defects in p-type GaAs: Peak temperature $T_0$ (for an emission rate of $70 \text{ s}^{-1}$ ), introduction rate $\tau$ for 1 MeV electron irradiation, energy level $E_e$ (from the valence band), capture cross-section $\sigma$ , annealing temperature $T_a$ [29], [31].	37
Table 1-3. Identification of 6.7 MeV proton irradiation induced defects in n-type GaAs: energy level $E_e$ (from the conduction band), capture cross-section $\sigma$ [34].	39
Table 1-4. Identification of 100 keV proton irradiation induced defects in n-type GaAs: energy level $E_e$ (from the conduction band), capture cross-section $\sigma$ [35].	39
Table 1-5. Identification of 1 MeV electron irradiated induced defects in n-type ( $1.2 \times 10^{19} \text{ cm}^{-3}$ ) GaInP: Peak temperature $T_0$ , introduction rate $\tau$ , thermal activation energy level $E_e$ (from $E_C$ for electron traps, from $E_V$ for hole traps), capture cross-section $\sigma$ , annealing temperature $T_a$ [43].	41
Table 1-6. Identification of 1 MeV electron irradiated induced defects in n <sup>+</sup> /p GaInP solar cell: Peak temperature $T_0$ , introduction rate $\tau$ , thermal activation energy level $E_e$ (from $E_C$ for electron traps, from $E_V$ for hole traps), capture cross-section $\sigma$ , annealing temperature $T_a$ [44].	42
Table 1-7. Identification of 3 MeV proton irradiated induced defects in n <sup>+</sup> /p GaInP solar cell: thermal activation energy level $E_e$ (from $E_C$ for electron traps, from $E_V$ for hole traps), density of traps $N_T$ [50].	43
Table 1-8. Identification of 1 MeV electron irradiated induced defects in n-type Ge: Thermal activation energy level $E_e$ (from $E_C$ for electron traps, from $E_V$ for hole traps), capture cross-section $\sigma$ [58].	46
Table 1-9. Identification of 2 MeV electron and proton irradiated induced defects in n-type Ge: Thermal activation energy level $E_e$ (from $E_C$ for electron traps, from $E_V$ for hole traps), capture cross-section $\sigma$ , annealing temperature, identifications, type of sample, and type of radiation particles are described [69].	48
Table 2-1. Calibration of the solar simulator using $I_{SC}$ measurement.	67
Table 2-2. Set of the range of voltage used for I-V measurement of cells at different temperatures.	69
Table 2-3. Test readiness review (TRR) of three TJ solar cells at 120 K: $I_{SC}$ , $V_{OC}$ and $P_{MAX}$ were recorded during three times of tests: AVG means averaged values measured at different steps at 120 K. STDEV is a standard deviation of the average. CV, coefficient of variation, indicates the value of standard deviation divided by average.	80
Table 2-4. In-situ test sequence during the irradiation at low temperature	84
Table 2-5. List of irradiated 3G28 and 3G 30 TJ cells during 2015 JUICE campaign.	85
Table 2-6. List of irradiated 3G28 TJ cells during 2016 JUICE campaign.	86
Table 3-1. Electrical properties of 1520-030 TJ cell measured at 123 and 300 K before and after 1 MeV proton irradiation at 123 K (fluence = $4 \times 10^{11} \text{ cm}^{-2}$ ).	94
Table 3-2. Isochronal annealing of remaining factor of $I_{SC}$ , $V_{OC}$ and $P_{MAX}$ of 1 MeV proton irradiated top and middle component cells (measured at 100 K. irradiated with a fluence of $1.6 \times 10^{12} \text{ cm}^{-2}$ ).	110
Table 4-1. Degradation measured at 123 and 300 K of $I_{SC}$ , $V_{OC}$ , FF, $P_{MAX}$ of 1 MeV electron irradiated TJ cell at 123 K ( $3 \times 10^{15} \text{ cm}^{-2}$ ).	122





**Titre :** Influence de l'irradiation dans les cellules solaires triple jonctions pour les applications spatiales

**Mots clés :** cellules solaires, irradiation, défauts induits par l'irradiation, recuit, tunnel, LILT

**Résumé :** Cette thèse est le résultat d'un travail sur l'effet d'irradiation de cellules solaires à triple jonction (TJ) GaInP/GaAs /Ge en forme de réseau dans des conditions LILT. Initié par les besoins de la compréhension des performances EOL des cellules solaires dans la mission JUICE, nous avons trouvé des phénomènes très particuliers qui ne sont pas supposés se produire si celle-ci a été irradiée à température ambiante. Tout d'abord, une cellule de composante inférieure montrait une plus grande chute d' $I_{sc}$  à une température plus basse, ce qui suggère potentiellement une limitation de courant par la sous-cellule inférieure dans la structure TJ. Une dépendance en température de la récupération  $RF(I_{sc})$  par un recuit isochrone et, la dépendance d'orientation de la dégradation  $I_{sc}$  de la cellule composante inférieure impliquaient que son mécanisme de dégradation pourrait être lié à des grappes de défauts formées comme des zones isolantes (non actives) pour les transporteurs minoritaires. Par ailleurs, nous avons observé en général une plus grande dégradation de FF et  $P_{MAX}$  des cellules TJ irradiées par les électrons, par rapport aux cellules irradiées aux protons. Cette nette différence provient surtout des sous-cellules supérieure et inférieure en raison de l'apparition d'un courant d'obscurité excessif.

Ce courant supplémentaire dans l'obscurité semble être lié à l'effet tunnel indirect par des défauts induits par l'irradiation électronique. En outre, EOL FF et  $P_{MAX}$  semblaient se propager de plus en plus d'une cellule à l'autre à mesure que la fluence des électrons augmentait. Une approche de dose d'endommagement par déplacement (DDD) a été appliquée à des cellules TJ irradiées par des électrons et des protons de 1 et 2 MeV et à ses cellules composantes. Il s'est avéré que les électrons de 2 MeV induisaient une plus grande dégradation que les autres pour tous les paramètres ( $I_{sc}$ ,  $V_{OC}$ , FF,  $P_{MAX}$ ). La cellule du milieu a montré une correspondance parfaite de DDD entre les cellules irradiées par électrons et protons en condition LILT, indiquant que les défauts finaux produits par les irradiations par électrons et protons sont peut-être les mêmes. La TJ et sa cellule de composant supérieur présentaient moins de dégradation sur les  $V_{OC}$  sous irradiation électronique que l'irradiation protonique. Pour la cellule du composant de Ge, l'irradiation électronique a induit une dégradation beaucoup plus importante des  $V_{OC}$ , FF et  $P_{MAX}$  par rapport à l'irradiation protonique. Pour améliorer la dureté de rayonnement des cellules en réduisant le courant d'obscurité en excès, il serait intéressant de diminuer la concentration en dopage des jonctions pour réduire la création de défauts secondaires liés aux impuretés.

**Title:** Irradiation effects in GaInP/GaAs/Ge triple junction solar cells for spatial applications

**Keywords:** solar cells, irradiation, radiation induced defects, annealing, tunneling, LILT

**Abstract:** This thesis is the result of work on the irradiation effect of lattice matched GaInP/GaAs/Ge triple junction (TJ) solar cells in LILT conditions. Initiated by needs of the understanding of EOL performances of the solar cells in JUICE mission, we have found very peculiar phenomena which are not supposed to occur if it was irradiated at room temperature. First, a bottom component cell exhibited a larger drop of  $I_{sc}$  at a lower temperature, which potentially proposes a current limiting by the bottom sub-cell in the TJ structure. A temperature dependence of  $RF(I_{sc})$  recovery by an isochronal annealing and the orientation dependence of  $I_{sc}$  degradation of the bottom component cell have implied that its degradation mechanism could be related to defect clusters formed along proton tracks, acting like insulating (non active) area for minority carriers. Second, we have observed in general larger degradation of FF and  $P_{MAX}$  from electron irradiated TJ cells compared to proton irradiated ones. This distinct difference has originated especially from the top and bottom sub-cells due to the occurrence of excess dark current.

This additional current in dark seems to be related to the indirect tunneling effect by defects induced by electron irradiation. Furthermore, EOL FF and  $P_{MAX}$  appeared to be more and more spread from cell to cell as the electron fluence increased. A displacement damage dose (DDD) approach was applied to 1 and 2 MeV electron and proton irradiated TJ cells and its component cells. It turned out that 2 MeV electrons induced greater degradation than others for all parameters ( $I_{sc}$ ,  $V_{OC}$ , FF,  $P_{MAX}$ ). The middle component cell showed almost a perfect match of DDD between electron and proton irradiated cells in LILT condition, indicating that the final defects produced by electron and proton irradiations are perhaps the same. TJ and its top component cell showed less degradation on  $V_{OC}$  under the electron irradiation compared to the proton irradiation. For the Ge bottom component cell, the electron irradiation induced much larger downgrading of  $V_{OC}$ , FF and  $P_{MAX}$  compared to the proton irradiation. To improve the radiation hardness of the cells by reducing the excess dark current, it would be worth to decrease the doping concentration of junctions to reduce the creation of secondary defects related to impurities.

